

529408

1688

TR/IN/02

NASA/TP-2001-210629



Flight, Wind-Tunnel, and Computational Fluid Dynamics Comparison for Cranked Arrow Wing (F-16XL-1) at Subsonic and Transonic Speeds

*John E. Lamar, Clifford J. Obara, and Bruce D. Fisher
Langley Research Center, Hampton, Virginia*

*David F. Fisher
Dryden Flight Research Center, Edwards, California*

February 2001

The NASA STI Program Office . . . in Profile

Since its founding, NASA has been dedicated to the advancement of aeronautics and space science. The NASA Scientific and Technical Information (STI) Program Office plays a key part in helping NASA maintain this important role.

The NASA STI Program Office is operated by Langley Research Center, the lead center for NASA's scientific and technical information. The NASA STI Program Office provides access to the NASA STI Database, the largest collection of aeronautical and space science STI in the world. The Program Office is also NASA's institutional mechanism for disseminating the results of its research and development activities. These results are published by NASA in the NASA STI Report Series, which includes the following report types:

- **TECHNICAL PUBLICATION.** Reports of completed research or a major significant phase of research that present the results of NASA programs and include extensive data or theoretical analysis. Includes compilations of significant scientific and technical data and information deemed to be of continuing reference value. NASA counterpart of peer-reviewed formal professional papers, but having less stringent limitations on manuscript length and extent of graphic presentations.
- **TECHNICAL MEMORANDUM.** Scientific and technical findings that are preliminary or of specialized interest, e.g., quick release reports, working papers, and bibliographies that contain minimal annotation. Does not contain extensive analysis.
- **CONTRACTOR REPORT.** Scientific and technical findings by NASA-sponsored contractors and grantees.
- **CONFERENCE PUBLICATION.** Collected papers from scientific and technical conferences, symposia, seminars, or other meetings sponsored or co-sponsored by NASA.
- **SPECIAL PUBLICATION.** Scientific, technical, or historical information from NASA programs, projects, and missions, often concerned with subjects having substantial public interest.
- **TECHNICAL TRANSLATION.** English-language translations of foreign scientific and technical material pertinent to NASA's mission.

Specialized services that complement the STI Program Office's diverse offerings include creating custom thesauri, building customized databases, organizing and publishing research results . . . even providing videos.

For more information about the NASA STI Program Office, see the following:

- Access the NASA STI Program Home Page at <http://www.sti.nasa.gov>
- Email your question via the Internet to help@sti.nasa.gov
- Fax your question to the NASA STI Help Desk at (301) 621-0134
- Telephone the NASA STI Help Desk at (301) 621-0390
- Write to:
NASA STI Help Desk
NASA Center for AeroSpace Information
7121 Standard Drive
Hanover, MD 21076-1320

NASA/TP-2001-210629



Flight, Wind-Tunnel, and Computational Fluid Dynamics Comparison for Cranked Arrow Wing (F-16XL-1) at Subsonic and Transonic Speeds

*John E. Lamar, Clifford J. Obara, and Bruce D. Fisher
Langley Research Center, Hampton, Virginia*

*David F. Fisher
Dryden Flight Research Center, Edwards, California*

National Aeronautics and
Space Administration

Langley Research Center
Hampton, Virginia 23681-2199

February 2001

Acknowledgments

Many individuals contributed to the gathering of the flight, wind-tunnel, and computational data in this report. A highly integrated effort was required in order to compare these data. To that end, a by-product of this paper was the development of a highly skilled and motivated team. This team consisted primarily of direct management and software support from the Langley Research Center (LaRC) and the Computer Sciences Corporation (CSC), Systems Sciences Division, Hampton, VA. At LaRC, the key people were Kathryn Stacy, Kurt S. Severance, Catherine K. Cronin, Donald P. Randall, Patricia A. Kerr, Michael D. Weisenborn, Susan J. Rickard, and David E. Hahne; at CSC, the key people were Christine G. Matthews, Dana P. Hammond, Raymond L. Gates, Robert C. Auberg, Joseph F. Reisel, Gerald H. Mall, Susan S. Bowen, S. Blake Williams, Rachel Gartenberg, Norma F. Bean, Javier A. Garriz, and David A. Wolverton. Individual contributions ranged from data translation done by Patricia A. Kerr, Dana P. Hammond, and Robert C. Auberg; image fusions done by Kathryn Stacy; special data comparisons done by Kurt S. Severance, David A. Wolverton, Gerald H. Mall, Susan S. Bowen, S. Blake Williams, Rachel Gartenberg, and Stephen J. Alter, Lockheed Martin Engineering and Sciences Corporation, Hampton, VA; data base management work done by Catherine K. Cronin, Donald P. Randall, Joseph F. Reisel, and Raymond L. Gates; initial geometry, computational gridding, and solution work done by Anutosh Moitra, High Technology Corporation, Hampton, VA; final geometry and computational gridding work done by Norma F. Bean; initial computational solutions on final grid performed by Javier A. Garriz; computational camera location and viewing work done by Michael D. Weisenborn; and low-speed wind-tunnel data provided by Susan J. Rickard and David E. Hahne.

The authors wish to thank the following people from LaRC for the many helpful suggestions arising from their review of this manuscript: Laurence D. Leavitt, Jerry M. Allen, Scott G. Anders, Jay M. Brandon, Wendy B. Lessard, Kurt S. Severance, and Georgina R. Branco of NASA Dryden Flight Research Center. Also, thanks are given to the Library and Media Services Branch of the Langley Research Center who published this document, with special acknowledgment to the NCI Technical Publications Support Group at Langley (Leanna Dee Bullock, Eloise Johnson, Una Thomas, Martha Jones, Patricia Gottschall, Mary Edwards, and Cathy Everett).

The use of trademarks or names of manufacturers in this report is for accurate reporting and does not constitute an official endorsement, either expressed or implied, of such products or manufacturers by the National Aeronautics and Space Administration.

Available from:

NASA Center for AeroSpace Information (CASI)
7121 Standard Drive
Hanover, MD 21076-1320
(301) 621-0390

National Technical Information Service (NTIS)
5285 Port Royal Road
Springfield, VA 22161-2171
(703) 605-6000

Contents

Symbols	v
Summary	1
Geometry	1
Flight, CFD, and Wind-Tunnel Surface Pressures	1
Boundary Layer	1
Data Fusion	1
Introduction	1
Basic Data Types and Test Conditions	2
Geometry	2
Airplane description	2
Details and comparisons	3
Flight	3
Data collected	3
Procedures and accuracy of data collection	3
Pressures	4
Visual	5
Hot film	5
Wind Tunnel	5
0.11-scaled model tests	5
0.18-scaled model test	5
0.04-scaled model test	6
CFD	6
CFL3D flow solver code and grid	6
Computer requirements and sample convergence histories	6
Using the solution file	6
CFD Comparisons	7
Surface Pressures	7
Subsonic	7
Transonic	8
Contours	9
Boundary-Layer Profiles at FC 7	9
Skin Friction at FC 7	10
On and Off Surface Flow Features at FC 46	11
EFD Basic Data and Comparisons	11
Forces and Moment in Wind Tunnel	11
Surface Pressures in Wind Tunnel	11
Effect of model scale and R_n on C_p at low speed	11
Transonic $C_{p,u}$ contours	12

On and Off Surface Flow (Air Dams Off) in Wind Tunnel	12
Surface Flow in Flight	12
Concluding Remarks	13
Appendix A—Visualization Tools	15
Appendix B—Data Processes and Management	17
Appendix C—Airplane Instrumentation	19
Appendix D—Description of Wind-Tunnel Test and Vapor-Screen Systems	29
References	33
Tables	35
Figures	63

Symbols

A	wing aspect ratio, $\frac{b^2}{S_{\text{ref}}}$, 1.75
AMRAAM	advanced medium range air-to-air missile
BART	Langley Basic Aerodynamic Research Tunnel
BL	butt line on airplane, positive on right wing, in. (see fig. 2)
b	wingspan, 32.4 ft (full scale)
C_D	drag coefficient
C_L	lift coefficient
C_m	pitching-moment coefficient
C_p	static-pressure coefficient
CAWAP	Cranked-Arrow Wing Aerodynamics Project
CFD	computational fluid dynamics
c_f	local skin friction coefficient
c_r	theoretical root chord for F-16XL airplane, 41.75 ft (full scale)
\bar{c}	reference wing chord, 24.7 ft (full scale)
EFD	experimental fluid dynamics, flight- or ground-based measurements
ESP	electronic scanning pressure
FAST	Flow Analysis Software Toolkit
FC	flight condition
Flt	flight number
FS	fuselage station on airplane, positive aft, in. (see fig. 2)
FV	flow visualization
GPS	global positioning system
HF	hot-film sensors
HUD	heads-up display
h	altitude, ft
I.D.	inside diameter
i, j, k	grid indices
L^2 (residual)	residual of the L^2 norm plotted on log scale
LE	leading edge
LS, low	lower surface
LT	loaded turn
M	Mach number
M_∞	free-stream Mach number
NAS	Numerical Aerodynamics Simulation
O.D.	outside diameter
PGME	propylene glycol methyl ether

PrISM	Program for Information Storage and Management
PSP	pressure sensitive paint
PT	modified Preston tubes
p	free-stream static pressure, lb/ft ²
q_∞	free-stream dynamic pressure, lb/ft ²
R_n	Reynolds number, flight value computed by $1.2583\bar{c}pM_\infty \left(\frac{T + 198.72}{T^2} \right) 10^6$ (based on ref. 1, eq. I.3.8-(1)); in figure keys, R is used for Reynolds number
R_θ	Reynolds number based on momentum thickness as computed by $\approx 0.407 \sin(70) \left[\frac{R_n/ft}{\cos(70)} \right]^{0.5}$
RK	boundary-layer rake
r	radius
S_{ref}	reference wing area, 600 ft ² (full scale)
SLFC	supersonic laminar flow control
T	absolute temperature, °R
TE	trailing edge
US _{up}	upper surface
V/V_{RE}	ratio of velocity magnitude in boundary layer to that at rake extreme total-pressure tube
VCR	video cassette recorder
WL	waterline on airplane, positive up, in. (see fig. 2)
WT	wind tunnel
WUT	wind-up turn
WWW	World Wide Web
x/c	fractional distance along local chord, positive aft
y	normal distance above surface at rake location, in.
y^+	Reynolds number like term for flat-plate turbulent boundary layer (ref. 2)
α	angle of attack, deg
β	angle of sideslip, deg
κ, ϕ, ω	Euler angles for camera orientation, deg (see fig. C6)
$2y/b$	fractional distance along local semispan, positive on right wing
2-D	two-dimensional
30_by_60	Langley 30- by 60-Foot Tunnel
3-D	three-dimensional
Subscripts:	
avg	average value
nom	nominal value
u	upper surface

Summary

This report summarizes an effort to compare geometrical, flight, computational fluid dynamics (CFD), and various wind-tunnel studies for the F-16XL-1 airplane and uses data fusion (overlapping) wherever possible to provide additional insight into the data sets. The resulting highly diverse types of data sets were obtained over a wide range of flow test conditions and have produced some novel results.

Geometry

With respect to geometry, the upper surface of the airplane and the numerical surface description have a reasonably good comparison. The largest difference measured over the wing was 0.24 in.

Flight, CFD, and Wind-Tunnel Surface Pressures

For flight and CFD pressures, overall comparisons have been expedited by use of computational graphical tools. At subsonic speeds, reasonably good agreement was noted at angles of attack up to 10.4° . For angles of attack above 10.4° , the agreements were much poorer because the suction peaks were underpredicted. At transonic speeds, generally good pressure agreement was noted, especially near the inboard leading edge at angle of attack (α) of 4.4° and free-stream Mach number (M_∞) of 0.97. The effect of small trailing-edge control-surface deflections ($\leq 2^\circ$) in flight, not modeled in CFD, led to poorer agreement for the aft pressures and a shock not predicted. By contrast, an experimental fluid dynamics comparison of the pressure contours from the wind tunnel at $\alpha = 4^\circ$ and $M_\infty = 0.95$ with the aforementioned flight data did show a wind-tunnel shock location near the hinge line for the aileron, which generally is in qualitative agreement with that determined from the transonic flight results.

Boundary Layer

Anticipated relaminarization of the boundary layer under the influence of high suction peaks near the leading edge was not supported by the turbulent signal output from flight hot-film gauges. Thus, the flight leading-edge attachment line was turbulent; this puts this data set in agreement with other flight data. The grid used in the CFL3D code produced *Reynolds number like term for flat-plate turbulent boundary layer* (y^+) values much larger

than 2 at flight conditions; in fact, they were ≈ 82 . The "wall function" option in the code proved sufficient at subsonic speeds to represent the boundary layers underneath attached flow and the primary vortex but insufficient underneath the secondary vortex system at nominal angle of attack of 13° . Moreover, the flight data indicate the presence of an interaction of the secondary vortex system and boundary layer, and the boundary-layer measurements show that the secondary vortex was located more outboard than predicted. Qualitative agreement exists between predicted and measured skin friction spanwise distributions because both CFD and flight results show at least two regions of high *local skin friction coefficient* (c_f), indicative of primary and secondary vortex presence, and they occur at spanwise positions near one another. However, the absolute levels of c_f and the indicated spanwise extent of the vortices differ.

Data Fusion

Data fusion (overlapping) has been applied to a variety of flow-visualization techniques for flight, wind-tunnel, and CFD investigations with insightful results. Among these are (1) combined surface tufts images from three flight cameras compared with CFD surface streamlines and vortex-core representation at $M_\infty = 0.53$ and $\alpha = 10.4^\circ$ show generally good comparison; (2) the flight results of oil flow with tufts and liquid crystals with tufts compared well; and (3) the wind-tunnel comparison of vortex-core and reattachment-point locations—as determined from vapor screen and compared with surface oil-flow traces—though showing promise, point to the need for further refinement.

Introduction

The increasing capability of CFD to simulate real airplane geometries and flow conditions is found in the literature for both fighter and transport airplanes, for example, the F-18 HARV (ref. 3) and the MD-11 (ref. 4). In the continuance of that trend, this report details the results of a comparative study of CFD, flight, and wind-tunnel data for the F-16XL-1 airplane (fig. 1) over a wide range of test conditions from subsonic to transonic speeds. Though this airplane is not new, its cranked-arrow planform is relevant to any high-speed (supersonic) fighter or transport, for example, the High-Speed

Civil Transport. When the F-16XL-1 airplane was new, the kinds of testing done were related to its operational characteristics (refs. 5 and 6) and not focused on an understanding of its basic flow physics, the subject of the current investigation. This understanding was the subject of the Cranked-Arrow Wing Aerodynamics Project (CAWAP) and the results reported herein. Since CFD predictions are being sought for purposes of comparison with measured data for this airplane, knowledge of the airplane geometry is first necessary. Hence, a geometrical comparison was undertaken for the complete airplane, including wingtip-mounted missiles and tail. Other comparisons are made between flight, wind-tunnel, and CFD data.

The scope of the planned comparisons was extensive, as shown in table 1; however, not all the needed data were collected during the testing process or proved reliable with the latter essentially eliminating the load-factor and R_n flight studies. Along with other constraints, this has led to the availability of only a subset of comparisons as detailed in table 2. The reasons for the dearth of data collection range from pressure sensitive paint (PSP) not yet calibrated for use in flight, along with other imaging and processing issues; hardware for the flight vapor screen not available during the testing time; and resource constraints forced the elimination of the propylene-glycol-methyl-ether (PGME) trace flight experiment. In addition to these, at least two other planned tasks were also not fully accomplished. For example, (1) the modified Preston tubes used to determine local skin friction were to be located at the same fuselage station as the boundary-layer rakes, but a more aft position for the tubes was necessitated because of easier installation on the airplane and avoiding the flow off a step in the leading-edge region and (2) an attempt to correct the transition point location used in CFD from the leading edge to some point aft proved unnecessary at flight conditions because the leading edge was already turbulent according to hot-film measurements.

Notwithstanding these issues, a number of comparisons were made; these include on and off surface flow characteristics, that is, surface pressures, upper surface flow, boundary-layer velocity profiles, and local skin friction distribution, as well as force and moment where possible. These comparisons are followed by analyses of data sets within a

given type, for example, wind tunnel only. (Ref. 7 details what was learned about the boundary-layer flow over the F-16XL-2 airplane—the one used in the supersonic laminar flow control (SLFC) flight experiments.)

In addition to the basic comparison effort, a brief introduction on the use of associated visualization software tools is given in appendix A, and a description of the data processes and management system used for this project is given in appendix B. Appendixes C and D contain a description of the airplane instrumentation used and the associated wind-tunnel test and vapor-screen systems, respectively.

Basic Data Types and Test Conditions

Four basic data types are associated with this comparison effort. Each type is important in its own right and when utilized together form the basis for this comprehensive undertaking. The data types are geometry, flight, wind tunnel, and CFD.

Geometry

Airplane description. The F-16XL-1 is a single-place fighter-type prototype airplane developed by the General Dynamics Corporation, Ft. Worth Division (now the Lockheed Martin-Tactical Aircraft Systems) by stretching the fuselage of a full-scale development F-16A and adding a cranked-arrow wing, a modified fuel system, and a modified flight control system. This airplane had scheduled leading-edge flaps, elevons, and ailerons on the wing for control. The technical specifications for the airplane are given in table 3. Details on the construction of the airplane and its intended missions are given in references 5, 6, and 8.

The design of the cranked-arrow wing was a cooperative effort of the Langley Research Center and the General Dynamics Corporation. The new wing was designed to provide the F-16 airplane with improved supersonic performance while maintaining transonic performance comparable with that provided by the current F-16 design. As shown in figure 2, the resultant design had a leading-edge sweep angle of 70° inboard and 50° outboard of the crank. At the juncture of the wing leading edge with the fuselage, an "S-blend curve" was placed in the leading edge to alleviate a pitch

instability that occurred at high angles of attack in wind-tunnel tests. Because the wing sweep and general arrangement of the cranked-arrow wing of the F-16XL-1¹ resembled the planform of a proposed high-speed commercial transport concept (fig. 3), this was reasoned to be a sufficient basis for using the airplane as a platform on which to conduct high-lift research for the NASA High Speed Research Program. All flight tests reported herein were with the air dams—upper surface fences mounted near the wing leading-edge crank—and wingtip missiles installed, as shown in figures 1(c) and 2.

Details and comparisons. Much effort was expended to have a consistent airplane, wind-tunnel model, and computational geometry so that comparisons between the various data sets of measured and computational results would be meaningful. To facilitate this consistency assessment, the measured geometries were compared with the numerical surface as generated from the geometry reports (refs. 9 and 10), files of lofting details, and digitization of a mold made from a portion of the airplane inlet region. This assessment was only fully done for the flight vehicle.

A partial geometrical assessment of the 0.04-scaled model determined that the wing panels had a slight asymmetry about the centerline. This model had no force/moment balance; therefore, the data collected for use herein are the oil flow, vapor screen, and surface pressures. Because the oil-flow and vapor-screen results are compared on the same wing with no other data, they are consistent. Moreover, PSP results obtained on both wings (ref. 11) show only a slight effect of the geometrical asymmetry on the results.

On the airplane, the upper surface of the geometry has been quantified to within 0.002 in. by using photogrammetry and 1089 targets. (See fig. 4.) The photogrammetry was done with the airplane defueled (only unpumpable fuel remaining), leveled on jacks, and the control surfaces set to zero. Figure 5 shows both the measured ge-

ometry and the numerical surface for the overall configuration (fig. 5(a)) and detailed cross sections (figs. 5(b) to (e)). The overall agreement is seen to be reasonable, with the maximum difference over the wing being 0.24 in. However, over the airplane forebody length of ≈ 92 in., figure 5(e) shows the maximum upper surface differences to be larger, reaching a vertical value of 1.65 in. or a normal-to-surface value of 0.91 in. near the nose—the measured surface was below the numerical one. This difference leads to a nose droop angle of only 1° . An implied assumption here is that the forebody lower surface follows the upper surface in the deflection, which is reasonable, and since no lower surface photogrammetry measurements were made, it is a logical choice. This value of nose droop angle should have minimal impact on the pressure results but could slightly impact lift at $\alpha = 0^\circ$ and pitching moment at zero lift. The relatively large difference at the nose, in comparison with those on the wing, is not fully explainable but is in the direction of structural deflection associated with cantilevered weights mounted ahead of the windshield. The weight is in two forms—ballast (674 lb) and racks of instruments.

Flight

Data collected. Seven different kinds of flight data were collected; four are shown schematically in figure 6. Three were pressure based—surface static pressures, boundary-layer rakes, and modified Preston tubes (ref. 12); three were video recorded—surface tufts, surface oil, and surface liquid crystals; and one was hot-film data. The pressure and surface-flow data are used for the purpose of establishing the effects of variation in Mach number on the local flow. These data serve as the basis for comparison with other data sets. The hot-film data are used to establish whether boundary-layer transition occurs and under what test conditions.

Procedures and accuracy of data collection. The subsonic flight data were obtained at stabilized flight conditions at 5000, 10000, 17500, and 24000 ft at $\alpha_{\text{nom}} = 5^\circ, 10^\circ, 13^\circ, 15^\circ, \text{ and } 20^\circ$ at $\beta = 0^\circ$ for 30 sec. Each stabilized point was followed by a slow β sweep and held at $\pm 5^\circ$ for at least 5 sec. Subsonic data were also obtained in stabilized level turns at altitudes of 5000, 10000, and

¹ The airplane was on loan to NASA from the U.S. Air Force F-16 Special Projects Office at Wright-Patterson Air Force Base, Ohio. The loan agreement permitted NASA to conduct research flights at both Dryden Flight Research Center and Langley Research Center.

17 500 ft at $M_\infty = 0.51$ and $\alpha = 10^\circ$, at $M_\infty = 0.42$ and $\alpha = 13^\circ$, and at $M_\infty = 0.38$ and $\alpha = 15^\circ$. By varying the altitude, transonic and supersonic data were obtained at $M_\infty = 0.9$ to 1.5 and constant $R_n = 3.6 \times 10^6/\text{ft}$ at stabilized 1g conditions and in slow wind-up turns (WUTs). At $M_\infty = 1.3$, the data were obtained in stabilized 1g flight conditions and slow WUTs at R_n from $2.0 \times 10^6/\text{ft}$ to $5.0 \times 10^6/\text{ft}$.

For M_∞ , the accuracy of key flight parameters is ± 0.003 at subsonic speeds and ± 0.005 at supersonic speeds; for α , $\pm 0.3^\circ$; for β , $\pm 0.5^\circ$; and for surface static pressure, ± 0.024 psi for the 5-psi module and ± 0.048 psi for the 10-psi module.

Pressures. The right-wing surface pressures—mostly upper surface—were measured by using 326 static ports, both flush and in streamwise belts, through eleven 32-port electronically scanning pressure (ESP) transducers, also called modules. (For the leading-edge ports, 10-psi modules were used and elsewhere 5-psi modules were used.) Table 4 shows that 360 ports were planned but only 337 were plumbed because of aircraft structural constraints or other valid reasons; of these ports, only 280 on the upper surface and 46 on the lower surface proved reliable. The ports were arranged so that a sufficient number would be at a given BL or FS for cross plotting, as well as for covering other regions of special interest, that is, the apex and ahead of and behind the hinge lines of the trailing-edge control surfaces. Figure 7 shows a schematic layout of the requested arrangement based on the port pattern of wind-tunnel model and the actual or as-flown arrangement on the airplane. Table 4 contains the requested, actual, and nominal port locations. Nominal FS and BL values for the ports were needed in order to facilitate comparisons between the different data sets; moreover, adjusting the flight BL values was needed in order to make chordwise plots of C_p . This need is due to the BL locations of the streamwise ports differing even on the same streamwise belt of pressure tubes because the belt was composed of a group of tubes located nominally at the requested location.

Figure 8 details the complete planned pressure instrumentation system layout on the airplane, including the distribution of the static ports by type, belt or flush, and boundary-layer rakes or modified Preston tubes. These static ports

are connected to internally mounted ESP modules through 0.0625-in.-O.D. tubes (0.028-in. I.D.). Each pressure tube in the belt was used to measure two separate values of pressure. This measurement was accomplished by sealing each tube about halfway along its length; thereby provision was made for one forward and one aft port. The numbers associated with the belt static ports in figure 8 were the values of the actual ports for that belt. Figure 9 shows a photograph of the pressure instrumentation suite flown on the right wing.

Boundary-layer measurements were made by using two rakes at a time at four different positions on the left wing with the most inboard one always used as a control. Each rake used 16 active tubes, 15 total pressure and 1 static pressure, of the 23 available. These two rakes were connected to one 32-port ESP module located inside the left wing. Figure 10 shows a sketch of the rake (overall height 2 in.) and denotes the active tubes. When mounted on the airplane, each rake was oriented into the local flow at an average angle over its height based on initial CFD predictions from the CFL3D code (refs. 13 and 14). The flow conditions were for the complete airplane (half-airplane modeled with symmetry assumed) at $\alpha = 13^\circ$, $M_\infty = 0.29$, and $R_n = 46.1 \times 10^6$, that is, flight condition (FC) 7 (table 5). Figure 11 shows the four locations chosen—one well inboard of the shed vortex systems, one underneath the primary vortex, and two associated with the secondary vortex, both underneath and at its separation point; all are at a nominal position of FS 295 along the predicted orientation which takes into account the flow at and slightly off the surface. The average of these local flow directions was used to establish the rake orientation angles. These angles were measured from the centerline with the rake pointing forward and inboard and have values of 7.5° , 45° , 27.5° , and 23.5° , for rakes 3, 4, 7, and 5, respectively.

The 16 modified Preston tubes (fig. 6)—the modification to each Preston tube is the integration of a static-pressure port with the total-pressure tube—are used for the determination of local skin friction across the left wing near FS 330. (See ref. 15 for a discussion of the basic Preston tube.) These 32 pressures use the same ESP as the rakes but not on the same flight. The tubes were aligned with the local flow by using the same

initial CFL3D solution at FC 7. The equation used to generate the experimental fluid dynamics (EFD) c_f values comes from reference 12 and relates, through a process of calibration, the pressure change between the total- and static-pressure tubes to the local skin friction.

Visual. Video data were recorded with up to six external cameras: two mounted atop the vertical tail, one on either side of the fuselage behind the canopy, and one in the nose of each dummy missile. An internally mounted heads-up display (HUD) camera was also used on occasion. Figure 12 shows the camera locations on the airplane. The time was added to each image by a time-code inserter (appendix C) so that the images could be compared to form a composite and the flight test conditions could be established. (See table 6 for the video-image times for the nominal flight conditions.) Images of interest were digitized in a 512- by 480-pixel format for further processing to develop quantifiable video data. In addition to the images, the other input quantities needed for the processes, given in appendix A, are the video targets (shown schematically in fig. 7) and the position and calibration characteristics of each camera/lens combination.

Hot film. Table 5 shows the minimum value of R_θ to be ≈ 122 . Reference 16 indicates that a laminar flow reattachment line is not expected for this 3-D wing unless R_θ is less than 100. Even though the calculated values of R_θ for this test exceed those expected for laminar flow, flow relaminarization was anticipated to occur because of the high suction peaks in the vicinity of the leading edge. Figure 13 shows the hot-film belt installed on the airplane. Although there were 24 gauges in a belt, only 12 were active on any one flight.

The anticipated relaminarization of the boundary layer along the leading edge for the F-16XL-1 was not evident in the traces made from these hot-film gauges; therefore, only turbulent flow was present over the airplane.

The F-16XL-2 airplane was used for SLFC flight experiments and employed hot-film sensors, as described in reference 7. The difference in application of the sensors was in the placement. For CAWAP, the sensors were around the leading edge in a belt,

whereas for the SLFC, they were at various chord locations.

Wind Tunnel

Table 7 provides a summary of the data previously collected as well as that taken specifically for this research project. Note the variety of model scales, Mach number, and Reynolds number over which tests were conducted. As can be seen from the table, not all models had the air dams installed; this prevented those data sets from being utilized in the ensuing comparisons. In general, the vast majority of the comparisons presented are for data sets from complete configurations; however, some Langley Basic Aerodynamic Research Tunnel (BART) results for a configuration subset—air dams off—are shown in the section “EFD Basic Data and Comparisons.” All wind-tunnel data are for the configuration with the control surfaces undeflected.

0.11-scaled model tests. The tests for the 0.11-scaled model tests were conducted in the Ames 11-Foot Tunnel on the model described in reference 17 and with the tabular results reported in reference 18. This model was specifically built to estimate the airloads for the airplane from $M_\infty = 0.60$ to 2.0 using 109 ports on the left wing upper surface and 81 on the right wing lower surface. The ports are located in streamwise rows and the positions are given in table 8 at airplane scale for both actual and nominal values. None of these streamwise rows nominally match those chosen for the airplane. Because of data release restrictions of these wind-tunnel C_p results, no direct comparisons are made with flight or CFD; however, unscaled transonic $C_{p,u}$ contours are presented later.

0.18-scaled model test. The test for the 0.18-scaled model was conducted in the Langley 30- by 60-Foot Tunnel; the pressure results have not been formally published elsewhere, but the force/moment results have been published in reference 19. The basic model has 30 right-wing, flush upper surface ports located to yield pressures for both streamwise and spanwise rows. These ports are given in table 9 at airplane scale for both actual and nominal values. These locations do not duplicate those on the 0.11-scaled model. The ports on the 0.18-scaled model are nominally duplicated

on the airplane. Only two runs—one force/moment and one pressure—are utilized from this test, and both are at $\beta = 0^\circ$.

0.04-scaled model test. The test for the 0.04-scaled model was conducted in the BART at $\beta = 0^\circ$. This model has 82 ports, 57 on the right-wing upper surface and 25 on the left-wing lower surface; the actual and nominal values are tabulated in table 10 at airplane scale. These 82 ports were specified to encompass the 30 ports of the 0.18-scaled model used in the 30- by 60-Foot Tunnel test. Moreover, the ports on the 0.04-scaled model are nominally duplicated on the airplane. Selected results from the BART test appear in reference 20, where they have been compared with Euler code predictions.

CFD

CFL3D flow solver code and grid. The flow solver code CFL3D was run in the Navier-Stokes mode with a turbulent boundary layer employing the Baldwin-Lomax with the Degani-Schiff turbulence model (in the j - k directions) on a multiblock, patched grid over a variety of wind-tunnel and flight test conditions. Two separate grids were used to model half the airplane configuration (with undeflected control surfaces) and external flow field. The initial grid had 36 blocks and was used with version 3 of the flow solver to produce the initial results upon which the locations and orientations of the surface instrumentation were set. The current grid had 30 blocks and was used with version 5 of the flow solver to obtain the comparative solutions reported herein. The current grid was needed for two reasons: (1) to have the grid more closely conform to the actual fuselage and wing geometries and (2) to improve the grid layout on the wing and fuselage surfaces. Figures 14 and 15 provide the two grids on the wing-fuselage surface and outer boundary, excluding the missile and missile rail grids, which were effectively unchanged. For the current grid, the inner region of the airplane was modeled by 16 blocks, the outer region by 14 blocks, and all 30 blocks are shown schematically in figure 16. The boundary conditions were symmetry, solid wall for the outer mold lines, flow into the duct inlet with the exhaust face faired over, and Riemann-type conditions at the far-field boundaries. A total of 1372096 cells (1707117 node points) were used to obtain solutions at specified

test conditions (i.e., α , M , grid R_n , T). To maximize computer resource allotments, the minimum number of cells was used. The resulting grid spacing normal to the numerical surface led to a value of y^+ of 2 at wind tunnel R_n , whereas at flight R_n the average value of y^+ was 82. In an effort to compensate for the insufficient grid spacing at flight conditions, the “wall function” option was used to augment the turbulence model in CFL3D. The wall function is defined as that boundary-layer growth rate expected from a turbulent mean flow near the wall (ref. 21).

Thirteen separate CFD solutions were obtained with the current grid and version 5 of CFL3D, and they are referenced in the Program for Information Storage and Management (PrISM) data base which is described in appendix B. In PrISM, these solutions are numbered from CFD:CFL3D(001)Run:1 through CFD:CFL3D(001)Run:13, with CFD:CFL3D(001)Run:4 and CFD:CFL3D(001)Run:12 not being converged, as shown in table 11. The latter group of twelve had improvements made in the grid and/or boundary-layer modeling, and selected ones from this set are used in the comparisons presented herein.

Computer requirements and sample convergence histories. All computations were performed on an NAS Cray C90, located at the Ames Research Center. On this machine, the algorithm uses 65 megawords of storage and requires approximately 13 $\mu\text{sec}/\text{cell}/\text{cycle}$. Converged results were nominally obtained in 5850 cycles requiring about 24 hr of computer time for the grid. (The minimum and maximum values of cycles/computing time were 5350/20 hr and 16850/79 hr, respectively.) The number of cycles was sufficient to reduce the residuals by 2 to 3 orders of magnitude and to reduce the oscillations in C_L and C_D to a negligible level. The computations were performed with multigrid and mesh sequencing. Two examples are shown in figure 17, one at high R_n and one at low R_n . The high R_n solution for FC 49 shows good convergence properties, whereas the low R_n solution for the BART test shows some small oscillations both in terms of L^2 (residual) and C_L through 10400 cycles.

Using the solution file. The solution file was readily usable in a standard postprocessing

package, as described in appendix B for surface pressure plotting; however, the processing needed to determine the velocity magnitudes for comparison with the boundary-layer rake data was not as straightforward. There were two reasons: (1) the initial and current grids differed over the surface so that the locations of the rakes did not occur at current grid points and (2) the velocities needed to be established along a normal to the surface at the specified points in order to be comparable with the rake data. Since most of the surface grid lines were not normal to the surface over the length needed, it was necessary to have software written to perform the data interpolation—the one chosen was IBM Data Explorer software (ref. 22)—and to establish these velocities along surface normals at the rake locations.

The c_f distribution, calculated in CFL3D on the wing upper surface near FS 330, has been extracted from the results files for the appropriate inboard, upper wing surface blocks and is placed into a single file for later comparison with the EFD results.

CFD Comparisons

This section contains CFD comparisons with measured surface pressures, boundary-layer profiles, local skin friction, and on and off surface flow features.

Surface Pressures

Comparisons of surface pressures were expedited by using the World Wide Web (WWW) for accessing the data files on the Langley mass storage system, as explained in appendix B. Flight pressure data are primarily available for flights 143 to 154 which had good image data and are denoted in table 5 by a filled cell. However, it turned out that not all the runs with good images in these flights had pressure data. To distinguish between the two, the table shows the ones with pressure data colored yellow and the ones missing the data colored red. Regardless of the image quality for the runs in flight 145, its pressure calibrations were not resolvable and hence the data not recoverable. (Note that the *nominal values of test parameters* are used only for identifying similar data sets for comparison, but in the figure caption the *actual values of test parameters* are given.)

Because of changes in R_n , differences between the flight and wind-tunnel pressure data sets are expected to range from slight to large for most test parameters. Additional slight changes are due to small differences in α and M_∞ at a nominal test point. Larger differences are associated with geometrical differences of control-surface (leading-edge flap, elevon, and aileron) deflections and aeroelastic deformations on the outboard wing panels during flight. In addition, there may be some flight pressure-field distortion caused by the flow over the pressure belts. (The preferred method of measuring surface pressures is with flush orifices, as done in the wind-tunnel tests and in the airplane leading-edge region; however, with the wing containing fuel—precluding the penetration of the skin for such orifices—pressure belts were used to provide the bulk of the flight surface-pressure measurements.) All flight results presented herein are at $1g$ conditions. For reference purposes, the white line on the airplane or model indicates the location of the row of C_p ports.

Subsonic. Eight separate CFD subsonic solutions were obtained (control surfaces undeflected) of which seven simulated flight test conditions and one simulated a BART test condition. The flight solutions correspond to FC 1, 7, 19, 25, 34, 46, and 49 from table 5. Unfortunately, the surface pressure data for FC 7 and 19 are not available; hence only data for the other five FCs are offered in figures 18, 19, 20, and 21 at $\alpha_{nom} = 5^\circ, 10^\circ, 13^\circ,$ and 20° , respectively. The fact that flight pressures are missing for FC 7 is especially noteworthy because they were for one of the chief flight conditions at $\alpha_{nom} = 13^\circ$ and $M_{nom} = 0.29$.

Three general observations can be made from the cited group of figures: the lower surface C_p data are well predicted; the upper surface C_p data are generally well predicted inboard of the crank; and all flight C_p data show an unusual and uncharacteristic variation near $2y/b = 0.6$ for FS 185. The ports for the latter comment are located in and towards the aft-end portion of the S-blend curve part of the airplane, a region of the airplane where the flow is very sensitive. Even with this unusual behavior of C_p , these results are retained because they do bracket the predicted data at these subsonic values of M_∞ . Figures 18 and 19, at the lower values of α of 5.5° and 10.4° , show the main C_p

features, including suction peaks, to be generally well predicted, both chordwise and spanwise, but not in all details. Whereas, at both higher values of α of 13.0° and 20.0° , figures 20 and 21 show the suction peaks to be underpredicted; the spanwise distributions are slightly better predicted than the chordwise but neither one really well.

Figures 18(o) and 19(o) present overall comparisons of CFD and flight C_p data for FC 1 ($\alpha = 5.5^\circ$) and FC 46 ($\alpha = 10.4^\circ$), respectively. These figures were developed by using FAST (ref. 23) with the CFD solution data serving as the background color mirrored about the centerline and with the flight C_p data superimposed. (These data are in PLOT3D (ref. 24) format.) The flight port locations are denoted as black dots and the associated C_p values by the color of the surrounding bubble outline. Both figures show the general overall agreement to be good in that the colors of the bubble outlines are indistinguishable from the CFD surface, with its associated C_p color bar, over a large part of the wing. More differences appear to occur between the data sets in figure 18(o) than in figure 19(o), because figure 19(o) has a more restricted C_p range. Where differences are noted in figure 18(o), the flight values are seen to be more positive than the CFD values with the exception of six ports in the apex region. Figure 19(o) shows some similar patterns; where differences do occur, the measured values are generally more positive. However, they are primarily restricted to the forward part of the wing. The exceptions occur in the apex region where the insert illustrates the measured suction pressures for five ports to be more negative than predicted, that is, a region of strong vortex influence. Figures 18 and 19 show the need for both the detail and overall C_p comparison graphs.

Figure 21 also contains the BART C_p data and CFD predictions. A comparison shows the agreement of the BART data with predictions to be no better than that noted for flight. However, there are oscillations in the predicted BART C_p observed over the aft part of the wing, which may be associated with the oscillations noted in the solution (fig. 17(b)); there is nothing in the flow physics to suggest such an oscillatory C_p behavior. This behavior could be indicative of the solution not being fully converged at $M_\infty = 0.10$ because solution convergence is known to be difficult

to obtain at very low values of M_∞ . In addition, figures 21(a) to (n) allow for two other comparisons between the two experimental data sets and the two CFD solutions. The experimental data comparison in this low subsonic range ($M_\infty \leq 0.24$) shows that the two sets roughly agree; this indicates a small R_n dependence but with the BART C_p values generally having slightly more suction. This result is consistent with flow at lower values of R_n leading to earlier separation and reaching higher suction peaks on wings with thin or sharp leading edges. Because the CFD solutions were for the test conditions, at least two of the test parameters are different between these sets: R_n differs by a factor of 30 and M differs only slightly. The result of the CFD comparison is that higher C_p suction peaks are predicted for flight than at BART test conditions and these occur at or slightly outboard of the BART locations. This prediction is not consistent with experimental experience, and this reversal in the R_n trend is likely attributed to the grid and turbulence model used. These modeling features worked well up to $\alpha = 10.4^\circ$ but, as already noted, do not yield the measured suction peaks at $\alpha = 13^\circ$.

Figure 21(o) presents $C_{p,u}$ for the BART test as determined from PSP (ref. 11) and corresponding CFD. Even though there is some misalignment distortion for the two halves of the figure, an assessment of $C_{p,u}$ shows that slightly more suction is generated over the upper surface in the wind-tunnel test than predicted. Regardless of these differences, it is encouraging to note that some of the key vortex-system features, such as location of vortex origin and footprint, are captured by both data types. (Note that even though the CFD solution does not show the missile or its rail, they were a part of the computation.)

Transonic. Four separate CFD transonic solutions were attempted (control surfaces undeflected) at the test parameters for FC 68, 69, 70, and 79 from table 5; however, only the one for FC 70 was run to convergence due to resource limitations. Hence, there is only one transonic C_p comparison presented for CFD and flight and it is contained in figure 22.

Figure 22(r) shows the distribution of CFD and flight C_p data at $M_\infty = 0.97$ and $\alpha = 4.4^\circ$ (FC 70; flight 152, run 5b); as before, the CFD solution

data serve as the background color mirrored about the centerline. The flight port locations are denoted as black dots and the associated C_p values by the color of the surrounding bubble outline. A comparison of the data in figure 22(r), including the insert, indicates very good overall agreement by using this global C_p scale because the colors of the bubble outlines are virtually indistinguishable from the CFD over the wing. Figures 22(a) to (q) show the detail agreement at both fixed BL and FS. As before, the detail comparisons are needed because the global C_p scale at FC 70 is too large for the entire upper surface of the airplane to capture the details that exist over just the wing alone. Nevertheless, remarkable detail agreement occurs all along the leading edge and along the chords at BL of 40 and 55. Regarding the interest in whether a shock crosses the hinge line of an aft control surface could be detected in flight and predicted at BL = 153.5, a shock is noted to occur near $x/c = 0.75$ in the flight data. (See fig. 22(h).) This location is aft of the aileron hinge line, and this feature is not captured by the CFD of the configuration with undeflected control surfaces.

The fact that the C_p agreement is better inboard and along the leading edge needs to be examined in light of the CFD assumptions that the flight control surfaces were undeflected and the wing was rigid. A postflight examination of the angles of control surfaces for flight 152, run 5b determined them to be for left elevon, 0.6° ; left aileron, 1.8° ; right elevon, 2.0° ; right aileron, 1.8° ; right leading-edge flap, -9.0° ; and left leading-edge flap, not available but assumed equal to that on the right side; positive control-surface deflection is defined for any surface for which the flap edge is down. Though these numbers for the trailing-edge control-surface deflections are $\leq 2^\circ$, they can have a powerful local effect on C_p and, consequently, on wing shock location. Note the large disagreement at the aftmost FS 450, 462.5, and 492.5 (figs. 22(o) to (q)); this indicates a shock hitting the surface near $2y/b = 0.4$ and outboard of $2y/b = 0.5$ for FS 492.5. Regarding wing rigidity, during the entire flight test the outer wing was not as rigid as the inboard wing, an expected occurrence; however, the effects at FC 70 should be minimal since it is for $1g$ flight.

Contours. Figure 23 shows C_p upper surface contours at $M_\infty = 0.97$ and $\alpha = 4.4^\circ$ (FC 70,

flight 152, run 5b) for both flight and CFD. (CFD contours are generated using FAST (ref. 23) and flight contours from Tecplot (ref. 25).) There are many similarities between these contours; overall, the CFD pressures are more negative, especially near the leading edge and over the aft part of the wing. Along the inboard edges, aft about one third of the distance from the S-blend curve, both the flight and CFD data of figure 23 show a shock followed by an expansion, whereas outboard only the flight data show a shock aft centered near the aileron hinge line. This elevon shock in flight has been previously noted (fig. 22(h)), and because it does not show up in the CFD solution it is most likely attributable to differences in the control-surface deflections. The CFD modeling is with the control surfaces undeflected, whereas the flight experiment has small, but measurable, trailing-edge deflections.

Boundary-Layer Profiles at FC 7

Figures 24(a), (b), (c), and (d) show the comparison of measured and predicted boundary-layer profiles for rake locations 3, 4, 7, and 5, respectively, at FC 7. (See tables 5 and 12.) These locations were chosen because they had flows which should be markedly different at $\alpha_{nom} = 13^\circ$ and subsonic speeds. At these respective positions, the flows range from (a) being nearly streamwise, (b) underneath the primary vortex, (c) at the secondary separation line, and (d) underneath the secondary vortex. Figure 24(a) also presents an estimate of the profile repeatability for rake 3 because this position was used as a control, flown with each of the others, and had the most benign flow. As can be seen, the experimental velocity ratios only have a small deviation from one another, and the profile is well estimated for $y > 0.25$. For $y \leq 0.25$, the measured profile develops more quickly near the surface than predicted, even with the "wall function" option being used in CFL3D.

Underneath the primary vortex (rake 4 location), figure 24(b) shows qualitative agreement between the measured and predicted results but not quantitative. In particular, for $y \leq 0.25$ the predictions are less than measured, and for $y > 0.25$ the reverse is true. Moreover, both results indicate a jet-type flow to commence at $y > 0.3$. Both flows also show regions of quasi-linear variation

of velocity with y , indicative of being outside the boundary layer and just into the influence of the primary vortex.

In the vicinity of the secondary vortex there is general disagreement between the measured and predicted values, as shown in figures 24(c) and (d). The predicted values are significantly different, whereas the measured ones look to be similar; moreover, the measured values do not look like what is seen at rake 3 or 4 in figures 24(a) or (b), respectively. Regarding the EFD/CFD disagreement for rake 7, the predictions indicate that at the originally estimated location of the secondary separation line, the profile develops the edge velocity value only a small distance off the surface and thereafter retains that level. This constancy is in contrast to the measured values which only reach edge velocity near the rake extreme. The measured velocity is not asymptotic at the rake extreme; this leads to the conclusion that the maximum velocity has not been achieved at this location. The measured profile for rake 5, underneath the originally estimated location of the secondary vortex, also only achieves edge velocity near the rake extreme; however, the predicted values are markedly different with jet-type flow velocities occurring near the surface over most of the rake height. Comparing only the EFD profiles for rakes 7 and 5 in figure 25(a) shows the velocity distributions are very similar. Although the plan was to use the results of an initial CFD solution to measure two different boundary-layer profiles associated with two different features of the secondary vortex over this part of the wing, it is apparent that only one was captured. The quasi-linear growth of velocity for $y > 0.5$ for these profiles is associated with vortices around these boundary-layer rakes because the velocity field produced outside a representative vortex system core varies as $1/r$.

Even though these predicted boundary-layer profiles were different than those measured, some understanding of the local flow measured closer to the surface may be gained by examining the final CFD solution. Figures 25(b) and (c) have been prepared for that purpose. Figure 25(b) shows the stagnation pressure contours at FS 295 and a representation of these two boundary-layer rakes. From this figure, one can see that the two rakes are computationally located in between the secondary vortex and a third vortex system, as indicated

by the streamwise ribbons, and are not at the planned positions associated with the secondary vortex. (Because the third vortex system is located outboard of the secondary vortex, this system is not called a tertiary vortex. Moreover a tertiary vortex would be under more of the influence of the secondary vortex than it would be of the primary system.) Figure 25(c) locates the origin of the third vortex system as coming from that portion of the flow which crosses the apex in the S-blend curve region and from there proceeds over the primary vortex. Hence, this flow gets swept under the primary and moves outboard where it remains in the vicinity of the wing leading edge, inboard of the crank. This flow interaction accounts for the third vortex sense of rotation. Such a vortex system is unexpected, not seen in experiments, and most likely an artifice of this CFD grid/solution.

Consider again the measured velocity profiles of rakes 7 and 5 in figure 25(a). Based on the close proximity of these two rakes, only a single vortex system outboard of the primary vortex can be confirmed and it is the secondary vortex. Moreover, the actual secondary vortex must be more outboard, and most likely larger, than the predicted one shown in figure 25(c). This flow feature is due to both rakes being encompassed by the actual secondary vortex and the third vortex not really a contributor.

Skin Friction at FC 7

Figure 26 provides the measured and predicted c_f values at FS 330 for similar conditions in flight and for CFD. This figure can be used to locate and assess the impact of the vortex systems because they produce high velocities on the surface which are measured by the modified Preston tubes. Qualitative agreement is shown because both data sets have at least two regions of high c_f , which is indicative of primary and secondary vortices. These vortices occur at BL values near one another, for example, -89 versus -84 for the primary and -108 versus -103 for the secondary, with the measured results given first. The significant differences for the primary vortex are (1) the more restrictive range of BL over which the vortex influence occurs in flight, and (2) the greater levels of c_f reached; that is, measured levels are 39 percent larger than predicted. For the secondary vortex, the measured and predicted levels are comparable

but the predicted vortex covers a much narrower range of BL. This result is consistent with the previous discussion of the predicted vortex systems given in figures 25(b) and (c) because the presence of the third vortex is expected to reduce the spanwise extent of the secondary vortex. Moreover, at least two other c_f plateaus or peaks are predicted outboard of the secondary vortex, one at BL -107 and one very near the leading edge at BL -113. The most inboard plateau or peak is more likely to reflect the presence of the predicted third vortex than the one very near the leading edge because at FS 295 the third vortex is located laterally midway between the secondary vortex and the leading edge. (See fig. 25(c).)

On and Off Surface Flow Features at FC 46

Figure 27 was constructed with Intelligent Light FIELDVIEW software (ref. 26) and shows the fusion (overlying) of surface tuft images from three flight cameras with CFD surface streamlines and vortex-core representation at $M_\infty = 0.53$ and $\alpha = 10.4^\circ$ (FC 46, flight 144, run 3b). In particular, figure 27(a) presents the combination of the three flight-camera images projected onto a grid representation of the airplane. Figure 27(b) shows the CFD surface streamlines compare well with these tuft images. Figure 27(c) presents iso-surfaces of the stagnation pressure (PLOT3D) at a value of 0.78 and represents the locations and extent of the various airplane vortex systems. Figures 27(b) and (c), with transparency employed for the vortex systems iso-surfaces, are combined to form figure 27(d). As expected from the results of the surface comparison, the vortex system is well located with respect to the flight tufts.

EFD Basic Data and Comparisons

This section provides basic, low-speed wind-tunnel force and moment data for the F-16XL-1 airplane and provides comparisons of wind-tunnel surface pressures, wind-tunnel on and off surface flow features, and flight surface flow features.

Forces and Moment in Wind Tunnel

Figure 28 presents the longitudinal forces and moment obtained on the 0.18-scaled model in the Langley 30- by 60-Foot Tunnel. The data show the model has well-behaved force characteristics

and is approximately neutrally stable over this range of α and C_L at low M_∞ . Moreover, if the aerodynamic center shift has been well controlled by planform shaping, one could expect only slight elevon deflections to be needed for trimmed flight from subsonic to supersonic speeds.

Surface Pressures in Wind Tunnel

The effects of model scale and R_n variation on C_p data from different facilities at low speed are presented along with transonic C_p contours in this section.

Effect of model scale and R_n on C_p at low speed. Figures 29 to 31 and figures 32 to 34 provide representative streamwise (constant BL) and spanwise (constant FS), respectively, C_p data collected during the BART and 30- by 60-Foot Tunnel tests for the 0.04- and 0.18-scaled models at R_n of 0.5×10^6 , 1.0×10^6 , 1.12×10^6 , and 2.1×10^6 and α of 5° , 13° , and 20° . This restricted set of data was further limited to only those BL or FS which had results (sometimes only on the upper surface) at all four values of R_n . Tables 9 and 10 confirm that these models have comparable numbers of upper surface ports at the values of BL and FS chosen. For reference, the resulting four values of BL have three locations inboard and one outboard of the air dam, and the two FS have locations well forward of and across the air dam. Two expected effects occurred from all these results, namely, little difference between the two data sets near $R_n \simeq 1.0 \times 10^6$ and larger R_n effects on the upper surface than the lower surface. A more detailed study of the remaining features begins with the BART data ($0.5 \times 10^6 \leq R_n \leq 1.12 \times 10^6$). For these three data sets, significant differences in C_p occur on the upper surface. However, a general assessment is that the suction peaks occur at the same locations and the peak values increase with R_n and α .

A comparison of the C_p data from the BART and 30- by 60-Foot Tunnel tests in figures 29 to 34 shows the general effect of increasing R_n from 1.0×10^6 to 2.1×10^6 is a higher suction peak in C_p for $\alpha = 5^\circ$ and 20° but lower peaks at $\alpha = 13^\circ$. A portion of this reversed trend at $\alpha = 13^\circ$ is attributable to the test results from the 30- by 60-Foot Tunnel being at 12.5° rather than the 13° in BART. Peak suction values of C_p

usually occur at the same location but the distributions are markedly different. Differences noted between the two wind-tunnel data sets are not well understood. Many factors, including differences in turbulence characteristics, flow quality, model scale, and model installation between these two tunnel tests would be expected to produce some of the differences noted. Therefore, even though R_n is highest in the 30- by 60-Foot Tunnel, due to its larger model, and the C_p peak values generally increase with R_n and α , there can be significant local differences pointing to model scale and R_n effects—only a portion of which can be sorted. Beyond the slight model asymmetry differences mentioned previously for the 0.04-scaled model, data uncertainty is an issue. The fact that the location of the peak C_p remains essentially fixed with changes in R_n attests to the aerodynamic sharpness of the wing leading edges of these models. (See ref. 27 for an example of C_p peak location dependency on R_n for a small-radius, rounded, leading edge.) The more negative values of C_p with increasing R_n for a fixed α is attributed to the vortex system becoming more tightly organized or coherent which leads to a stronger influence on the surface flow and pressure field.

Transonic $C_{p,u}$ contours. Figure 35 is developed from the 0.11-scaled model data from 109 upper surface pressure ports (ref. 18), reflected about the centerline, from which the unscaled $C_{p,u}$ contours were created by FAST. This figure shows the effect of increasing α from -2.27° to 20.04° at $M_\infty = 0.95$ and is used to assess when the shock crosses the trailing-edge hinge line. Between $\alpha = 2.04^\circ$ and 4.27° , the coalescence of positive C_p isobars is evidence of a shock crossing the aileron hinge line. This shock strengthens on the aileron hinge line and moves inboard onto the elevon surface by $\alpha = 6.54^\circ$. Figure 35 shows that the trailing-edge shock remains a prominent flow feature through $\alpha = 11.35^\circ$, even in the presence of the leading-edge vortex system. However, by $\alpha = 15.44^\circ$, the leading-edge vortex system and its attendant cross-flow features in a transonic flow cause the trailing-edge shock to be pushed beyond the last set of ports. With the distribution of pressure ports available, no strong shock forms across the elevon hinge line over the entire range of α . The location of the shock near the hinge line of the

aileron is generally in qualitative agreement with that determined from the transonic FC 70 flight results reported previously. (See fig. 22(h).)

On and Off Surface Flow (Air Dams Off) in Wind Tunnel

Some examples of using FAST to fuse on and off surface data are presented in figure 36 for visual data taken in BART at low speeds. This figure shows the superposition of vortex core and reattachment point paths extracted from vapor-screen images² onto surface oil-flow images for $\alpha = 10^\circ$, 13° , and 15° at $R_n = 1 \times 10^6$ and 0.5×10^6 on the model with the air dams off. The general trend is for the core projections to agree well with the surface oil-flow features and for the reattachment projections to be slightly outboard of the features. As expected, progressive inboard movement of both projected paths occurs with increasing α , and only a small change in the surface oil flows occurs with increasing R_n at a particular α because of the small/sharp leading-edge radius. Overall, the best agreement between the data sets occurs for $\alpha = 15^\circ$ and $R_n = 0.5 \times 10^6$.

Improvements in the comparisons of these data sets can only be achieved by two refinements. The first is to improve the quality of the image data collected by doing more thorough planning and execution of the vapor-screen portion of the test. The second is to improve the application of the image-process algorithms.

Surface Flow in Flight

Two examples of the fusion of image data are given for upper surface flows on the F-16XL-1 airplane: tufts with liquid crystals (fig. 37) and tufts with oil flow (fig. 38). All tuft and liquid crystal image data were taken on the left wing with the right wing reserved for oil flow. These images were taken from two cameras mounted near the top of the vertical tail, left and right side. Both

² Some of the projection paths, as discussed in appendix A, are not straight but disjointed. This is primarily associated with the particular vapor-screen image used and, with four exceptions, all images were of the instantaneous type. The exceptions used the average image and were employed when the instantaneous image did not contain all the vortex features. They occurred for (1) $\alpha = 13^\circ$ and $R_n = 0.5 \times 10^6$ at FS 435; (2) $\alpha = 13^\circ$ and $R_n = 1.0 \times 10^6$ at FS 225; (3) $\alpha = 15^\circ$ and $R_n = 1.0 \times 10^6$ at FS 257.5; and (4) $\alpha = 15^\circ$ and $R_n = 1.0 \times 10^6$ at FS 350.

figures show that the tuft data are represented by “vectors,” solid-line segments with the same orientation, origin, and length of the respective trailing tufts. (See appendix B and ref. 28.)

Figure 37 shows the liquid crystals exhibit a high shear (dark) region, which is caused by the highly energetic vortex core and system scrubbing the upper surface for the test condition of $\alpha \approx 13^\circ$, $M_\infty = 0.28$, and $R_n = 47 \times 10^6$. Thus, the liquid crystal data correspond well with the flow features detailed by the tuft data. (See section “Skin Friction” for a discussion of corresponding on and off surface flow.)

Figure 38 displays tuft data mirrored about the aircraft centerline, “vectorized,” and then overlaid onto a portion of the right wing with the oil flow, also at $\alpha \approx 13^\circ$, $M_\infty = 0.28$, and $R_n = 47 \times 10^6$. Good agreement is observed between these two types of surface flow techniques in the highlighted and enlarged region shown at the right.

Concluding Remarks

This report has focused on the comparative efforts regarding data obtained from flight, computational fluid dynamics (CFD), and wind-tunnel studies for the F-16XL-1 airplane supported, wherever possible, with the aid of data fusion (overlapping). The resulting highly diverse set of data types was obtained over a wide range of test conditions. From these comparative studies and the basic data taken, the following remarks and observations can be made:

1. The aircraft geometry compared closely with the numerical surface description, differing by at most 0.24 in. over the wing; one exception was over the airplane forebody where the differences were larger and reached a maximum value of 1.65 in. near the nose. However, even this difference leads to a nose droop angle of only 1° , which should have minimal impact on the pressure results.
2. Overall upper surface pressure coefficient ($C_{p,u}$) comparisons of CFD and flight results have been expedited by use of computational graphical tools.
3. At subsonic speeds, the flight suction peaks and distributions were generally well predicted at $\alpha = 5.5^\circ$ and 10.4° (where α is angle of attack), but underpredicted at $\alpha_{\text{nom}} = 13^\circ$ and 20° (where α_{nom} is nominal angle of attack).
4. At transonic speeds, generally good pressure agreement was noted for flight and CFD at $\alpha = 4.4^\circ$ especially near the leading edge in-board of the crank. The effect of small trailing-edge control-surface deflections ($\leq 2^\circ$) in flight, not modeled with CFD, may have led to poorer agreement for the aft pressures and to an un-predicted shock.
5. The location of the shock near the hinge line of the aileron, as determined from wind-tunnel $C_{p,u}$ contours near $\alpha = 4^\circ$ at a free-stream Mach number (M_∞) of 0.95, is generally in qualitative agreement with that determined from the transonic flight results at $\alpha = 4.4^\circ$ and $M_\infty = 0.97$.
6. Turbulent signal output from hot-film gauges demonstrated that the flight leading-edge attachment line was turbulent; this makes this data set in agreement with other flight data and does not support the anticipated relaminarization of this boundary layer under the influence of high suction peaks near the leading edge.
7. The grid used in the CFL3D code produced Reynolds number like term for flat-plate turbulent boundary layer (y^+) values much larger than 2 at flight conditions; in fact they were ≈ 82 . The “wall function” option in the code proved sufficient at subsonic speeds to represent the underneath attached flow and the primary vortex of the boundary layers but insufficient underneath the secondary vortex system at $\alpha_{\text{nom}} = 13^\circ$. Moreover, the flight data indicate the presence of an interaction of the secondary vortex system and boundary layer.
8. Qualitative agreement is indicated between predicted and measured skin friction spanwise distributions at subsonic speeds because both CFD and flight results show at least two regions of high local skin friction coefficient (c_f), which is indicative of primary and secondary vortices at spanwise positions near one another. However, the absolute levels of c_f and the indicated spanwise extent of the vortices differ.
9. Data fusion (overlapping) has been applied to a variety of flow-visualization techniques for

flight, wind tunnel, and CFD with insightful results. In particular, combined surface tuft images from three flight cameras compared with CFD surface streamlines and vortex-core representation show generally good agreement at $M_\infty = 0.53$ and $\alpha = 10.4^\circ$, and the flight results

of oil flow with tufts and liquid crystals with tufts compared well, but the wind-tunnel comparison of vortex core and reattachment locations—as determined from vapor screen and point compared with surface oil-flow traces—though showing promise, point to a need for further refinement.

Appendix A

Visualization Tools

Four different visualization tools are discussed—ILLUME, MAPPER, Core- and Reattachment-Point Locator, and Tuft Representer. An explanation of each tool and its function are as follows.

ILLUME

Light-sheet flow visualization experiments performed in wind tunnels or in flight require configuring a recording camera to capture the experiment and a light sheet to illuminate particles in the flow field. Often valuable experimental time is expended trying to determine the optimal placement of the camera and light sheet. The software package named ILLUME (Interactive Light Sheet Locator Utility and Modeling Environment) allows for the computer simulation of either experimental wind-tunnel or flight test camera and light sheet locations, in combination with the geometry of interest, in order to ensure a high degree of visualization success before the start of the test. ILLUME is interactive and allows the user to simulate the position and orientation of one or more cameras and one or more light sheets while viewing, from a selected camera, the intersection of these elements. For each camera, the user can simulate the effect of changing the lens on the field of view to determine the preferred one from those available for the test.

ILLUME can also be used, as done for this test, to view the geometry and any surface features of interest. This viewing could include those representing the location of the video targets. A sufficient number (≥ 6) of viewable video targets per video camera are required in order to establish the camera position and orientation; this process is called *space resection* in reference 29. This can lead to the establishment of flow features as *quantifiable data* when the video images are projected to the surface. Additional information about ILLUME can be found in reference 30.

MAPPER

MAPPER is an updated version of a software package called Reconstructor (refs. 27 and 31), which enables a 2-D visual image, existing at a camera image plane, to be projected onto the 3-D surface where it occurred. This process has been applied to both wind-tunnel vapor-screen and flight surface-flow (tuft) images in these references. (These papers are retrievable from the NASA Langley Technical Report Server at <http://techreports.larc.nasa.gov/ltrs/ltrs.html>.) Additional information about the use of this process is also available from reference 32.

Core- and Reattachment-Point Locator

The Core- and Reattachment-Point Locator software tool is an update of the Extractor package described in reference 27. Its use is to locate the vortex-core and approximate reattachment-point positions from vapor-screen images obtained in the BART. It can be exercised from UNIX platforms using the Precision Visuals Workstation Analysis and Visualization Environment (PV WAVE) software system.

Tuft Representer

The Tuft-Representer software tool depicts individual tufts in a tuft image as a straight-line segment. The origin is on the surface at the base of the free trailing tuft with the segment pointing along the average direction of the trailing tuft. With the characteristics of origin and direction, this representation is a vector (without arrowhead) in nature and is so referred to in that manner. This tool operates on a Sun workstation and requires the locations of the video targets and camera parameters as input data. (Flight values of video targets and a schematic representation are given in table A1 and fig. 7, respectively.) With the use of MAPPER, this vector representation can be projected onto the upper surface of the airplane. Additional details about the Tuft Representer can be found in reference 20.

Table A1. Video Targets Measured at Dryden Flight Research Center on F-16XL-1 Airplane

Target	FS	BL	WL
1	159.712	-24.391	102.008
2	163.961	-38.667	90.697
3	174.118	-30.260	95.106
4	172.851	-40.776	91.630
5	187.337	-20.662	111.121
6	182.924	-39.493	93.194
7	182.040	-53.637	90.917
8	195.672	-41.192	94.583
9	195.025	-52.305	92.941
10	202.439	-11.686	120.854
11	218.023	-21.643	109.554
12	209.345	-54.023	94.248
13	207.507	-66.298	91.365
14	255.566	-9.497	118.915
15	276.779	-20.845	108.481
16	275.204	-37.794	99.424
17	254.526	-71.183	94.841
18	268.979	-90.684	89.992
19	282.760	-80.433	94.617
20	319.019	-70.367	96.999
21	311.541	-94.559	93.405
22	305.890	-103.870	89.276
23	354.705	-35.863	100.601
24	345.123	-71.892	96.859
25	327.117	-111.547	88.813
26	353.944	-90.010	95.659
27	345.800	-118.396	88.436
28	383.740	-62.037	96.447
29	380.734	-95.101	95.466
30	378.884	-118.190	92.682
31	402.714	-38.917	101.689
32	403.856	-72.841	95.834
33	401.002	-103.350	94.970
34	398.664	-126.490	92.244
35	431.257	-69.354	95.169
36	429.992	-93.525	94.958
37	433.816	-115.440	94.295
38	452.936	-67.818	94.603
39	449.874	-84.811	94.600
40	450.587	-101.896	94.438
41	466.305	-82.975	94.283
42	460.331	-124.085	97.253
43	470.263	-179.820	93.004
44	457.041	-197.147	91.778
45	440.980	-197.296	90.903
46	423.935	-198.037	90.136
47	202.557	-26.507	73.928
48	249.466	-28.655	76.361
49	276.735	-28.553	79.282

Appendix B

Data Processes and Management

Two main topics are covered in this appendix: the various processes used to get the data from its as-received or reduced form to that needed for display and the management of the data and its meta-data. These two topics have been handled in an integrated manner from near the beginning of this project.

Data Processes

Data from experimental tests in wind tunnels and flight along with predicted values from CFD all require some processing in order to be utilized in a comprehensive way. They are discussed in order.

After defining a common data format—TOAD (ref. 33)—for the pressure and force and moment data and employing data translators to bring all experimental results into that format, the files of pressure data generally required two other processes applied before they could be used. The first was, if necessary, to split the pressure files of complete upper and lower surface data into separate files, `split_flight` or `split_BART`, and the second was to slightly alter the coordinates of the ports from actual to nominal values, `act_to_nom`, in order that the C_p values be directly comparable with other data sets. These two processes, along with the TOAD file plotting package, `tpplot`, can be exercised from UNIX platforms by using the Precision Visuals Workstation Analysis and Visualization Environment (PV WAVE) software system.

Additional antecedent processes were required in order to get the flight pressure time histories, collected at the Dryden Flight Research Center, ready for use in the preceding processes. First, a particular time interval from the flight time history had to be established by examining the video data from the three cameras to determine a 2-sec segment when acceptable image data were recorded from all cameras. Second, the pressure files were processed at Dryden for these times. Third, these files were transferred to Langley where they were rewritten into the TOAD format. Also transferred were selected parameter statistics and the associated pressure file name so that a summary report (meta-file) could be created. Fourth, these summary reports were processed locally on a Silicon Graphics workstation using the nonnumeric TOAD editor procedure, `nnted`, a variation of the TOAD editor procedure (ref. 34), `ted`, that can accommodate nonnumeric data in printing, and the results sent to the data management system for automatic data-field population. Only the items related to **Test Technique** were added to the database for each flight/run.

Two processes were required to generate the needed CFD C_p files. First, the software package FIELDVIEW (ref. 26) was utilized to cut the entire solution at the surface for selected BL and FS values on both the upper and lower surfaces and to save the resulting files. Second, these files were translated into TOAD format for subsequent use.

Data Management

System. The Program for Information Storage and Management (PrISM) (ref. 35) is a graphical, direct-manipulation Structured Query Language (SQL) interpreter. Users are able to query, add to, and modify data in a database without needing to know the internal representation of the data as tables and columns.

PrISM consists of a graphical user interface, database interface functions, and PrISM internal database tables. The PrISM internal database tables consist of core tables, which are constant and unchanging across all PrISM databases; kernel tables, the values of which depend upon the specific PrISM database and determine the PrISM functionality available to users; and tables which support the PrISM Security System.

The application of PrISM to the F-16XL-1 High-Lift Project and the Cranked-Arrow Wing Aerodynamics Project (CAWAP) involves the storage of information about flight tests, wind-tunnel tests, and CFD solutions. The database stores administrative information about the tests (meta-data) and the full, mass storage, path name of the resulting data files. For EFD measurements, the experimental data stored

are files of pressure, force/moment, still photographs, and two-dimensional images digitized from videotape (both instantaneous and time averaged); for CFD predictions, the grid and solution files are stored as well as C_p data at selected FSs and BLs. The F-16XL-1 database also supports the viewing of 3-D renderings of the 2-D flight images through MAPPER. Queries for selected pressure data and 2-D flight image data are available to WWW users by completing the appropriate form under **Program for Information Storage and Management, F16XL High-Lift Project CAWAP** given in reference 36. As a result of performing such a query, data retrievals are possible. For example, depending on the selection made, one may have either (1) the contents of selected pressure files viewed through hypertext links and/or the files retrieved and made local for further processing or (2) the 2-D flight image files viewed through hypertext links.

Pressure file naming convention. Designations of particular F-16XL components making up a configuration tested, the facility used in its testing, the research engineer, and/or the test conditions may appear in the names of the pressure files saved on mass storage. Three basic F-16XL wind-tunnel configurations have been tested and they are designated as b1, b2, and b3 configurations. Configuration b1 is the model with air dams, b2 is the model with air dams and missiles, and b3 is the model with missiles. At Langley, low-speed tests were made for all three configurations in BART but only for configurations b2 and b3 in the Langley 30- by 60-Foot Tunnel. At the Ames Research Center, high-speed tests were made for configuration b2 in the Ames 11-Foot Tunnel.

The file names used in the keys in the presented pressure data plots differ from the names by which they have been saved on mass storage in four ways: (1) they have been simplified by removing nonvital information, (2) they have been simplified by removing test or solution information, which has been placed in the figure caption, (3) they reflect the wind-tunnel facility and not the test engineer, and (4) they are pressure surface specific as a result of processing the saved file. Examples of the changes to the file names for wind-tunnel and flight are as follows: the file name "dmss:@jelama/BART/press.bart.Q40.b2.basic" is split into two files "BART,up" and "BART,low" for the basic F-16XL model with air dams and missiles (configuration b2) at $q_\infty = 40 \text{ lb/ft}^2$ or $M_\infty = 0.17$ and $R_n = 1.12 \times 10^6$; the file "dmss:@jelama/hahne/press.409.b2.basic" becomes "30_by_60,up" for the same configuration at $q_\infty = 6.7 \text{ lb/ft}^2$ or $M_\infty \approx 0.07$; and the flight file "dmss:@jelama/f16XL.flight/flight144/ft0144.tp16b.cp.toad" is split into two files "Flt144.Run16b,up" and "Flt144.Run16b,low," thereby, uniquely identifying the flight-and-run and consequently the specific nominal flight conditions from table 5 for the same configuration. For certain wind-tunnel data comparisons with an R_n variation, the simplified filename will have a suffix added, e.g., "R2.1" to signify $R_n = 2.1 \times 10^6$. A CFD example is file "dmss:@jelama/garriz/F16XL/aoa19.84m0.242/BL55.up.toad" being reported as "CFL3D" at FS 55 and the **actual flight conditions** of $\alpha = 19.8^\circ$ and $M_\infty = 0.24$.

Files of flight, nominalized upper and lower surface pressures have also been saved on mass storage and have a naming convention typified by "dmss:@jelama/f16XL.flight/flight144/ft0144.tp16b.cp.up.tmp" and "dmss:@jelama/f16XL.flight/flight144/ft0144.tp16b.cp.low.tmp," respectively.

Appendix C

Airplane Instrumentation

Due to the complexity of the airborne research systems for the basic airplane, the flight testing was divided into three parts, designated "Parts 1A to 1C." These were ordered according to increased levels of instrumentation complexity. Part 1A was the initial phase and had a limited but sufficient instrumentation suite for airplane documentation at the Langley Research Center. The suite also included video cameras to capture the images from the HUD and some surface-flow features. Part 1B, also performed at Langley, was done with additional instrumentation for both airplane positioning and surface-flow studies and included additional video cameras. Part 1C, later known as CAWAP, was performed at the Dryden Flight Research Center and had the most extensive instrumentation suite for detail surface-flow measurements. This suite included instrumentation to measure the pressures from flush and belted static ports, boundary-layer rakes, modified Preston tubes, and the electrical signals from a hot-film belt. (See fig. 6.) Details of the instrumentation suites, the modifications made, and flight practices with them are given in the following sections.

Instrumentation Suite

The core of the airborne instrumentation systems was the Airborne Test Instrumentation System (ATIS). The ATIS had associated with it either a first- or second-generation System Control Unit (SCU) so that the final designation is either ATIS-SCU1 or ATIS-SCU2. The ATIS-SCU1 is a 10-bit (-5.12 to $+5.12$ V) pulse-code modulated (PCM) modular data system and was installed originally by General Dynamics for USAF flight testing. For the Cranked-Arrow Wing Aerodynamics Project (CAWAP), ATIS-SCU2, a 12-bit (-10.24 to $+10.24$ V) PCM was used and the system reprogrammed to accommodate the measurements list. Some airplane parameters proved to be from difficult to impossible to recalibrate after the upgrade from the 10-bit to the 12-bit system; therefore, the existing 10-bit calibrations were used but only after rescaling the parameter voltages (and engineering units) to 12-bit decimal counts. For example, if a 10-bit system channel was programmed with Offset = 0 and Gain = 1, -5.12 V would correspond to 0 counts and $+5.12$ V to 1023 counts. In the 12-bit system, -10.24 V corresponds to 0 counts and $+10.24$ V to 4095 counts. Therefore, a parameter whose voltage output for a

given engineering unit value is -2.56 V would equal 256 counts in a 10-bit system but 1536 counts in a 12-bit system. Zero offset and gain settings for each PCM channel were taken into consideration when doing calibration conversions. The parameters that were corrected in this manner included pitch, roll, and yaw as well as rudder, elevon, and aileron forces and hinge moments (which all together accounted for 16 measured parameters). All other airplane parameters were recalibrated using the 12-bit data system. The ATIS also provided time code for insertion into the five airborne video cassette recorders for synchronization of data in the CAWAP.

Modifications

The specific research modifications relative to the basic airplane instrumentation suite for the preliminary on surface-flow measurements, Part 1A, were as follows:

- External paint scheme for on and off surface flow visualization

- Externally mounted lipstick cameras on either side at the top of the vertical tail with associated VCRs and time code inserters, one for every two VCRs, in the forward equipment bay

- Video camera for the HUD and associated VCR and time code inserter in the forward equipment bay

- Enclosure of the lower surface AMRAAM missile cavities

- Enclosure of the gun muzzle trough

The external paint scheme (fig. 1(a)) was based on the scheme used on the Dryden F-18 High-Angle-of-Attack Research Vehicle. The upper surfaces of the airplane were painted flat black to provide sufficient contrast with the tufts, oil, and liquid crystals so that the on surface flow patterns could be visualized in Parts 1A and 1B. The gold stripes on the wing were used to identify the leading edge in the video images and were to be of particular value for the off surface flow-visualization portion of the test, which did not occur.

Two tail-mounted video cameras (left tail camera shown in fig. C1) were used to provide coverage over the upper surfaces of the wings. The locations of these cameras are shown in figure 12. The fields of view of these cameras could be changed by three methods: (1) installing lenses of different focal length, (2) adjusting the camera pivot angle (angle of the camera centerline with respect

to vertical) up to $\pm 25^\circ$, and (3) installing one of four camera mounting blocks, which provided cant angles (angle between the camera centerline and the longitudinal axis of the airplane) of 8.5° , 17.5° , 26° , and 36° . Lenses used in these locations were almost exclusively 7.5 mm.

The AMRAAM lower surface cavities were covered with plates to produce a flat surface. The gun muzzle trough was smoothed over with a plug to preclude the formation of extraneous vortices not associated with the basic cranked-arrow wing planform. The gun trough is shown with and without the plug in figure C2.

Part 1B began with the instrumentation suite of Part 1A and added other items to bring it to the required level. The changes included

Modifications to the ammo drum bay instrumentation pallet

Global Positioning System (GPS)

Wingtip video cameras installed in dummy missiles noses (2)

Fuselage-mounted video cameras (2)

Enhanced measurements of airplane state parameters (linear accelerometers at the airplane center of gravity, attitude gyros, rate gyros, flow vanes, and nose-boom pitot-static transducers)

Engine instrumentation

Tail-mounted microphones (3)

An instrumentation pallet, based on a design provided by the Air Force Armament Laboratory, was installed in the ammo drum bay which is an unpressurized compartment in the fuselage located aft of the cockpit. The pallet, shown in figure C3, could be raised while installed in the airplane to permit access to components located on the lower shelves. The pallet contained components associated with the GPS, the measurement of the enhanced airplane parameters, and the microphones. It also contained the two additional VCRs added for Part 1B and their associated time code inserter.

The GPS was installed to provide accurate real-time airplane position and to improve the accuracy of the airspeed calibrations. Because of the limited internal volumes in the airplane, the components were distributed throughout the vehicle including on the ammo drum bay pallet.

For Part 1B, there were seven video cameras and five VCRs, an increase of four and two, respectively, over Part 1A. These were added to provide a more complete video coverage of the wing

apex regions and leading edges. Note that the apex regions were viewed by lipstick cameras mounted externally on the fuselage (fig. C4), just behind and to the side of the cockpit, whereas the cameras used to view the leading edges were mounted in the heads (fig. C5) of dummy, but properly mass distributed and ballasted, AIM-9L missile bodies. The fuselage cameras had 4-mm lenses and were configured such that they could feed video signals to either the VCRs located in the forward equipment bay or the ammo bay, depending on the cameras needed for a particular flight. The missile cameras had 15-mm lenses and were configured to only feed video signals to the VCRs in the ammo bay. (Table C1 summarizes the nominal center of lens camera locations for the video cameras, and table C2 summarizes both lens location and orientation, as determined by resection (ref. 29), for the CAWAP flights. The camera angles are defined in fig. C6.)

The CAWAP instrumentation suite began with that of Part 1B and other items were added to bring it to the required level. The changes occurred because of the need to measure the following items:

Pressures for flush and belted static ports

Pressures from boundary-layer rakes

Pressures from modified Preston tubes

Electrical signals from a hot-film belt

Practices

Pressure location measurements and assignments. In order to compare the pressure measurements from the flight experiments with CFD predictions and wind-tunnel model measurements, the ports on the airplane were distributed in the same relative locations as those on the wind-tunnel models. Because the airplane had more available pressure measurements, additional ports were included in both spanwise and chordwise distributions. In particular, flush ports were located in the leading-edge region of the right main wing with the pressure belts being used to complement these locations on the main and outboard right wing panels. The pressure belts, composed of multiples of 10 tube subbelts, were necessary because the wing contains the fuel and cannot be pierced except at a few cavity locations. Care was taken in the selection and installation of the belts in order to minimize the effect of the belts on the measured pressures. Tubing diameter was kept at a minimum by maintaining short belt lengths to the appropriate pressure transducer. In addition, noninstrumented

tubing was placed outside of the tubes with ports, and then ramps from the wing surface to the top of the tubes were faired in. Figure C7 shows a cross-sectional sketch of the tubing and ramp layout on the wing. Similarly, a single ramp was added to the forward end of the tubes, in the vicinity of the leading edge, in order that the flow be disturbed as little as possible, as shown in the photograph of figure C7.

The first step in placing the ports on the wing was to identify the desired locations by measuring from known reference points on the wing. After the pressure belts were installed, the static-pressure measurement (port) holes were punched into the belt material at the desired locations. Some ports had to be relocated because of wing surface conditions. Once the ports were in place, a second measurement was made by using a theodolite method to determine the exact location of each port on the wing surface. Since the geometry of the airplane was first measured with photogrammetry, leading-edge and trailing-edge locations and chord lengths were determined from these measurements.

Differences were noted between the specified port locations and those laid out. The differences were due to keeping the pressure belts streamwise, which makes the BL values vary along the FS, and the physical constraints associated with the underlying structure in the vicinity of the wing apex and leading edge. Therefore, these measurements had to be adjusted to nominal values after installation in order that comparison plotting could be done.

For the belts it was just a matter of changing the BL value from actual to nominal. However, for the flush ports along the leading edge and in the apex region, an adjustment in the actual BL and FS was needed. In order to make these flush port adjustments, each port was assigned a nominal FS and BL based on the actual value of the FS and the desired BL. The FS for the flush ports was established based on the intersection of the desired BL with the wing leading edge. Table 4 lists the actual locations as measured and the new nominal locations.

Video. Prior to each flight, the researchers selected the five video cameras whose signals were to be recorded. Typically, the HUD camera was recorded only during airspeed calibrations and the aeroacoustics and handling qualities flights. During the flow-visualization flights, the outputs from as many as five external cameras were recorded. (See fig. 12.)

For CAWAP, an initial video recording was made on the right wing to establish the status of the pressure belts. The cameras were located on the right side of the airplane atop the vertical tail and on the fuselage. During later flights, the focus was the wing surface flow field as depicted by the tuft patterns on the left wing. These patterns were video recorded from the cameras located atop the left vertical tail, on the fuselage, and in the left missile nose.

Table C1. Nominal Center of Lens Camera Locations for Part 1B and CAWAP

Camera position	FS	BL	WL	Lens, mm
Left tail	563.322	-2.042	223.058	7.5
Left fuselage	181.24	-15.9	119.7	4
Left missile	403.68	-201.046	91.74	15
Right tail	563.322	2.042	223.058	7.5
Right fuselage	181.24	15.9	119.7	4
Right missile	403.68	201.046	91.74	15

Table C2. CAWAP Center of Lens Camera Locations and Orientations as Determined by Resection

Camera position	FS	BL	WL	ω , deg	ϕ , deg	κ , deg	Lens, mm
Left tail	559.309	-2.044	226.817	-131.800	44.528	121.073	7.8223
Left fuselage	181.388	-19.125	117.798	-149.290	-3.384	154.513	3.9106
Left missile	408.016	-206.524	89.185	-1.082	44.565	-0.795	15.877

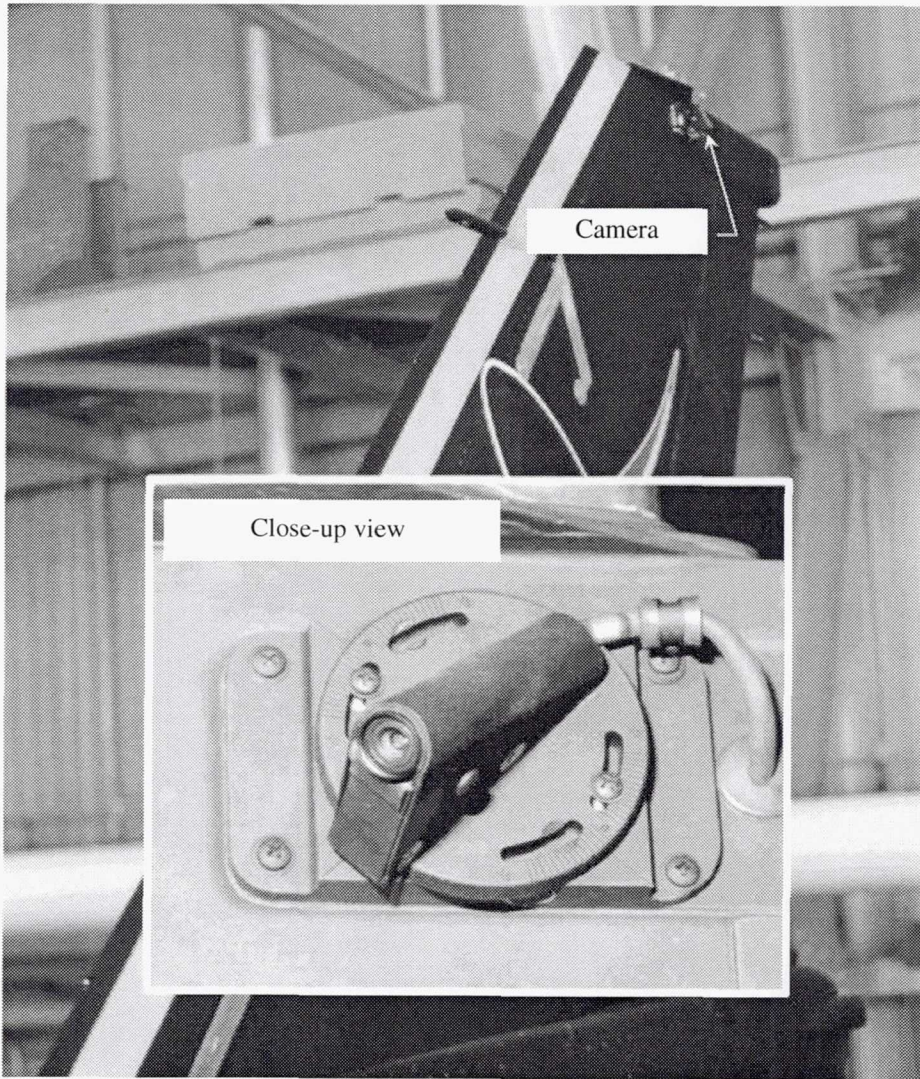
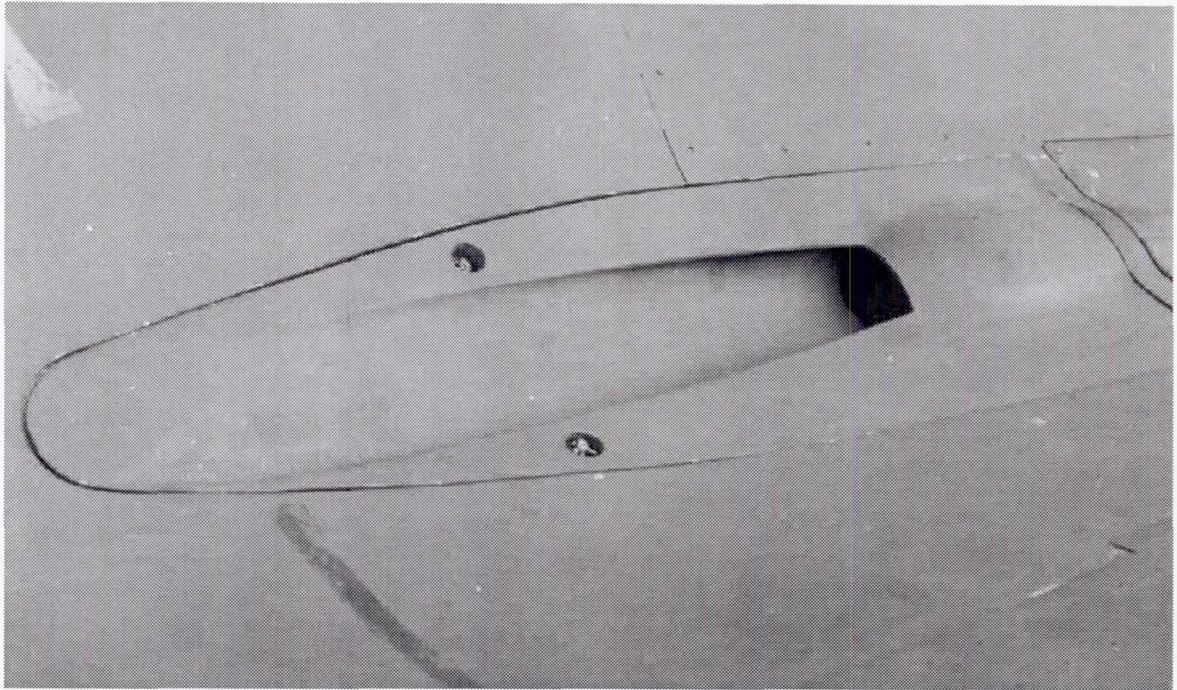
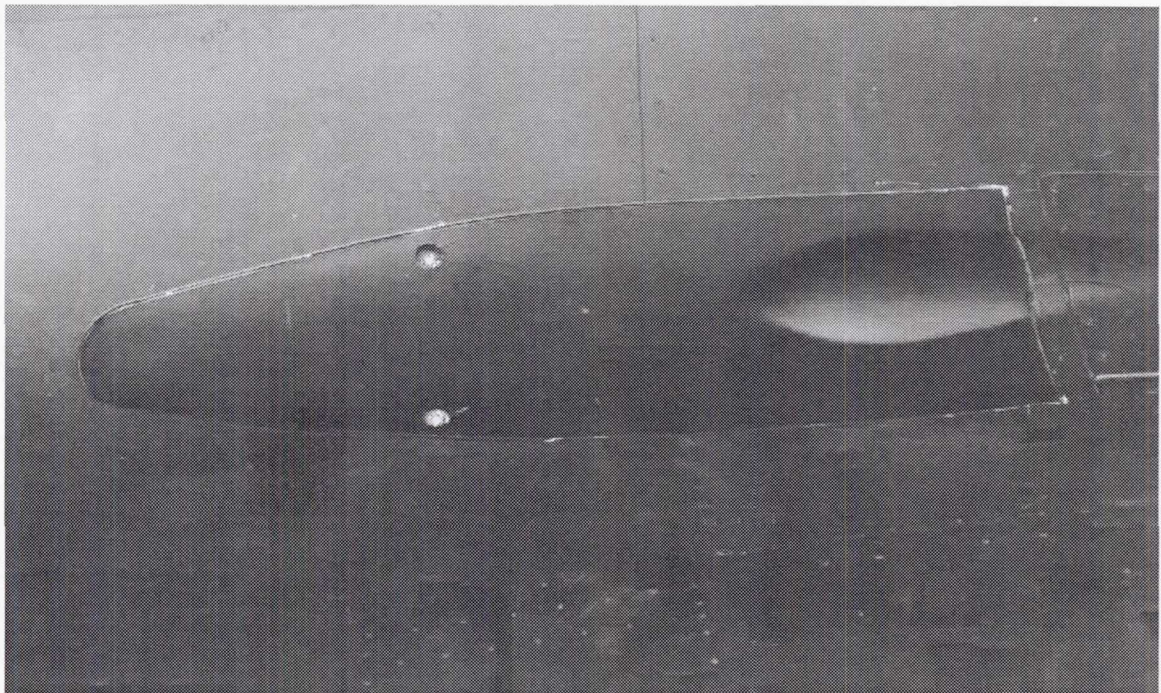


Figure C1. Video camera installation on vertical tail (left side) of F-16XL-1 airplane.



(a) Without plug.



(b) With plug.

Figure C2. Gun muzzle with and without plug.

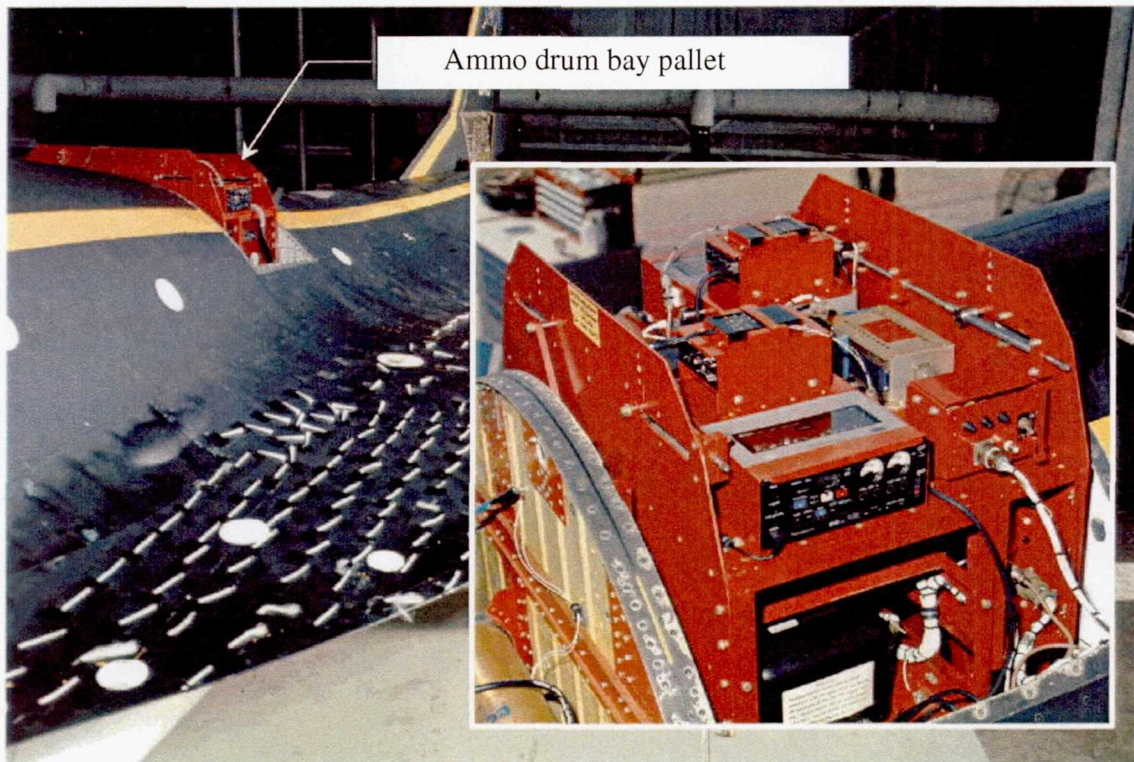


Figure C3. Ammo drum bay instrumentation pallet.

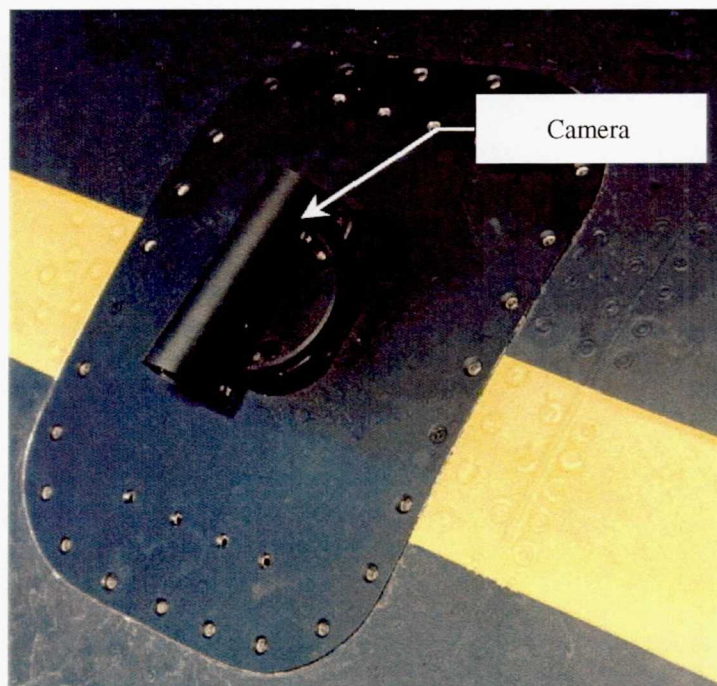


Figure C4. Fuselage-mounted video camera used for viewing leading-edge apex region of wing.

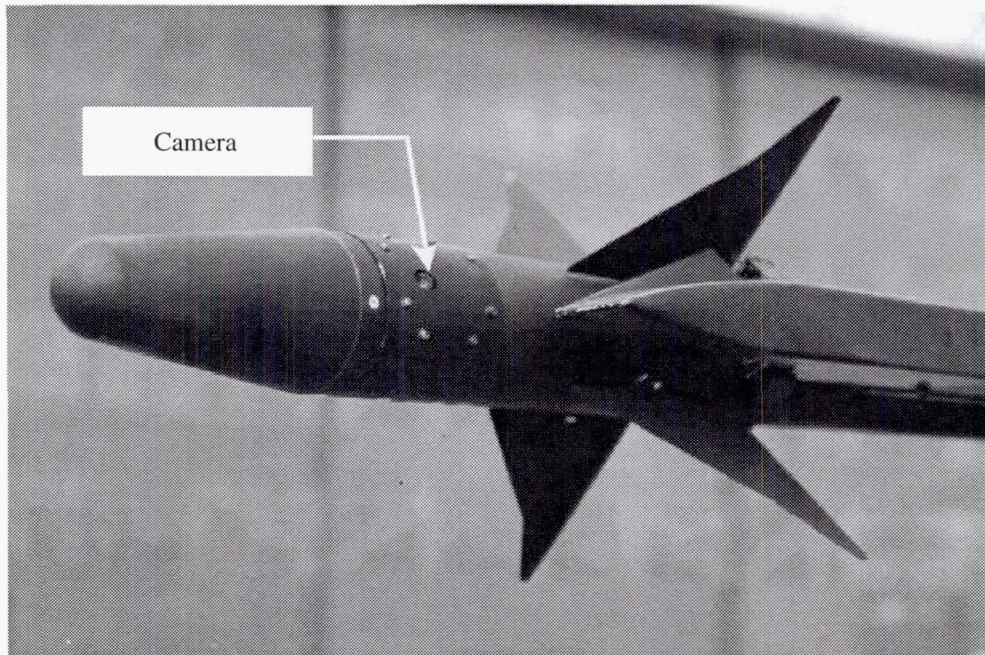


Figure C5. Dummy AIM-9L Sidewinder missile used as wingtip video camera pod.

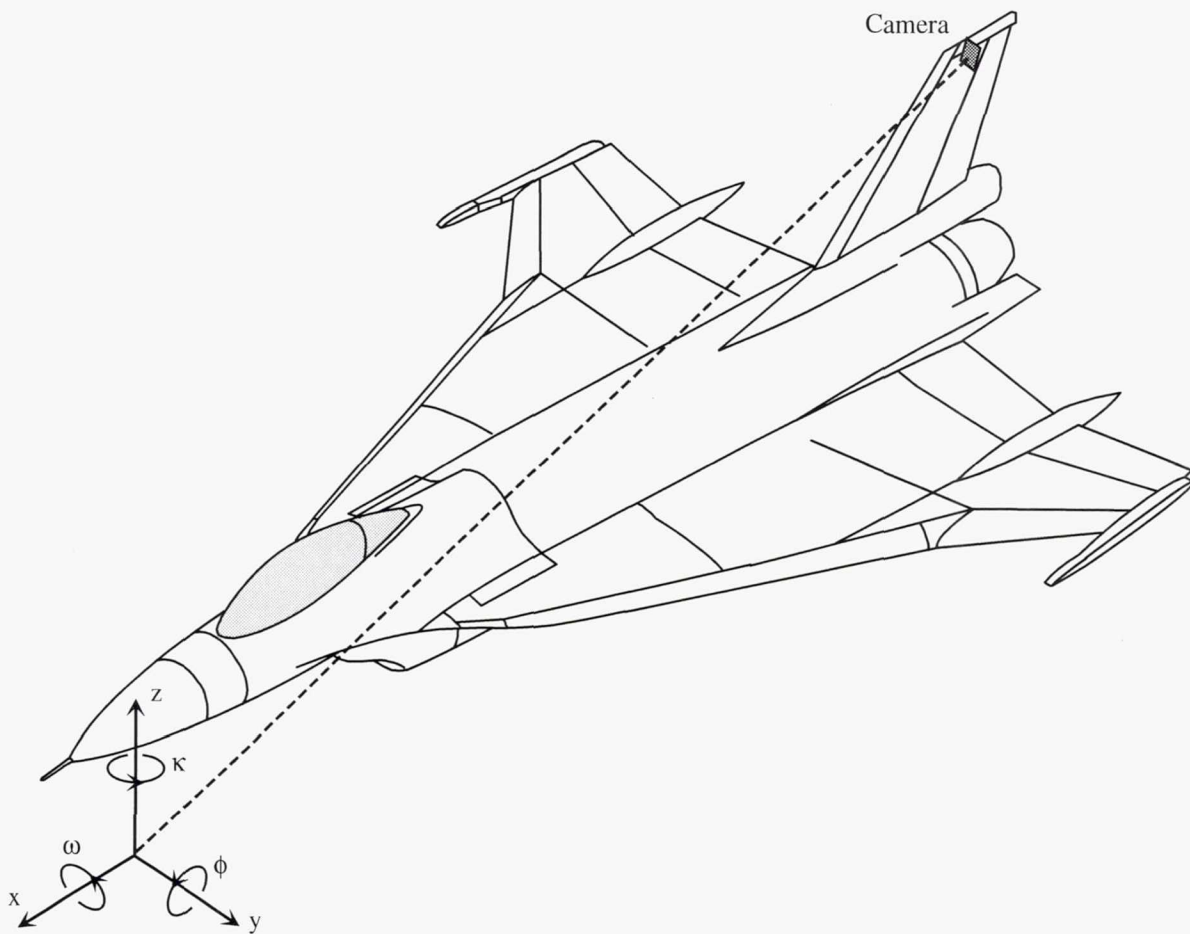


Figure C6. Euler angles used for airplane cameras.

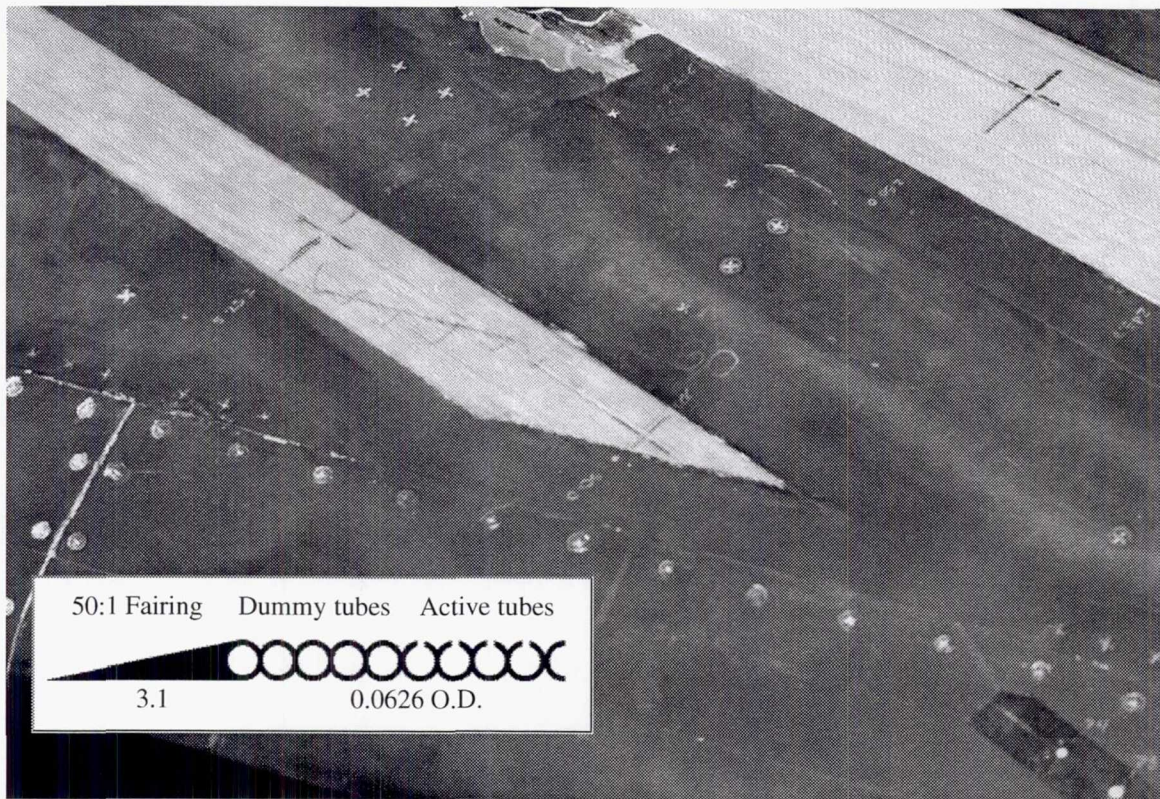


Figure C7. Sketch of pressure belt cross section showing active tubes and ramps. Dimensions are in inches.

Appendix D

Description of Wind-Tunnel Test and Vapor-Screen Systems

In support of this project, three Langley wind-tunnel tests of F-16XL models were conducted, one in the Langley 30- by 60-Foot Tunnel (ref. 37) as test 50 in 1994 and two in the Langley Basic Aerodynamics Research Tunnel (ref. 38) as tests 3 and 4 also in 1994. A brief description of tests 50 and 3 follow. Test 4 is described in reference 11 and it was a pressure sensitive paint study of the upper surface *with no air dams*, which has no counterpart in flight or CFD.

Test in Langley 30- by 60-Foot Tunnel

This open-jet wind-tunnel force/moment and surface pressure measurement test 50 was conducted in the 30- by 60-Foot Tunnel with a 0.18-scaled model mounted on a six-component balance in an aft-sting arrangement (fig. D1) at $M_\infty \approx 0.07$ or $q_\infty = 6.7 \text{ lb/ft}^2$ and $R_n = 2.1 \times 10^6$. The model was tested at $\alpha = -5.0^\circ, -2.5^\circ, 0.0^\circ, 2.5^\circ, 5.0^\circ, 7.5^\circ, 10.0^\circ, 12.5^\circ, 15.0^\circ, 17.5^\circ, 20.0^\circ, 22.5^\circ, 25.0^\circ, 27.5^\circ, \text{ and } 30.0^\circ$ and at $\beta = -20.0^\circ, -8.0^\circ, -2.5^\circ, 0.0^\circ, 2.5^\circ, 8.0^\circ, \text{ and } 20.0^\circ$. Various combinations of control-surface deflections and other geometrical variations of the baseline model were tested. Only the results for the baseline model at $\beta = 0^\circ$ are reported because no other flight or CFD results are available for comparison. (The pressure port locations on this model are nominally represented on the airplane by a subset. Compare tables 9 and 4.)

For reference, off surface flow results were obtained by using the vapor-screen technique. The flow was seeded with propylene diglycol vapor, illuminated by a nearly normal laser sheet (located far outside the tunnel flow) sweeping over the right half of the model in a small arc, and recorded with a fixed video camera located behind the model. However, because of the difficulty in resolving the camera parameters, these results could

only be considered qualitative and therefore are not presented.

Test in BART

BART has an open return and a test section made of Rohm and Haas Plexiglas material. The test 3 was conducted with a 0.04-scaled model, mounted on a single pedestal (fig. D2), for ranges of M_∞ , q_∞ , and R_n from 0.07 to 0.17, 8.4 lb/ft^2 to 40 lb/ft^2 , and 0.50×10^6 to 1.12×10^6 , respectively. The model was tested at corrected values of α , which took into account the influence of the sidewall pressures determined at start of test. The test values of α were $0.0^\circ, 5.0^\circ, 10.0^\circ, 13.0^\circ, 15.0^\circ, \text{ and } 20.0^\circ$ at $\beta = 0^\circ$. No control surfaces were deflected but different model components and geometrical variations were examined. In addition to surface pressures, an oil-flow study was done on the surface for the same values of α . The pressure port locations on this model are nominally represented on the airplane by a subset. (Compare tables 10 and 4.) Off surface studies using a five-hole probe and vapor screen were done over a restricted set of the test α ; namely, $10^\circ, 13^\circ, \text{ and } 15^\circ$. This was done to emphasize the take-off and landing portion for the High Speed Civil Transport study. The five-hole probe data were collected within survey boxes which used the model right wing upper numerical surface description as a lower boundary at two fuselage stations, which have full-scale values of FS 225 and FS 350. The other boundaries for the two boxes were BL 41.5 and BL 50.625 inboard, BL 92.15 and BL 145.55 outboard, WL 125 and WL 150 top, and WL 87.5 and WL 87.5 bottom at FS 225 and FS 350, respectively. The vapor-screen studies were done by seeding the flow with propylene diglycol vapor, illuminating the flow with a translating laser sheet (mounted outside and atop the tunnel) shining on the top of the model, and recording images with a fixed video camera mounted atop and ahead of the test section. Images were taken at seven fuselage stations which have full-scale values of FS 167.5, FS 225, FS 257.5, FS 300, FS 350, FS 390, and FS 435. Sample images are shown in figure D3.

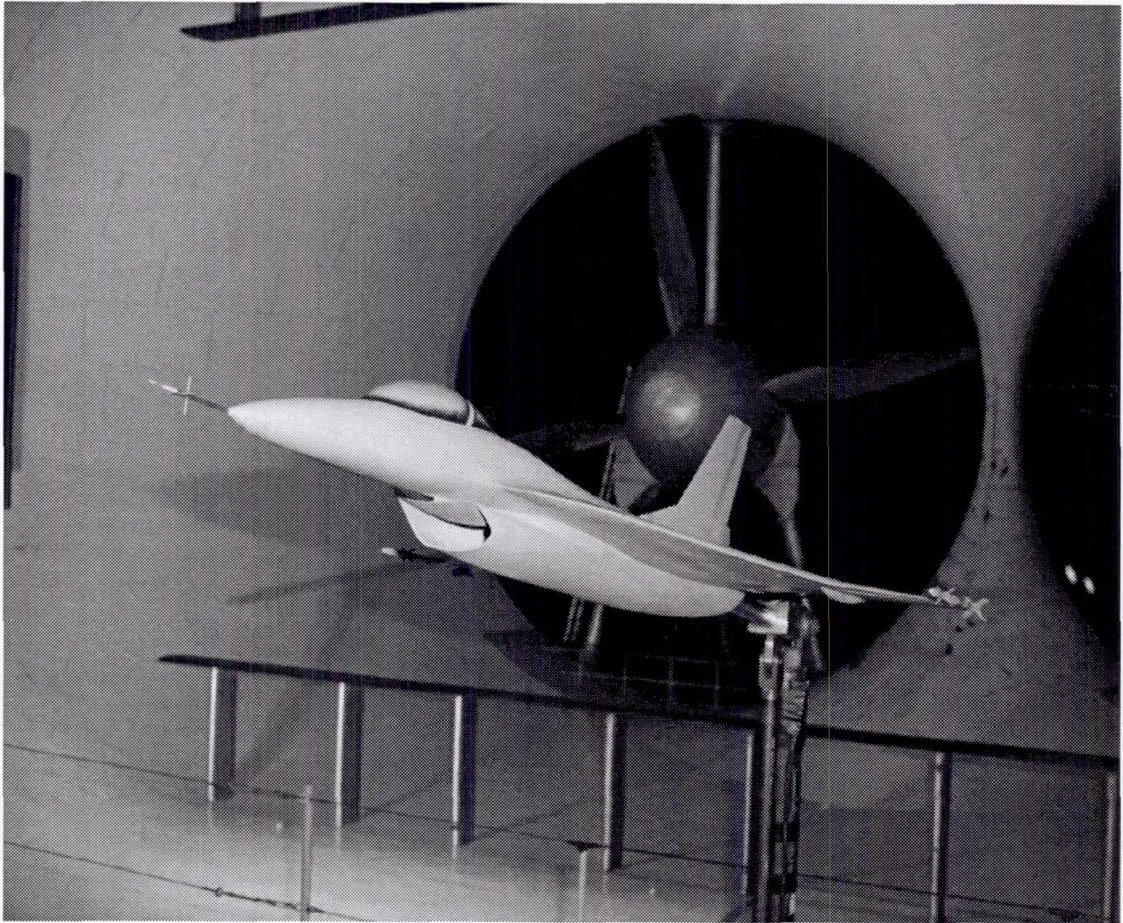


Figure D1. 0.18-scaled model of F-16XL in Langley 30- by 60-Foot Wind Tunnel.

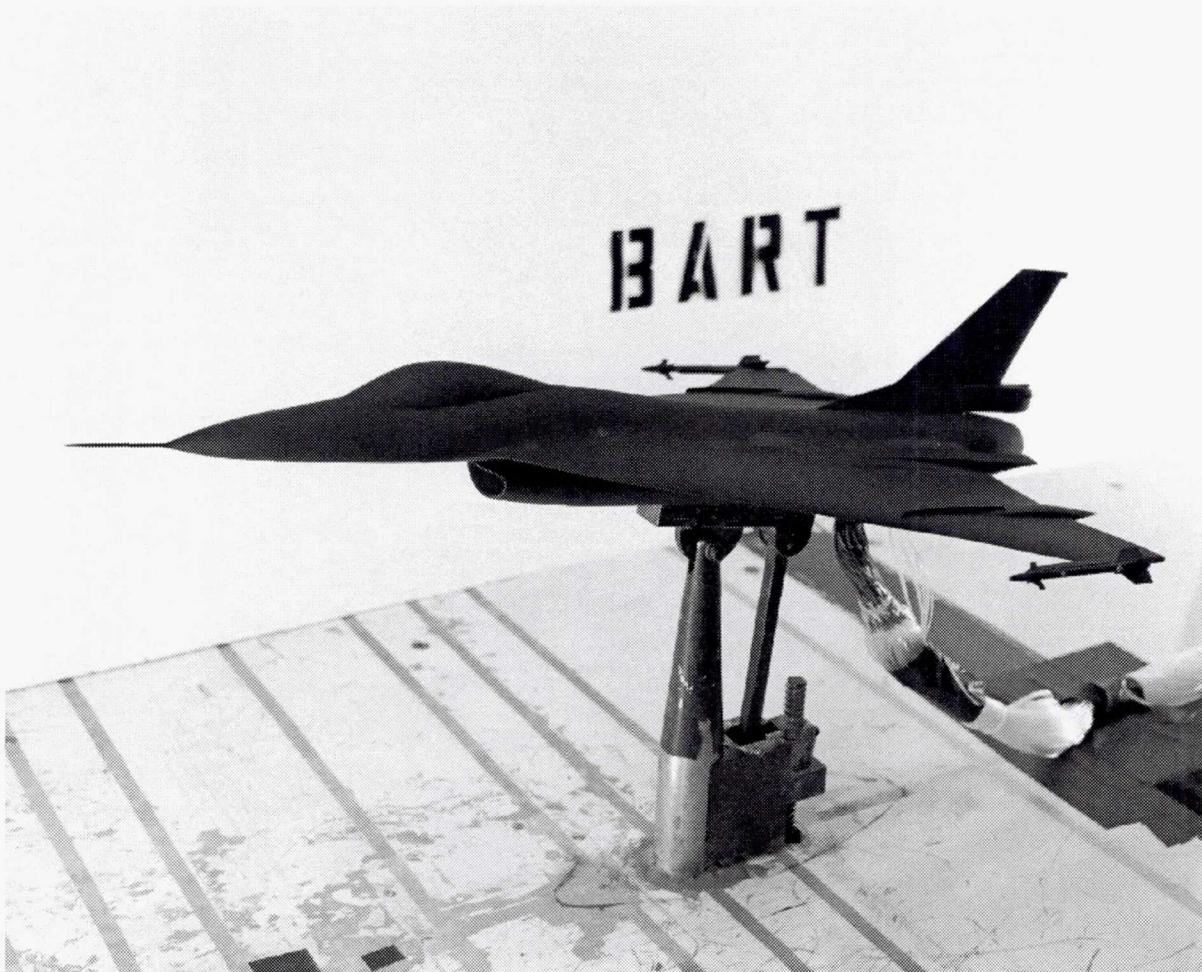


Figure D2. 0.04-scaled model of F-16XL in Langley BART.

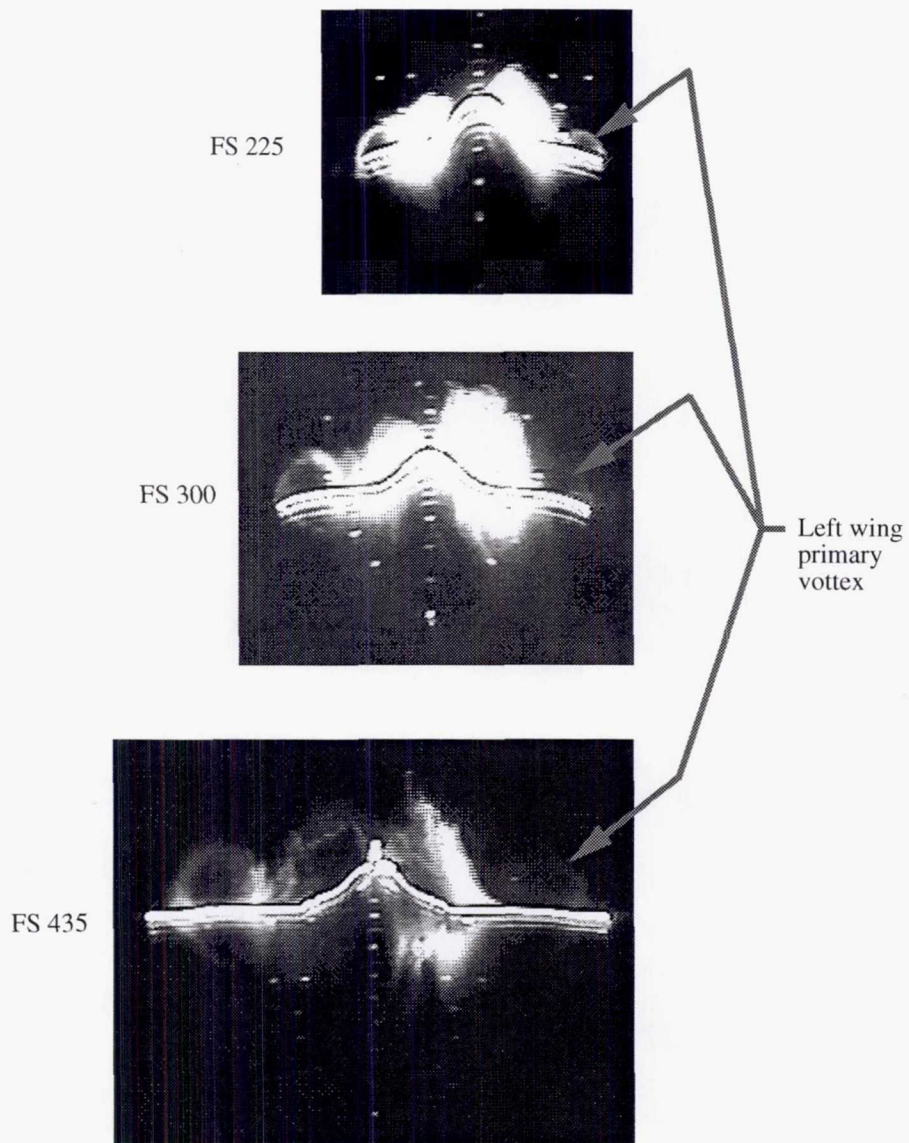


Figure D3. Sample vapor-screen images for 0.04-scaled model of F-16XL airplane in Langley BART at $\alpha = 15^\circ$, $M_\infty = 0.15$, and $R_n = 1 \times 10^6$.

References

1. *U.S. Standard Atmosphere, 1962*. NASA, U.S. Air Force, and U.S. Weather Bureau, Dec. 1962.
2. Bertin, John J.; and Smith, Michael L.: *Aerodynamics for Engineers*, Second ed. Prentice-Hall, Inc., 1989, p. 146.
3. Ghaffari, Farhad: *Navier-Stokes, Flight, and Wind Tunnel Flow Analysis for the F/A-18 Aircraft*. NASA TP-3478, 1994.
4. Potsdam, M. A.; Intemann, G. A.; Frink, N. T.; Campbell, R. L.; Smith, L. A.; and Pirzadeh, S.: *Wing/Pylon Fillet Design Using Unstructured Mesh Euler Solvers*. AIAA-93-3500, Aug. 1993.
5. Hillaker, H. J.: *F-16XL Flight Test Program Overview*. AIAA-83-2730, Nov. 1983.
6. Talty, Patrick K.; and Caughlin, Donald J.: *F-16XL Demonstrates New Capabilities in Flight Test at Edwards Air Force Base*. *J. Aircr.*, vol. 25, no. 3, Mar. 1988, pp. 206-215.
7. Anders, Scott G.; and Fischer, Michael C.: *F-16XL-2 Supersonic Laminar Flow Control Flight Test Experiment*. NASA/TP-1999-209683, 1999.
8. Bower, J. N.; and Scott, S. R.: *The F-16XL Flight Test Program*. *Society of Flight Test Engineers 15th Annual Symposium*, Aug. 1984, pp. 9-1-9-5.
9. Bates, J. D.; and Livengood, J. T.: *F-16E Basic Lines Data Report—Volume 1*. Rep. no. 400PR011, General Dynamics Corp., Dec. 1981.
10. Bates, J. D.; and Livengood, J. T.: *F-16E Basic Lines Data Report—Volume 2*. Rep. no. 400PR011, General Dynamics Corp., Jan. 1982.
11. Rickard, Susan J.; Washburn, Anthony E.; Morris, Martin J.; and Donovan, John F.: *Pressure Sensitive Paint Studies of Vortical Flow at Low Speed*. SAE Paper 951989, Sept. 1995.
12. Bertelrud, A.: *Total Head/Static Measurements of Skin Friction and Surface Pressure*. *AIAA J.*, vol. 15, no. 3, Mar. 1977, pp. 436-438.
13. Thomas, J. L.; Krist, S. T.; and Anderson, K. W.: *Navier-Stokes Computations of Vortical Flows Over Low-Aspect-Ratio Wings*. *AIAA J.*, vol. 28, no. 2, Feb. 1990, pp. 205-212.
14. Thomas, James L.; Weston, Robert P.; Luckring, James M.; Walters, Robert W.; Reu, Taekyu; and Ghaffari, Farhad: *A Patched-Grid Algorithm for Complex Configurations Directed Towards the F-18 Aircraft*. AIAA-89-0121, 1989.
15. Goldstein, Richard J., ed.: *Fluid Mechanics Measurements*. Hemisphere Publ. Corp., 1983, pp. 565-569.
16. Fisher, David F.; and Fischer, Michael C.: *Development Flight Tests of Jetstar LFC Leading-Edge Flight Test Experiment*. *Research in Natural Laminar Flow and Laminar-Flow Control*, Jerry N. Hefner and Frances E. Sabo, compilers, NASA CP-2487, Pt. 1, 1987, pp. 117-140.
17. Spellman, M. W.: *Model and Test Information Report 1/9-Scale F-16E Force and Loads Model*. Rep. no. 400PR026, General Dynamics Corp., Aug. 1991.
18. Elbers, W. K.: *Wind Tunnel Data Report 1/9-Scale F-16E Pressure Model NASA Ames Research Center Tests 517-1-11 and 517-1-97*. Rep. no. 400PR037, Vol. II, General Dynamics Corp., Dec. 1981.
19. Hahne, David E.: *Low-Speed Aerodynamic Data for an 0.18-Scale Model of an F-16XL With Various Leading-Edge Modifications*. NASA/TM-1999-209703, 1999.
20. Lessard, Wendy B.: *Subsonic Analysis of 0.04-Scale F-16XL Models Using an Unstructured Euler Code*. NASA TP-3597, 1996.
21. White, Frank M.: *Viscous Fluid Flow*. McGraw-Hill, Inc., 1974, pp. 474-476.

22. *IBM Visualization Data Explorer Version 3.1 Users Guide*, Sixth ed. Thomas J. Watson Res. Center Publ. No. SC38-0496-05, IBM Corp., 1995.
23. Walatka, Pamela P.; Clucas, Jean; McCabe, R. Kevin; Potter, Rick; and FAST programmers at ARC: *FAST User Guide: Version 1.1a*. RND-3-010, NASA Ames Research Center, Aug. 3, 1999.
24. Walatka, Pamela P.; Buning, Pieter G.; Pierce, Larry; and Elson, Patricia A.: *PLOT3D User's Manual*. NASA TM-101067, 1990.
25. *Tecplot Version 7.5 User's Manual*. Amtec Eng. Inc., 1988-1998.
26. *FIELDVIEW Version 6 User's Guide*. Intelligent Light, May 1999.
27. Lamar, John E.; Brandon, Jay; Stacy, Kathryn; Johnson, Thomas D., Jr.; Severance, Kurt; and Childers, Brooks A.: *Leading-Edge Vortex-System Details Obtained on F-106B Aircraft Using a Rotating Vapor Screen and Surface Techniques*. NASA TP-3374, 1993.
28. Bowen, Susan S.: *Computer Vision as a Tool for Image Synthesis*. International Symposium on Electronic Imaging, 1995.
29. Wolf, Paul R.: *Elements of Photogrammetry*. McGraw-Hill, Inc., 1974.
30. Stacy, Kathryn: Computer Graphics—Custom Application: ILLUME. <http://dval-www.larc.nasa.gov/DVAL/Capabilities/Cg/index7.html> Accessed Jan. 4, 2001.
31. Stacy, Kathryn; Severance, Kurt; and Childers, Brooks A.: Computer-Aided Light-Sheet Flow Visualization Using Photogrammetry. NASA TP-3416, 1994.
32. Stacy, Kathryn: Spotlight Application—Image Reconstruction. <http://dval-www.larc.nasa.gov/DVAL/Spotlight/index6.html> Accessed Jan. 4, 2001.
33. Bingel, Bradford; and Hammond, Dana: *Transferable Output ASCII Data (TOAD) File Format Description*. NASA CR-178361, 1987.
34. Bingel, Bradford D.; Shea, Anne L.; and Hoffer, Alicia S.: *Transferable Output ASCII Data (TOAD) Editor Version 1.0 User's Guide*. NASA CR-187507, 1991.
35. Reisel, Joseph F.: The F16XL Database. http://dval-www.larc.nasa.gov/~optics/f16xl_delivery/index.html Accessed Jan. 4, 2001.
36. Cronin, Catherine K.: Program for Information Storage and Management—F16XL High Lift Project (CAWAP). <http://f16xl-prism.larc.nasa.gov/cgi-bin/webprism.cgi?f16xl@remote-dbsrv1> Accessed Jan. 4, 2001.
37. Baals, Donald D.; and Corliss, William R.: *Wind Tunnels of NASA*. NASA SP-440, 1981.
38. Sellers, William L., III; and Kjelgaard, Scott O.: The Basic Aerodynamics Research Tunnel—A Facility Dedicated to Code Validation. AIAA-88-1997, May 1988.

Table 1. Planned F-16XL CAWAP Data Comparisons

Item	Data comparison	Data source
1	On and off surface flow Tufts Static pressures in a row Vapor screen Particle traces	Flight Flight Flight CFD
2	Surface flow and pressure Oil flow Pressure sensitive paint	Wind tunnel Wind tunnel
3	Surface pressure Pressure sensitive paint Calculations	Wind tunnel CFD
4	Vortex core location Vapor screen Particle traces	Wind tunnel CFD
5	Vortex core location Vapor screen Particle traces	Flight, wind tunnel CFD
6	Surface flow Oil flow Tufts Liquid crystals	Flight Flight Flight
7	Surface flow Oil flow Tufts Particle traces	Flight Flight CFD
8	Surface flow Oil flow Particle traces	Flight, wind tunnel CFD
9	Surface pressure Pressure sensitive paint Static pressures in a row	Wind tunnel Wind tunnel
10	Off surface flow Vapor screen Five-hole probe	Flight, wind tunnel Wind tunnel
11	On and off surface flow Oil flow Vapor screen Particle traces	Flight Flight CFD
12	On and off surface flow Oil flow Vapor screen Five-hole probe	Flight, wind tunnel Flight, wind tunnel Wind tunnel
13	Surface flow Oil flow Tufts Liquid crystals Propylene-glycol-methyl-ether traces	Flight Flight Flight Flight

Table 1. Concluded

Item	Data comparison	Data source
14	Surface flow Oil flow Tufts Particle traces Propylene-glycol-methyl-ether traces	Flight Flight CFD Flight
15	Vortex core location Vapor screen Dye traces Particle traces	Wind tunnel Water tunnel CFD
16	Surface pressure contours Static pressures Calculations	Flight, wind tunnel CFD
17	Surface pressure Pressure sensitive paint Static pressures in a row	Flight Flight, wind tunnel
18	Surface pressure Pressure sensitive paint Static pressures in a row Static-pressure surfaces	Flight Flight, CFD CFD
19	On and off surface flow Tufts Particle traces Stagnation pressure contours	Flight CFD CFD
20	Boundary-layer profile Rake Velocities	Flight CFD

Table 2. Actual F-16XL CAWAP Data Comparisons

Item (a)	Data comparison	Data source
3	Surface pressure contours Pressure sensitive paint Calculations	Wind tunnel CFD
6	Surface flow Oil flow Tufts Liquid crystals	Flight Flight Flight
12a	On and off surface flow Oil flow Vapor screen	Wind tunnel Wind tunnel
16a	Surface pressure contours Static pressures Calculations	Flight CFD
17a	Surface pressure Static pressures in a row	Flight, wind tunnel
18a	Surface pressure Static pressures in a row Static-pressure surfaces	Flight, CFD CFD
19	On and off surface flow Tufts Particle traces Stagnation pressure contours	Flight CFD CFD
20	Boundary-layer profile Rake Velocities	Flight CFD

^a“a” in item number signifies reduction in number of items being compared.

Table 3. Airplane Specifications

Aspect ratio, A	1.75
Wingspan, b , ft	32.4
Wing area, ft^2	646.37
Wing surface area, S_{ref} , ft^2	600
Reference wing chord, \bar{c} , ft	24.7
Theoretical root chord, c_r , ft	41.75
Height, ft	17.606
Length, ft	54.155
Typical takeoff weight, lb	35 000
Engine	Pratt & Whitney F100-PW-200
Maximum thrust, lb	23 830

Table 4. Requested, Actual, and Nominal Aircraft Pressure Port Locations

Port (a)	Requested		Actual		Nominal		Port type (b)
	FS	BL	FS	BL	FS	BL	
1	160.75	36.00	160.95	35.88	161.10	36.00	Flush, US
2	161.25	36.00	161.45	35.89	161.59	36.00	Flush, US
3	165.50	36.00	165.63	35.88	165.77	36.00	Flush, US
4	166.00	36.00	166.12	35.89	166.24	36.00	Flush, US
5	169.00	36.00	169.12	35.90	169.24	36.00	Flush, US
6	170.00	36.00	170.08	35.90	170.20	36.00	Flush, US
7	171.00	36.00	171.06	35.91	171.16	36.00	Flush, US
8	172.00	36.00	172.06	35.90	172.18	36.00	Flush, US
9	176.00	36.00	176.03	35.93	176.12	36.00	Flush, US
10	185.00	36.00	184.94	35.95	185.00	36.00	Flush, US
11	162.00	37.00	162.19	36.87	162.35	37.00	Flush, US
12	162.50	37.00	162.69	36.87	162.85	37.00	Flush, US
13	163.25	38.00	163.46	37.87	163.61	38.00	Flush, US
14	163.75	38.00	163.93	37.89	164.07	38.00	Flush, US
15	166.00	38.00	167.14	37.88	167.28	38.00	Flush, US
16	169.00	38.00	169.14	37.88	169.29	38.00	Flush, US
17	170.00	38.00	170.13	37.88	170.27	38.00	Flush, US
18	171.00	38.00	171.12	37.88	171.26	38.00	Flush, US
19	172.00	38.00	172.11	37.89	172.24	38.00	Flush, US
20	176.00	38.00	176.08	37.89	176.21	38.00	Flush, US
21	185.00	38.00	184.97	37.90	185.07	38.00	Flush, US
22	164.50	39.00	164.73	38.87	164.88	39.00	Flush, US
23	165.00	39.00	165.23	38.87	165.39	39.00	Flush, US
24	165.50	40.00	165.72	39.87	165.87	40.00	Flush, US
25	166.00	40.00	166.22	39.86	166.38	40.00	Flush, US
26	169.00	40.00	169.18	39.87	169.33	40.00	Flush, US
27	170.00	40.00	170.17	39.87	170.31	40.00	Flush, US
28	171.00	40.00	171.15	39.87	171.29	40.00	Flush, US
29	172.00	40.00	172.14	39.87	172.28	40.00	Flush, US
30	176.00	40.00	176.12	39.87	176.26	40.00	Flush, US
31	180.00	40.00	180.06	39.87	180.20	40.00	Flush, US
32	185.00	40.00	185.02	39.88	185.15	40.00	Flush, US
129	202.50	40.00	202.50	39.78	202.50	40.00	Belt
130	215.00	40.00	215.00	39.84	215.00	40.00	Belt
131	230.00	40.00	230.00	39.78	230.00	40.00	Belt
132	240.00	40.00	Does not exist				
133	250.00	40.00	250.00	39.48	250.00	40.00	Belt
134	257.50	40.00	257.50	39.46	257.50	40.00	Belt
135	282.50	40.00	282.50	39.60	282.50	40.00	Belt
136	300.00	40.00	300.00	39.66	300.00	40.00	Belt
137	337.50	40.00	337.50	39.76	337.50	40.00	Belt
138	375.00	40.00	375.00	39.86	375.00	40.00	Belt
139	390.00	40.00	390.00	40.07	390.00	40.00	Belt
140	407.50	40.00	407.50	40.10	407.50	40.00	Belt
141	425.00	40.00	425.00	40.15	425.00	40.00	Belt
142	437.50	40.00	437.50	40.09	437.50	40.00	Belt
143	450.00	40.00	450.00	40.14	450.00	40.00	Belt

^a Deleted port.

^b LE is leading edge; LS is lower surface; US is upper surface.

Table 4. Continued

Port (a)	Requested		Actual		Nominal		Port type (b)
	FS	BL	FS	BL	FS	BL	
144	462.50	40.00	462.50	40.18	462.50	40.00	Belt
145	183.00	55.00	183.00	54.09	183.00	55.00	Belt
146	184.00	55.00	184.00	54.17	184.00	55.00	Belt
147	185.00	55.00	185.00	54.24	185.00	55.00	Belt
148	187.50	55.00	187.50	54.37	187.50	55.00	Belt
149	190.00	55.00	190.00	54.45	190.00	55.00	Belt
150	192.50	55.00	192.50	54.55	192.50	55.00	Belt
151	195.00	55.00	195.00	54.66	195.00	55.00	Belt
152	197.50	55.00	197.50	54.73	197.50	55.00	Belt
153	200.00	55.00	200.00	54.75	200.00	55.00	Belt
154	202.50	55.00	202.50	54.84	202.50	55.00	Belt
155	205.00	55.00	205.00	54.97	205.00	55.00	Belt
156	210.00	55.00	210.00	55.06	210.00	55.00	Belt
157	215.00	55.00	215.00	55.14	215.00	55.00	Belt
158	220.00	55.00	220.00	55.21	220.00	55.00	Belt
159	230.00	55.00	230.00	55.26	230.00	55.00	Belt
160	240.00	55.00	240.00	55.64	240.00	55.00	Belt
161	250.00	55.00	250.00	55.72	250.00	55.00	Belt
162	257.50	55.00	257.50	55.75	257.50	55.00	Belt
163	265.00	55.00	265.00	55.81	265.00	55.00	Belt
164	282.50	55.00	282.50	55.86	282.50	55.00	Belt
165	300.00	55.00	300.00	55.97	300.00	55.00	Belt
166	337.50	55.00	337.50	56.06	337.50	55.00	Belt
167	375.00	55.00	375.00	56.07	375.00	55.00	Belt
168	390.00	55.00	390.00	56.16	390.00	55.00	Belt
169	407.50	55.00	407.50	56.16	407.50	55.00	Belt
170	425.00	55.00	425.00	56.18	425.00	55.00	Belt
171	437.50	55.00	Does not exist				
172	450.00	55.00	Does not exist				
173	462.50	55.00	Does not exist				
174	465.00	55.00	Does not exist				
182	500.00	55.00	Does not exist				
33	208.51	70.00	206.38	69.12	209.56	70.00	Flush, LE
36	210.00	70.00	207.82	69.14	210.92	70.00	Flush LS
37	210.50	70.00	208.33	69.15	211.42	70.00	Flush, LS
34	210.75	70.00	208.58	69.11	211.77	70.00	Flush, LS
38	211.00	70.00	208.81	69.16	211.86	70.00	Flush, LS
35	211.50	70.00	209.31	69.11	212.49	70.00	Flush, LS
39	212.00	70.00	209.76	69.14	212.85	70.00	Flush, LS
40	213.00	70.00	210.82	69.18	213.99	70.00	Flush, LS
41	214.00	70.00	211.84	69.09	215.07	70.00	Flush, LS
42	215.00	70.00	212.81	69.06	216.08	70.00	Flush, LS
43	216.00	70.00	213.84	69.06	217.12	70.00	Flush, LS
44	209.00	70.00	207.10	69.11	210.30	70.00	Flush, US
45	209.50	70.00	207.37	69.13	210.52	70.00	Flush, US
46	210.00	70.00	207.84	69.13	210.99	70.00	Flush, US
47	210.50	70.00	208.31	69.15	211.39	70.00	Flush, US

^a ♠ Deleted port.^b LE is leading edge; LS is lower surface; US is upper surface.

Table 4. Continued

Port (a)	Requested		Actual		Nominal		Port type (b)
	FS	BL	FS	BL	FS	BL	
48	211.00	70.00	208.82	69.15	211.91	70.00	Flush, US
49	212.00	70.00	209.77	69.16	212.80	70.00	Flush, US
50	213.00	70.00	210.79	69.20	213.72	70.00	Flush, US
51	214.00	70.00	211.79	69.23	214.64	70.00	Flush, US
52	215.00	70.00	212.76	69.24	215.57	70.00	Flush, US
53	216.00	70.00	213.78	69.26	216.54	70.00	Flush, US
183	220.00	70.00	220.50	67.69	220.50	70.00	Belt
184	222.50	70.00	222.50	68.07	222.50	70.00	Belt
185	225.00	70.00	225.00	68.13	225.00	70.00	Belt
186♠	227.50	70.00	227.50	68.22	227.50	70.00	Belt
187	230.00	70.00	230.00	68.32	230.00	70.00	Belt
188	232.50	70.00	232.50	68.42	232.50	70.00	Belt
189	235.00	70.00	235.00	68.50	235.00	70.00	Belt
190♠	237.50	70.00	237.50	68.60	237.50	70.00	Belt
191♠	240.00	70.00	240.00	68.70	240.00	70.00	Belt
192♠	245.00	70.00	245.00	68.85	245.00	70.00	Belt
193	250.00	70.00	250.00	68.99	250.00	70.00	Belt
194	255.00	70.00	255.00	69.02	255.00	70.00	Belt
195	257.50	70.00	257.50	69.11	257.50	70.00	Belt
196	265.00	70.00	265.00	69.22	265.00	70.00	Belt
197	270.00	70.00	270.00	69.27	270.00	70.00	Belt
198	275.00	70.00	275.00	69.30	275.00	70.00	Belt
199	282.50	70.00	282.50	69.40	282.50	70.00	Belt
200♠	290.00	70.00	290.00	69.50	290.00	70.00	Belt
201	295.00	70.00	295.00	69.65	295.00	70.00	Belt
202	300.00	70.00	300.00	69.74	300.00	70.00	Belt
203	310.00	70.00	310.00	69.85	310.00	70.00	Belt
204	320.00	70.00	320.00	69.96	320.00	70.00	Belt
205	330.00	70.00	330.00	70.00	330.00	70.00	Belt
206	337.50	70.00	337.50	70.15	337.50	70.00	Belt
207	350.00	70.00	350.00	70.18	350.00	70.00	Belt
208	360.00	70.00	360.00	70.42	360.00	70.00	Belt
209	375.00	70.00	375.00	70.48	375.00	70.00	Belt
210	390.00	70.00	390.00	70.53	390.00	70.00	Belt
211	407.50	70.00	407.50	70.60	407.50	70.00	Belt
212	425.00	70.00	425.00	70.60	425.00	70.00	Belt
213	437.50	70.00	437.50	70.72	437.50	70.00	Belt
214	450.00	70.00	450.00	70.00	450.00	70.00	Belt
215	462.50	70.00	462.50	70.00	462.50	70.00	Belt
216	465.00	70.00	464.50	70.00	464.50	70.00	Belt
217	470.00	70.00	Does not exist				
218	472.50	70.00	Does not exist				
219	475.00	70.00	475.00	69.69	475.00	70.00	Belt
220	477.50	70.00	477.50	69.76	477.50	70.00	Belt
221	480.00	70.00	480.00	69.83	480.00	70.00	Belt
222	485.00	70.00	485.00	69.88	485.00	70.00	Belt
223	492.50	70.00	492.50	69.98	492.50	70.00	Belt

^a ♠ Deleted port.

^b LE is leading edge; LS is lower surface; US is upper surface.

Table 4. Continued

Port (a)	Requested		Actual		Nominal		Port type (b)
	FS	BL	FS	BL	FS	BL	
224	500.00	70.00	500.00	70.07	500.00	70.00	Belt
54	235.50	80.00	232.85	78.97	236.57	80.00	Flush, LE
64	243.00	80.00	233.10	79.02	236.69	80.00	Flush, LS
55	236.00	80.00	233.40	78.92	237.26	80.00	Flush, LS
56	236.50	80.00	233.90	78.96	237.65	80.00	Flush, LS
57	237.00	80.00	234.39	78.97	238.10	80.00	Flush, LS
58	237.50	80.00	234.89	79.01	238.49	80.00	Flush, LS
59	238.00	80.00	235.38	79.02	238.95	80.00	Flush, LS
60	239.00	80.00	236.39	79.05	239.88	80.00	Flush, LS
61	240.00	80.00	237.38	79.07	240.79	80.00	Flush, LS
62	241.00	80.00	238.39	79.08	241.77	80.00	Flush, LS
63	235.70	80.00	239.37	79.11	242.66	80.00	Flush, LS
66	236.70	80.00	232.96	78.97	236.71	80.00	Flush, US
67	237.15	80.00	234.52	79.03	238.08	80.00	Flush, US
65	236.00	80.00	234.77	79.07	238.22	80.00	Flush, US
68	237.50	80.00	234.85	79.03	238.41	80.00	Flush, US
69	238.45	80.00	235.79	79.04	239.31	80.00	Flush, US
71	240.00	80.00	237.26	79.09	240.64	80.00	Flush, US
72	241.00	80.00	238.28	79.12	241.57	80.00	Flush, US
73	242.00	80.00	239.27	79.11	242.56	80.00	Flush, US
74	243.00	80.00	240.24	79.13	243.48	80.00	Flush, US
70	244.00	80.00	241.22	79.14	244.41	80.00	Flush, US
225	250.00	80.00	250.00	78.99	250.00	80.00	Belt
226	257.50	80.00	257.50	79.19	257.50	80.00	Belt
227	270.00	80.00	270.00	79.42	270.00	80.00	Belt
228	282.50	80.00	282.50	79.55	282.50	80.00	Belt
229	300.00	80.00	300.00	79.69	300.00	80.00	Belt
230	320.00	80.00	320.00	79.88	320.00	80.00	Belt
231	337.50	80.00	337.50	79.99	337.50	80.00	Belt
232	350.00	80.00	350.00	80.06	350.00	80.00	Belt
233	375.00	80.00	375.00	80.00	375.00	80.00	Belt
175	470.00	55.00	470.00	80.00	470.00	80.00	Belt
176	472.50	55.00	472.50	80.00	472.50	80.00	Belt
177	475.00	55.00	475.00	80.00	475.00	80.00	Belt
178	477.50	55.00	477.50	80.00	477.50	80.00	Belt
179	480.00	55.00	480.00	80.00	480.00	80.00	Belt
180	485.00	55.00	485.00	80.00	485.00	80.00	Belt
181	492.50	55.00	492.50	80.00	492.50	80.00	Belt
75	276.41	95.00	274.08	93.99	277.09	95.00	Flush, LE
76	277.00	95.00	274.61	94.06	277.43	95.00	Flush, LS
77	277.50	95.00	275.10	94.11	277.76	95.00	Flush, LS
78	278.00	95.00	275.60	94.18	278.08	95.00	Flush, LS
79	278.50	95.00	276.09	94.20	278.50	95.00	Flush, LS
80	279.00	95.00	276.58	94.26	278.84	95.00	Flush, LS
81	280.00	95.00	277.55	94.33	279.61	95.00	Flush, LS
82	281.00	95.00	278.54	94.40	280.42	95.00	Flush, LS
83	282.00	95.00	279.53	94.45	281.24	95.00	Flush, LS

^a ♠ Deleted port.^b LE is leading edge; LS is lower surface; US is upper surface.

Table 4. Continued

Port (a)	Requested		Actual		Nominal		Port type (b)
	FS	BL	FS	BL	FS	BL	
84	282.50	95.00	280.02	94.48	281.67	95.00	Flush, LS
85	283.00	95.00	280.53	94.51	282.09	95.00	Flush, LS
86	277.00	95.00	274.60	94.02	277.51	95.00	Flush, US
87	277.50	95.00	275.08	94.05	277.91	95.00	Flush, US
88	278.00	95.00	275.56	94.07	278.31	95.00	Flush, US
89	278.50	95.00	276.05	94.10	278.74	95.00	Flush, US
90	279.00	95.00	276.53	94.12	279.17	95.00	Flush, US
91	280.00	95.00	277.51	94.14	280.07	95.00	Flush, US
92	281.00	95.00	278.48	94.17	280.96	95.00	Flush, US
93	282.00	95.00	279.44	94.18	281.87	95.00	Flush, US
94	282.50	95.00	279.94	94.19	282.36	95.00	Flush, US
95	283.00	95.00	280.42	94.19	282.83	95.00	Flush, US
234	287.50	95.00	Does not exist				
235	290.00	95.00	Does not exist				
236	292.50	95.00	292.50	92.76	292.50	95.00	Belt
237	295.00	95.00	295.00	92.85	295.00	95.00	Belt
238	297.50	95.00	297.50	92.95	297.50	95.00	Belt
239	300.00	95.00	300.00	93.08	300.00	95.00	Belt
240	302.50	95.00	302.50	93.18	302.50	95.00	Belt
241	305.00	95.00	305.00	93.30	305.00	95.00	Belt
242	307.50	95.00	307.50	93.39	307.50	95.00	Belt
243	310.00	95.00	310.00	93.49	310.00	95.00	Belt
244	315.00	95.00	315.00	93.63	315.00	95.00	Belt
245	320.00	95.00	320.00	93.76	320.00	95.00	Belt
246	325.00	95.00	325.00	93.85	325.00	95.00	Belt
247	330.00	95.00	330.00	93.87	330.00	95.00	Belt
248	337.50	95.00	337.50	94.00	337.50	95.00	Belt
249	350.00	95.00	350.00	94.14	350.00	95.00	Belt
250	360.00	95.00	360.00	94.18	360.00	95.00	Belt
251	375.00	95.00	375.00	94.29	375.00	95.00	Belt
252	390.00	95.00	390.00	94.41	390.00	95.00	Belt
253	407.50	95.00	407.50	94.48	407.50	95.00	Belt
254	425.00	95.00	425.00	94.61	425.00	95.00	Belt
255	437.50	95.00	437.50	95.00	437.50	95.00	Belt
256	450.00	95.00	450.00	95.00	450.00	95.00	Belt
257	462.50	95.00	462.50	95.00	462.50	95.00	Belt
258	465.00	95.00	465.00	95.00	465.00	95.00	Belt
259	470.00	95.00	470.00	94.82	470.00	95.00	Belt
260	472.50	95.00	472.50	94.87	472.50	95.00	Belt
261	475.00	95.00	475.00	94.92	475.00	95.00	Belt
262	477.50	95.00	477.50	94.96	477.50	95.00	Belt
263	480.00	95.00	480.00	95.05	480.00	95.00	Belt
264	485.00	95.00	485.00	95.15	485.00	95.00	Belt
265	492.50	95.00	492.50	95.22	492.50	95.00	Belt
266	500.00	95.00	500.00	95.34	500.00	95.00	Belt
96	304.15	105.00	301.61	104.04	304.09	105.00	Flush, LE
103	304.30	105.00	301.81	104.01	304.36	105.00	Flush, LS

^a Deleted port.^b LE is leading edge; LS is lower surface; US is upper surface.

Table 4. Continued

Port (a)	Requested		Actual		Nominal		Port type (b)
	FS	BL	FS	BL	FS	BL	
97	304.50	105.00	302.13	103.98	304.76	105.00	Flush, LS
98	305.00	105.00	302.61	103.98	305.25	105.00	Flush, LS
99	305.50	105.00	303.14	104.02	305.65	105.00	Flush, LS
100	305.70	105.00	303.35	104.01	305.90	105.00	Flush, LS
101	306.50	105.00	304.12	104.04	306.57	105.00	Flush, LS
102	307.00	105.00	304.63	104.04	307.06	105.00	Flush, LS
104	308.00	105.00	305.62	104.05	308.01	105.00	Flush, LS
105	308.50	105.00	306.12	104.05	308.52	105.00	Flush, LS
107	309.50	105.00	307.13	104.08	309.42	105.00	Flush, LS
108	310.00	105.00	307.65	104.11	309.88	105.00	Flush, LS
106	310.50	105.00	308.12	104.10	310.36	105.00	Flush, LS
109	311.00	105.00	308.64	104.12	310.84	105.00	Flush, LS
110	312.00	105.00	309.62	104.12	311.77	105.00	Flush, LS
111	313.00	105.00	310.65	104.15	312.73	105.00	Flush, LS
112	314.00	105.00	311.66	104.15	313.74	105.00	Flush, LS
116	304.30	105.00	301.83	104.05	304.26	105.00	Flush, US
113	304.50	105.00	302.14	104.06	304.56	105.00	Flush, US
114	305.00	105.00	302.62	104.09	304.96	105.00	Flush, US
115	305.30	105.00	302.94	104.13	305.16	105.00	Flush, US
117	306.70	105.00	304.28	104.14	306.45	105.00	Flush, US
118	307.00	105.00	304.54	104.15	306.70	105.00	Flush, US
119	307.50	105.00	305.02	104.16	307.13	105.00	Flush, US
120	308.00	105.00	305.51	104.17	307.58	105.00	Flush, US
121	308.50	105.00	306.00	104.18	308.05	105.00	Flush, US
122	309.00	105.00	306.49	104.20	308.48	105.00	Flush, US
123	309.50	105.00	306.99	104.21	308.95	105.00	Flush, US
124	310.00	105.00	307.48	104.22	309.41	105.00	Flush, US
125	311.00	105.00	308.46	104.26	310.29	105.00	Flush, US
126	312.00	105.00	309.45	104.28	311.21	105.00	Flush, US
127	313.00	105.00	310.43	104.30	312.13	105.00	Flush, US
128	314.00	105.00	311.41	104.32	313.05	105.00	Flush, US
267	317.50	105.00	Does not exist				
268	320.00	105.00	320.00	102.64	320.00	105.00	Belt
269♠	322.50	105.00	322.50	102.70	322.50	105.00	Belt
270♠	325.00	105.00	325.00	102.81	325.00	105.00	Belt
271	327.50	105.00	327.50	102.93	327.50	105.00	Belt
272♠	330.00	105.00	330.00	103.04	330.00	105.00	Belt
273	332.50	105.00	332.50	103.11	332.50	105.00	Belt
274	335.00	105.00	335.00	103.19	335.00	105.00	Belt
275♠	337.50	105.00	337.50	103.26	337.50	105.00	Belt
276	340.00	105.00	340.00	103.37	340.00	105.00	Belt
277	342.50	105.00	342.50	103.47	342.50	105.00	Belt
278	345.00	105.00	345.00	103.55	345.00	105.00	Belt
279	347.50	105.00	347.50	103.62	347.50	105.00	Belt
280♠	350.00	105.00	350.00	103.67	350.00	105.00	Belt
281	355.00	105.00	355.00	103.68	355.00	105.00	Belt
282	360.00	105.00	360.00	103.76	360.00	105.00	Belt

^a♠ Deleted port.

^b LE is leading edge; LS is lower surface; US is upper surface.

Table 4. Continued

Port (a)	Requested		Actual		Nominal		Port type (b)
	FS	BL	FS	BL	FS	BL	
283	365.00	105.00	365.00	103.86	365.00	105.00	Belt
284	370.00	105.00	370.00	103.93	370.00	105.00	Belt
285	375.00	105.00	375.00	104.01	375.00	105.00	Belt
286	390.00	105.00	390.00	104.12	390.00	105.00	Belt
287	407.50	105.00	407.50	104.24	407.50	105.00	Belt
288	425.00	105.00	425.00	104.31	425.00	105.00	Belt
289	437.50	105.00	437.50	104.41	437.50	105.00	Belt
290	450.00	105.00	450.00	105.00	450.00	105.00	Belt
291	462.50	105.00	462.50	105.00	462.50	105.00	Belt
292	465.00	105.00	465.00	105.00	465.00	105.00	Belt
293	470.00	105.00	470.00	104.63	470.00	105.00	Belt
294	472.50	105.00	472.50	104.75	472.50	105.00	Belt
295	475.00	105.00	475.00	104.84	475.00	105.00	Belt
296	477.50	105.00	477.50	104.92	477.50	105.00	Belt
297	480.00	105.00	480.00	105.00	480.00	105.00	Belt
298	485.00	105.00	485.00	105.09	485.00	105.00	Belt
299	492.50	105.00	492.50	105.19	492.50	105.00	Belt
300	500.00	105.00	500.00	105.28	500.00	105.00	Belt
301	370.00	127.50	Does not exist				
302	372.50	127.50	372.50	126.71	372.50	127.50	Belt
303	375.00	127.50	375.00	126.87	375.00	127.50	Belt
304	377.50	127.50	377.50	127.03	377.50	127.50	Belt
305	380.00	127.50	380.00	127.18	380.00	127.50	Belt
306	382.50	127.50	382.50	127.30	382.50	127.50	Belt
307	385.00	127.50	385.00	127.37	385.00	127.50	Belt
308	390.00	127.50	390.00	127.52	390.00	127.50	Belt
309	395.00	127.50	395.00	127.66	395.00	127.50	Belt
310	400.00	127.50	400.00	127.70	400.00	127.50	Belt
311	407.50	127.50	407.50	127.80	407.50	127.50	Belt
312	415.00	127.50	415.00	127.88	415.00	127.50	Belt
313	425.00	127.50	425.00	127.94	425.00	127.50	Belt
314	415.00	153.50	415.00	152.86	415.00	153.50	Belt
315	417.50	153.50	417.50	153.02	417.50	153.50	Belt
316	420.00	153.50	420.00	153.11	420.00	153.50	Belt
317	422.50	153.50	422.50	153.24	422.50	153.50	Belt
318	425.00	153.50	425.00	153.35	425.00	153.50	Belt
319	427.50	153.50	427.50	153.47	427.50	153.50	Belt
320	430.00	153.50	430.00	153.50	430.00	153.50	Belt
321	432.50	153.50	432.50	153.57	432.50	153.50	Belt
322	437.50	153.50	Does not exist				
323	445.00	153.50	445.00	152.91	445.00	153.50	Belt
324	450.00	153.50	450.00	153.01	450.00	153.50	Belt
325	455.00	153.50	455.00	153.01	455.00	153.50	Belt
326	462.50	153.50	462.50	153.22	462.50	153.50	Belt
327	470.00	153.50	470.00	153.29	470.00	153.50	Belt
328	475.00	153.50	475.00	153.41	475.00	153.50	Belt
329	477.50	153.50	477.50	153.45	477.50	153.50	Belt

^a ♠ Deleted port.^b LE is leading edge; LS is lower surface; US is upper surface.

Table 4. Concluded

Port (a)	Requested		Actual		Nominal		Port type (b)
	FS	BL	FS	BL	FS	BL	
330	485.00	153.50	485.00	153.28	485.00	153.50	Belt
331	487.50	153.50	487.50	153.37	487.50	153.50	Belt
332	490.00	153.50	490.00	153.44	490.00	153.50	Belt
333	492.50	153.50	492.50	153.51	492.50	153.50	Belt
334	495.00	153.50	495.00	153.59	495.00	153.50	Belt
335	500.00	153.50	500.00	153.73	500.00	153.50	Belt
336	510.00	153.50	510.00	153.50	510.00	153.50	Belt
337	450.00	184.50	450.00	184.06	450.00	184.50	Belt
338	452.50	184.50	452.50	184.19	452.50	184.50	Belt
339	455.00	184.50	455.00	184.30	455.00	184.50	Belt
340	457.50	184.50	457.50	184.43	457.50	184.50	Belt
341 [♣]	460.00	184.50	460.00	184.55	460.00	184.50	Belt
342	465.00	184.50	465.00	184.12	465.00	184.50	Belt
343	470.00	184.50	470.00	184.22	470.00	184.50	Belt
344	475.00	184.50	475.00	184.27	475.00	184.50	Belt
345	480.00	184.50	480.00	184.39	480.00	184.50	Belt
346	485.00	184.50	485.00	184.49	485.00	184.50	Belt
347	487.50	184.50	487.50	184.57	487.50	184.50	Belt
348	490.00	184.50	Does not exist				
349	495.00	184.50	Does not exist				
350	497.50	184.50	Does not exist				
351	500.00	184.50	500.00	184.36	500.00	184.50	Belt
352	510.00	184.50	510.00	184.45	510.00	184.50	Belt
353	520.00	184.50	520.00	184.53	520.00	184.50	Belt

^a ♣ Deleted port.

^b LE is leading edge; LS is lower surface; US is upper surface.

Table 6. F-16XL CAWAP Tuft Video Times for Flights and Runs at Specified Flight Conditions

Flight	Run	Video (yr, 1966) day:hr:min:sec	FC	M_{nom}	h_{nom} , ft	α_{nom} , deg	β_{nom} , deg	Load $_{nom}$, g units
144	3b	074:09:18:30	46	0.51	24000	10	0	1
144	3c	074:09:19:09	47	0.51	24000	10	5	1
144	3d	074:09:19:28	48	0.51	24000	10	-5	1
144	4b	074:09:20:36	49	0.42	24000	13	0	1
144	4c	074:09:21:13	50	0.42	24000	13	5	1
144	4d	074:09:21:31	51	0.42	24000	13	-5	1
144	5b	074:09:22:35	52	0.38	24000	15	0	1
144	5c	074:09:23:15	53	0.38	24000	15	5	1
144	5d	074:09:23:35	54	0.38	24000	15	-5	1
144	6b	074:09:24:30	55	0.32	24000	21	0	1
144	9b	074:09:37:30	34	0.37	17500	13	0	1
144	9c	074:09:38:11	35	0.37	17500	13	5	1
144	9d	074:09:38:35	36	0.37	17500	13	-5	1
144	9e	074:09:39:28	63	0.42	17500	13	0	1
144	10b	074:09:41:17	37	0.34	15700	15	0	1
144	10c	074:09:42:22	38	0.34	17500	15	5	1
144	10d	074:09:42:43	39	0.34	17500	15	-5	1
144	10e	074:09:43:23	66	0.38	17500	15	0	1.3
144	11b	074:09:45:06	40	0.28	17500	21	0	1
144	11c	074:09:45:54	41	0.28	17500	21	5	1
144	16b	074:10:04:03	25	0.24	10000	21	0	1
144	16c	074:10:04:43	26	0.24	10000	21	5	1
144	16d	074:10:05:03	27	0.24	10000	21	-5	1
145	5b	078:13:26:12	28	0.71	17500	5	0	1
145	6b	078:13:29:09	31	0.44	17500	10	0	1
145	6c	078:13:30:04	32	0.44	17500	10	5	1
145	6d	078:13:30:30	33	0.44	17500	10	-5	1
145	6e	078:13:31:44	60	0.51	17500	10	0	1.3
145	9e	078:13:41:36	59	0.51	10000	10	0	1.8
145	10e	078:13:46:19	62	0.42	10000	13	0	1.7
145	11b	078:13:47:53	22	0.29	10000	15	0	1
145	11c	078:13:48:47	23	0.29	10000	15	5	1
145	11d	078:13:49:18	24	0.29	10000	15	-5	1
145	16b	078:14:03:44	7	0.29	5000	13	0	1
145	16c	078:14:04:47	8	0.29	5000	13	5	1
145	16d	078:14:05:23	9	0.29	5000	13	-5	1
145	17b	078:14:07:01	10	0.26	5000	15	0	1
146	3b	079:13:06:49	74	0.9	8700	2.9	0	1
146	5b	079:13:10:50	68	0.9	19600	3.7	0	1
146	5d	079:13:13:32	79	0.9	19600	9.3	0	3.7
146	6d	079:13:16:17	80	0.95	21300	8.8	0	3.5
146	10b	079:13:32:15	72	1.3	30800	3	0	1
146	11d	079:13:38:09	84	1.5	34900	5.8	0	2.5
151	2c	^a 100:08:20:15	43	0.81	24000	5	0	1
151	2d	^a 100:08:20:56	44	0.81	24000	5	5	1
151	2e	^a 100:08:21:17	45	0.81	24000	5	-5	1
151	3b	^a 100:08:27:27	45	0.32	24000	20	5	1

^aFlight where reported video times were 1 hr earlier than other data because chronometers for video time code inserters were not updated when change made to Pacific daylight time.

Table 6. Concluded

Flight	Run	Video (yr, 1966) day:hr:min:sec	FC	M_{nom}	h_{nom} , ft	α_{nom} , deg	β_{nom} , deg	Load $_{nom}$, g units
151	3c	^a 100:08:27:43	57	0.32	24000	20	-5	1
151	5b	^a 100:08:29:36	42	0.28	17500	20	-5	1
151	4b	^a 100:08:38:48	29	0.71	17500	5	5	1
151	4c	^a 100:08:39:08	30	0.71	17500	5	-5	1
151	6b	^a 100:08:44:11	13	0.61	10000	5	0	1
151	6c	^a 100:08:44:51	14	0.61	10000	5	5	1
151	6d	^a 100:08:45:09	15	0.61	10000	5	-5	1
152	2c	102:09:14:51	67	0.6	6000	4.6	0	1
152	2e	102:09:16:16	78	0.6	6000	12	0	3.7
152	3d	102:09:19:48	85	0.9	8700	8.4	0	5
152	4b	102:09:23:37	69	0.95	21300	3.6	0	1
152	5b	102:09:26:51	70	0.98	22300	3.6	0	1
152	5d	102:09:28:13	81	0.98	22300	8.1	0	3.2
152	6b	102:09:36:15	76	1.3	20800	2.3	0	1
152	6d	102:09:37:40	87	1.3	20800	5.1	0	3
152	7b	102:09:33:54	21	1.1	25800	3.3	0	1
152	7d	102:09:35:03	82	1.1	25800	7.4	0	3
152	8b	102:09:49:31	73	1.5	34900	2.7	0	1
152	9b	102:09:46:09	75	0.9	36800	6.3	0	1
152	9d	102:09:47:30	86	0.9	36800	10.5	0	2
152	11b	102:09:55:40	16	0.38	10000	10	0	1
152	11c	102:09:57:08	17	0.38	10000	10	5	1
152	11d	102:09:56:45	18	0.38	10000	10	-5	1
151	6d	^a 100:08:45:09	15	0.61	10000	5	-5	1
151	6d	^a 100:08:45:09	15	0.61	10000	5	-5	1
151	6d	^a 100:08:45:09	15	0.61	10000	5	-5	1
151	6d	^a 100:08:45:09	15	0.61	10000	5	-5	1
151	6d	^a 100:08:45:09	15	0.61	10000	5	-5	1
151	6d	^a 100:08:45:09	15	0.61	10000	5	-5	1
151	6d	^a 100:08:45:09	15	0.61	10000	5	-5	1
151	6d	^a 100:08:45:09	15	0.61	10000	5	-5	1
152	12b	102:10:04:06	1	0.56	5000	5	0	1
152	12c	102:10:04:58	3	0.56	5000	5	-5	1
152	13b	102:10:07:45	4	0.35	5000	10	0	1
152	13c	102:10:08:26	5	0.35	5000	10	5	1
152	13d	102:10:08:48	6	0.35	5000	10	-5	1
152	13e	102:10:10:10	58	0.51	5000	10	0	2.2
152	15c	102:10:15:55	11	0.26	5000	15	5	1
153	2c	107:13:29:56	2	0.56	5000	5	5	1
153	3b	107:13:31:34	61	0.42	5000	13	0	2.1
153	4b	107:13:33:27	12	0.26	5000	15	-5	1
153	4c	107:13:35:06	64	0.38	5000	15	0	2.1
153	5b	107:13:39:09	19	0.32	10000	13	0	1
153	5c	107:13:40:01	20	0.32	10000	13	5	1
153	5d	107:13:40:27	21	0.32	10000	13	-5	1
153	6b	107:13:41:16	65	0.38	10000	15	0	1.7
153	8b	107:13:54:40	77	1.3	44500	4.9	0	1
153	8d	107:13:55:32	88	1.3	44500	6.8	0	1.5
154	5f	109:10:37:48	83	1.3	30800	6.5	0	2.7

^aFlight where reported video times were 1 hr earlier than other data because chronometers for video time code inserters were not updated when change made to Pacific daylight time.

Table 7. Summary of Wind-Tunnel Tests

Tunnel	Model (a)	M	R_n	α , deg	β , deg	Data type
Langley 30- by 60-Foot	18 percent	< 0.08	2.1×10^6	-5 to 30	-20 to 20	Force and moment Pressure Vapor screen
Langley BART	4 percent	≤ 0.165	≤ 1.12	5 to 20	0	Pressure Oil flow Vapor screen 5-hole probe Pressure sensitive paint
Langley Water	2.5 percent	0	0.014	5 to 20	0	Colored-dye injection
Calspan 8-Foot	Lockheed 7 percent, no missiles, no air dams	0.6 to 1.2	1.5	0 to 30	0	Pressure
Ames 6- by 6-Foot	Lockheed 7 percent, no missiles, no air dams	0.6 to 1.2	1.5	-2 to 26	0	Force Pressure
Ames 11-Foot	Lockheed 11 percent	0.6 to 2.0	2.3 and 2.75	-1.94 to 28.75	0	Force Pressure

^aModel includes baseline configuration plus missiles and air dams unless otherwise noted.

Table 8. Actual and Nominal Pressure Port Locations at Airplane Scale for 0.11-Scaled Model

Port	Actual		Nominal	
	FS	BL	FS	BL
293	175.09	48.00	175.09	48.00
294	183.93	48.00	183.93	48.00
295	194.98	48.00	194.98	48.00
296	209.33	48.00	209.33	49.00
297	242.10	48.00	242.10	48.00
298	281.87	48.00	281.87	48.00
299	328.62	48.00	328.62	48.00
300	372.07	48.00	372.07	48.00
301	417.35	48.00	417.35	48.00
302	462.27	48.50	462.27	48.00
303	475.53	48.50	475.53	48.00
304	487.68	48.50	487.68	48.00
305	504.24	48.50	504.24	48.00
306	516.02	48.50	516.02	48.00
308	211.73	69.00	211.73	69.00
309	220.66	69.00	220.66	69.00
310	235.75	69.00	235.75	69.00
311	257.01	69.00	257.01	69.00
312	284.12	69.00	284.12	69.00
313	317.08	69.00	317.08	69.00
314	356.51	69.00	356.51	69.00
315	392.55	69.00	392.55	69.00
316	427.35	69.00	427.35	69.00
317	462.78	69.00	462.78	69.00
318	475.41	69.00	475.41	69.00
319	486.50	69.00	486.50	69.00
320	502.52	69.00	502.52	69.00
323	262.86	88.00	262.86	88.00
324	270.21	88.00	270.21	88.00
325	282.64	88.00	282.64	88.00
326	299.89	88.00	299.89	88.00
327	322.21	88.00	322.21	88.00
328	349.35	88.00	349.35	88.00
329	381.56	88.00	381.56	88.00
330	411.23	88.00	411.23	88.00
331	437.10	88.00	437.10	88.00
332	462.97	88.00	462.97	88.00
333	475.14	88.00	475.14	88.00
334	485.80	88.00	485.80	88.00
335	500.76	88.00	500.76	88.00
338	319.37	109.00	319.37	109.00
339	324.79	109.00	324.79	109.00
340	334.27	109.00	334.27	109.00
341	347.24	109.00	347.24	109.00
342	364.26	109.00	364.26	109.00
343	384.77	109.00	384.77	109.00
344	409.15	109.00	409.15	109.00
345	431.60	109.00	431.60	109.00
346	447.46	109.00	447.46	109.00

Table 8. Continued

Port	Actual		Nominal	
	FS	BL	FS	BL
347	463.33	109.00	463.33	109.00
348	474.75	109.00	474.75	109.00
349	484.81	109.00	484.81	109.00
350	498.93	109.00	498.93	109.00
353	378.52	131.00	378.52	131.00
354	382.40	131.00	382.40	131.00
355	388.70	131.00	388.70	131.00
356	397.68	131.00	397.68	131.00
357	409.21	131.00	409.21	131.00
358	423.29	131.00	423.29	131.00
359	439.91	131.00	439.91	131.00
360	455.19	131.00	455.19	131.00
361	468.59	131.00	468.59	131.00
362	478.65	131.00	478.65	131.00
363	487.90	131.00	487.90	131.00
364	500.77	131.00	500.77	131.00
368	401.86	142.00	401.86	142.00
369	406.59	142.00	406.59	142.00
370	416.29	142.00	416.29	142.00
371	424.26	142.00	424.26	142.00
372	433.96	142.00	433.96	142.00
373	446.89	142.00	446.89	142.00
374	459.82	142.00	459.82	142.00
375	472.75	142.00	472.75	142.00
376	482.34	142.00	482.34	142.00
377	491.23	142.00	491.23	142.00
378	503.58	142.00	503.58	142.00
383	419.11	157.00	419.11	157.00
384	422.75	157.00	422.75	157.00
385	430.72	157.00	430.72	157.00
386	437.18	157.00	437.18	157.00
387	445.06	157.00	445.06	157.00
388	456.26	157.00	456.26	157.00
389	467.27	157.00	467.27	157.00
390	478.37	157.00	478.37	157.00
391	487.46	157.00	487.46	157.00
392	495.84	157.00	495.84	157.00
393	506.84	157.00	506.84	157.00
398	435.76	172.00	435.76	172.00
399	438.79	172.00	438.79	172.00
400	445.01	172.00	445.01	172.00
401	450.11	172.00	450.11	172.00
402	456.25	172.00	456.25	172.00
403	465.50	172.00	465.50	172.00
404	474.84	172.00	474.84	172.00
405	484.09	172.00	484.09	172.00
406	492.56	172.00	492.56	172.00
407	500.34	172.00	500.34	172.00
408	511.32	172.00	511.32	172.00

Table 8. Continued

Port	Actual		Nominal	
	FS	BL	FS	BL
413	452.76	187.00	452.76	187.00
414	454.99	187.00	454.99	187.00
415	459.30	187.00	459.30	187.00
416	462.97	187.00	462.97	187.00
417	467.43	187.00	467.43	187.00
418	474.92	187.00	474.92	187.00
419	482.32	187.00	482.32	187.00
420	489.81	187.00	489.81	187.00
421	497.65	187.00	497.65	187.00
422	504.98	187.00	504.98	187.00
423	515.20	187.00	515.20	187.00
458	196.19	-48.00	196.19	48.00
459	204.48	-48.00	204.48	48.00
461	228.31	-48.00	228.31	48.00
463	296.35	-48.00	296.35	48.00
465	380.97	-48.00	380.97	48.00
467	465.60	-47.50	465.60	48.00
468	478.03	-47.50	478.03	48.00
469	489.43	-47.50	489.43	48.00
470	504.97	-47.50	504.97	48.00
473	211.73	-69.00	211.73	69.00
474	220.66	-69.00	220.66	69.00
476	257.01	-69.00	257.01	69.00
478	317.08	-69.00	317.08	69.00
480	392.55	-69.00	392.55	69.00
482	462.78	-69.00	462.78	69.00
483	475.41	-69.00	475.41	69.00
484	486.50	-69.00	486.50	69.00
485	502.52	-69.00	502.52	69.00
488	262.86	-88.00	262.86	88.00
489	270.21	-88.00	270.21	88.00
491	299.89	-88.00	299.89	88.00
493	349.35	-88.00	349.35	88.00
495	411.23	-88.00	411.23	88.00
497	462.97	-88.00	462.97	88.00
498	475.14	-88.00	475.14	88.00
499	485.80	-88.00	485.80	88.00
500	500.76	-88.00	500.76	88.00
503	319.37	-109.00	319.37	109.00
504	324.79	-109.00	324.79	109.00
506	347.24	-109.00	347.24	109.00
508	384.77	-109.00	384.77	109.00
510	431.60	-109.00	431.60	109.00
512	463.33	-109.00	463.33	109.00
513	474.75	-109.00	474.75	109.00
514	484.81	-109.00	484.81	109.00
515	498.93	-109.00	498.93	109.00
518	378.52	-131.00	378.52	131.00
519	382.40	-131.00	382.40	131.00

Table 8. Concluded

Port	Actual		Nominal	
	FS	BL	FS	BL
521	397.68	-131.00	397.68	131.00
523	423.29	-131.00	423.29	131.00
525	455.19	-131.00	455.19	131.00
526	468.59	-131.00	468.59	131.00
527	478.65	-131.00	478.65	131.00
528	487.90	-131.00	487.90	131.00
529	500.77	-131.00	500.77	131.00
533	401.86	-142.00	401.86	142.00
534	406.59	-142.00	406.59	142.00
536	424.26	-142.00	424.26	142.00
537	433.96	-142.00	433.96	142.00
538	446.89	-142.00	446.89	142.00
540	472.75	-142.00	472.75	142.00
541	482.34	-142.00	482.34	142.00
542	491.23	-142.00	491.23	142.00
543	503.58	-142.00	503.58	142.00
548	419.11	-157.00	419.11	157.00
549	422.75	-157.00	422.75	157.00
551	437.18	-157.00	437.18	157.00
552	445.06	-157.00	445.06	157.00
553	456.26	-157.00	456.26	157.00
555	478.37	-157.00	478.37	157.00
556	487.46	-157.00	487.46	157.00
557	495.84	-157.00	495.84	157.00
558	507.45	-157.00	507.45	157.00
563	435.76	-172.00	435.76	172.00
564	438.79	-172.00	438.79	172.00
566	450.11	-172.00	450.11	172.00
567	456.25	-172.00	456.25	172.00
568	465.50	-172.00	465.50	172.00
570	484.09	-172.00	484.09	172.00
571	492.56	-172.00	492.56	172.00
572	500.34	-172.00	500.34	172.00
573	511.32	-172.00	511.32	172.00
578	452.76	-187.00	452.76	187.00
579	454.99	-187.00	454.99	187.00
581	462.97	-187.00	462.97	187.00
582	467.43	-187.00	467.43	187.00
583	474.92	-187.00	474.92	187.00
585	489.81	-187.00	489.81	187.00
586	497.65	-187.00	497.65	187.00
587	504.98	-187.00	504.98	187.00
588	515.20	-187.00	515.20	187.00

Table 9. Actual and Nominal Pressure Port Locations at Airplane Scale for 0.18-Scaled Model

Port	Actual		Nominal	
	FS	BL	FS	BL
1	184.87	55.49	185.00	55.00
2	201.55	55.49	201.55	55.00
3	215.17	55.49	215.00	55.00
4	250.20	55.49	250.00	55.00
5	295.24	55.49	295.24	55.00
6	215.17	69.72	215.00	70.00
7	229.35	69.72	229.35	70.00
8	250.20	69.72	250.00	70.00
9	295.24	69.72	295.24	70.00
10	340.55	69.72	340.55	70.00
11	282.17	95.24	282.17	95.00
12	298.85	95.24	300.00	95.00
13	319.70	95.24	319.70	95.00
14	347.50	95.24	347.50	95.00
15	375.30	95.24	375.00	95.00
16	407.83	95.24	407.50	95.00
17	375.30	127.49	375.00	127.50
18	389.20	127.49	389.20	127.50
19	407.83	127.49	407.50	127.50
20	430.90	127.49	430.90	127.50
21	407.83	148.01	407.50	147.50
22	423.95	148.01	423.95	147.50
23	440.35	148.01	440.35	147.50
24	458.70	148.01	458.70	147.50
25	436.46	172.64	436.46	172.50
26	448.97	172.64	450.00	172.50
27	461.48	172.64	462.50	172.50
28	479.55	172.64	480.00	172.50
29	407.83	111.20	407.50	111.20
30	407.83	76.45	407.50	76.45

Table 10. Actual and Nominal Pressure Port Locations at Airplane Scale for 0.04-Scaled Model

Port	Actual		Nominal	
	FS	BL	FS	BL
10	160.00	-30.00	160.00	30.00
11	160.00	30.00	160.00	30.00
12	160.00	33.25	160.00	33.25
14	185.00	-55.00	185.00	55.00
15	185.00	-50.00	185.00	50.00
16	185.00	37.50	185.00	37.50
17	185.00	42.50	185.00	40.00
18	185.00	50.00	185.00	50.00
19	185.00	55.00	185.00	55.00
21	202.50	55.00	202.50	55.00
22	215.00	-70.00	215.00	70.00
23	215.00	-62.50	215.00	62.50
24	215.00	-55.00	215.00	55.00
25	215.00	42.50	215.00	40.00
26	215.00	50.00	215.00	50.00
27	215.00	55.00	215.00	55.00
28	215.00	62.50	215.00	62.50
29	215.00	70.00	215.00	70.00
30	230.00	70.00	230.00	70.00
31	257.50	-85.00	257.50	85.00
32	257.50	-80.00	257.50	80.00
33	257.50	-70.00	257.50	70.00
34	257.50	-55.00	257.50	55.00
35	257.50	55.00	257.50	55.00
36	257.50	62.50	257.50	62.50
37	257.50	70.00	257.50	70.00
38	257.50	80.00	257.50	80.00
39	257.50	85.00	257.50	85.00
40	282.50	95.00	282.50	95.00
41	300.00	-100.00	300.00	100.00
42	300.00	-95.00	300.00	95.00
43	300.00	-80.00	300.00	80.00
44	300.00	-55.00	300.00	55.00
45	300.00	55.00	300.00	55.00
46	300.00	70.00	300.00	70.00
47	300.00	80.00	300.00	80.00
48	300.00	87.50	300.00	87.50
49	300.00	95.00	300.00	95.00
50	300.00	100.00	300.00	100.00
51	337.50	62.50	337.50	62.50
52	337.50	80.00	337.50	80.00
53	337.50	95.00	337.50	95.00
54	337.50	105.00	337.50	105.00
55	337.50	115.00	337.50	115.00
56	375.00	70.00	375.00	70.00
57	375.00	95.00	375.00	95.00
58	375.00	105.00	375.00	105.00
59	375.00	120.00	375.00	120.00
60	375.00	127.50	375.00	127.50

Table 10. Concluded

Port	Actual		Nominal	
	FS	BL	FS	BL
61	390.00	127.50	390.00	127.50
62	407.50	-147.50	407.50	147.50
63	407.50	-137.50	407.50	137.50
64	407.50	-105.00	407.50	105.00
65	407.50	-55.00	407.50	55.00
67	407.50	95.00	407.50	95.00
68	407.50	120.00	407.50	120.00
69	407.50	127.50	407.50	127.50
70	407.50	137.50	407.50	137.50
71	407.50	147.50	407.50	147.50
72	425.00	62.50	425.00	62.50
73	425.00	147.50	425.00	147.50
74	425.00	160.00	425.00	160.00
75	437.50	147.50	437.50	147.50
76	437.50	160.00	437.50	160.00
77	437.50	172.50	437.50	172.50
78	450.00	80.00	450.00	80.00
79	450.00	147.50	450.00	147.50
80	450.00	160.00	450.00	160.00
81	450.00	172.50	450.00	172.50
82	462.50	-172.50	462.50	172.50
83	462.50	-147.50	462.50	147.50
84	462.50	-105.00	462.50	105.00
86	462.50	105.00	462.50	105.00
88	462.50	172.50	462.50	172.50
89	492.50	-172.50	492.50	172.50
90	492.50	-147.50	492.50	147.50
91	492.50	-105.00	492.50	105.00
92	492.50	-55.00	492.50	55.00
93	492.50	80.00	492.50	80.00
94	492.50	120.00	492.50	120.00
95	492.50	147.50	492.50	147.50
96	492.50	160.00	492.50	160.00

Table 11. CFD Solutions for Flight and Wind Tunnel Conditions
 [B.L. is boundary layer]

CFL3D(001) solution run	Flight and WT test condition						Solution feature		
	FC	Test	Run	α_{nom} , deg	M_{nom}	R_n	Grid refinement	B.L. model refinement	Solution convergence
^a 1	^a 7	^a 16	^a 1.1	^a 13	^a 0.285	^a 46.1 $\times 10^6$	^a No	^a No	^a Yes
^a 2	^a 7	^a 145	^a 16b	^a 13	^a 0.29	^a 44.37 $\times 10^6$	^a Yes	^a Yes	^a Yes
3	1	152	12b	5	0.56	77.71 $\times 10^6$	Yes	No	Yes
4	68	146	5b	3.7	0.9	85.7 $\times 10^6$	Yes	No	No
5	25	144	16b	20	0.24	32.22 $\times 10^6$	Yes	Yes	Yes
6	BART	3	12	20	0.1	1.12 $\times 10^6$	Yes	No	Yes
7	19	153	5b	13	0.32	46.811 $\times 10^6$	Yes	No	Yes
^a 8	^a 7 (two repeats)	^a 145	^a 16b	^a 13	^a 0.29	^a 44.37 $\times 10^6$	^a Yes	^a Yes	^a Yes
9	34	144	9b	13	0.37	40.045 $\times 10^6$	Yes	Yes	Yes
10	46 (repeat)	144	3b	10	0.51	46.904 $\times 10^6$	Yes	Yes	Yes
11	49 (repeat)	144	4b	13	0.42	38.966 $\times 10^6$	Yes	Yes	Yes
12	69	152	4b	3.6	0.95	87.822 $\times 10^6$	Yes	Yes	No
13	70	152	5b	3.6	0.98	88.765 $\times 10^6$	Yes	Yes	Yes

^aFlight pressure data not available.

Table 12. Boundary-Layer Velocity Profiles

(a) Flight 135

y, in.	Boundary-layer profile for run—							
	6b at—	6b at—	10b at—	10b at—	11b at—	11b at—	12b at—	12b at—
	RK 3	RK 5	RK 3	RK 5	RK 3	RK 5	RK 3	RK 5
0.02	0.690	0.718	0.692	0.711	0.709	0.711	0.709	0.702
0.06	0.742	0.781	0.738	0.789	7.750	0.781	0.753	0.779
0.10	0.760	0.821	0.764	0.828	0.773	0.819	0.782	0.815
0.14	0.781	0.846	0.780	0.850	0.792	0.838	0.799	0.839
0.18	0.798	0.874	0.799	0.875	0.808	0.862	0.813	0.862
0.28	0.848	0.909	0.848	0.907	0.951	0.989	0.858	0.895
0.38	0.874	0.932	0.878	0.926	0.888	0.915	0.892	0.915
0.48	0.898	0.940	0.910	0.939	0.913	0.922	0.939	0.929
0.58	0.928	0.951	0.938	0.948	0.942	0.938	0.951	0.935
0.68	0.942	0.952	0.957	0.953	0.966	0.942	0.971	0.941
0.88	0.970	0.930	0.980	0.960	0.980	0.954	0.990	0.951
1.08	0.982	0.963	0.988	0.968	0.998	0.960	0.999	0.960
1.28	0.991	0.972	0.993	0.974	0.995	0.968	0.988	0.972
1.48	0.995	0.980	0.999	0.982	0.999	0.972	0.995	0.978
1.88	1.000	1.000	1.000	1.000	1.000	1.000	1.000	1.000

(b) Flight 137

y, in.	Boundary-layer profile for run—							
	4b at—	4b at—	9b at—	9b at—	14b at—	14b at—	19b at—	19b at—
	RK 3	RK 7	RK 3	RK 7	RK 3	RK 7	RK 3	RK 7
0.02	0.702	0.670	0.700	0.670	0.715	0.666	0.709	0.671
0.06	0.743	0.754	0.739	0.755	0.752	0.750	0.749	0.762
0.10	0.768	0.791	0.762	0.785	0.776	0.789	0.774	0.791
0.14	0.786	0.817	0.782	0.826	0.795	0.821	0.789	0.815
0.18	0.801	0.850	0.798	0.843	0.811	0.851	0.809	0.841
0.28	0.843	0.879	0.840	0.872	0.856	0.884	0.846	0.876
0.38	0.872	0.917	0.877	0.909	0.892	0.924	0.887	0.906
0.48	0.903	0.925	0.906	0.916	0.921	0.928	0.913	0.914
0.58	0.924	0.938	0.940	0.930	0.949	0.938	0.939	0.925
0.68	0.939	0.942	0.950	0.938	0.968	0.940	0.956	0.932
0.88	0.971	0.953	0.976	0.945	0.990	0.949	0.980	0.939
1.08	0.980	0.969	0.985	0.962	0.995	0.960	0.988	0.958
1.28	0.991	0.974	0.994	0.968	0.999	0.970	0.990	0.961
1.48	0.995	0.980	0.999	0.981	1.000	0.980	0.992	0.978
1.88	1.000	1.000	1.000	1.000		1.000	1.000	1.000

Table 12. Concluded

(c) Flight 138

y , in.	Boundary layer profile for run—									
	2c at—	2c at—	4b at—	4b at—	9b at—	9b at—	14b at—	14b at—	19b at—	19b at—
	RK 3	RK 4	RK 3	RK 4	RK 3	RK 4	RK 3	RK 4	RK 3	RK 4
0.02	0.738	0.921	0.701	0.799	0.709	0.798	0.711	0.810	0.706	0.805
0.06	0.780	1.018	0.750	0.886	0.760	0.888	0.760	0.900	0.758	0.895
0.10	0.810	1.068	0.775	0.937	0.780	0.938	0.785	0.944	0.781	0.942
0.14	0.822	1.125	0.789	0.968	0.797	0.969	0.804	0.981	0.797	0.975
0.18	0.843	1.145	0.809	0.988	0.820	0.991	0.818	1.000	0.811	0.990
0.28	0.872	1.162	0.850	1.009	0.855	1.009	0.864	1.018	0.860	1.011
0.38	0.900	1.818	0.882	1.024	0.892	1.023	0.898	1.027	0.891	1.022
0.48	0.920	0.880	0.911	0.849	0.927	0.840	0.931	0.838	0.921	0.838
0.58	0.935	1.172	0.939	1.022	0.950	1.023	0.956	1.027	0.949	1.021
0.68	0.941	1.161	0.951	1.020	0.965	1.022	0.970	1.025	0.964	1.023
0.88	0.960	1.140	0.972	1.019	0.991	1.020	0.995	1.041	0.989	1.020
1.08	0.974	1.122	0.990	1.017	0.998	1.018	1.000	1.029	0.999	1.012
1.48	0.991	1.071	0.977	1.013	1.002	1.010	1.004	1.011	0.998	1.010
1.88	1.000	1.000	1.000	1.000	1.000	1.000	1.000	1.000	1.000	1.000

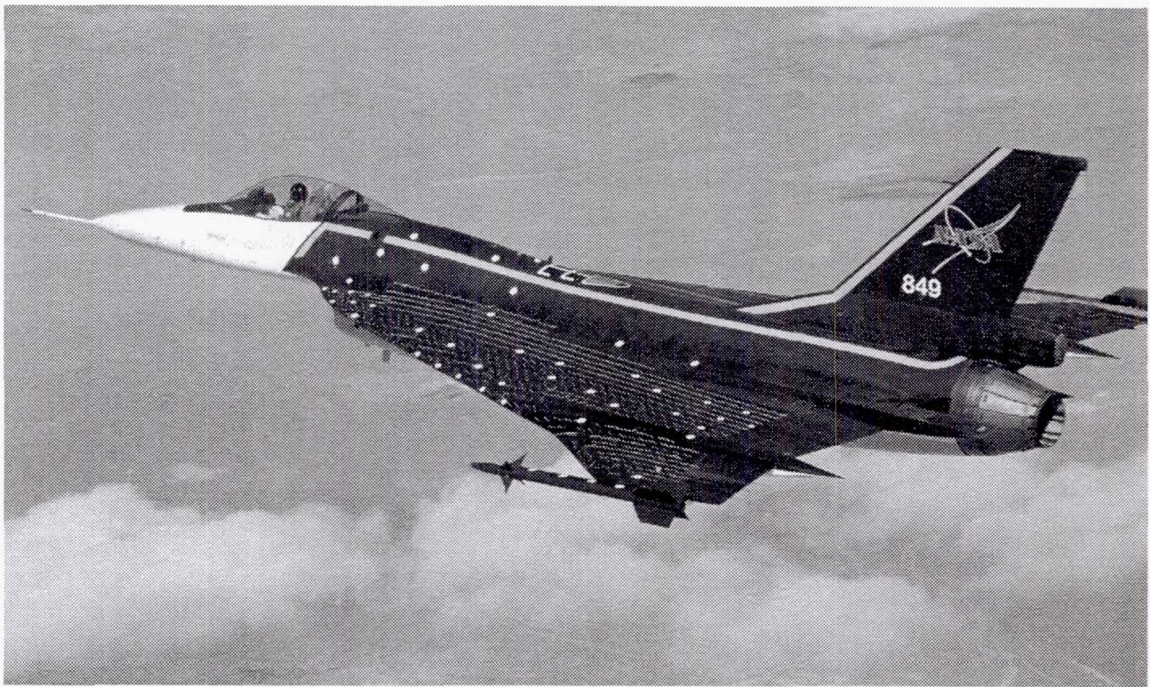


(a) Initial flow-visualization paint scheme on airplane near Langley Research Center.



(b) Modified flow-visualization paint scheme and video targets on airplane at Dryden Flight Research Center.

Figure 1. F-16XL-1 airplane in-flight.



(c) Missiles, tufts, modified flow-visualization paint scheme, and video targets on airplane at Dryden Flight Research Center.

Figure 1. Concluded.

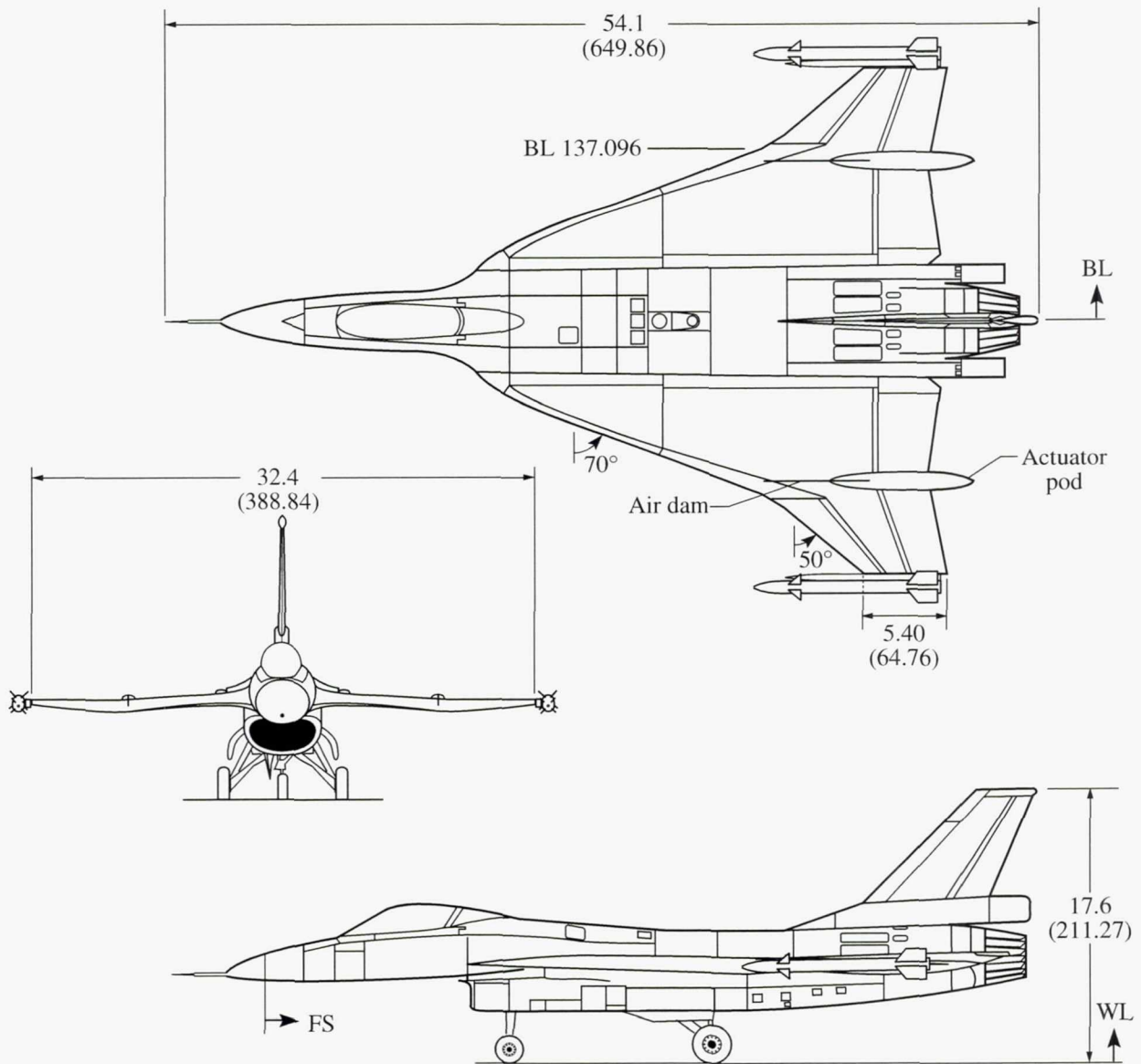


Figure 2. Three-view drawing of F-16XL-1 airplane. Linear dimensions are in feet (inches).

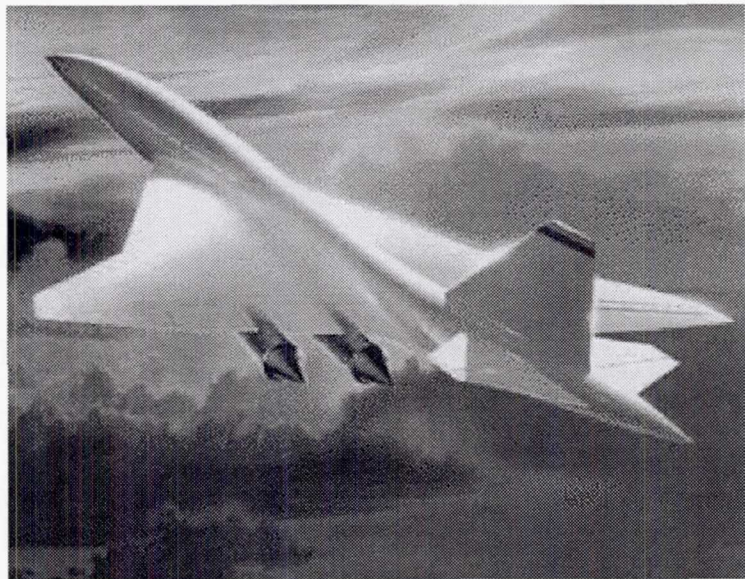


Figure 3. Artist's rendition of a High-Speed Civil Transport concept.

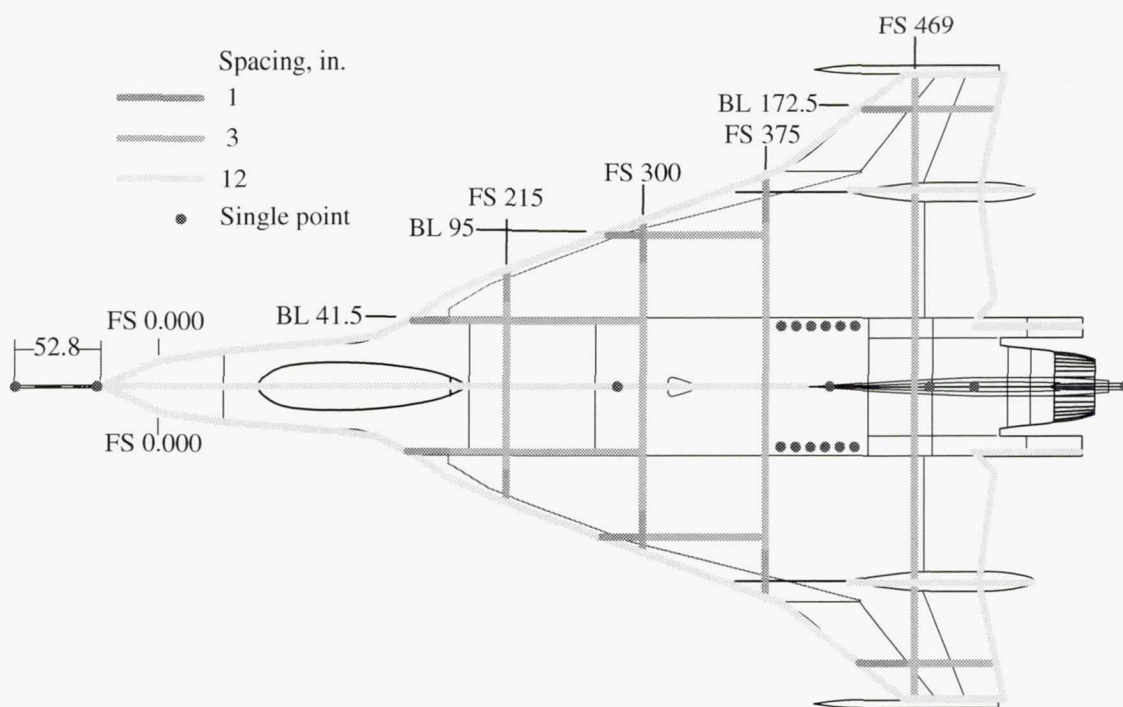
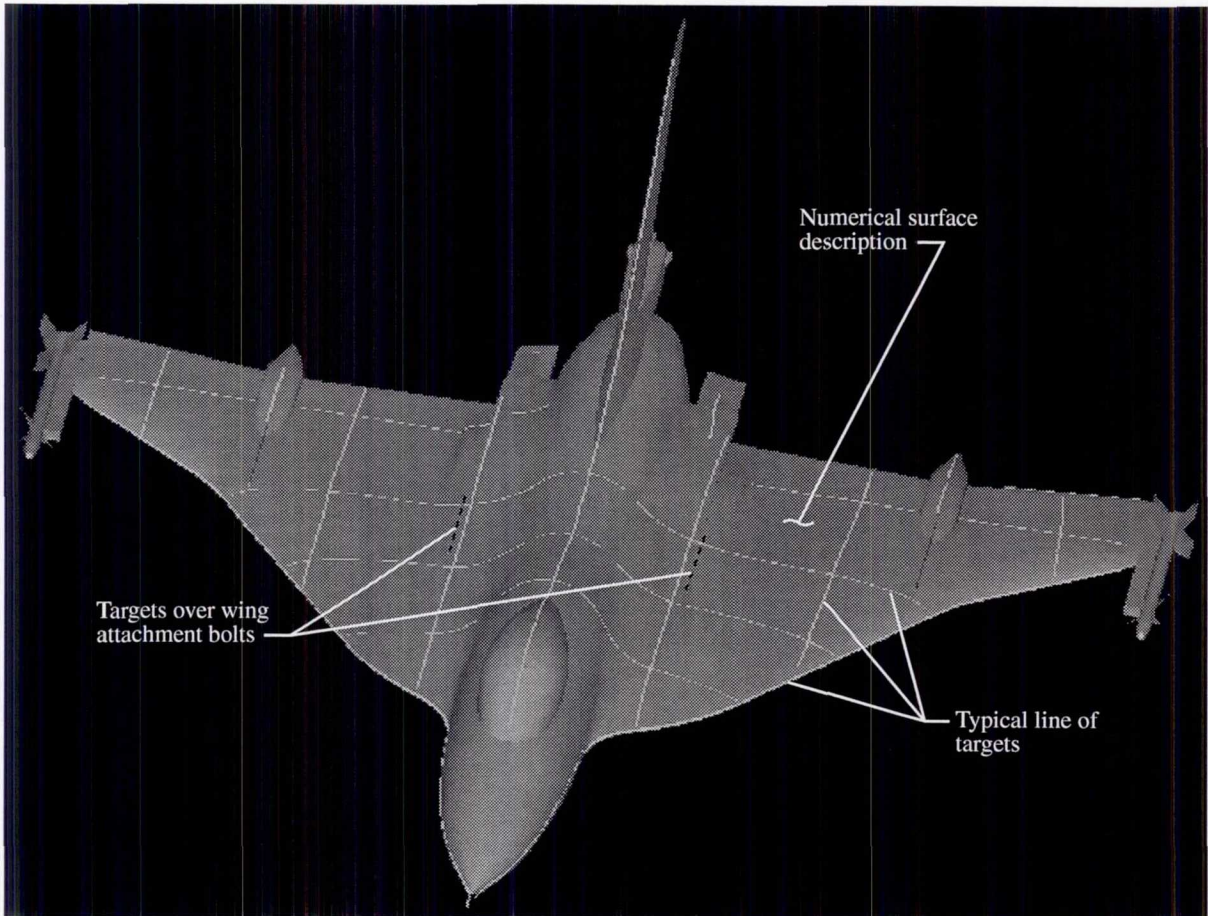
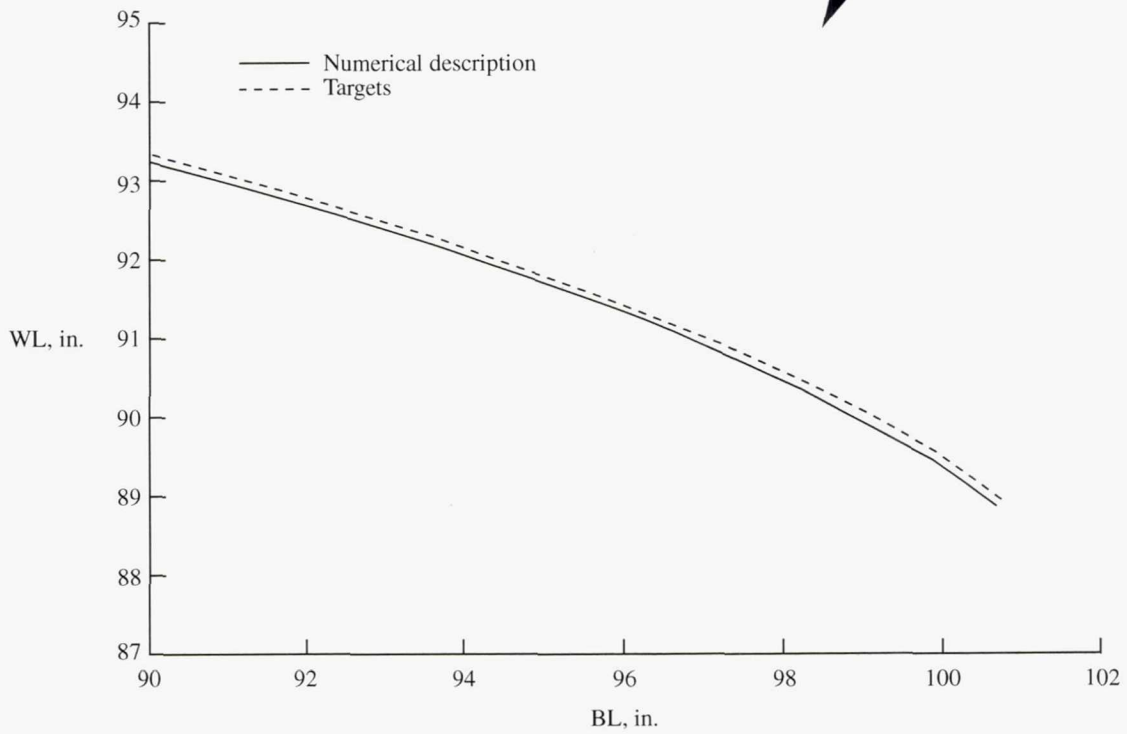
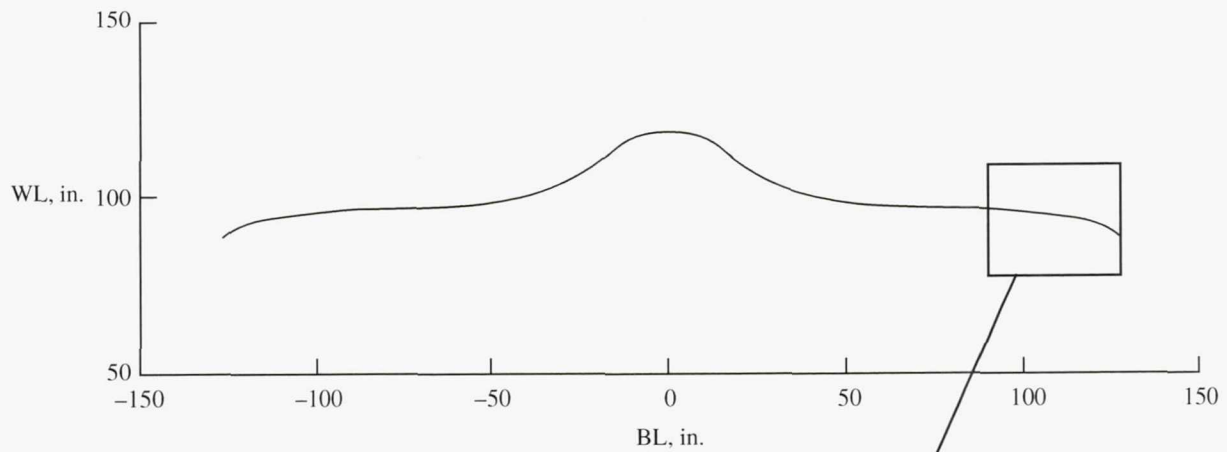


Figure 4. Layout of photogrammetric targets on F-16XL-1 airplane. Approximately 32 additional single points from previous measurements; approximately 30 additional single points of white flow viz targets.



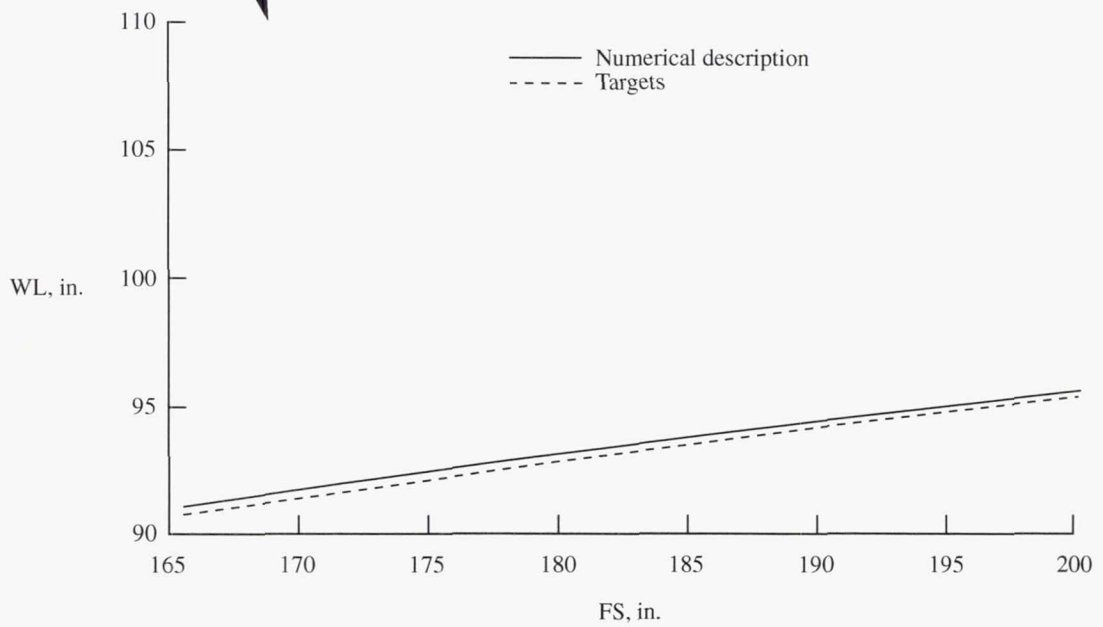
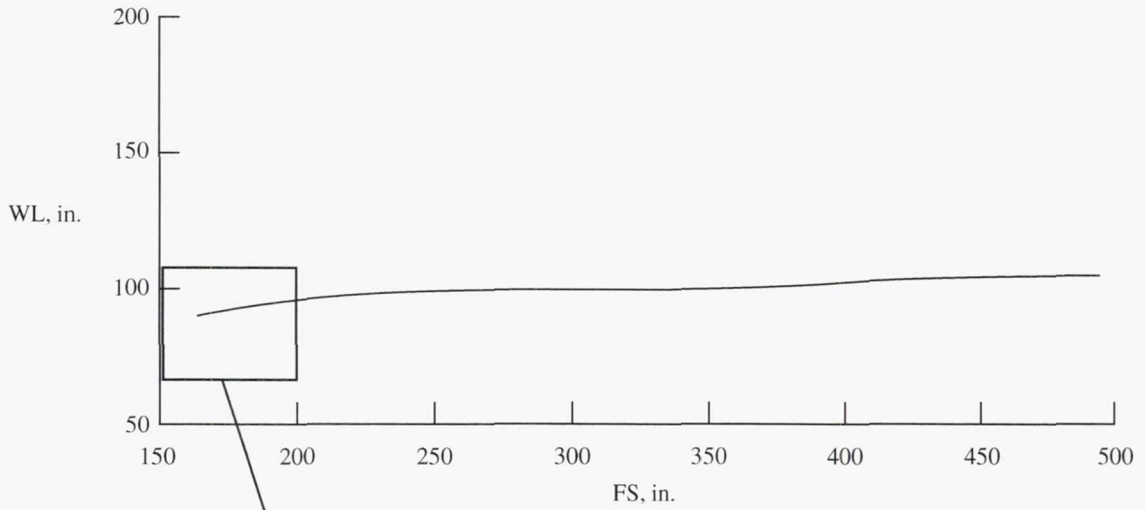
(a) General.

Figure 5. Geometrical superposition of upper surface photogrammetric targets (depicted by lines) with numerical surface description of F-16XL-1 airplane.



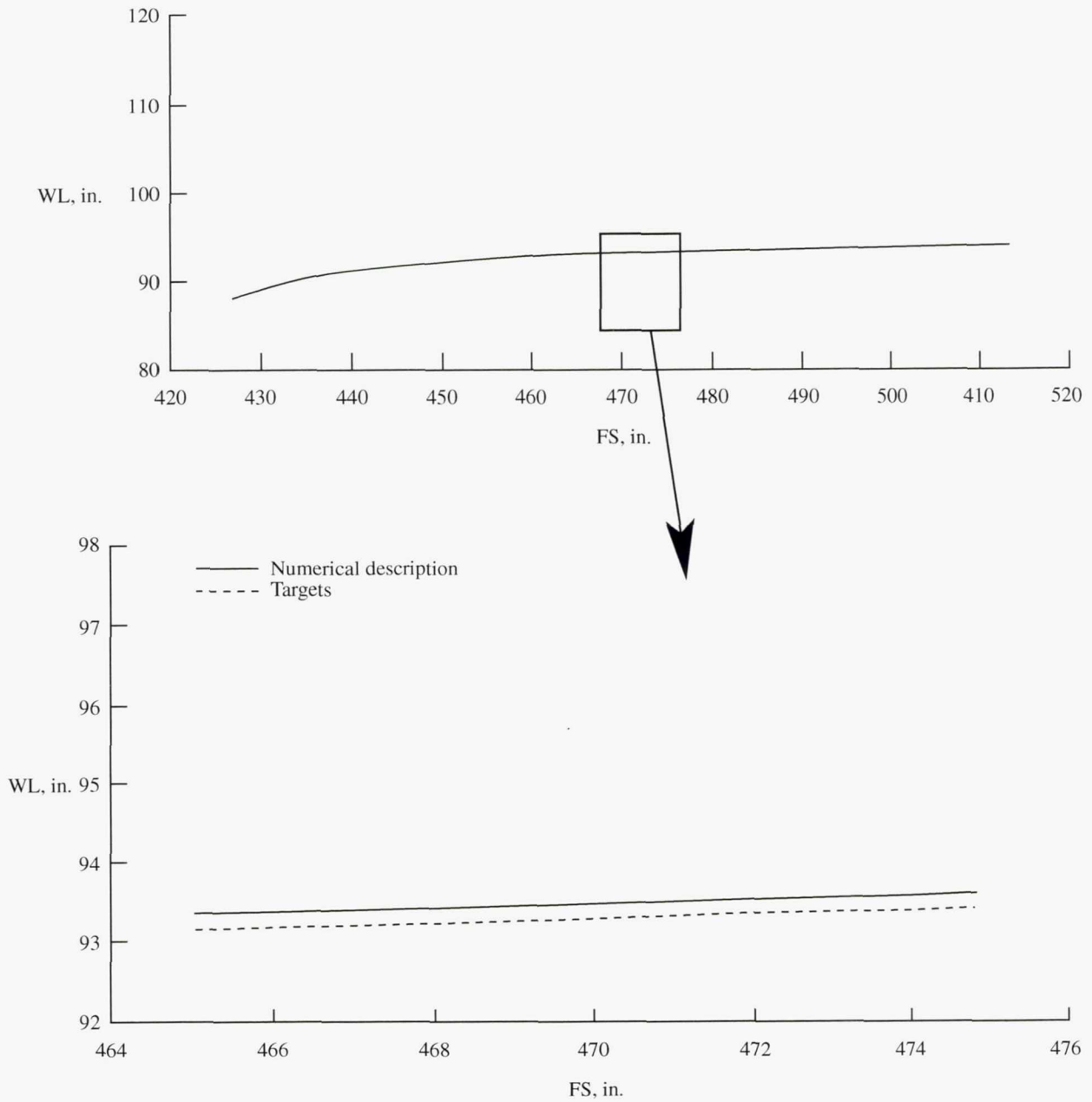
(b) Cross section of airplane at FS 295 and details on left wing; maximum difference 0.09 in.

Figure 5. Continued.



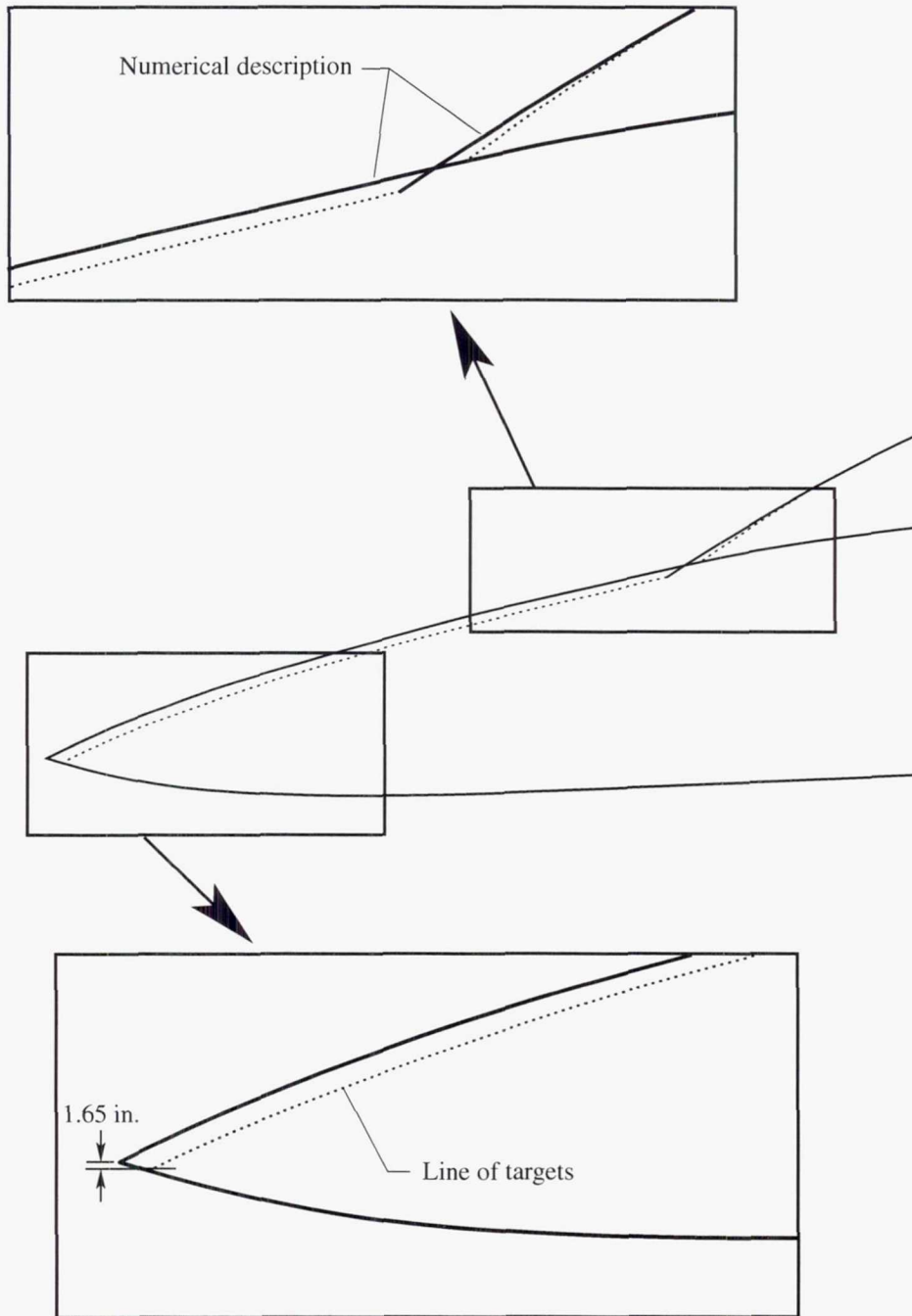
(c) Cross section of port wing at BL 40 and leading-edge details; maximum difference 0.24 in.

Figure 5. Continued.



(d) Cross section of right wing at BL 165 and midchord details; maximum difference 0.19 in.

Figure 5. Continued.



(e) Cross section of forebody at BL 0 with details at nose and canopy.

Figure 5. Concluded.

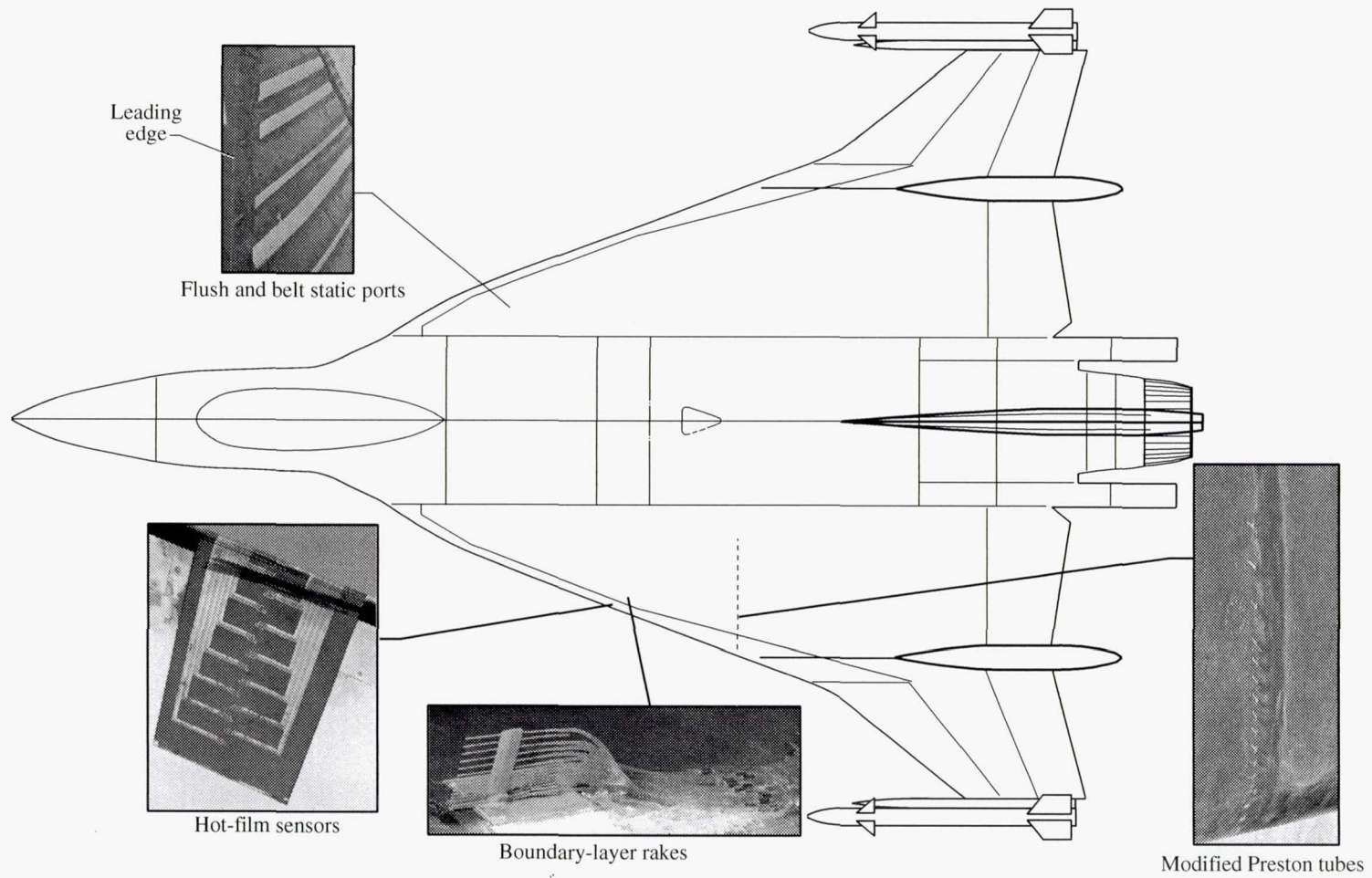


Figure 6. Schematic of instrumentation on surface of airplane.

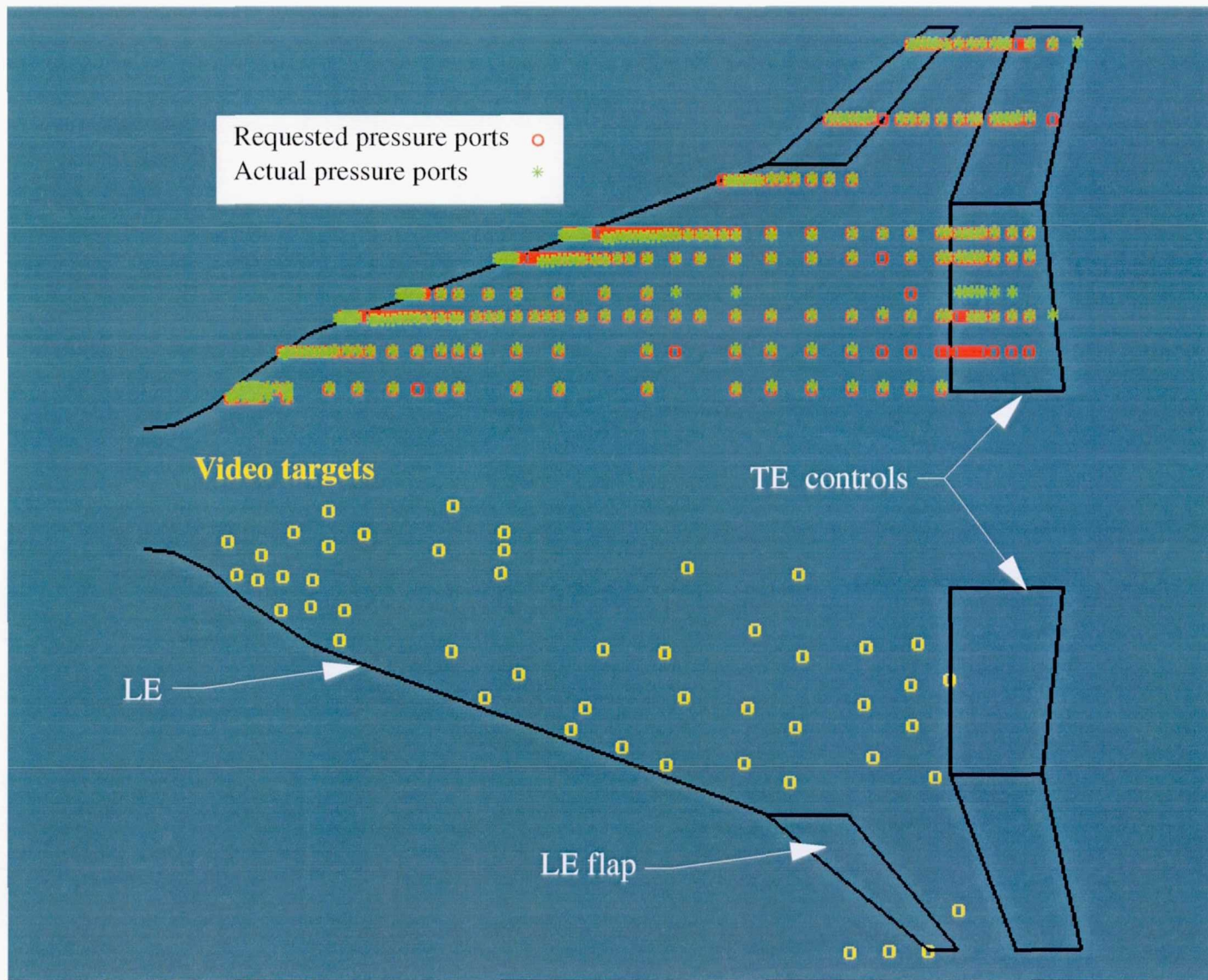
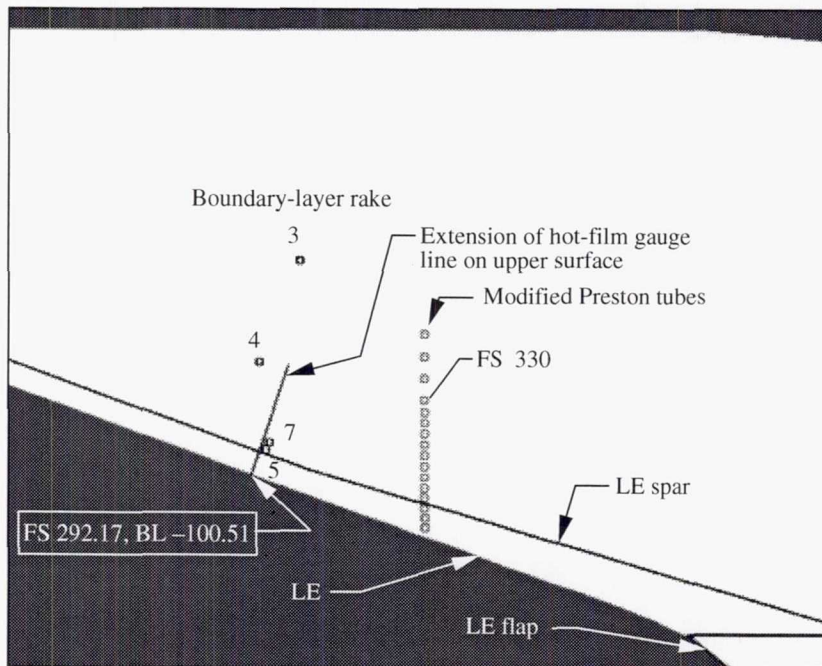


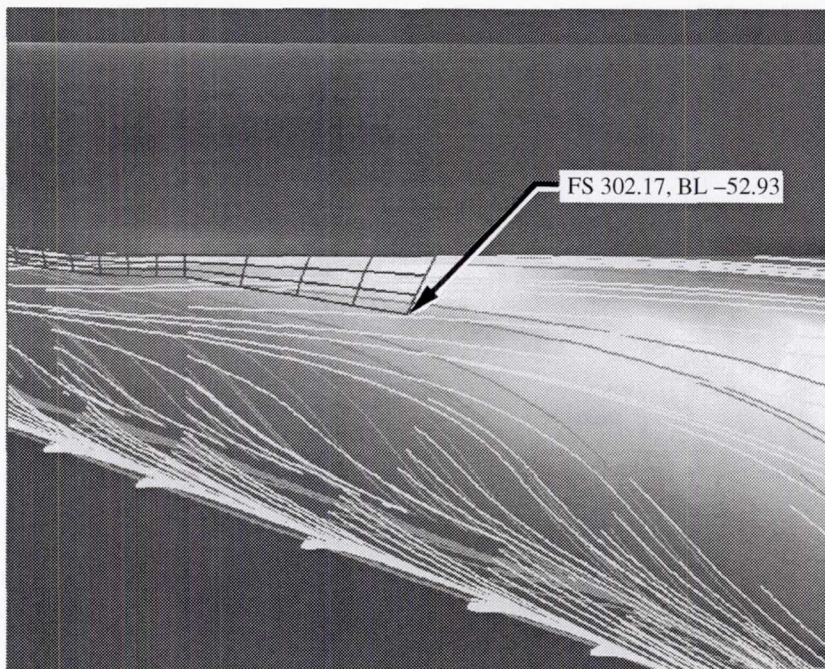
Figure 7. Schematic of requested and actual pressure port layout and flight video targets on airplane.



Figure 9. Front view of pressure instrumentation layout on right wing of F-16XL-1 airplane.

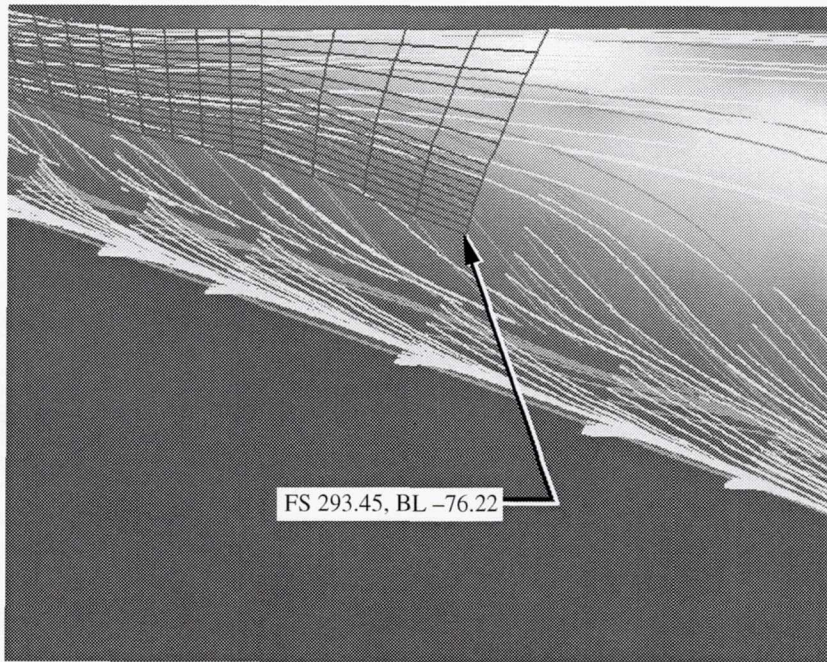


(a) General arrangement.

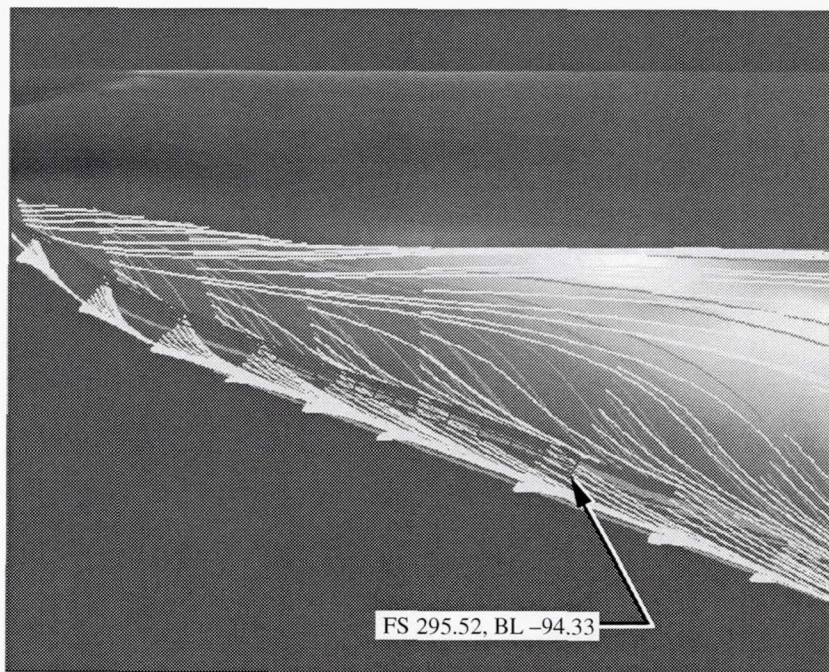


(b) Rake 3.

Figure 11. Suite of instruments on F-16XL-1 left wing, including rake locations and predicted local flow near surface. $\alpha = 13^\circ$; $M_\infty = 0.28$; $R_n = 46.1 \times 10^6$.

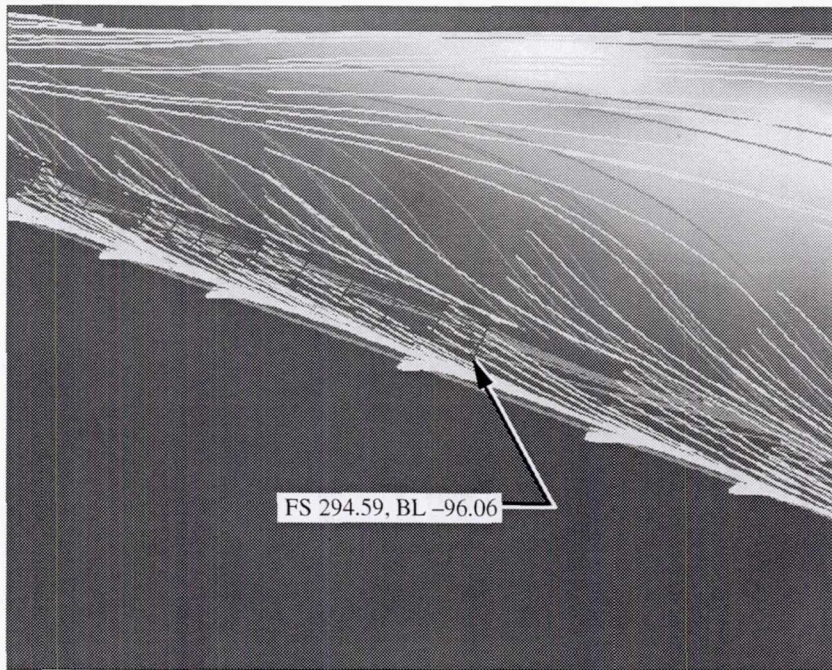


(c) Rake 4.



(d) Rake 7.

Figure 11. Continued.



(e) Rake 5.

Figure 11. Concluded.

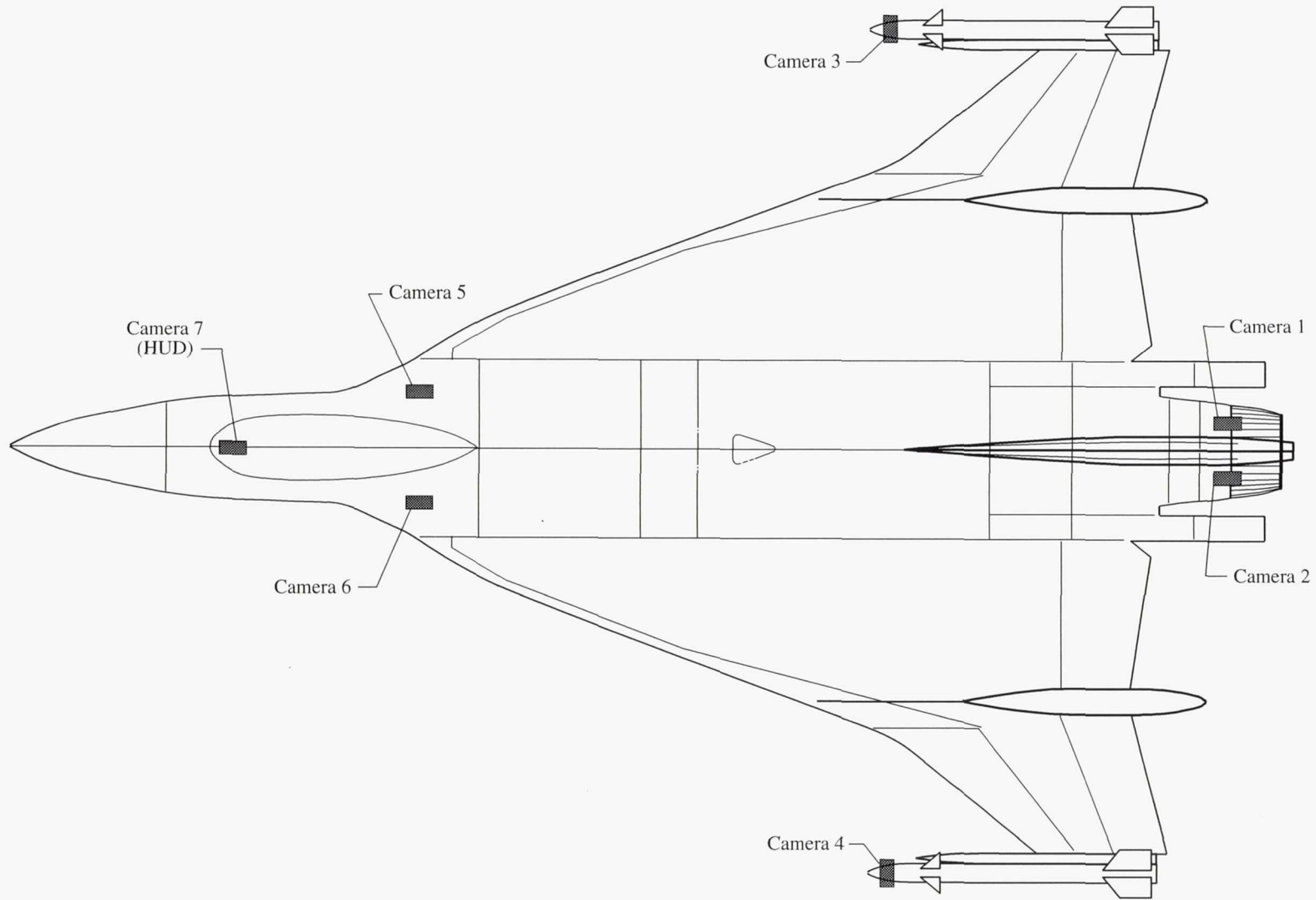
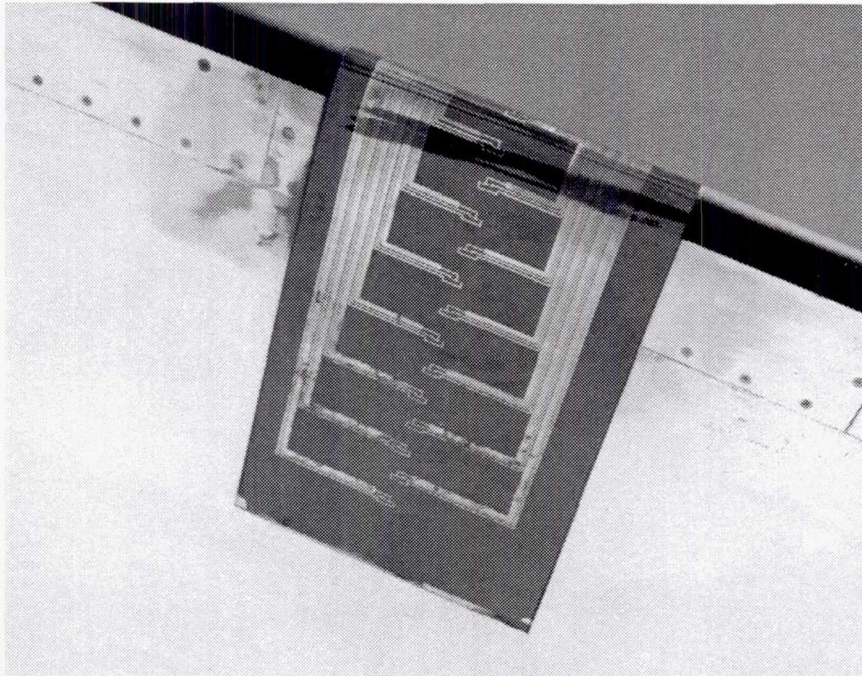


Figure 12. Locations of components of airborne video system installed on F-16XL-1 airplane.

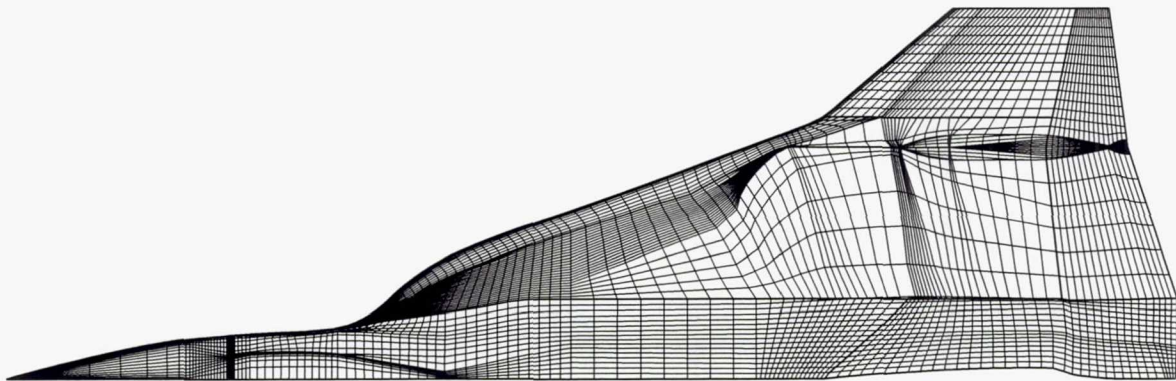


(a) General.

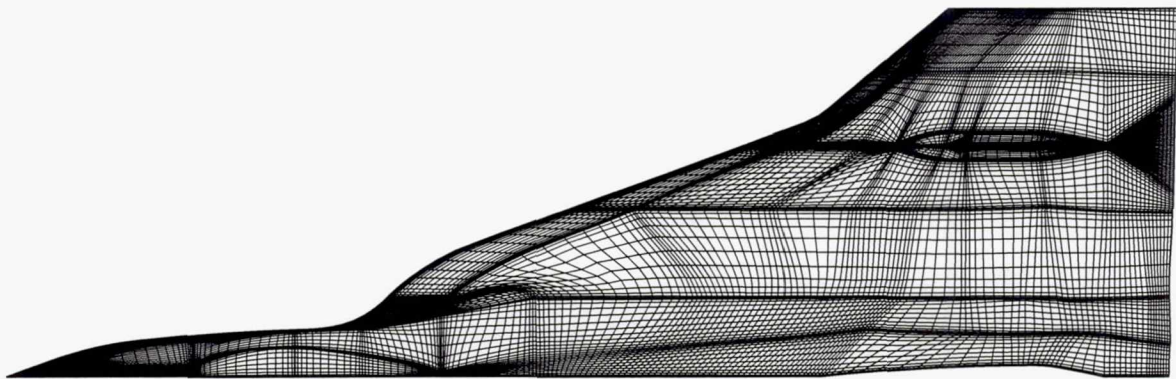


(b) Surface details.

Figure 13. Hot-film belt layout on airplane.

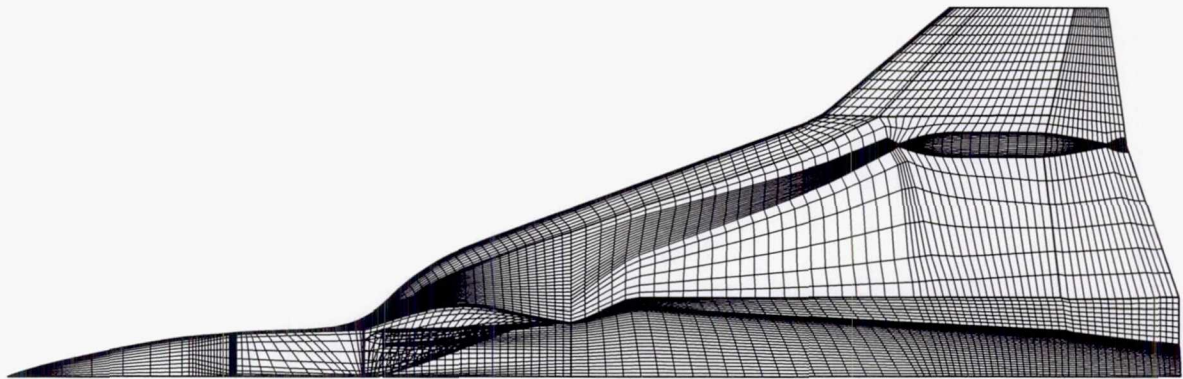


(a) Initial.

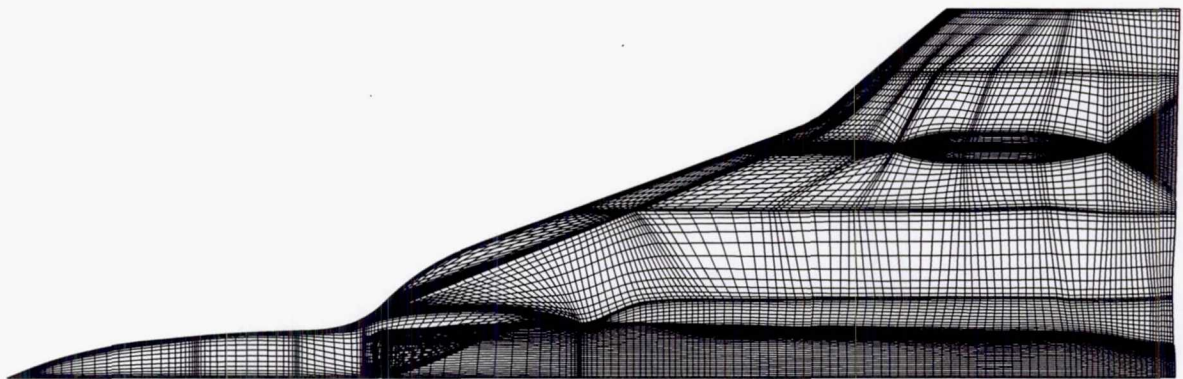


(b) Current.

Figure 14. Grid on wing-fuselage upper surface.

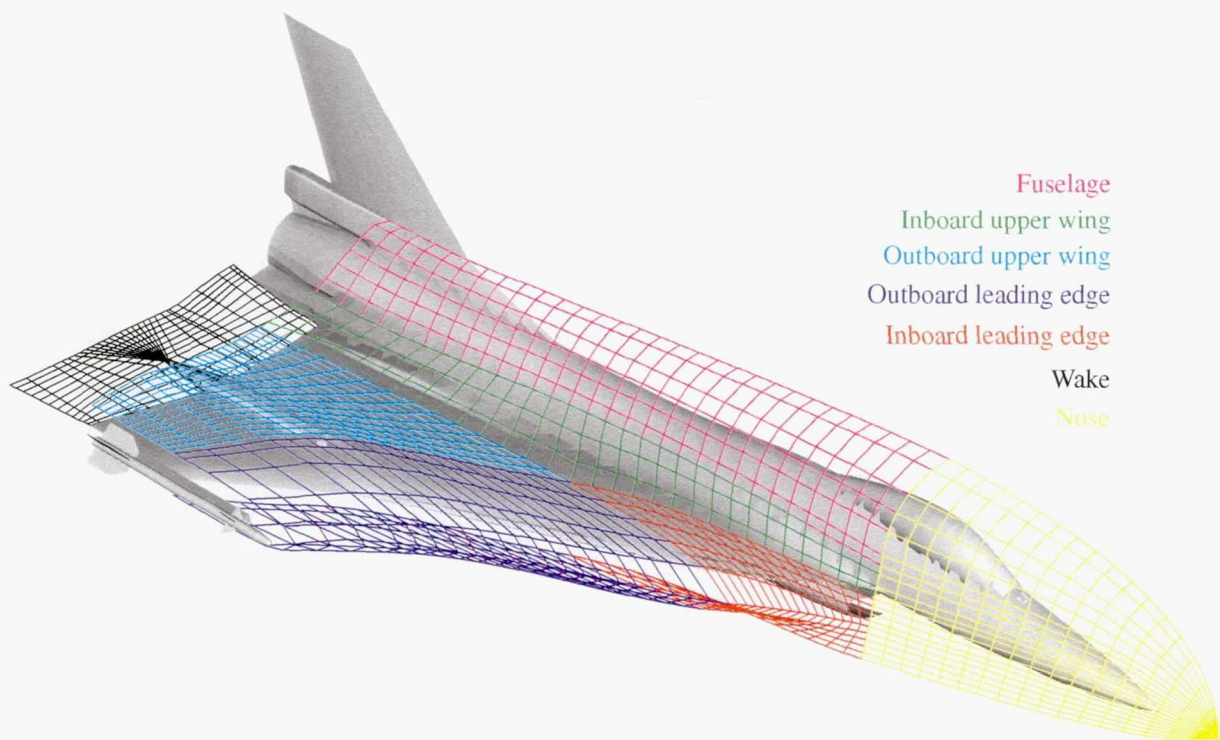


(a) Initial.



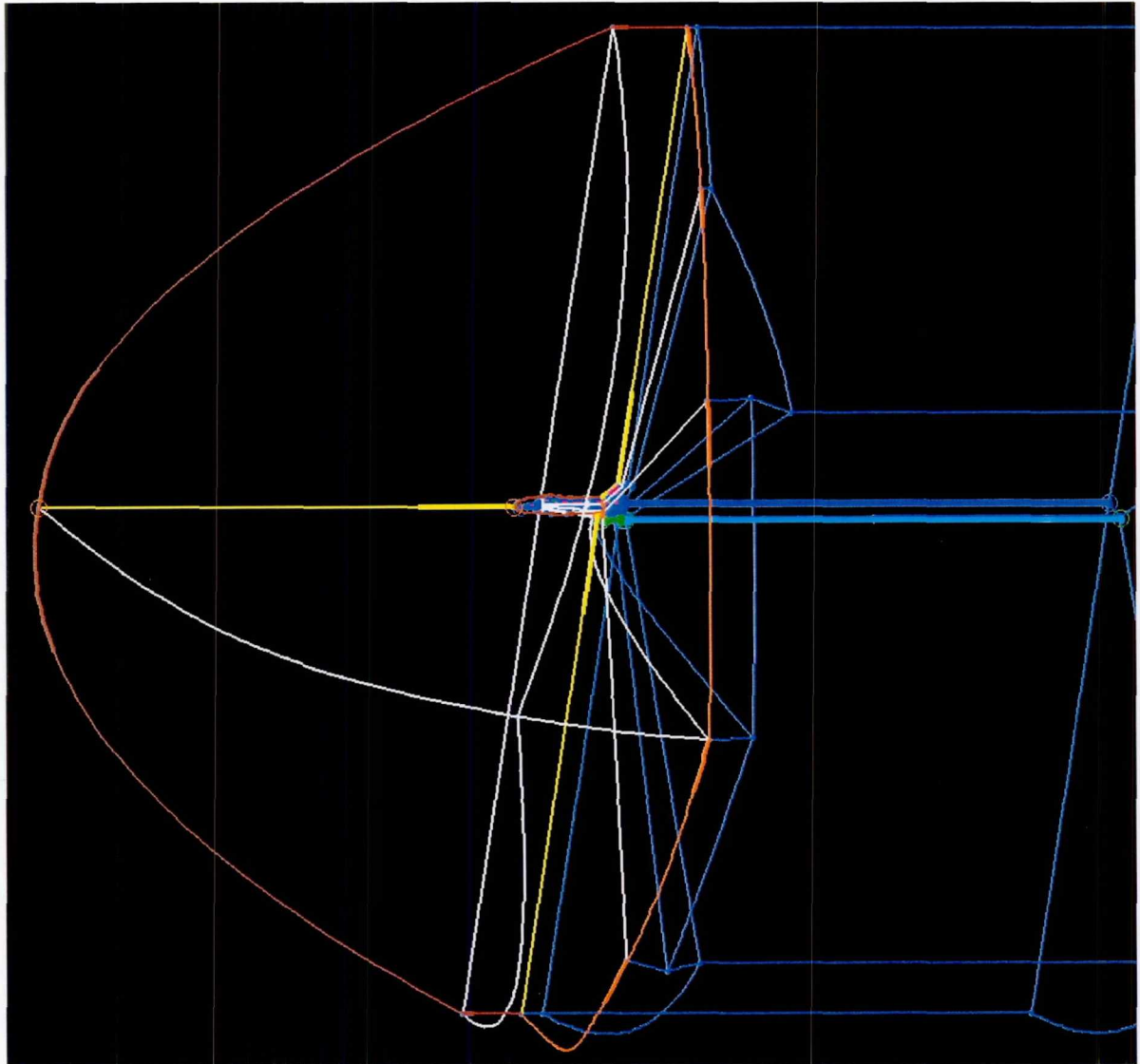
(b) Current.

Figure 15. Grid on wing-fuselage lower surface.



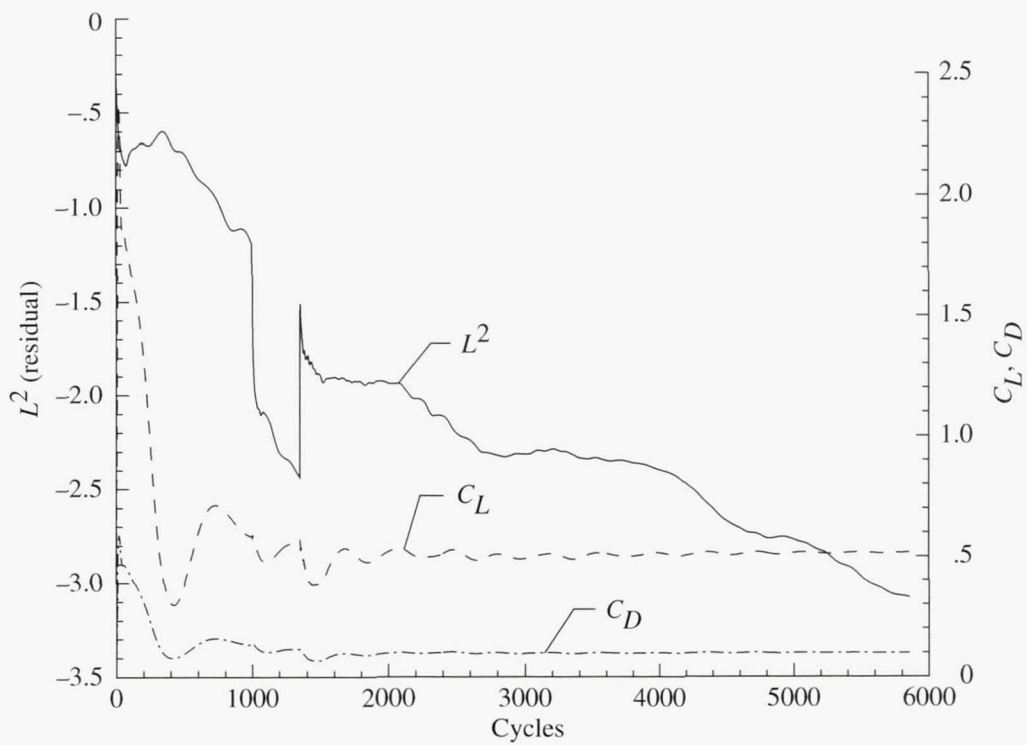
(a) Inner.

Figure 16. CFD block structure layout for F-16XL-1 airplane.



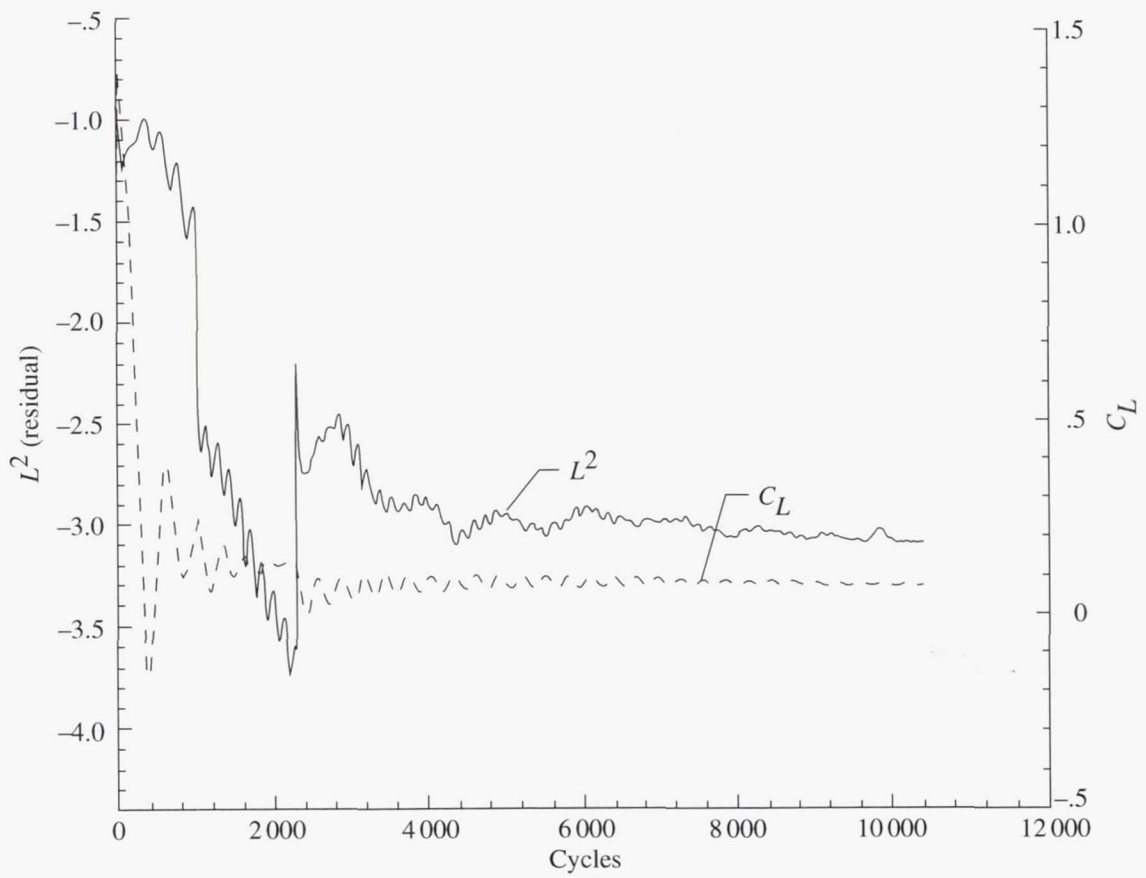
(b) Outer.

Figure 16. Concluded.



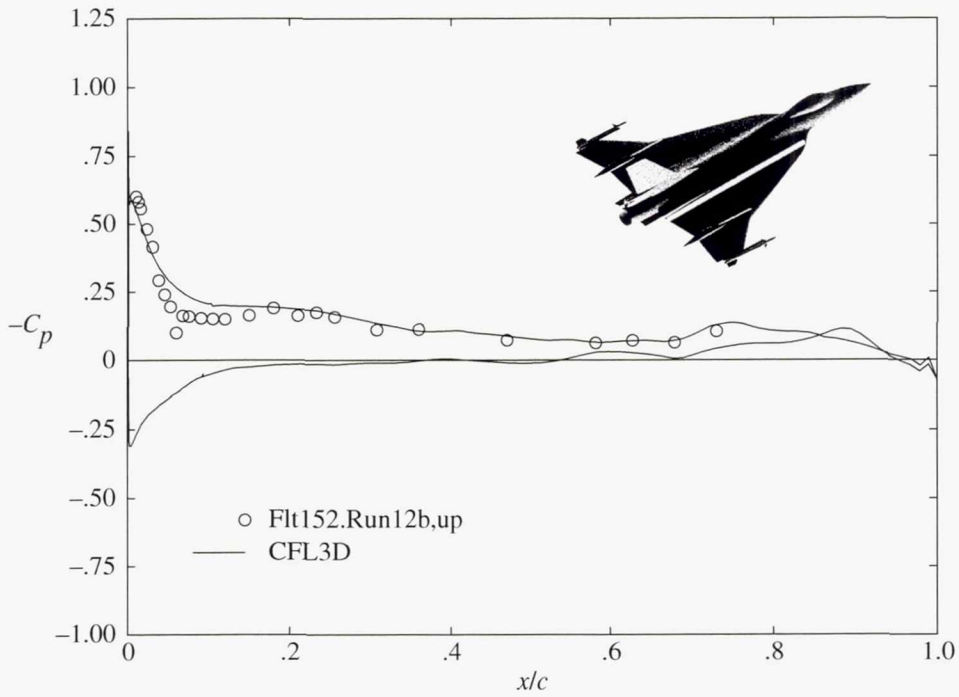
(a) $R_n = 38.97 \times 10^6$.

Figure 17. Reynolds number effect on convergence histories for two solutions.

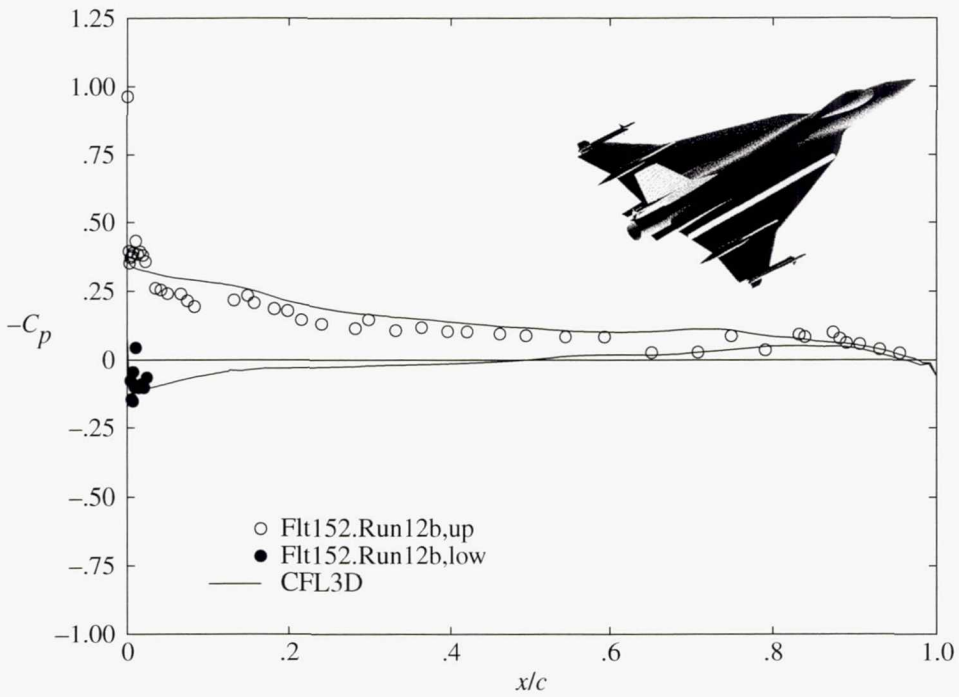


(b) $R_n = 1.12 \times 10^6$.

Figure 17. Concluded.

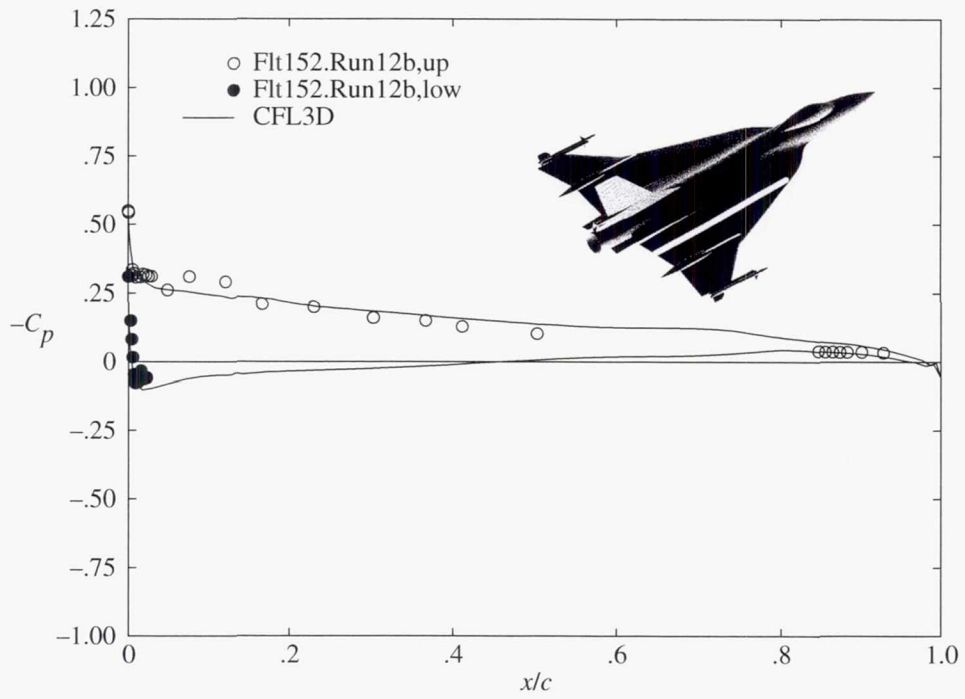


(a) BL 55.

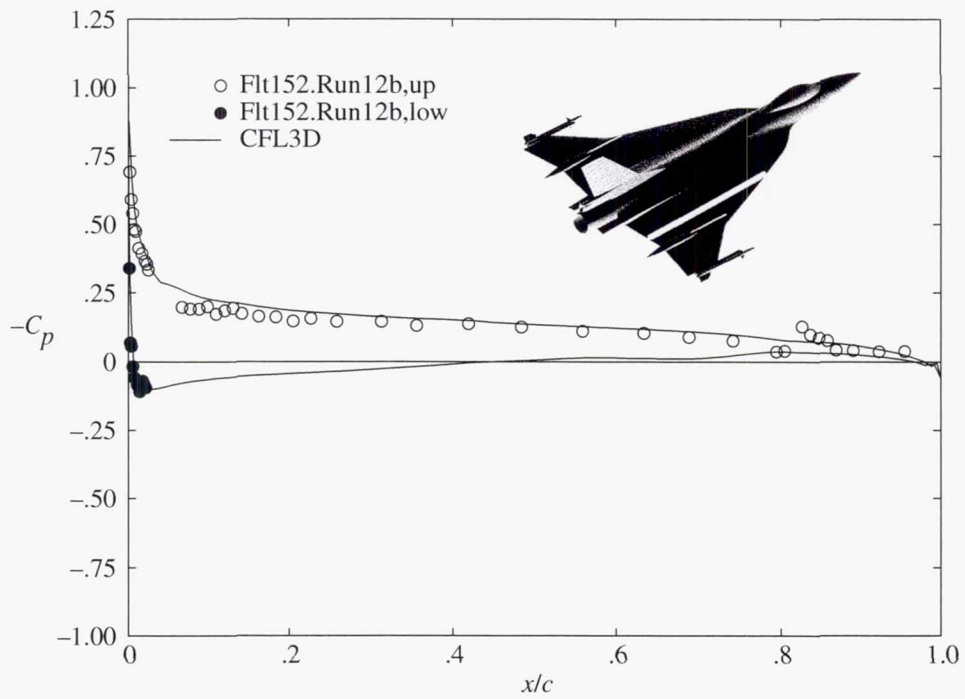


(b) BL 70.

Figure 18. Predicted and measured flight C_p distribution on F-16XL-1 airplane at FC 1 ($\alpha = 5.5^\circ$; $M_\infty = 0.52$; $R_n = 77.71 \times 10^6$).

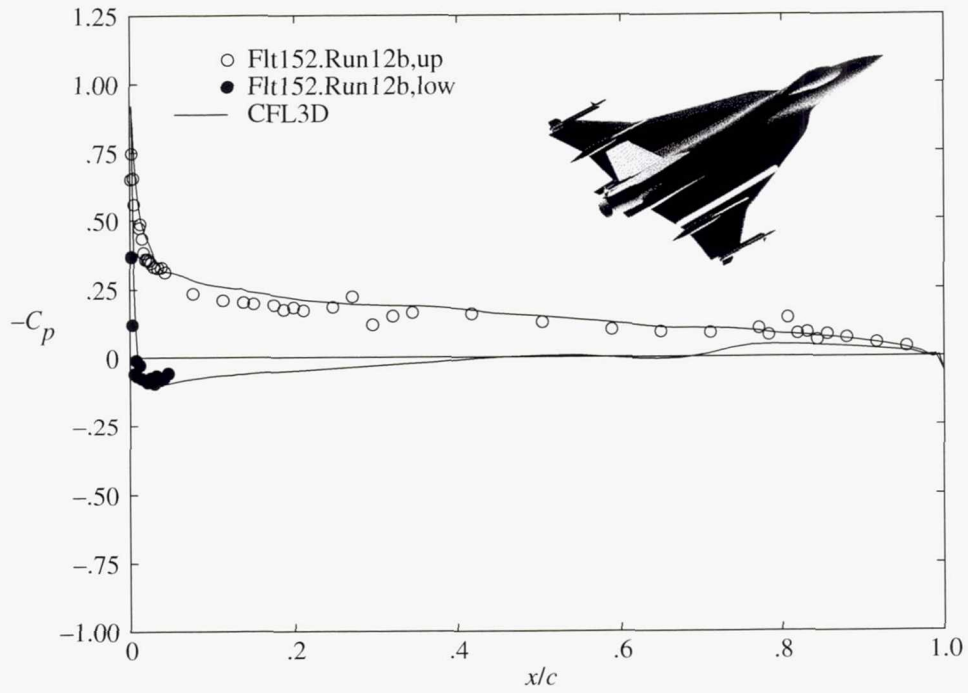


(c) BL 80.

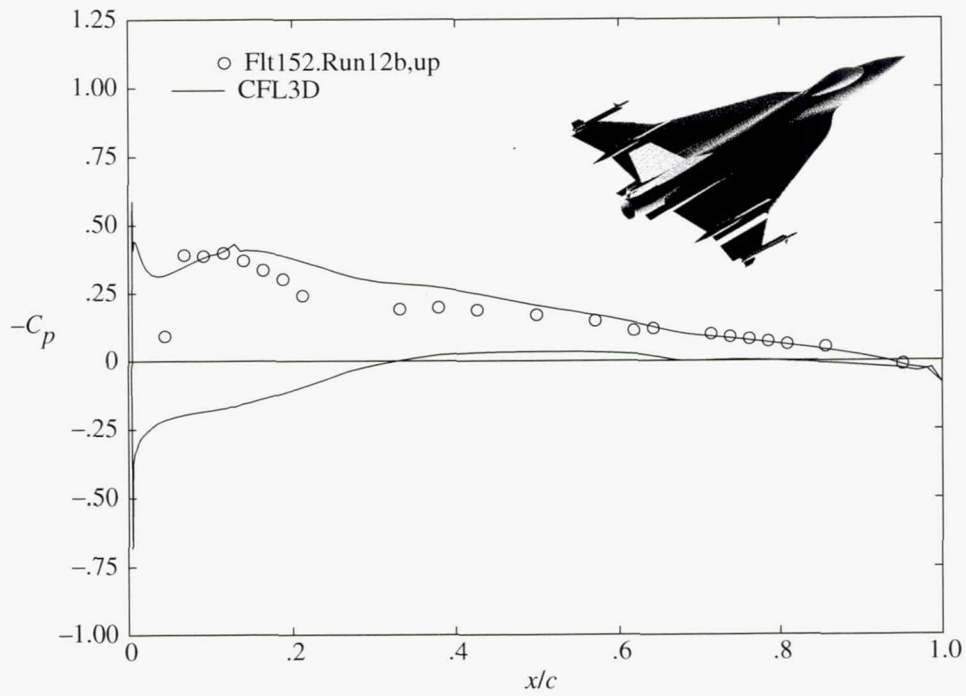


(d) BL 95.

Figure 18. Continued.

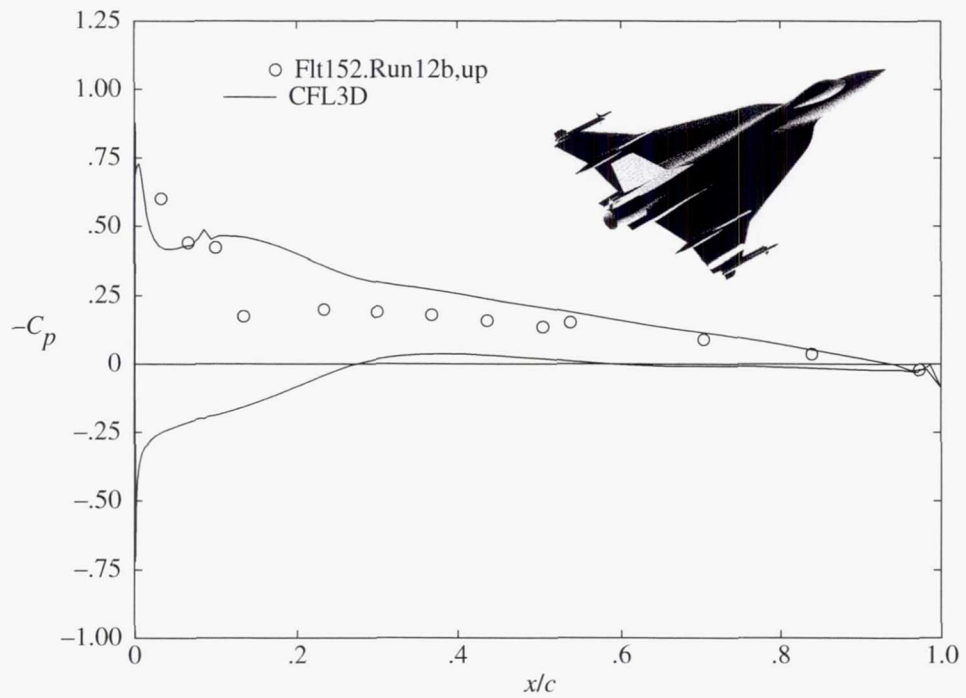


(e) BL 105.

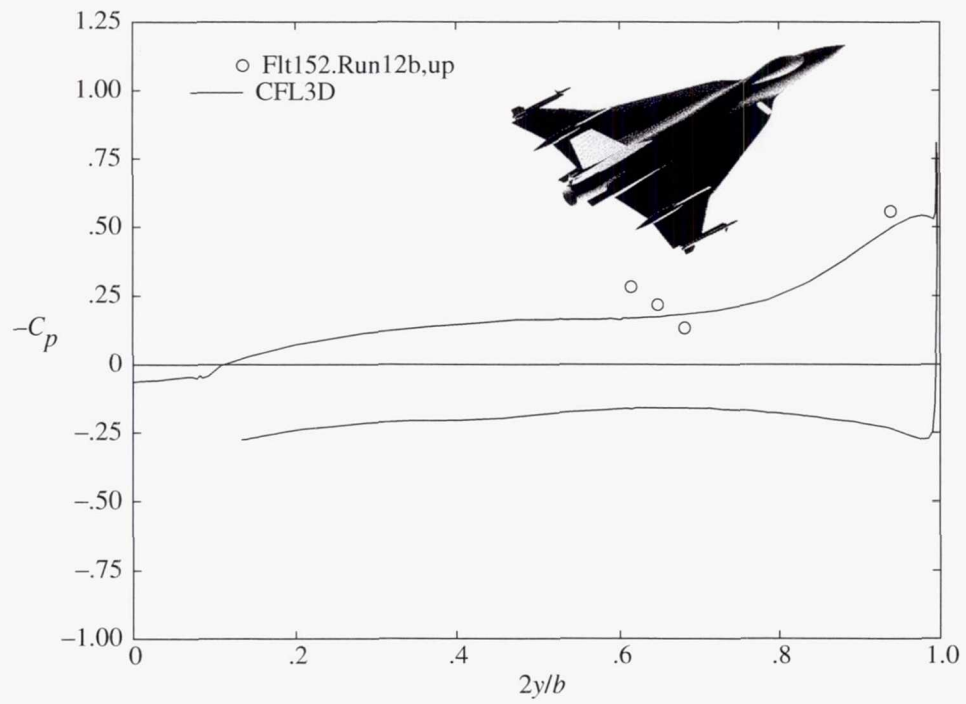


(f) BL 153.5.

Figure 18. Continued.

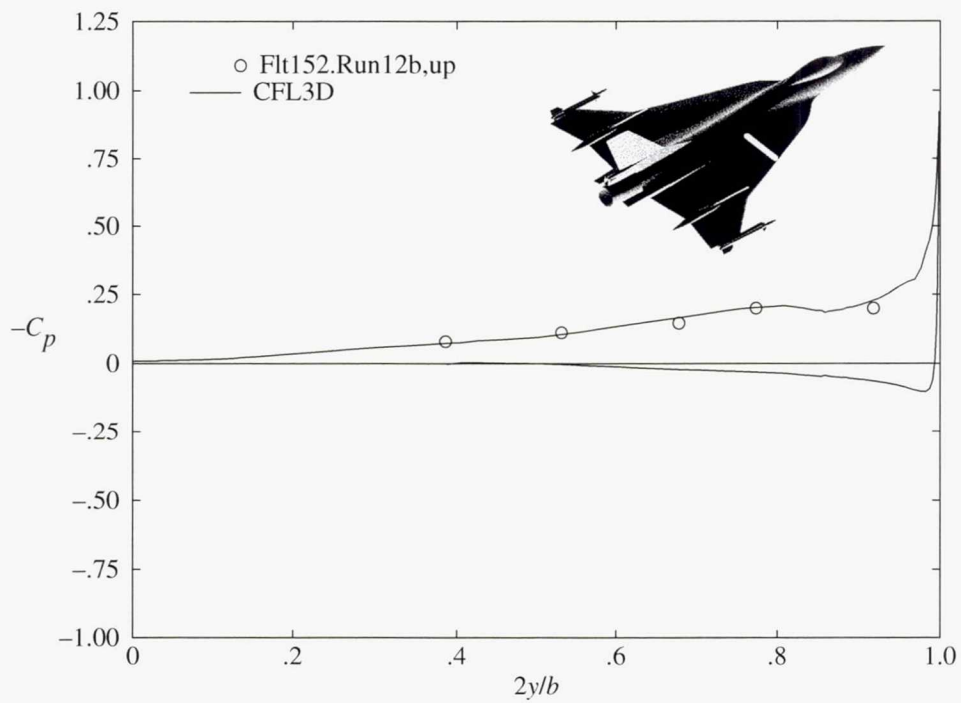


(g) BL 184.5.

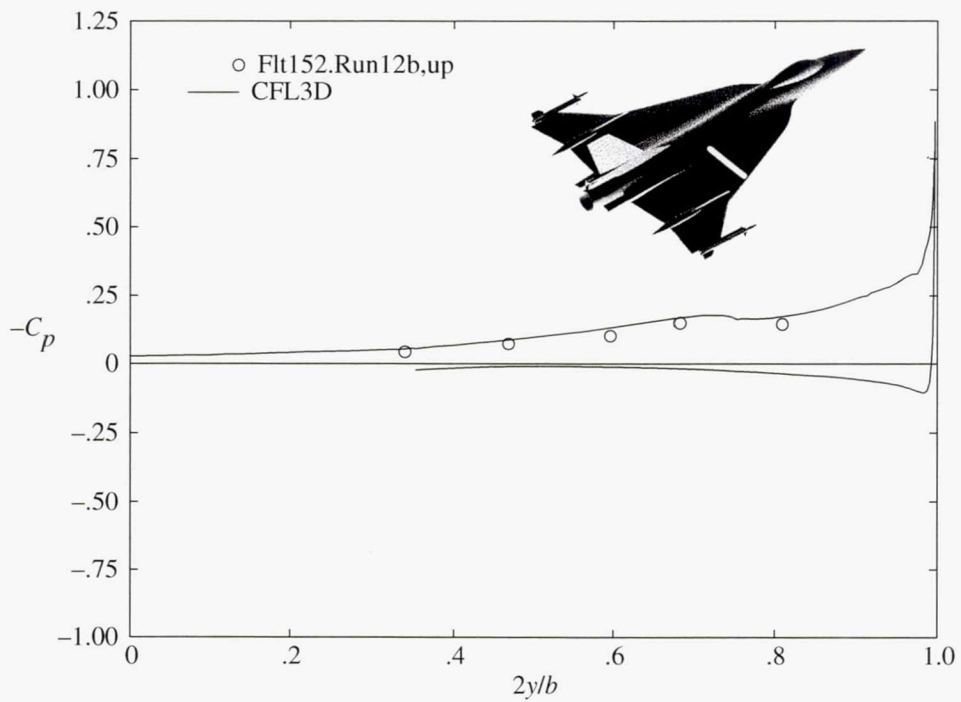


(h) FS 185.

Figure 18. Continued.

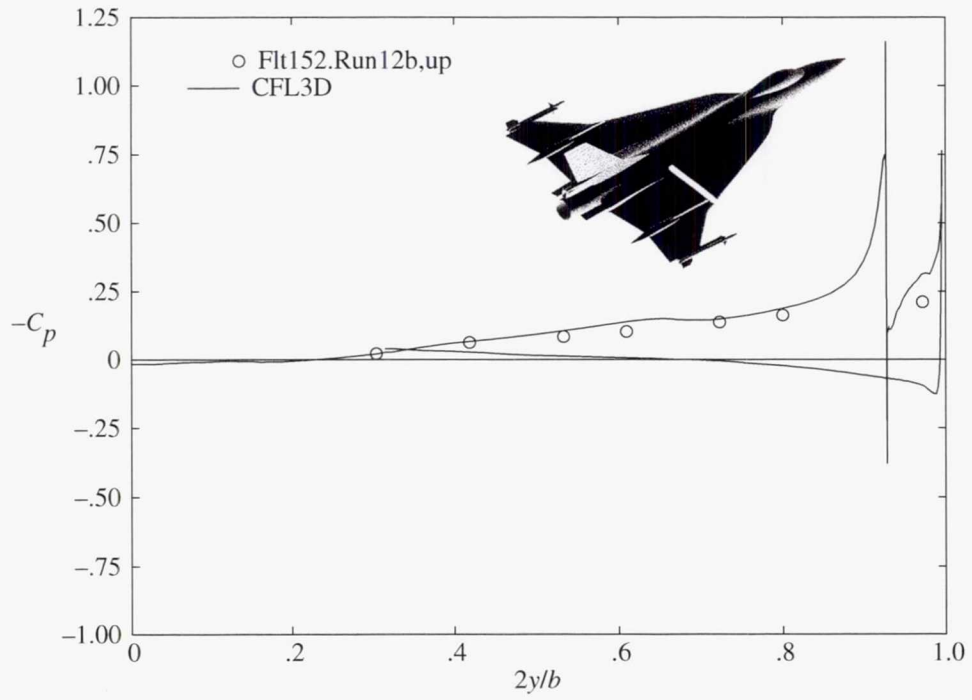


(i) FS 300.

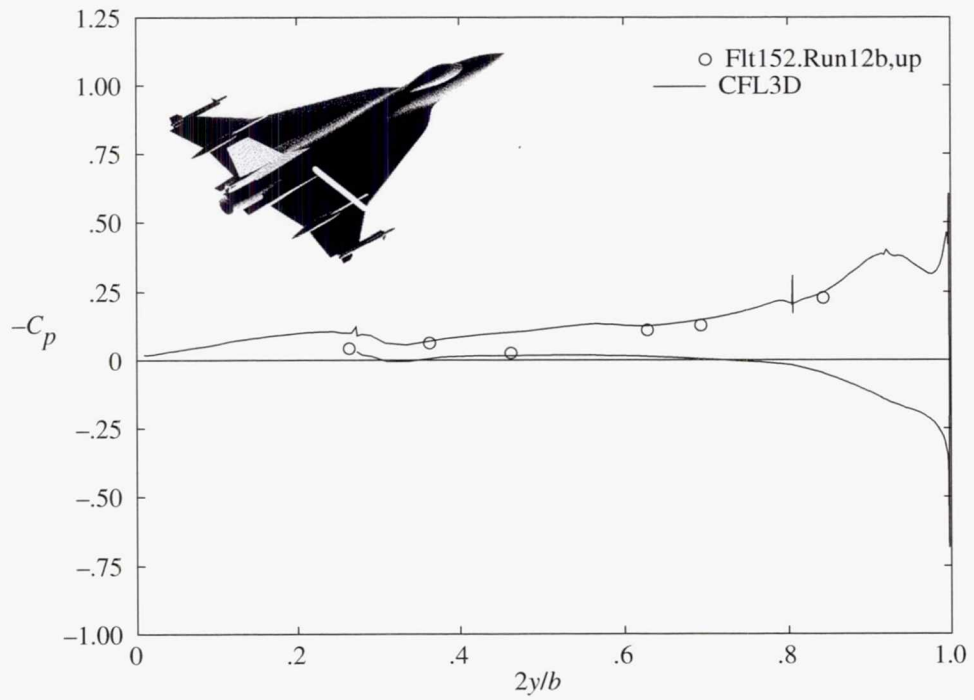


(j) FS 337.5.

Figure 18. Continued.

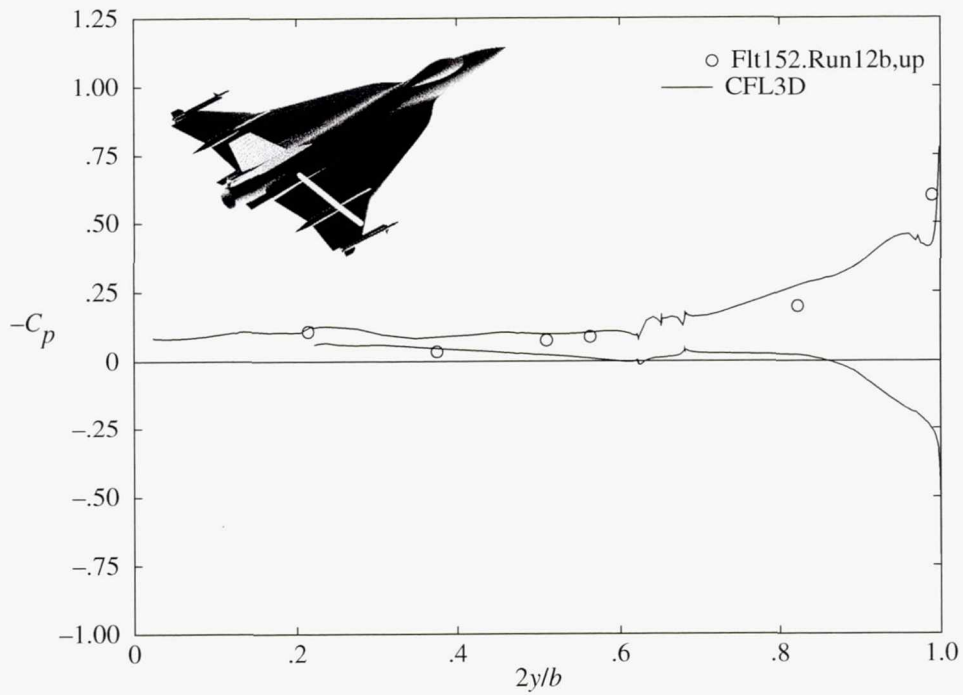


(k) FS 375.

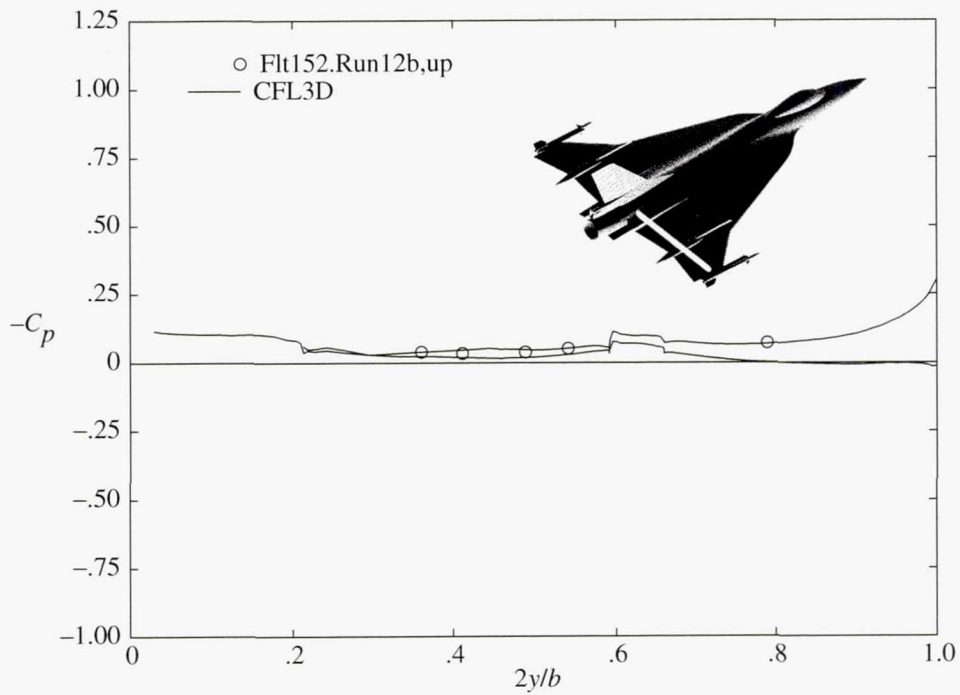


(l) FS 407.5.

Figure 18. Continued.

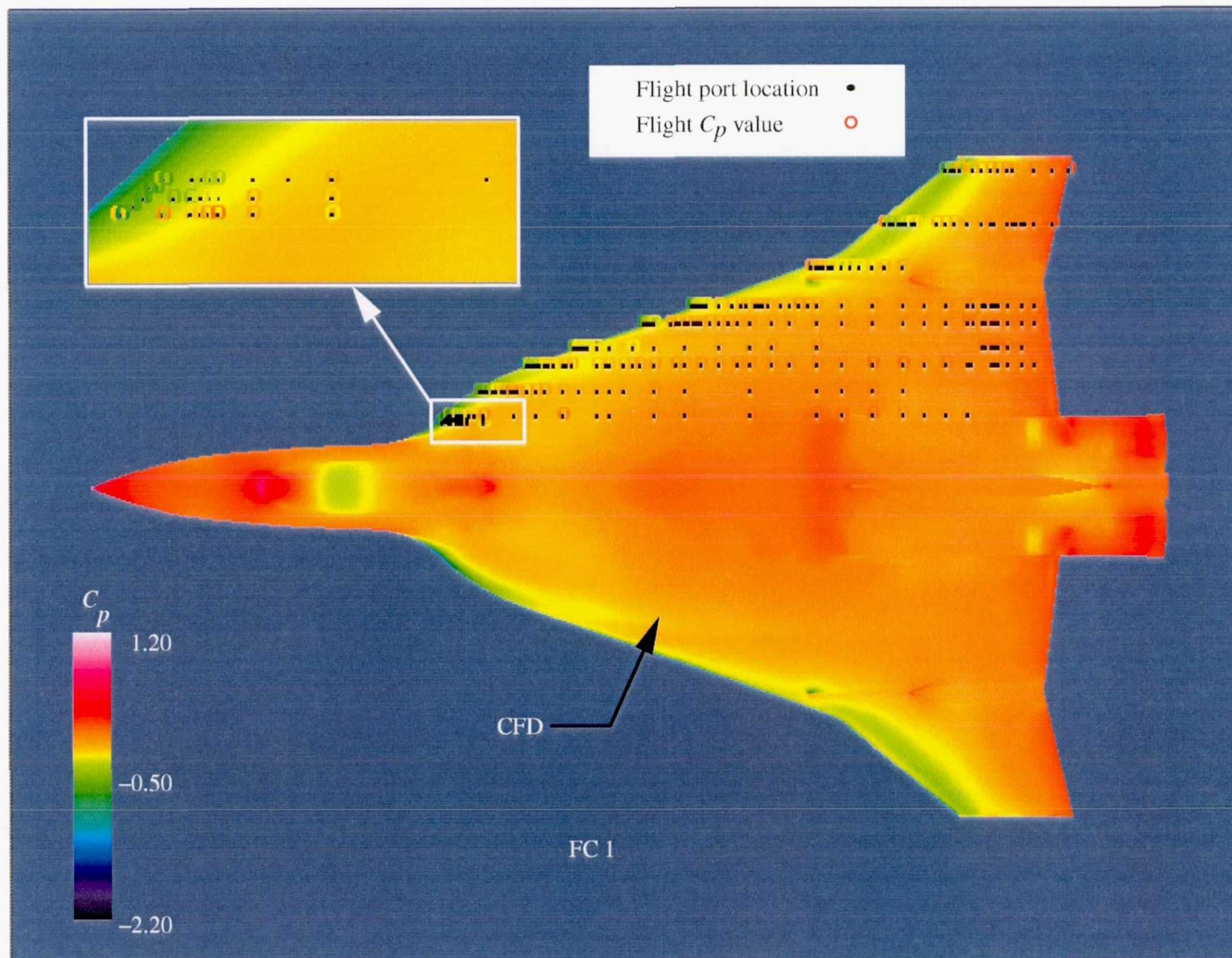


(m) FS 450.



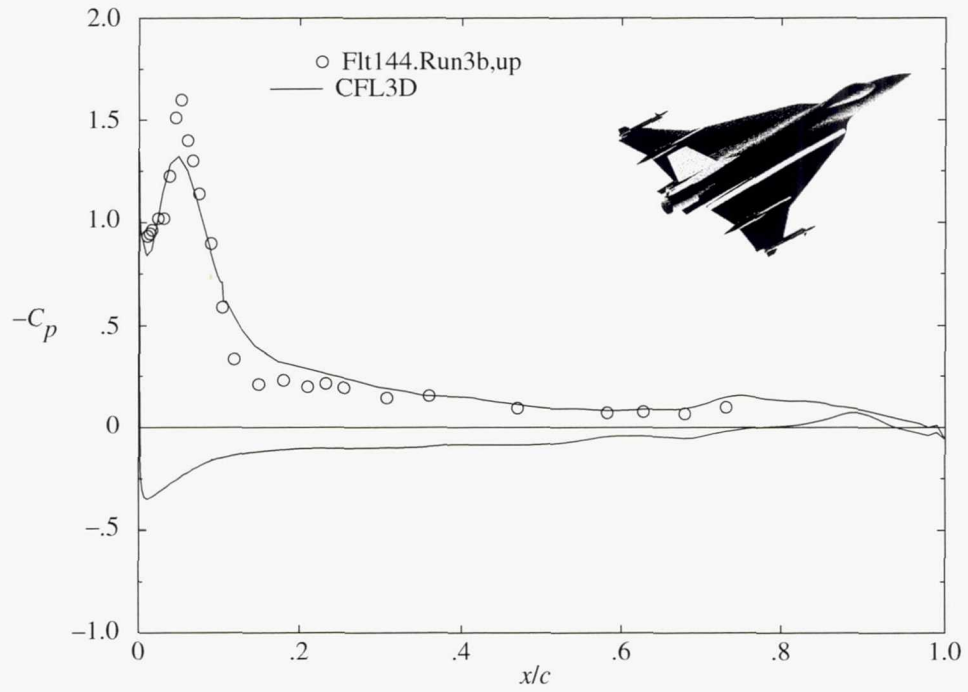
(n) FS 492.5.

Figure 18. Continued.

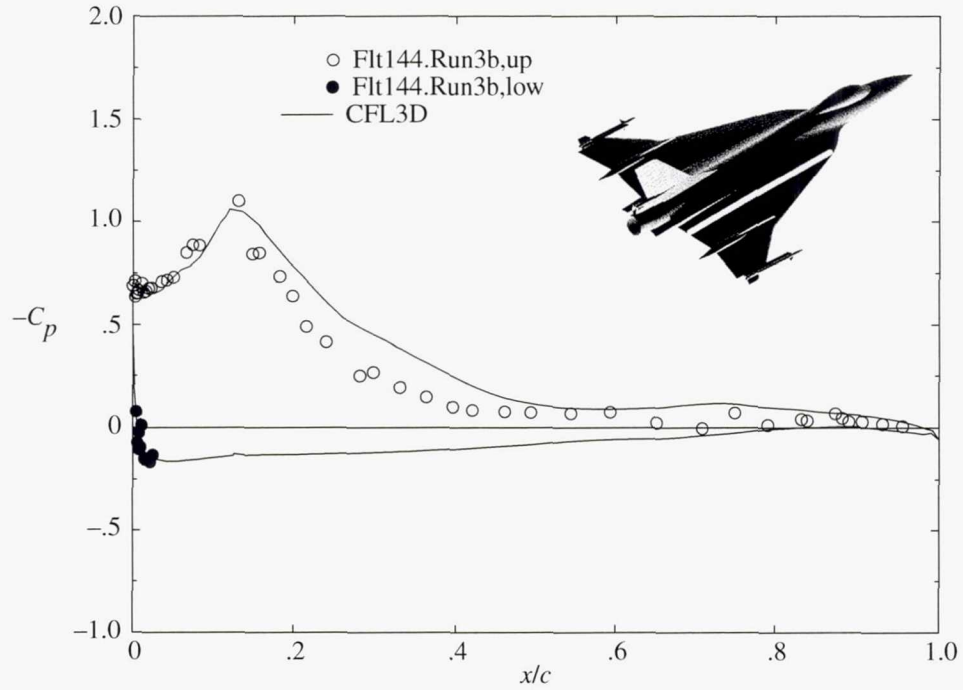


(o) Upper surface C_p distribution.

Figure 18. Concluded.

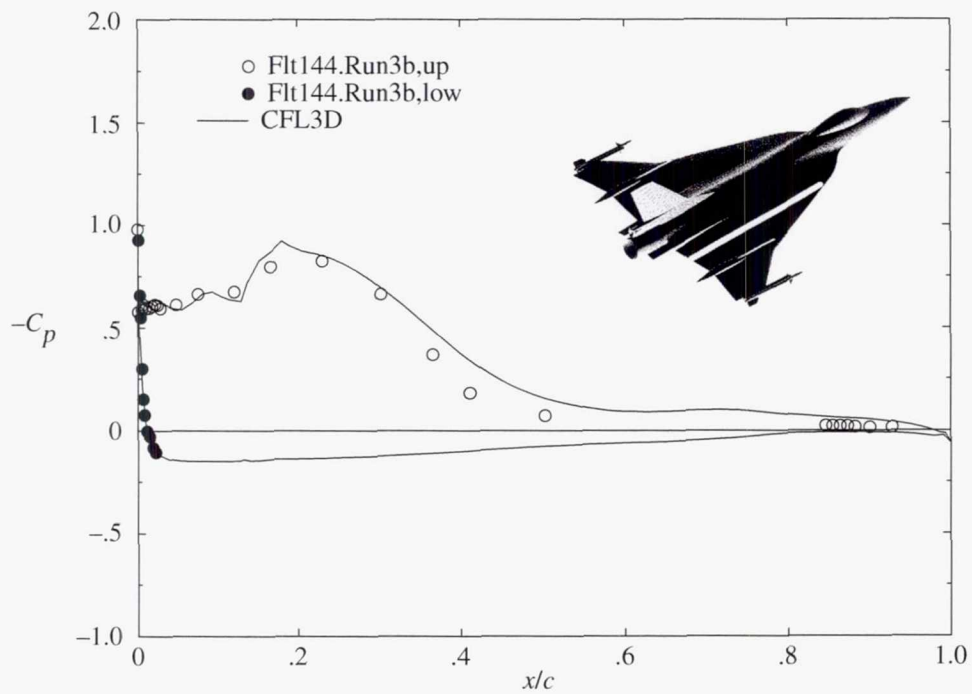


(a) BL 55.

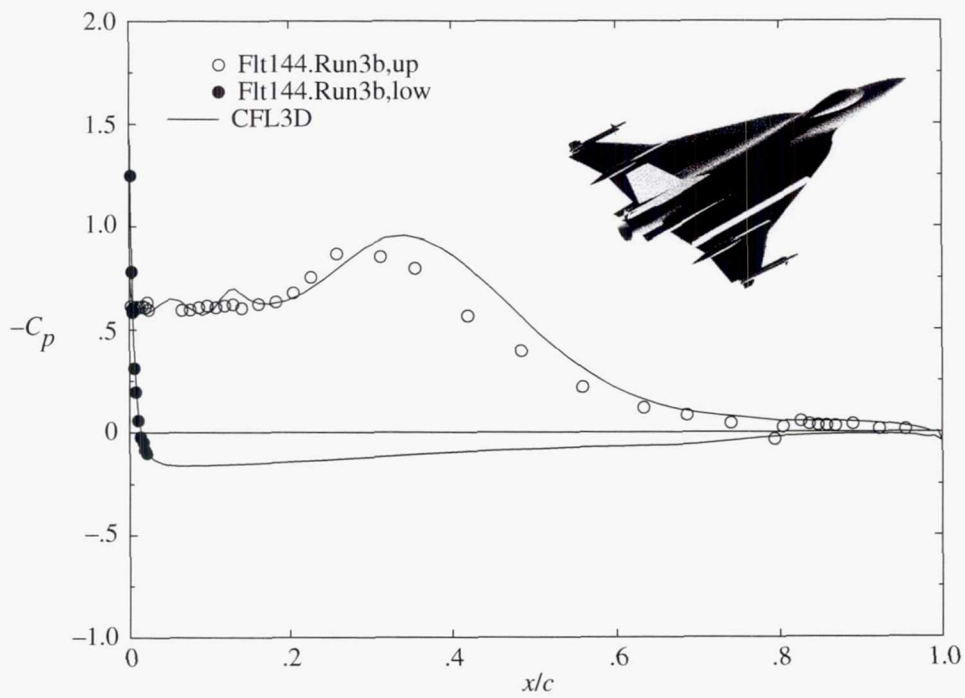


(b) BL 70.

Figure 19. Predicted and measured flight C_p distribution on F-16XL-1 airplane at FC 46 ($\alpha = 10.4^\circ$; $M_\infty = 0.53$; $R_n = 46.90 \times 10^6$).

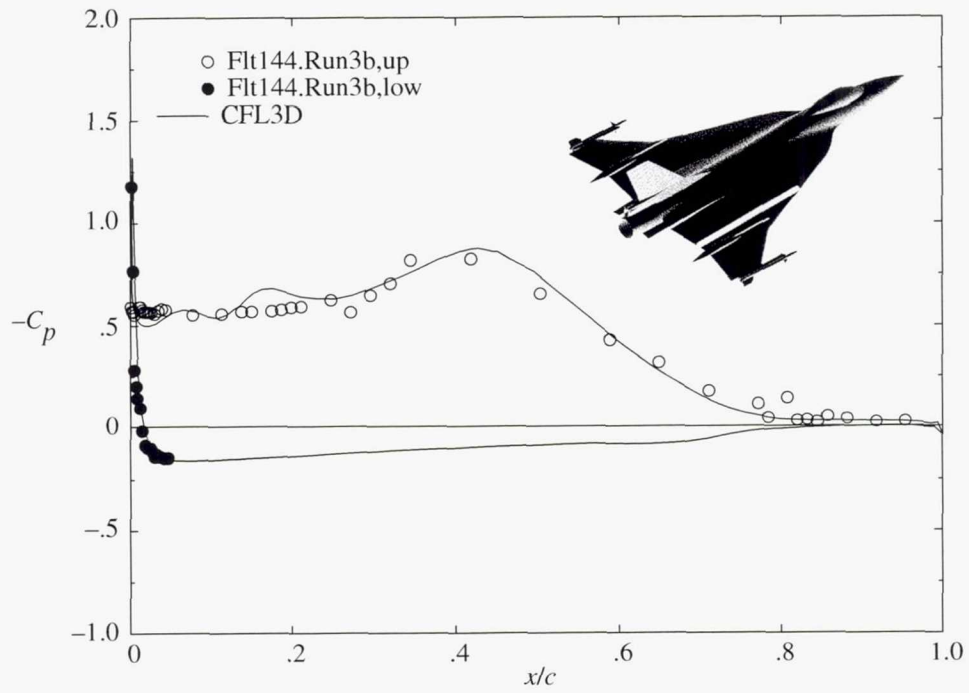


(c) BL 80.

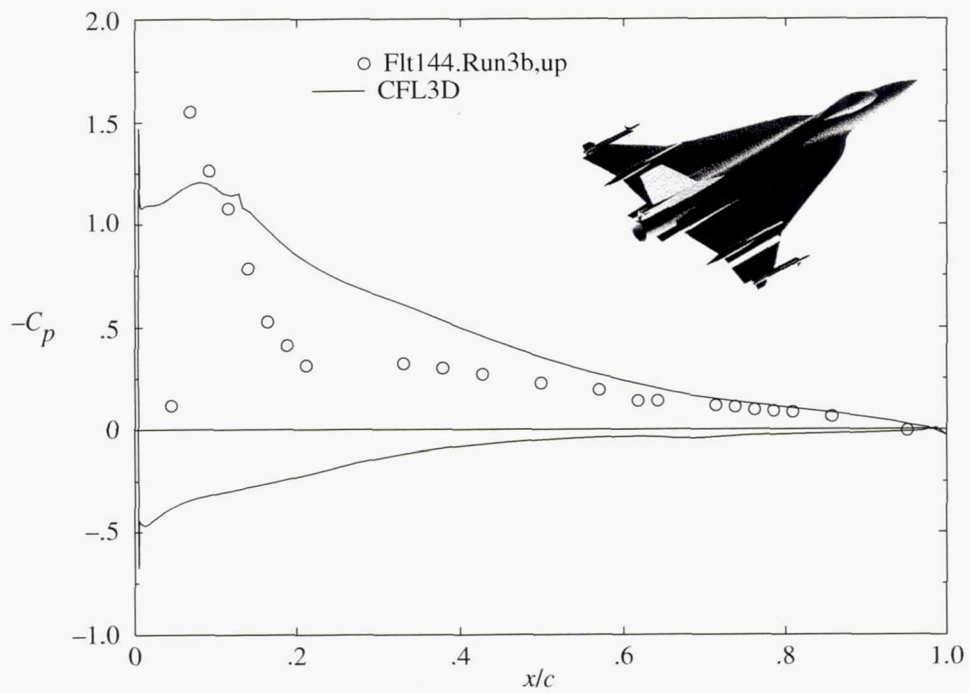


(d) BL 95.

Figure 19. Continued.

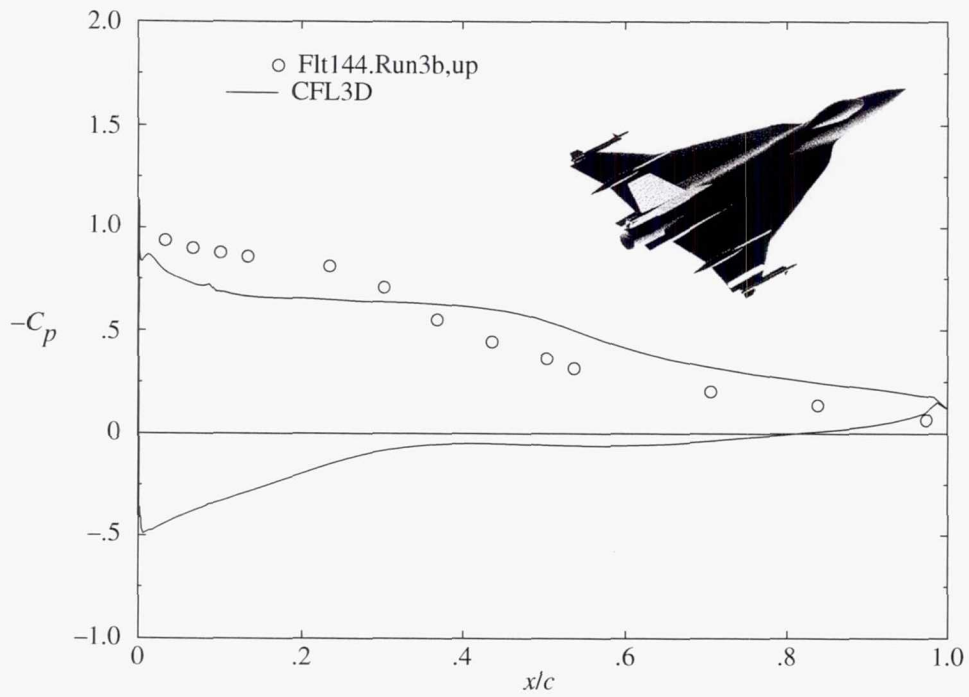


(e) BL 105.

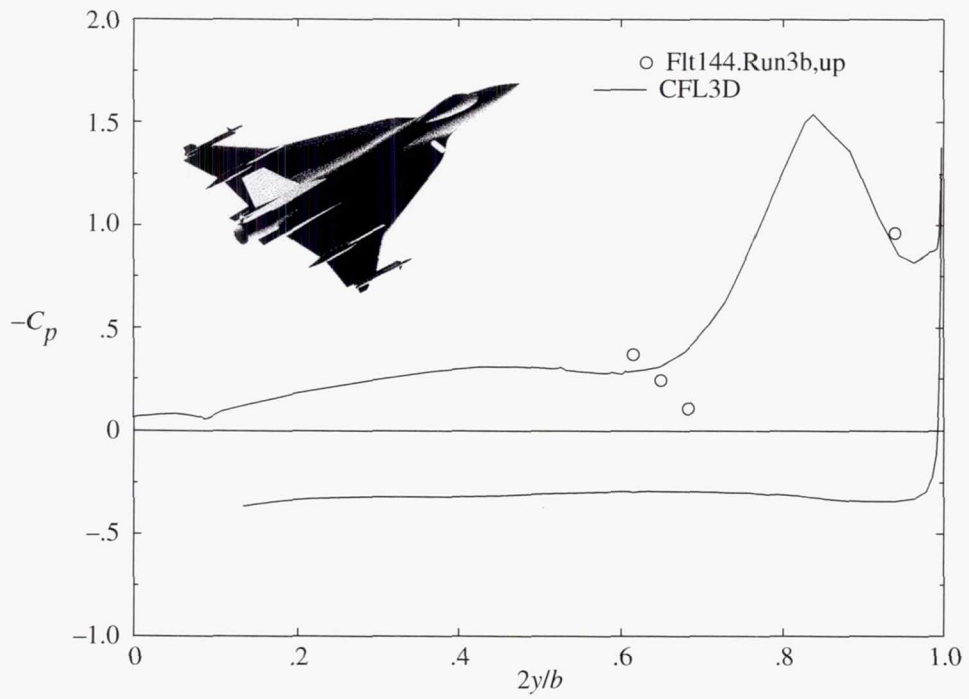


(f) BL 153.5.

Figure 19. Continued.

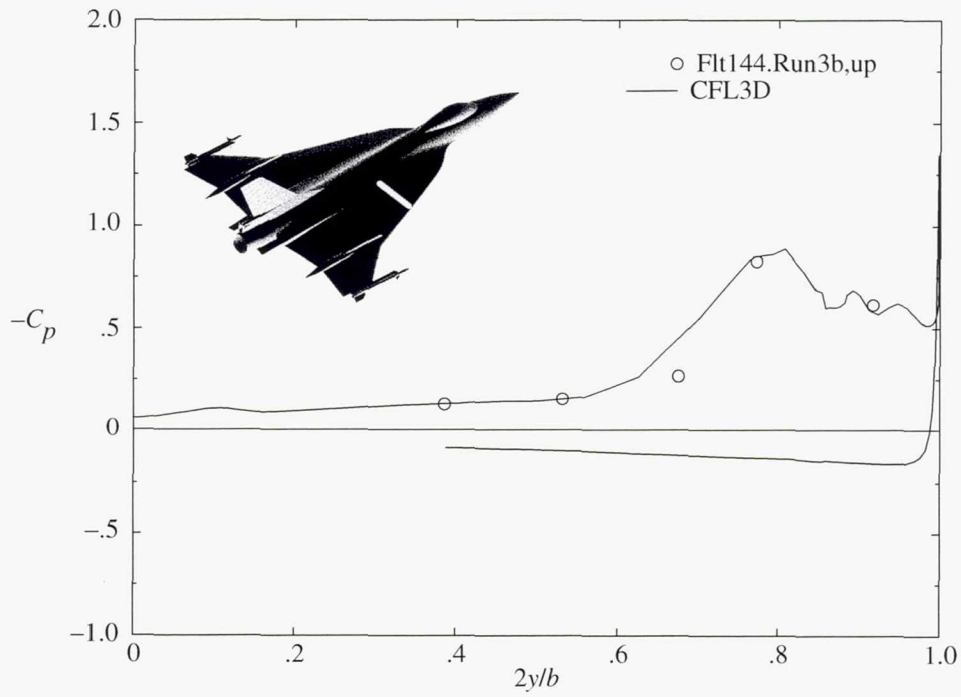


(g) BL 184.5.

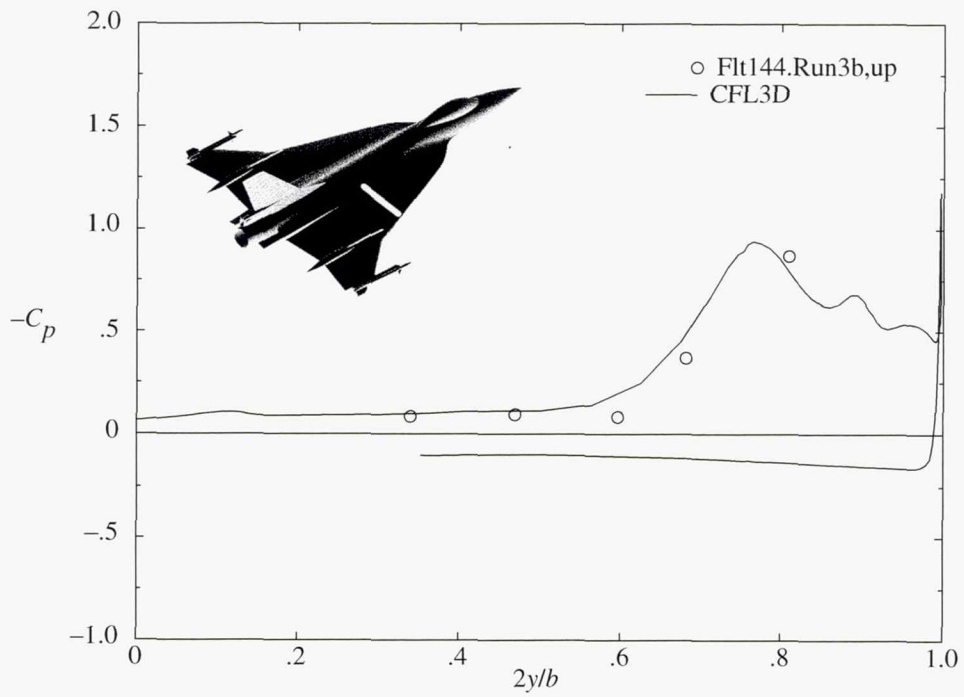


(h) FS 185.

Figure 19. Continued.

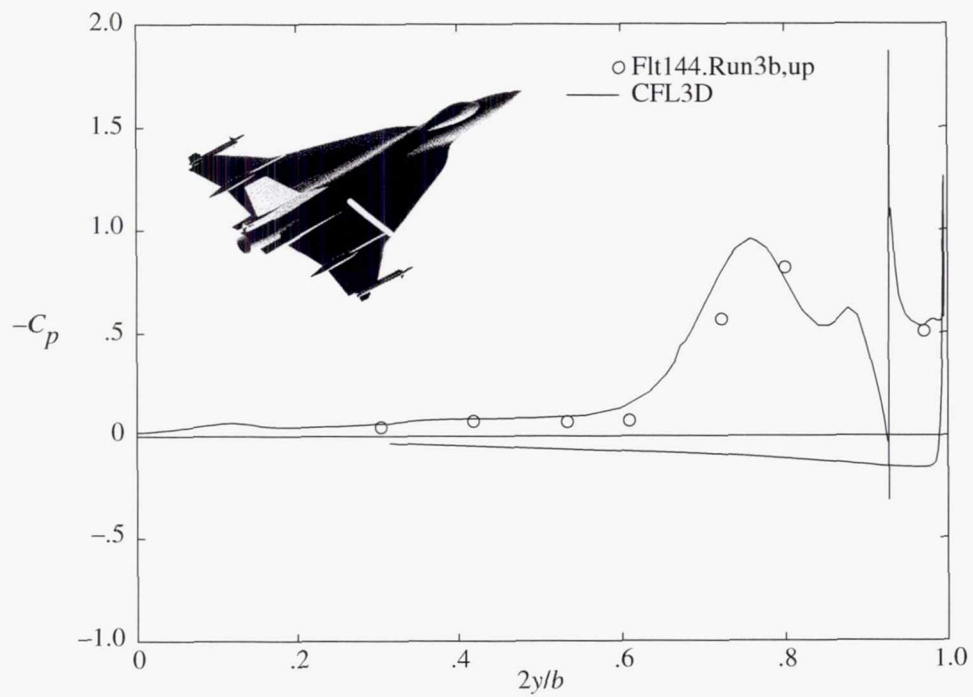


(i) FS 300.

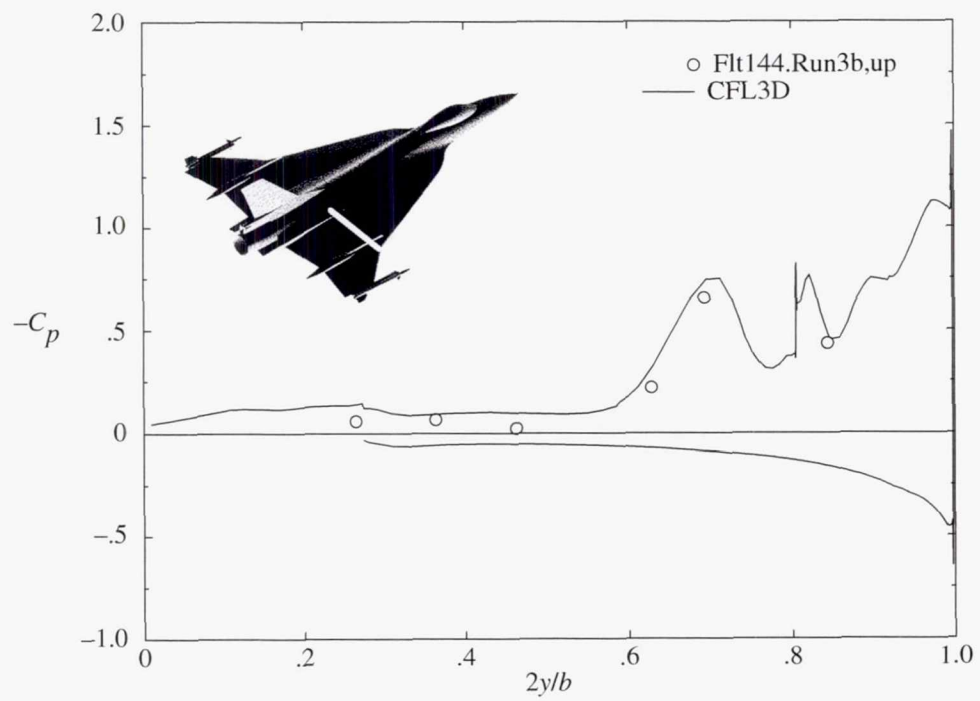


(j) FS 337.5.

Figure 19. Continued.

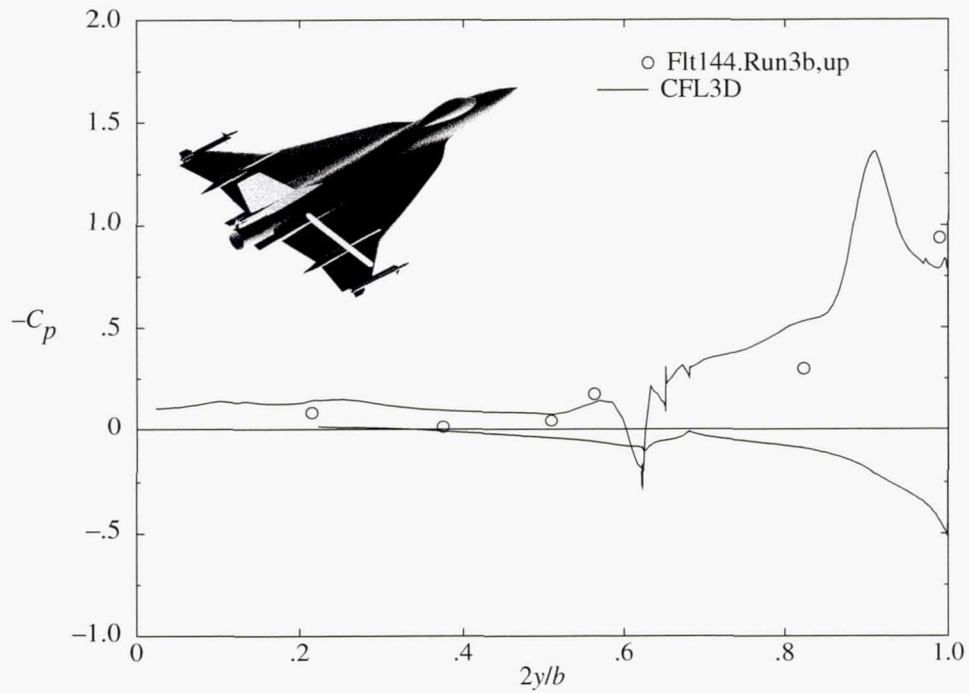


(k) FS 375.

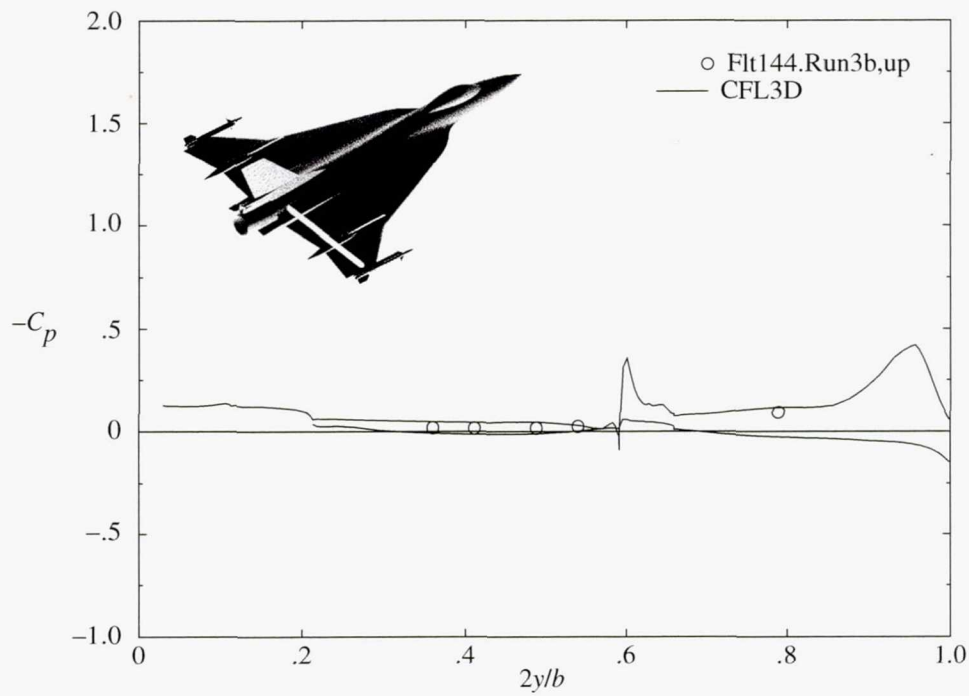


(l) FS 407.5.

Figure 19. Continued.

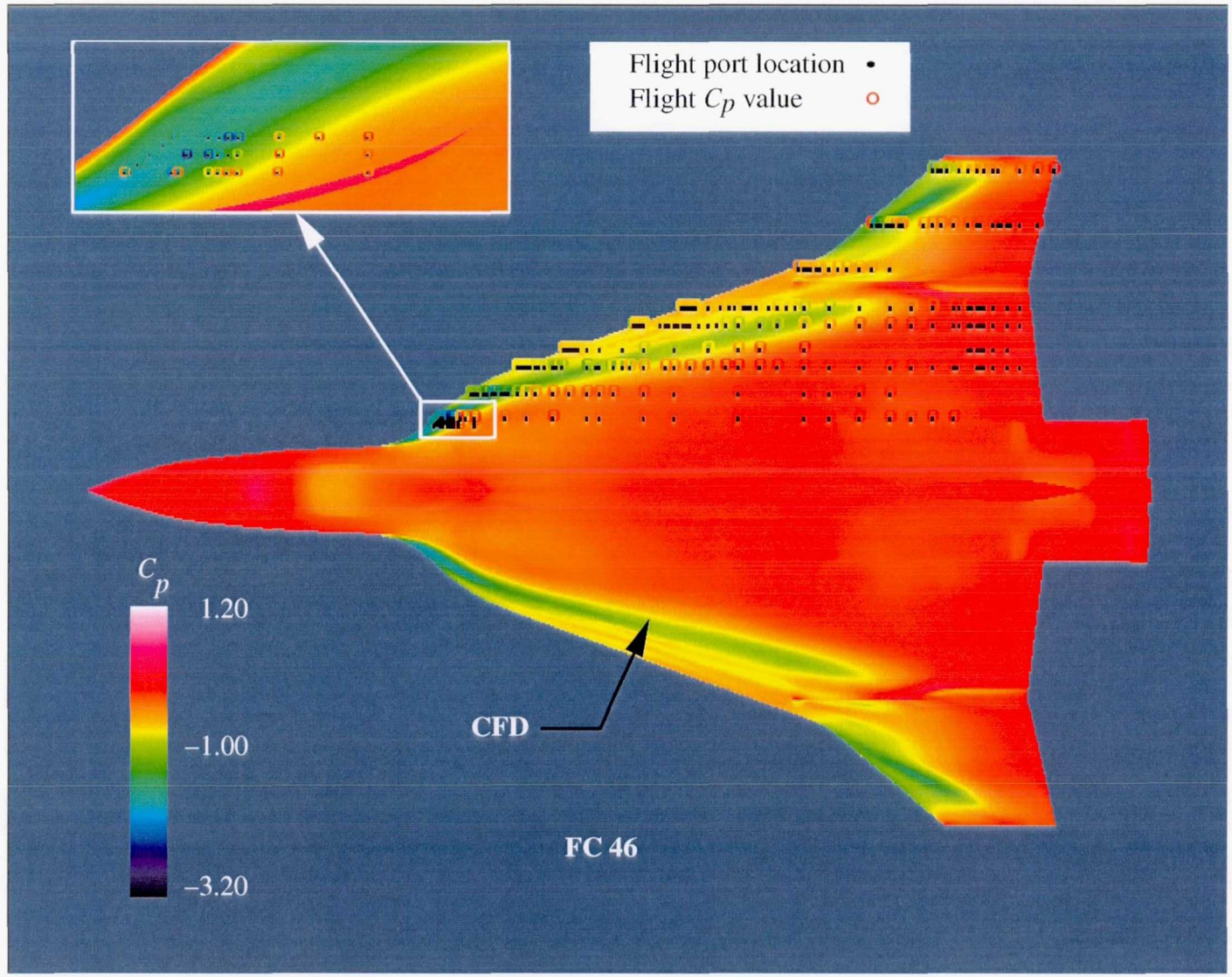


(m) FS 450.



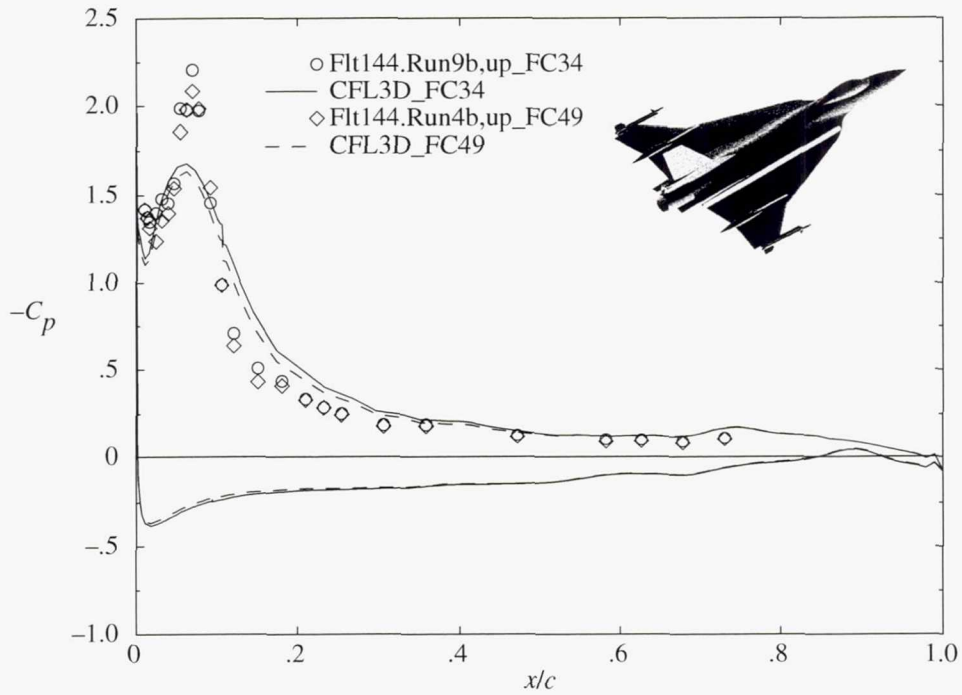
(n) FS 492.5.

Figure 19. Continued.

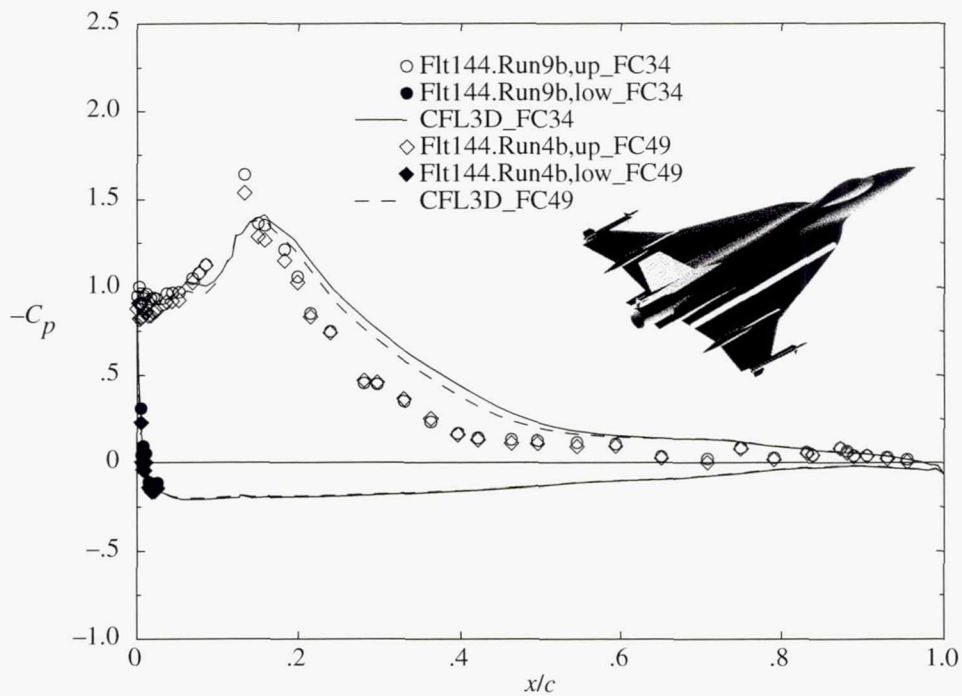


(o) Upper surface C_p distribution.

Figure 19. Concluded.

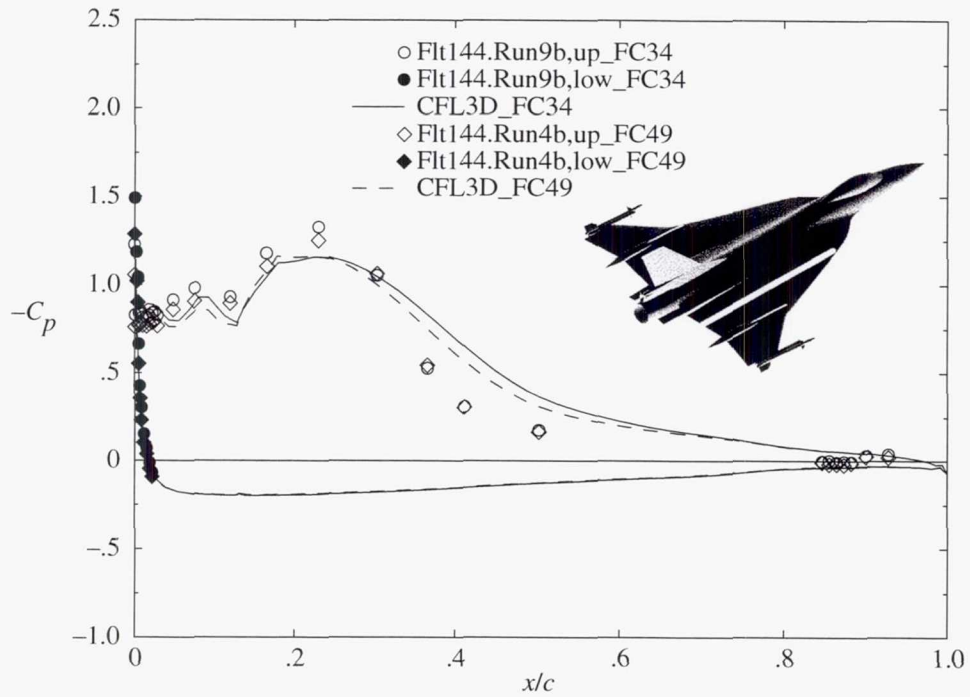


(a) BL 55.

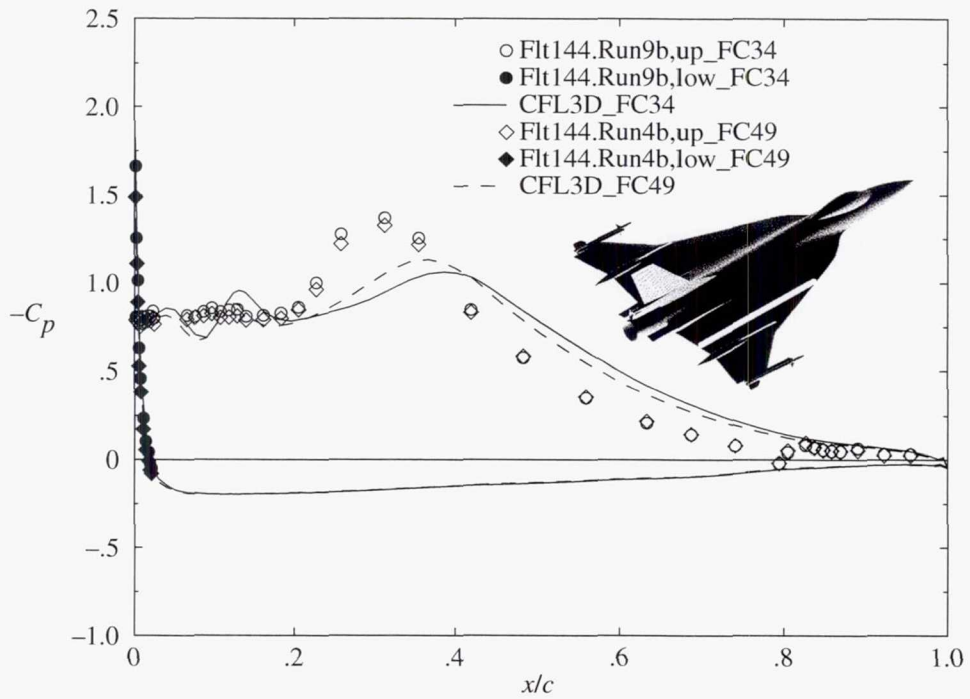


(b) BL 70.

Figure 20. Predicted and measured flight C_p distribution on F-16XL-1 airplane at $\alpha_{nom} = 13^\circ$ for FC 34 ($\alpha = 13.5^\circ$; $M_\infty = 0.37$; $R_n = 40.05 \times 10^6$) and FC 49 ($\alpha = 13.0^\circ$; $M_\infty = 0.44$; $R_n = 38.97 \times 10^6$).

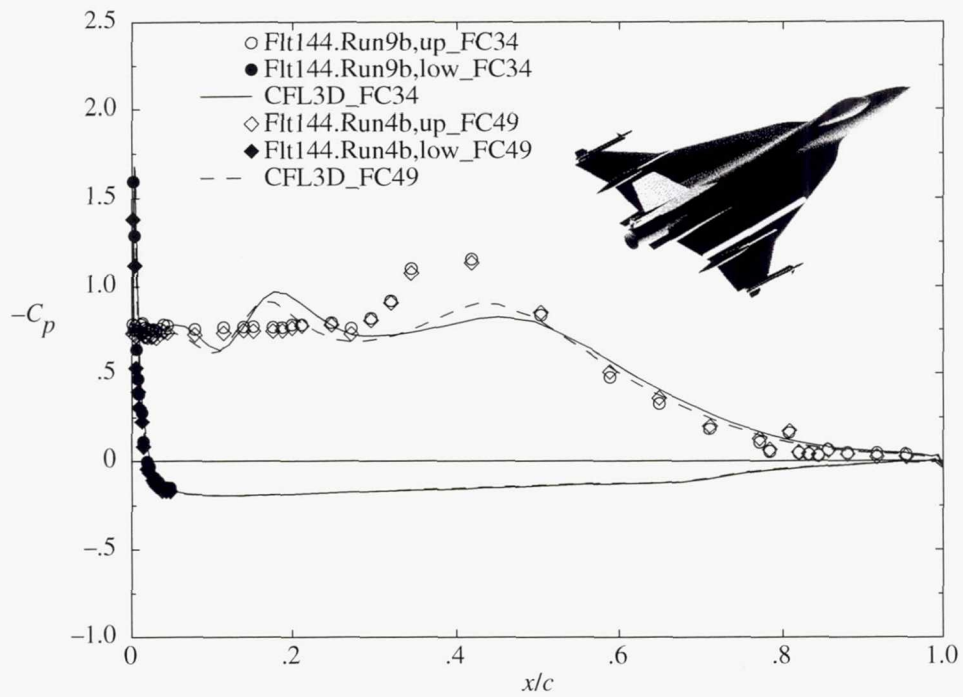


(c) BL 80.

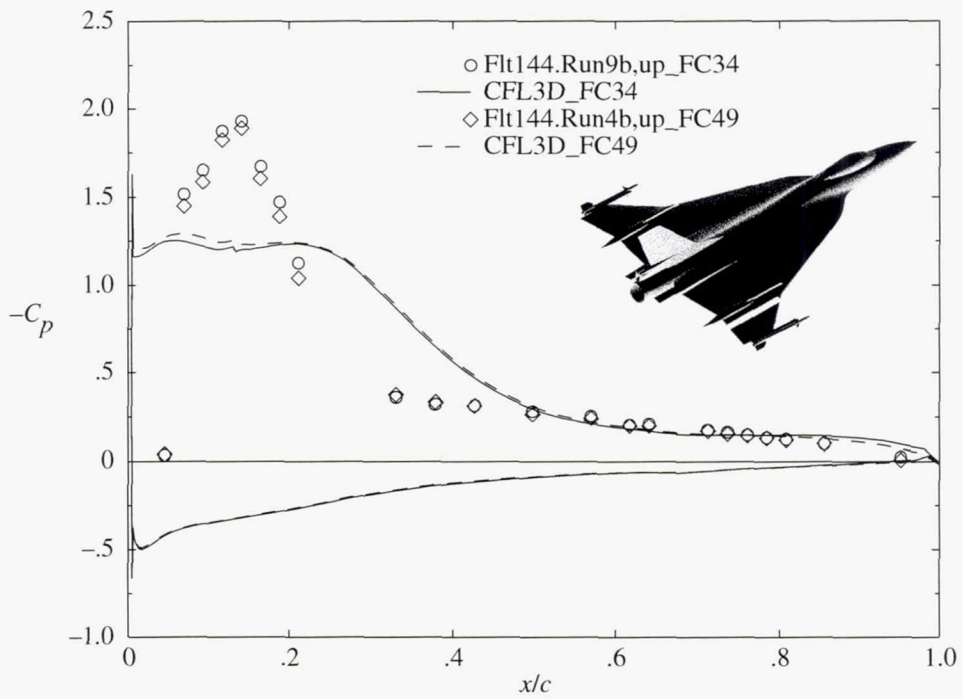


(d) BL 95.

Figure 20. Continued.

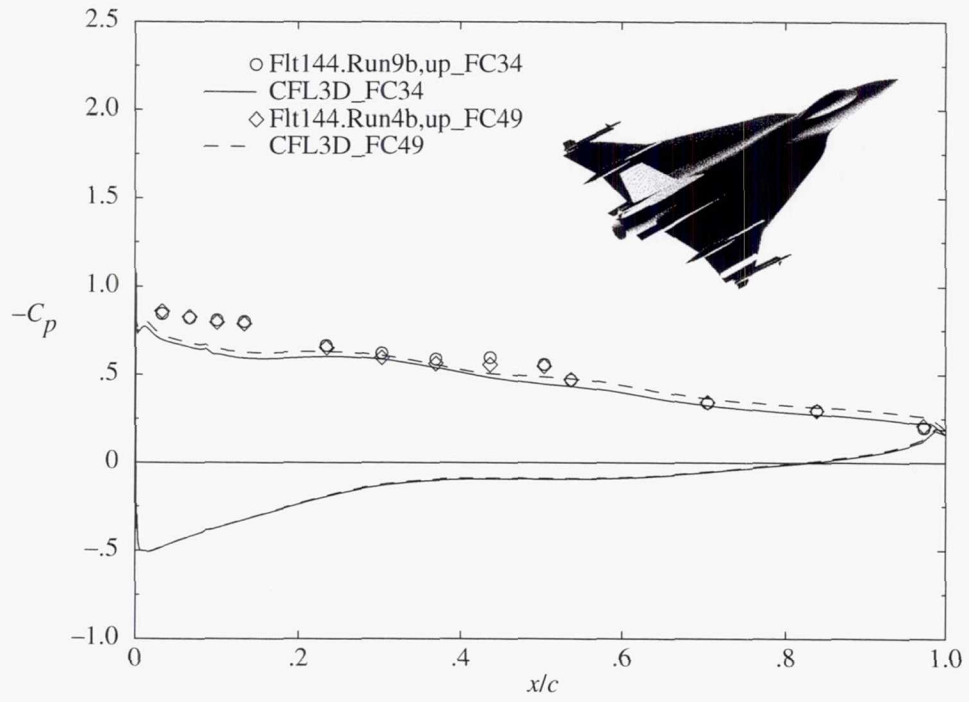


(e) BL 105.

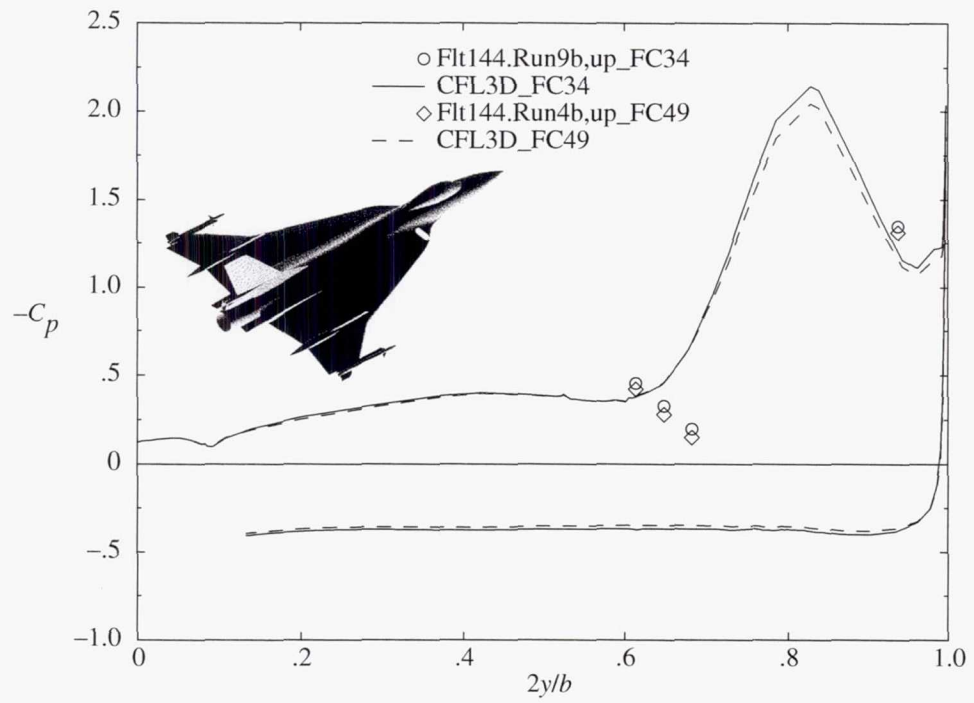


(f) BL 153.5.

Figure 20. Continued.

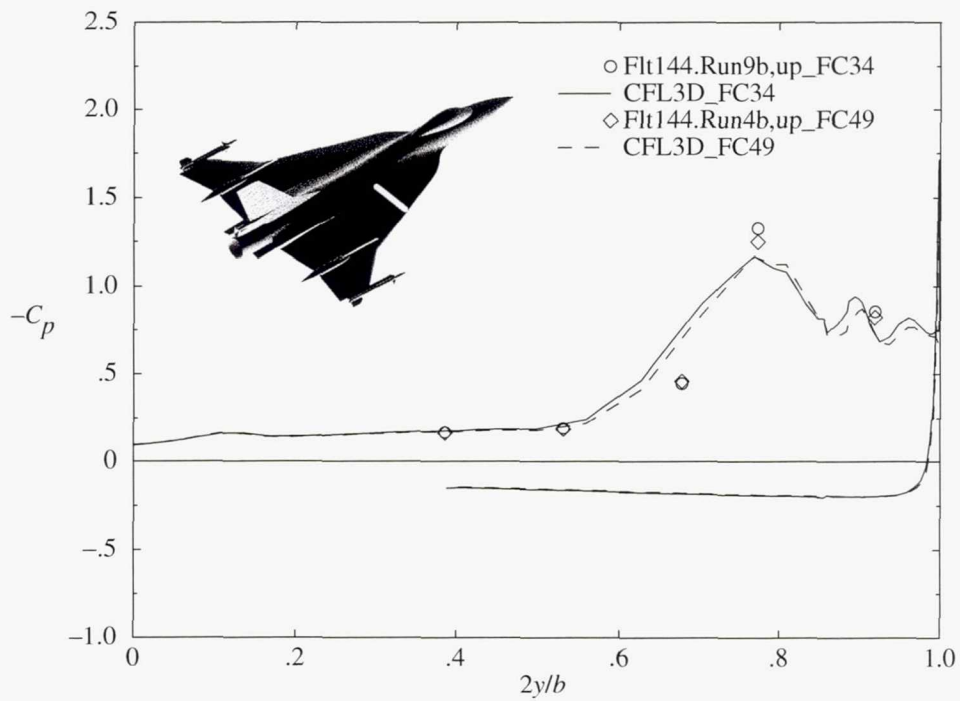


(g) BL 184.5.

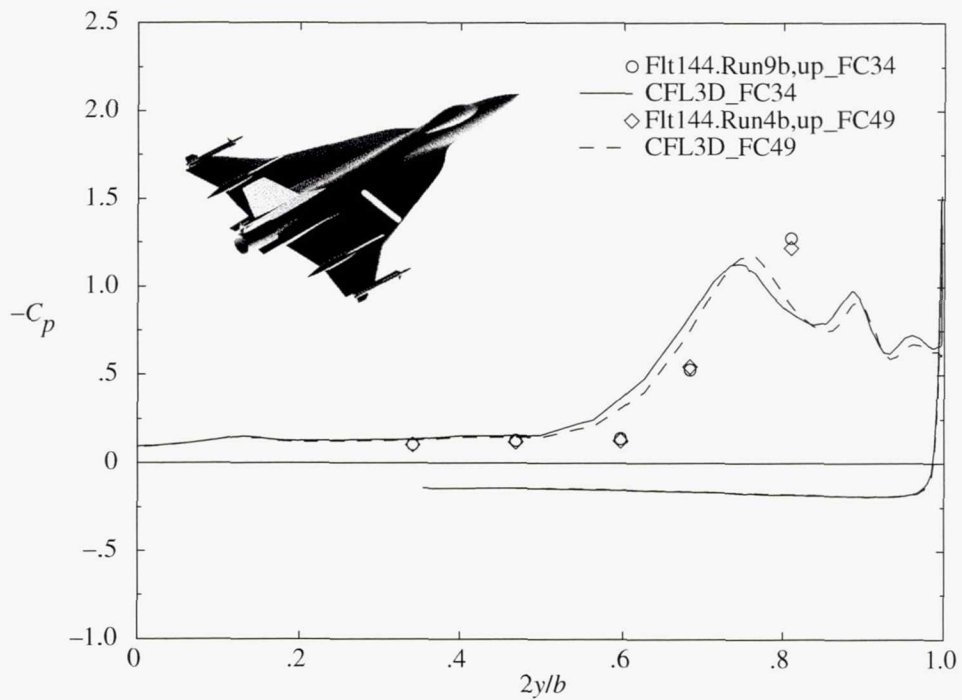


(h) FS 185.

Figure 20. Continued.

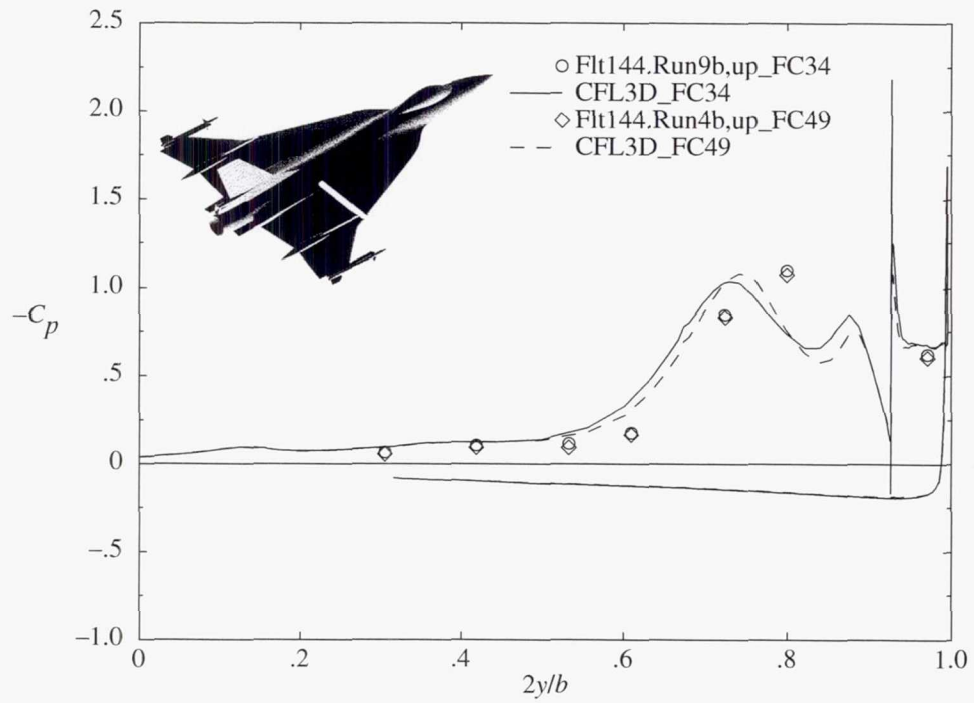


(i) FS 300.

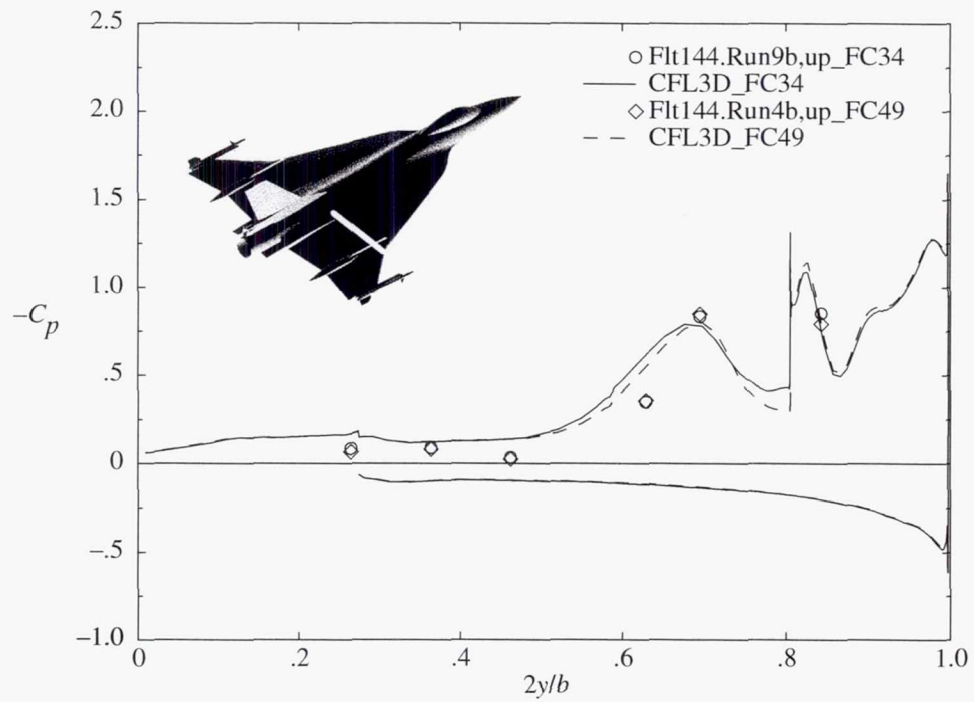


(j) FS 337.5.

Figure 20. Continued.

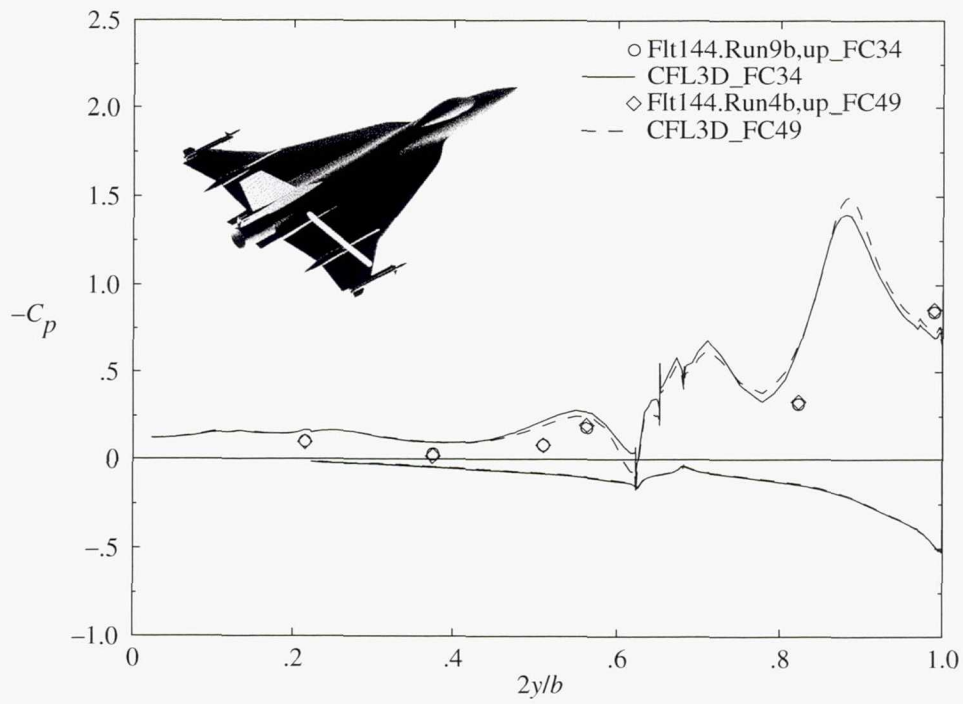


(k) FS 375.

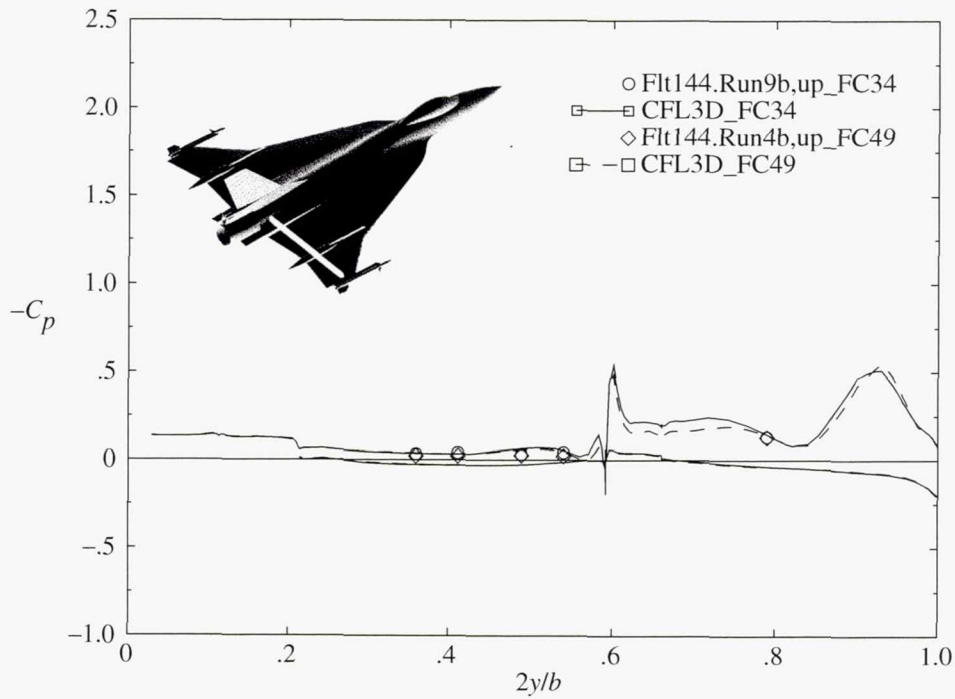


(l) FS 407.5.

Figure 20. Continued.

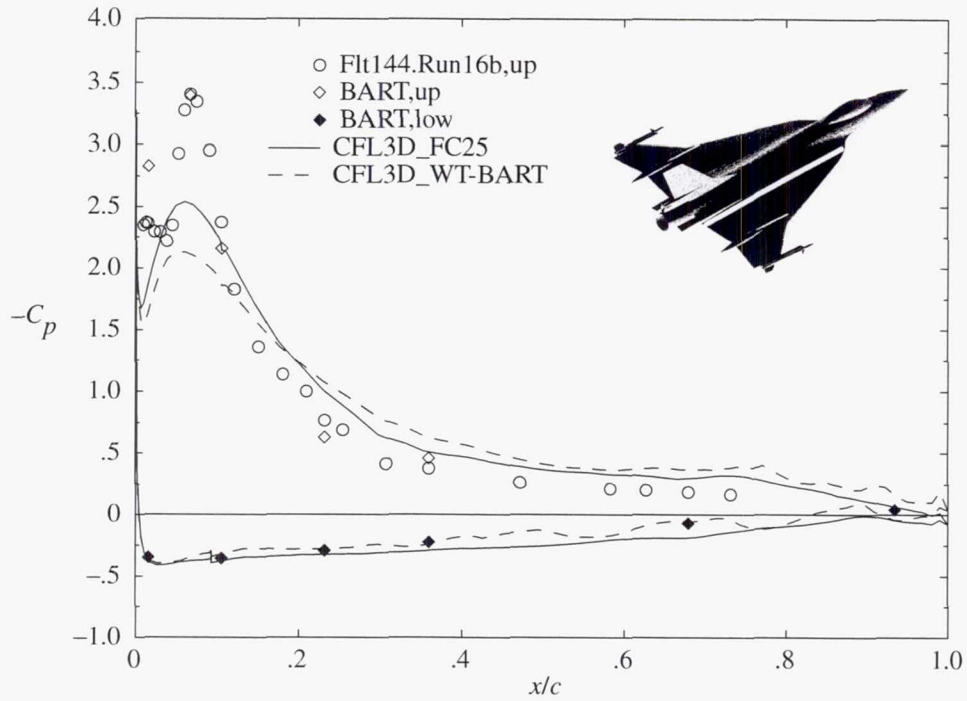


(m) FS 450.

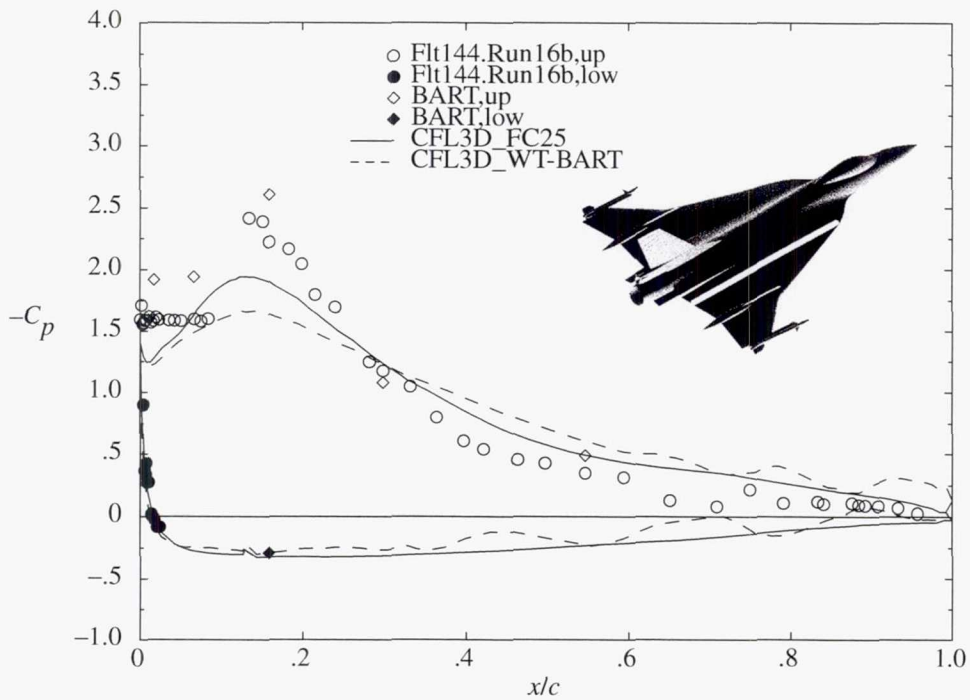


(n) FS 492.5.

Figure 20. Concluded.

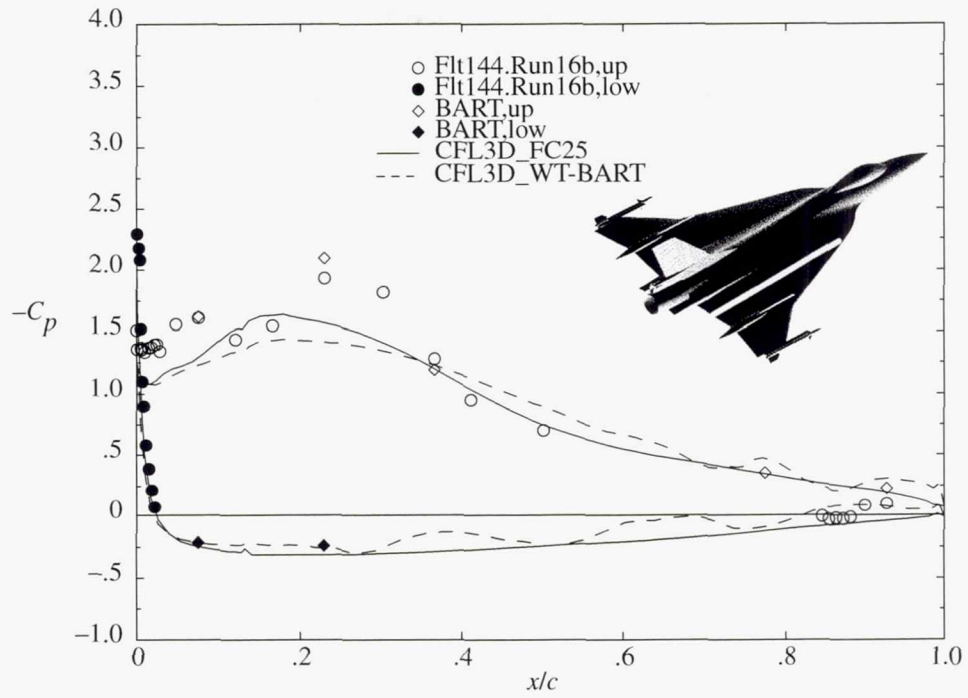


(a) BL 55.

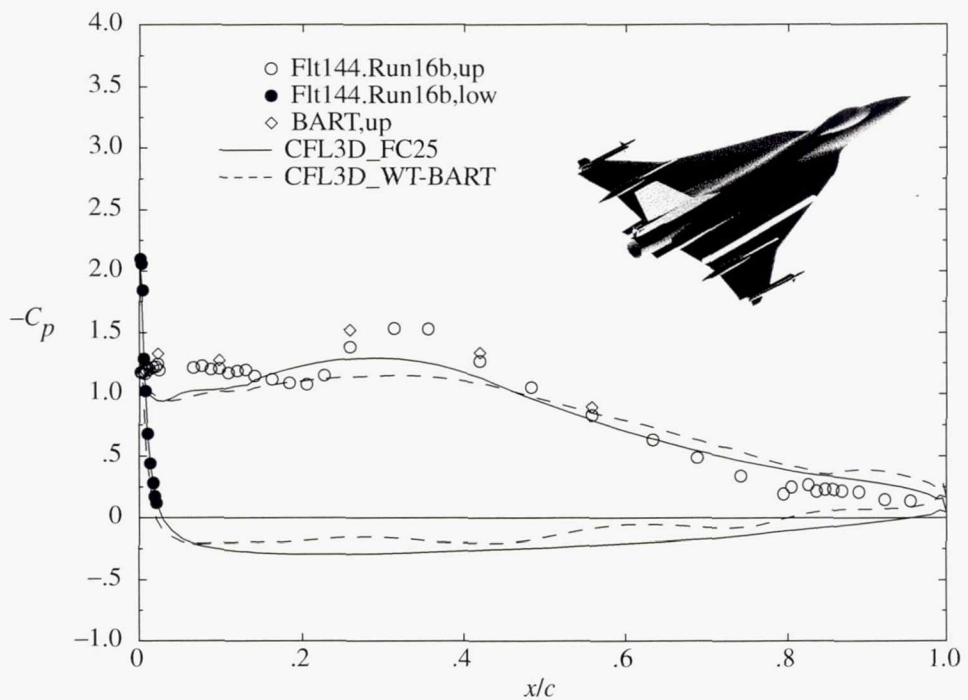


(b) BL 70.

Figure 21. Predicted and measured flight and WT C_p distributions on F-16XL-1 airplane at $\alpha_{nom} = 20^\circ$ for FC 25 ($\alpha = 19.8^\circ$; $M_\infty = 0.24$; $R_n = 32.22 \times 10^6$), BART ($\alpha = 20.0^\circ$; $M_\infty = 0.15$; $R_n = 1.06 \times 10^6$), and CFD for BART ($\alpha = 20.0^\circ$; $M_\infty = 0.10$; $R_n = 1.12 \times 10^6$).

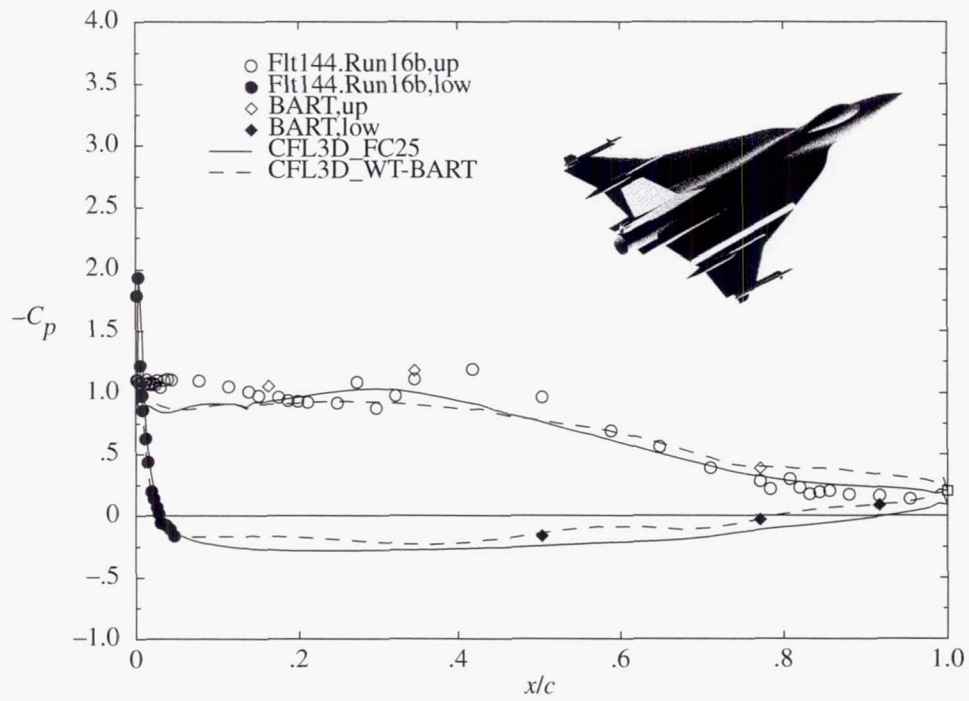


(c) BL 80.

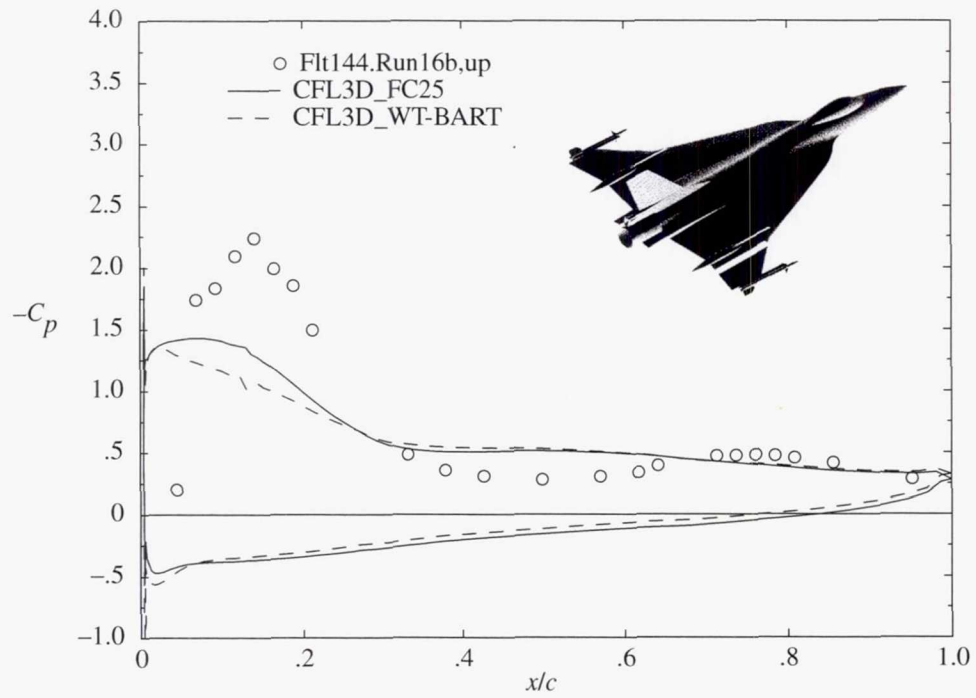


(d) BL 95.

Figure 21. Continued.

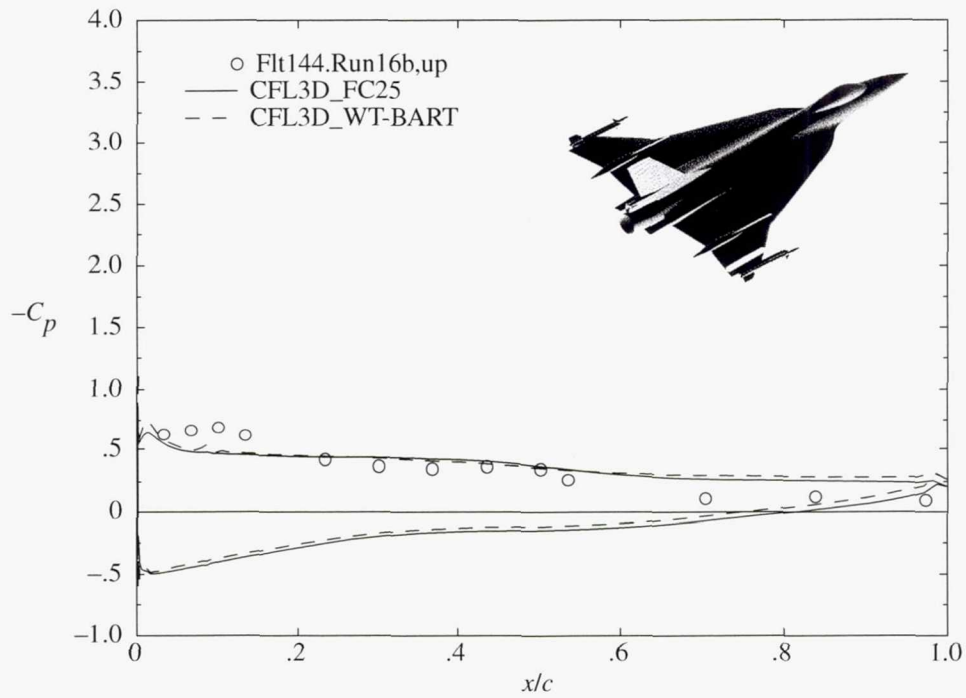


(e) BL 105.

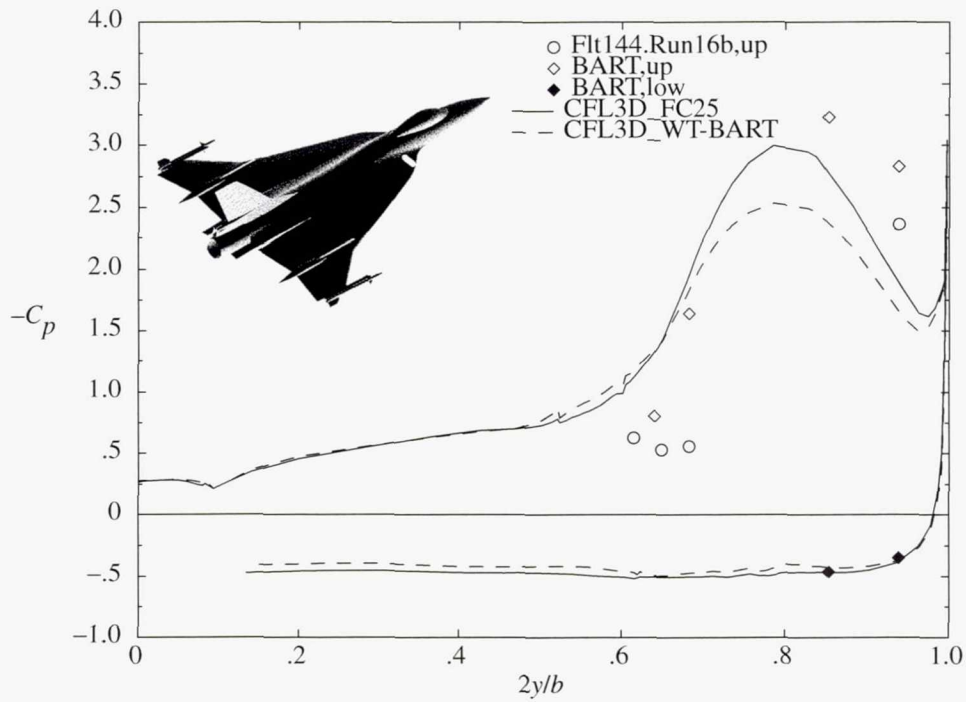


(f) BL 153.5.

Figure 21. Continued.

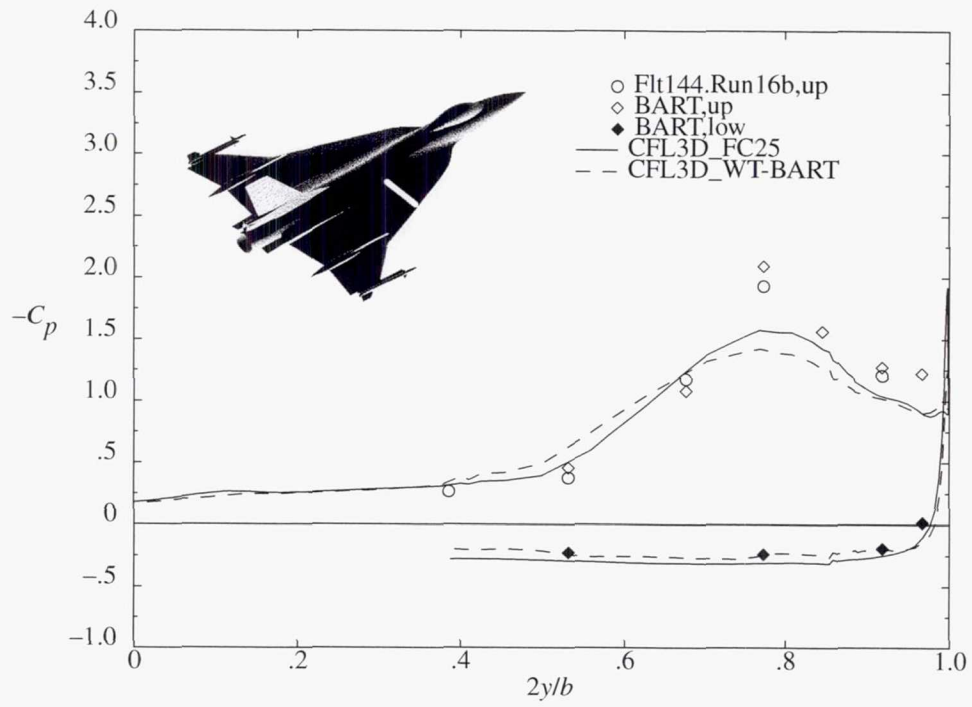


(g) BL 184.5.

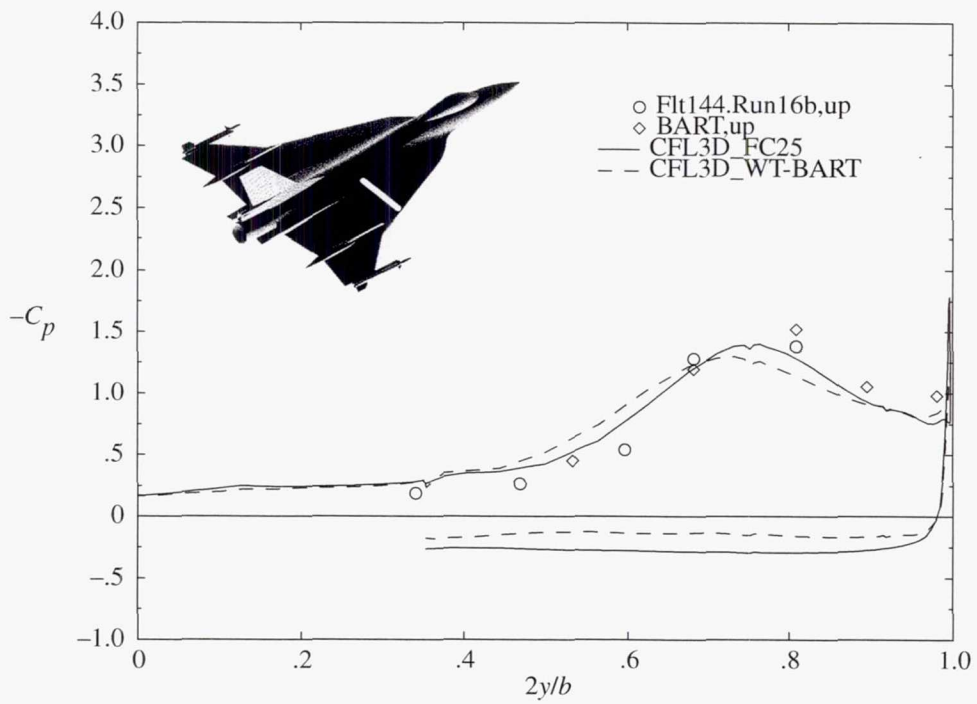


(h) FS 185.

Figure 21. Continued.

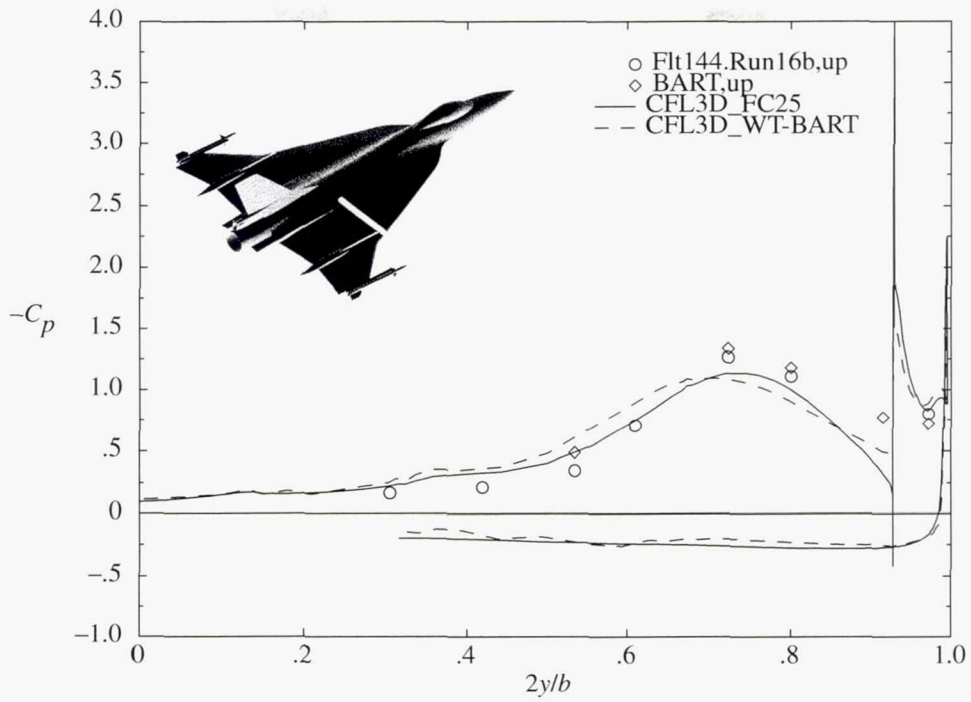


(i) FS 300.

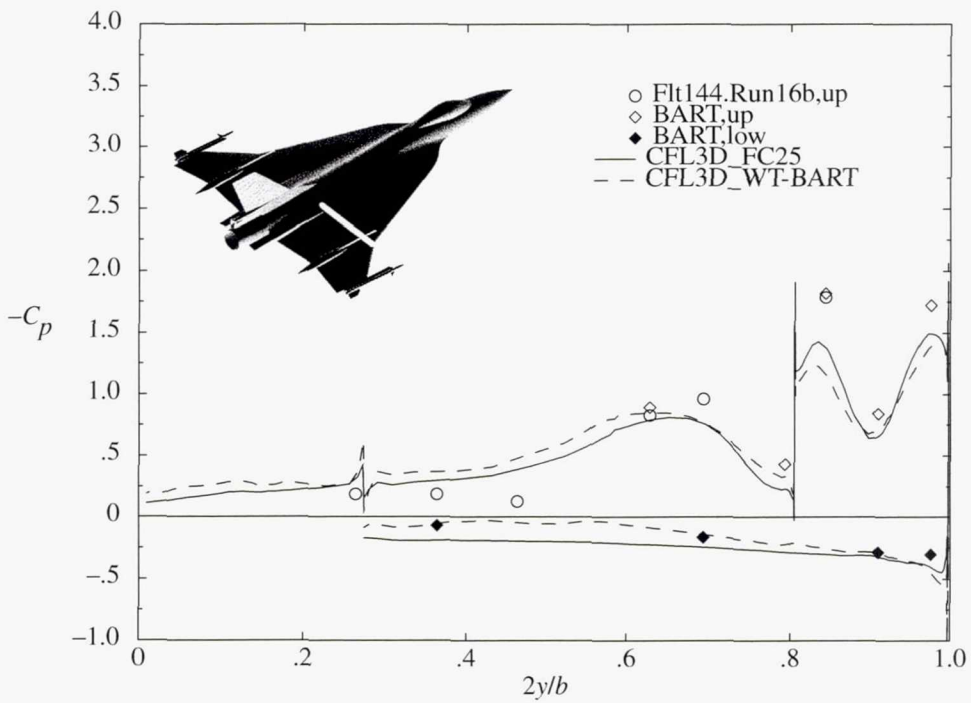


(j) FS 337.5.

Figure 21. Continued.

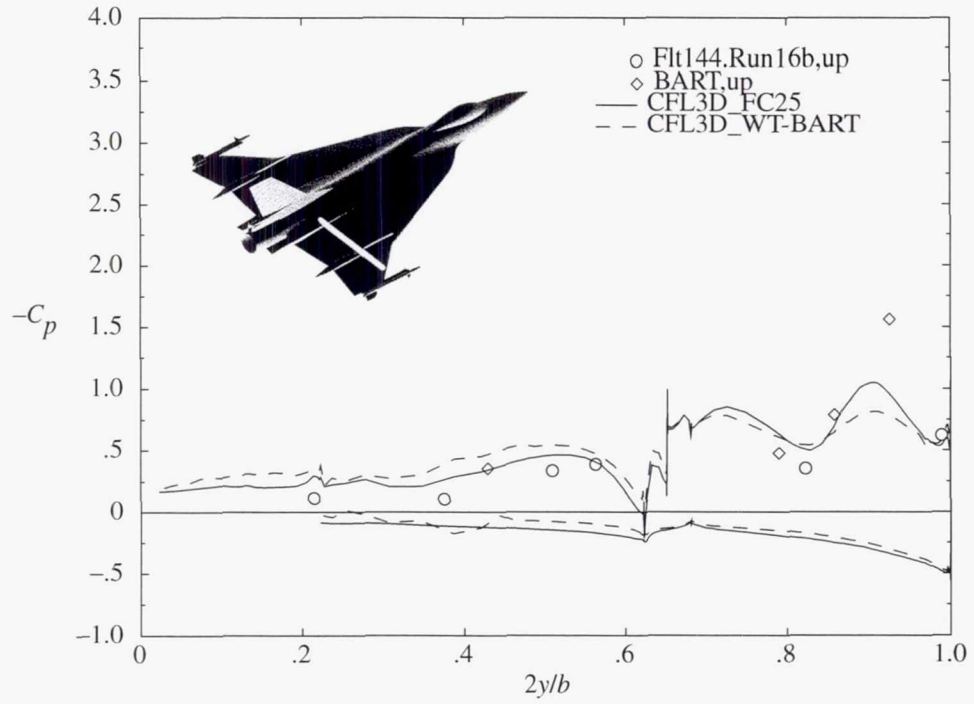


(k) FS 375.

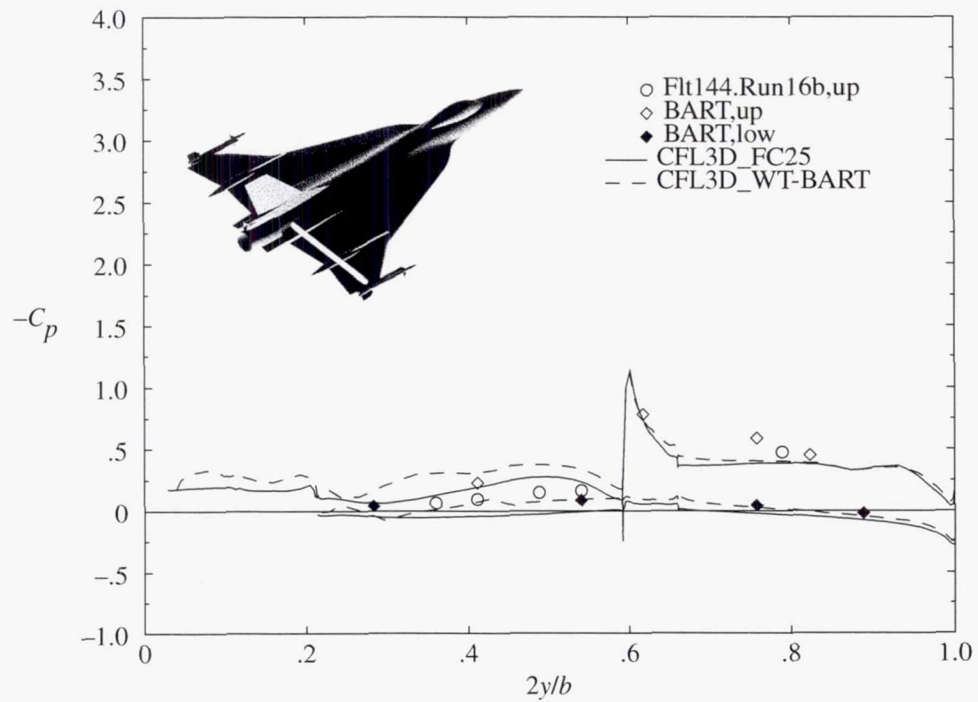


(l) FS 407.5.

Figure 21. Continued.

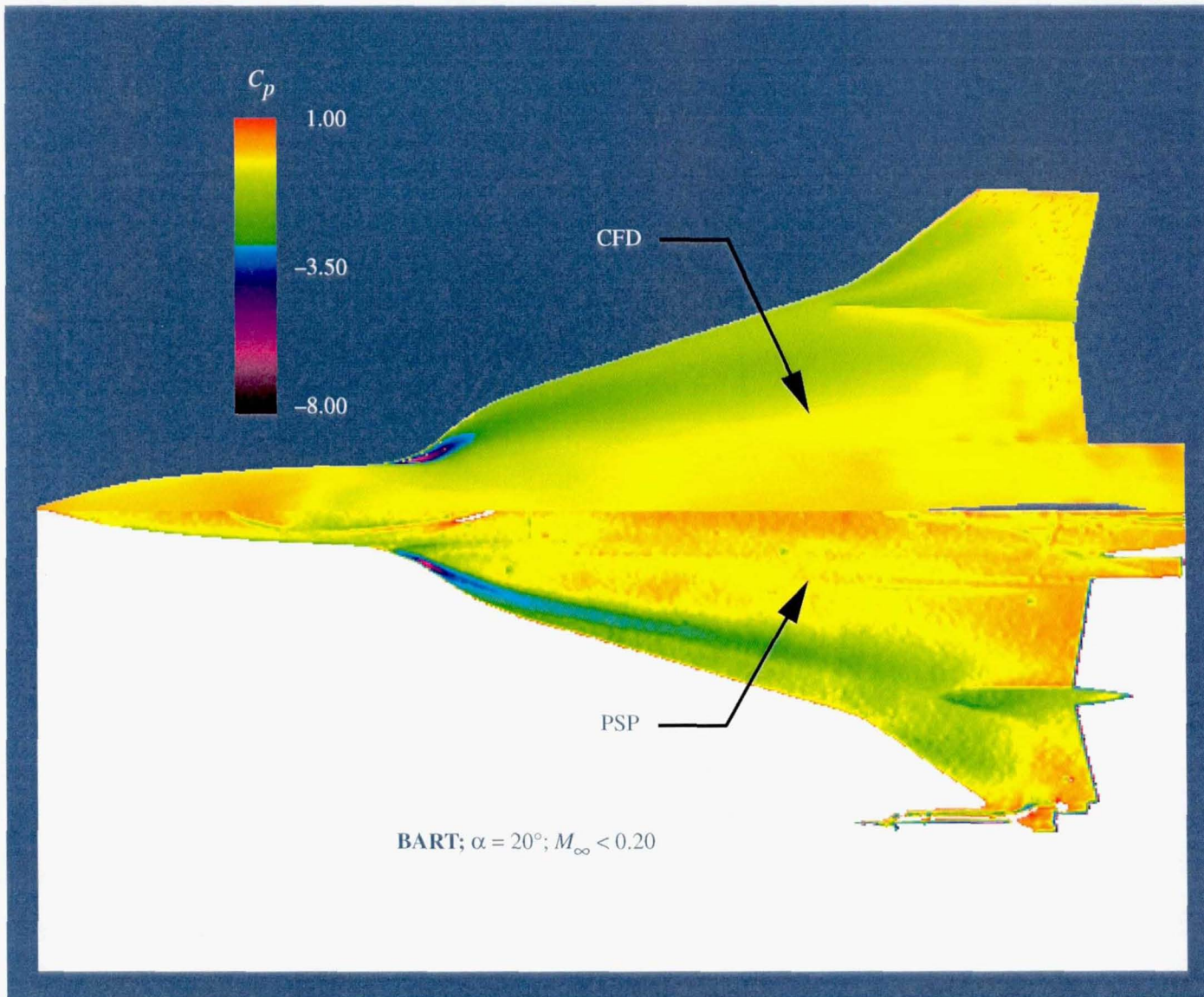


(m) FS 450.



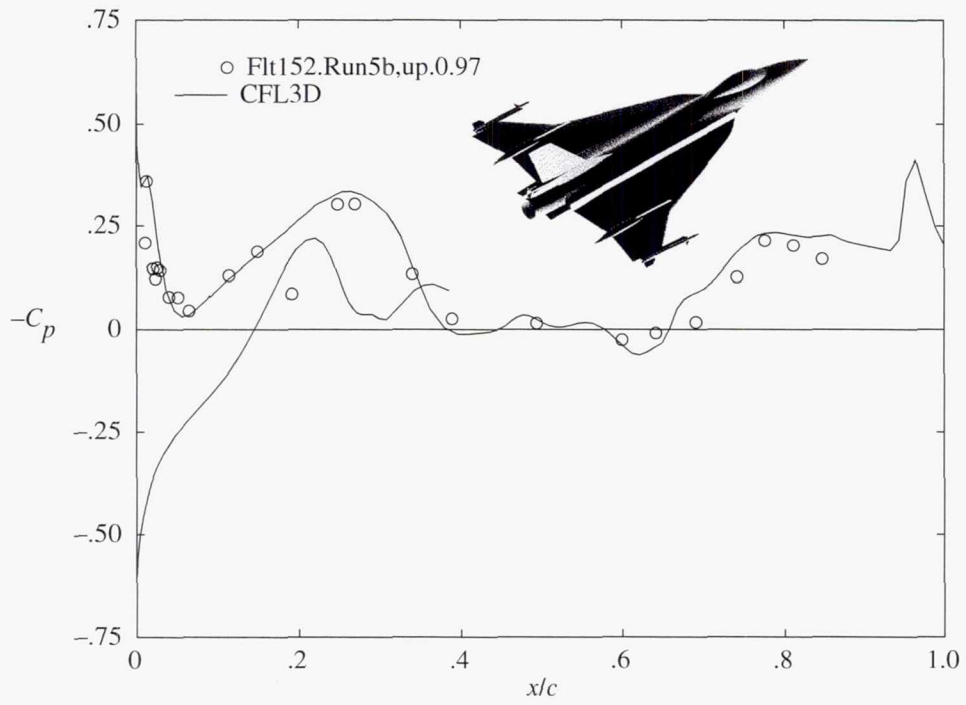
(n) FS 492.5.

Figure 21. Continued.

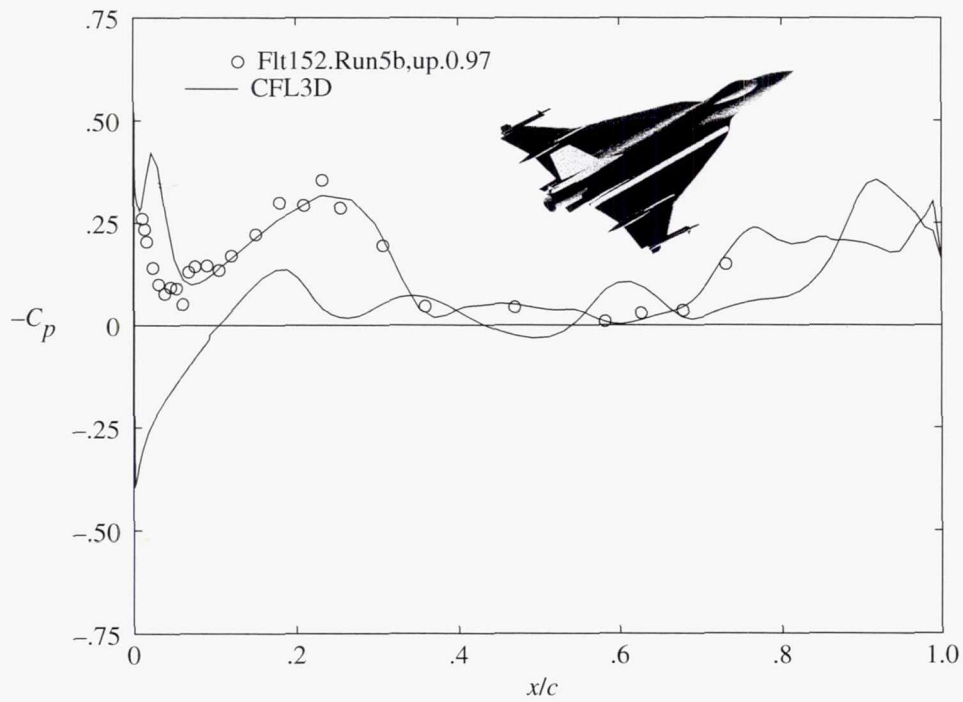


(o) Upper surface C_p distribution of BART PSP results and CFD.

Figure 21. Concluded.

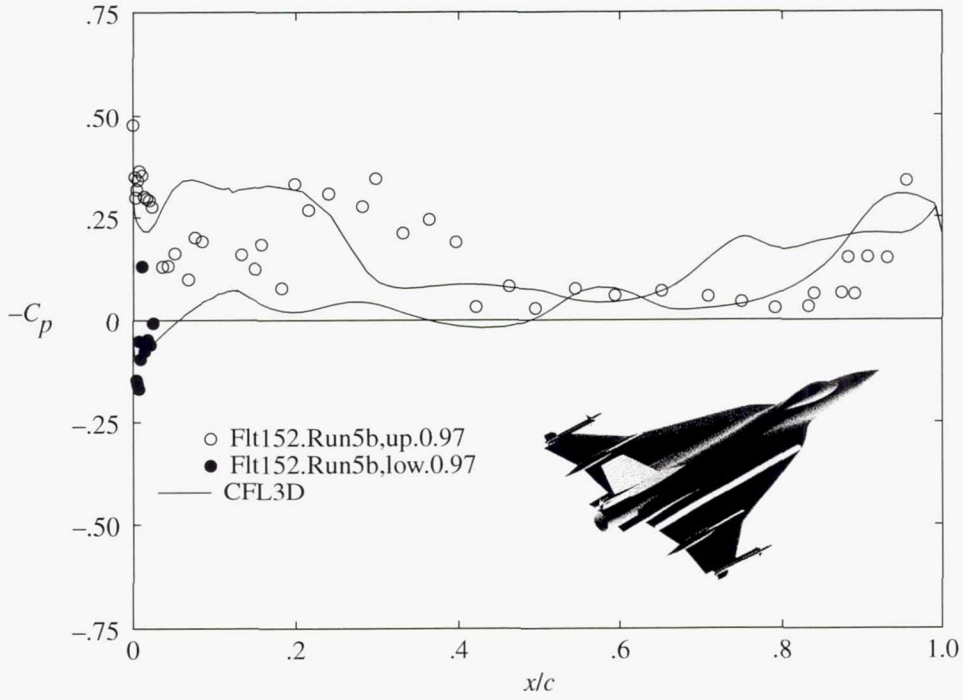


(a) BL 40.

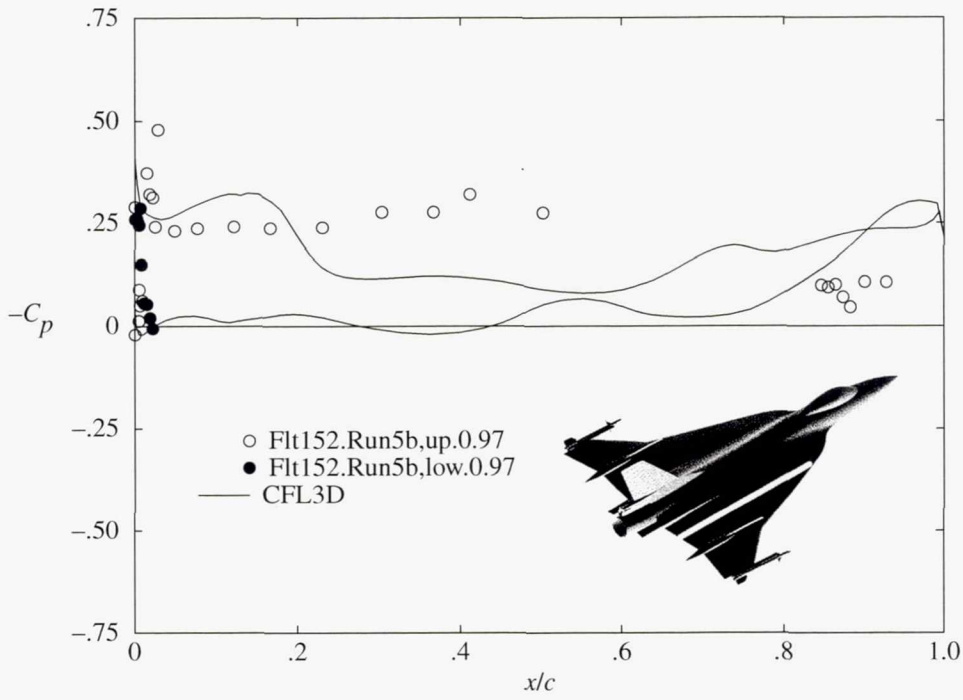


(b) BL 55.

Figure 22. Predicted and measured flight C_p distribution on F-16XL-1 airplane for FC 70 ($\alpha = 4.4^\circ$; $M_\infty = 0.97$; $R_n = 88.77 \times 10^6$).

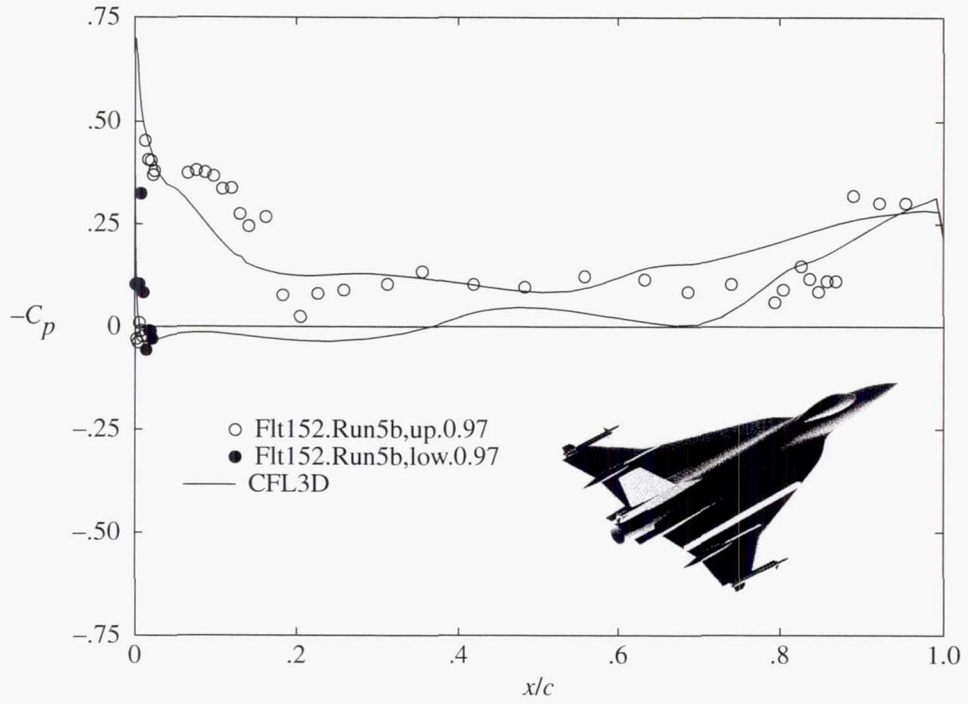


(c) BL 70.

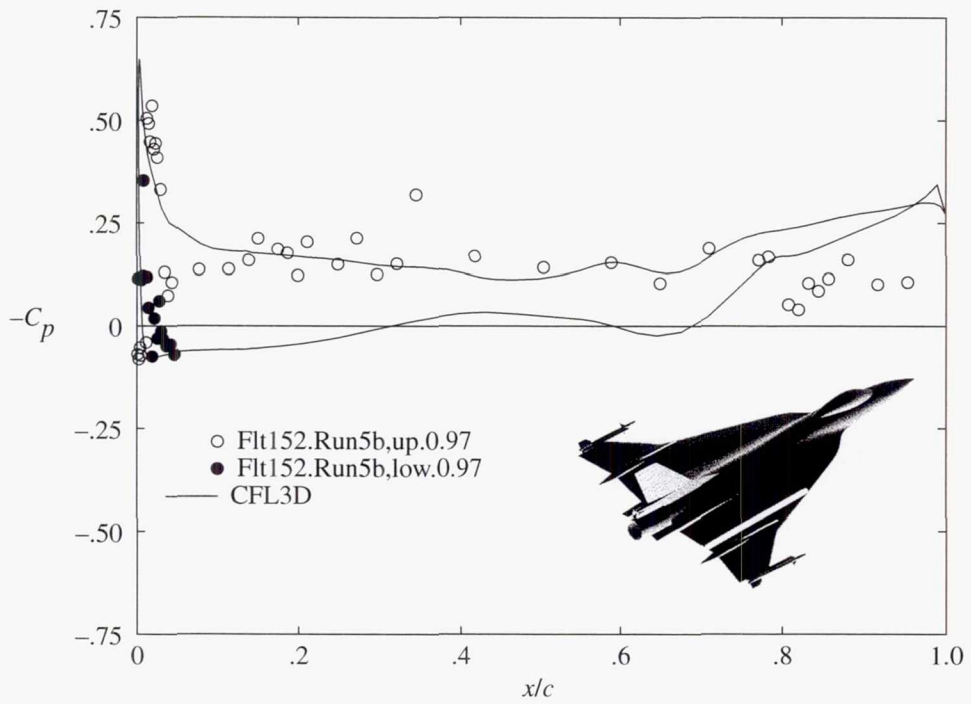


(d) BL 80.

Figure 22. Continued.

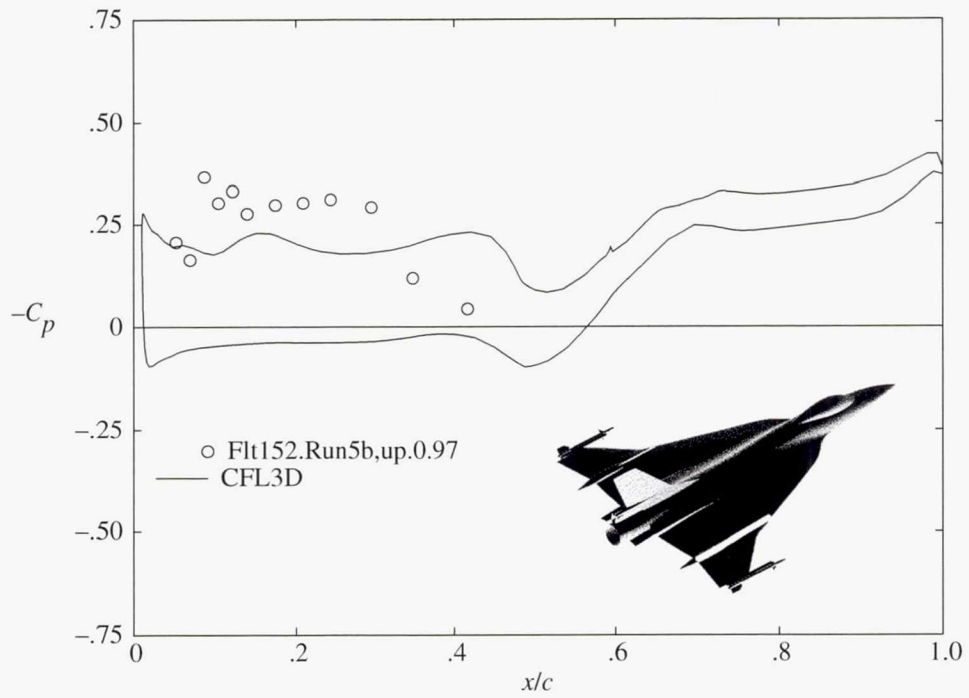


(e) BL 95.

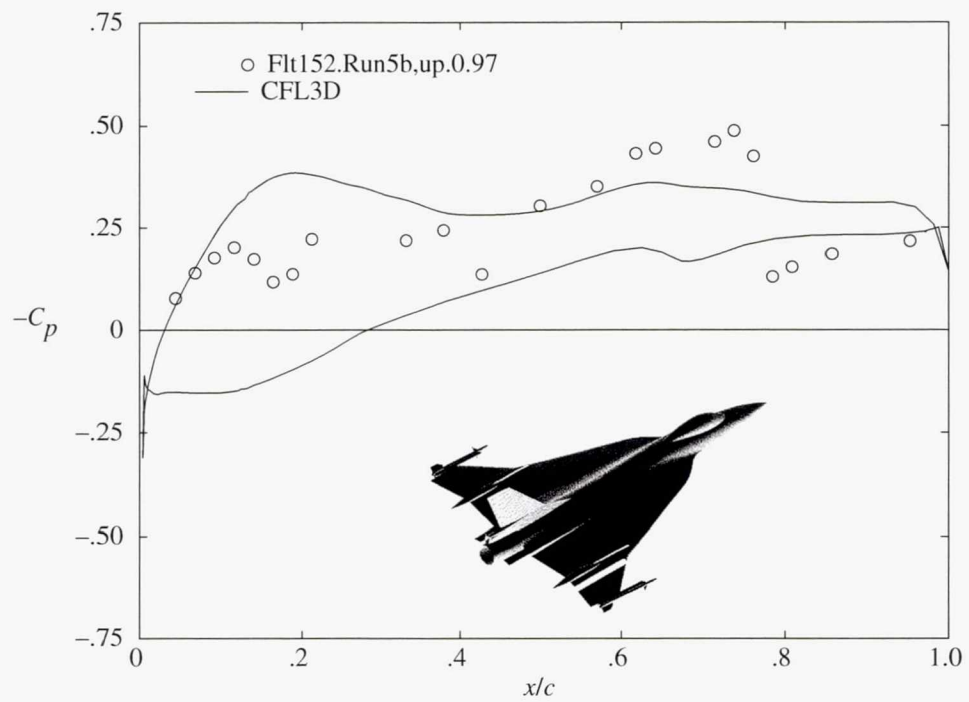


(f) BL 105.

Figure 22. Continued.

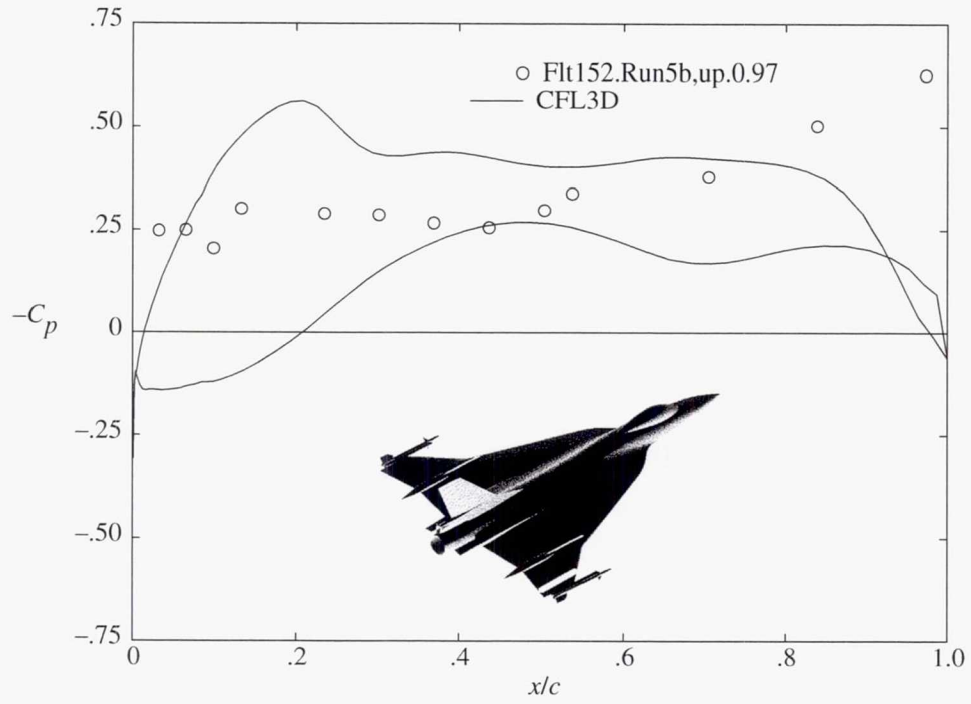


(g) BL 127.5.

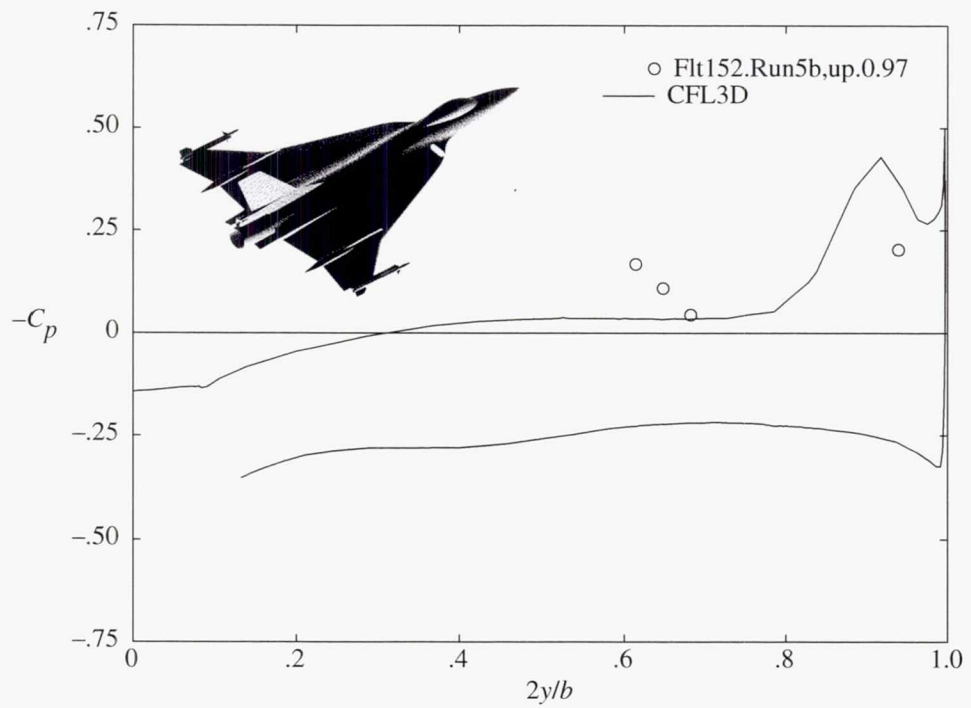


(h) BL 153.5.

Figure 22. Continued.

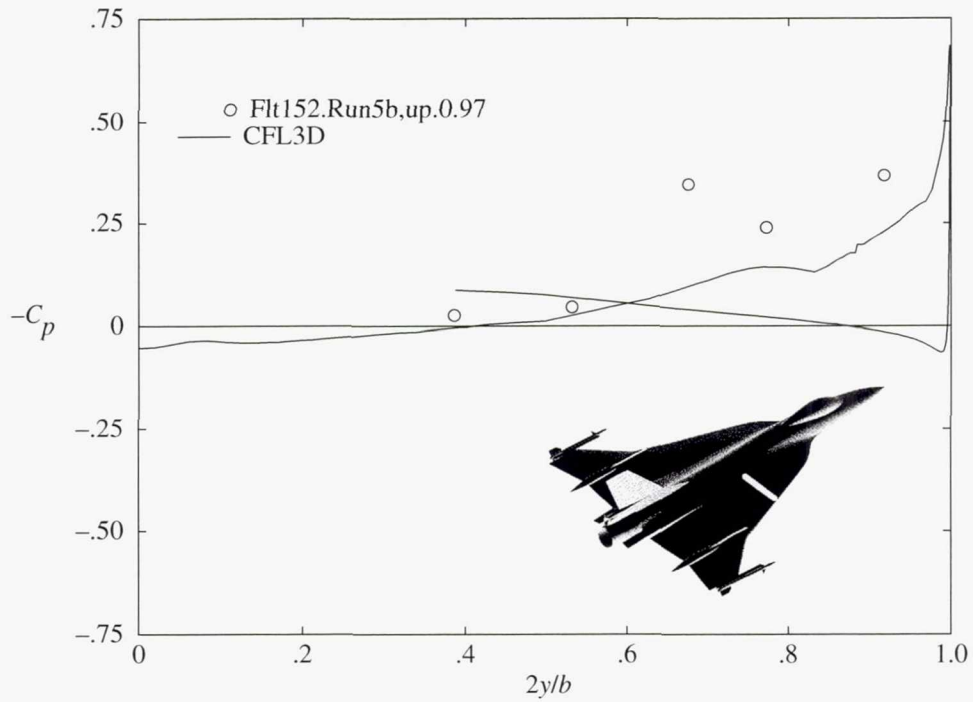


(i) BL 184.5.

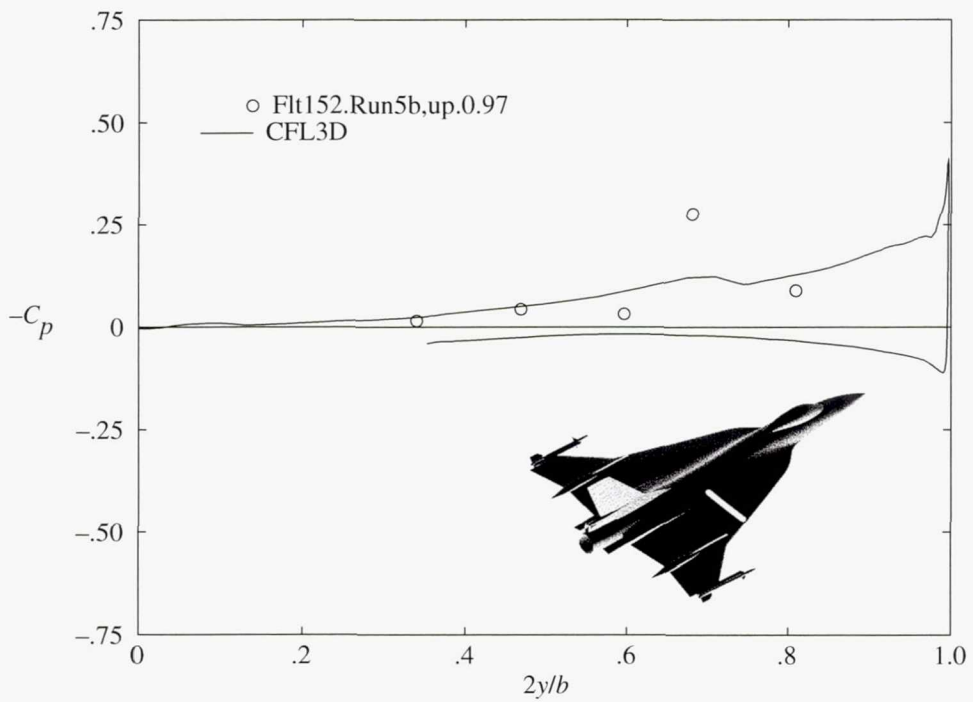


(j) FS 185.

Figure 22. Continued.

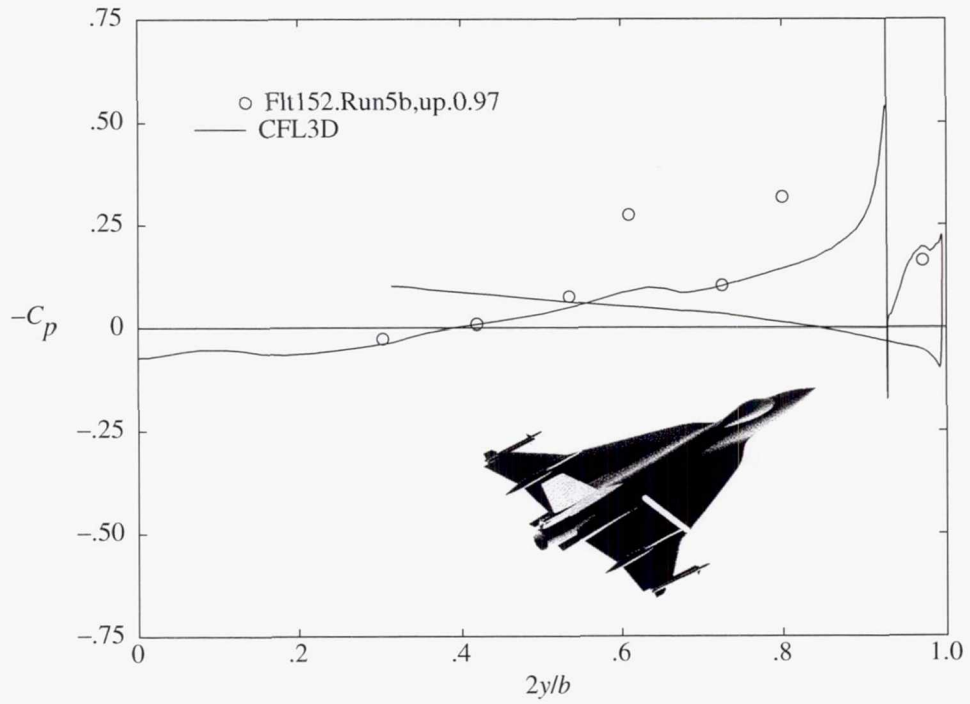


(k) FS 300.

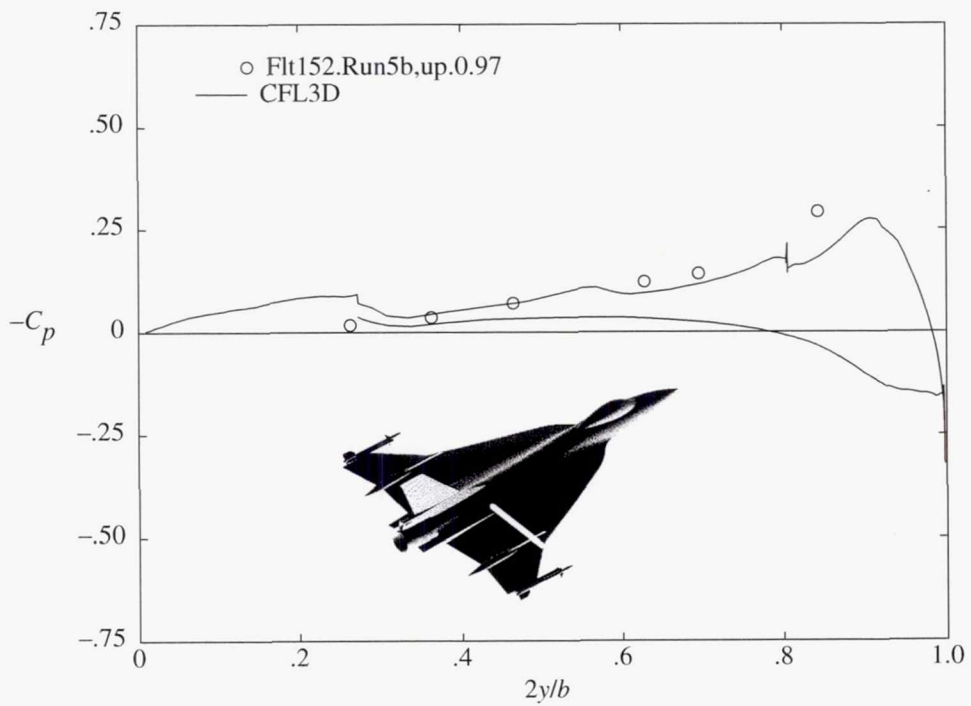


(l) FS 337.5.

Figure 22. Continued.

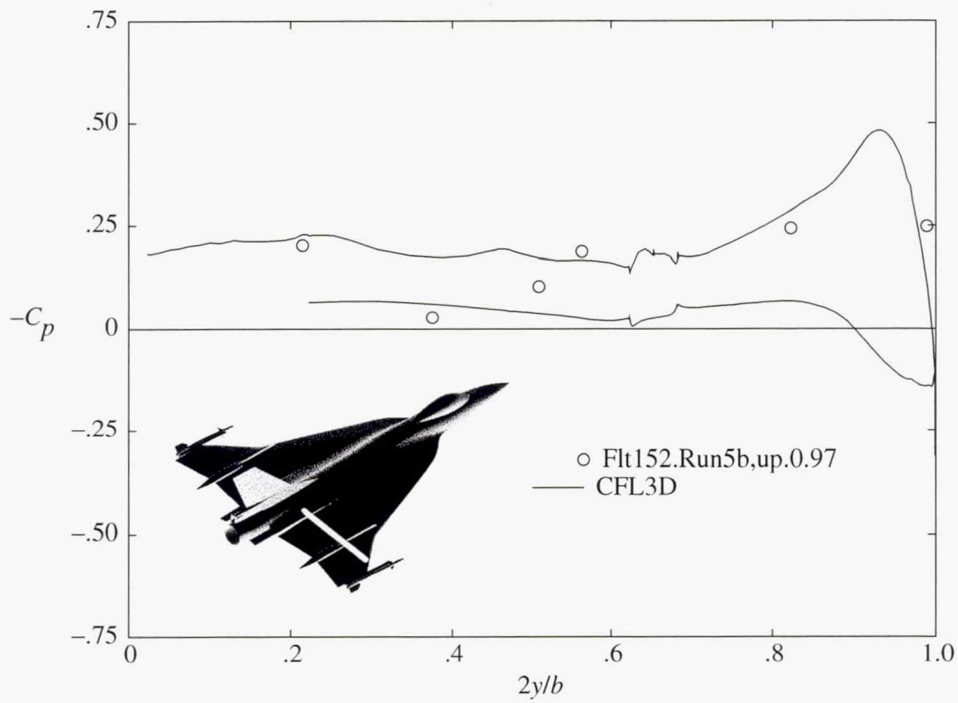


(m) FS 375.

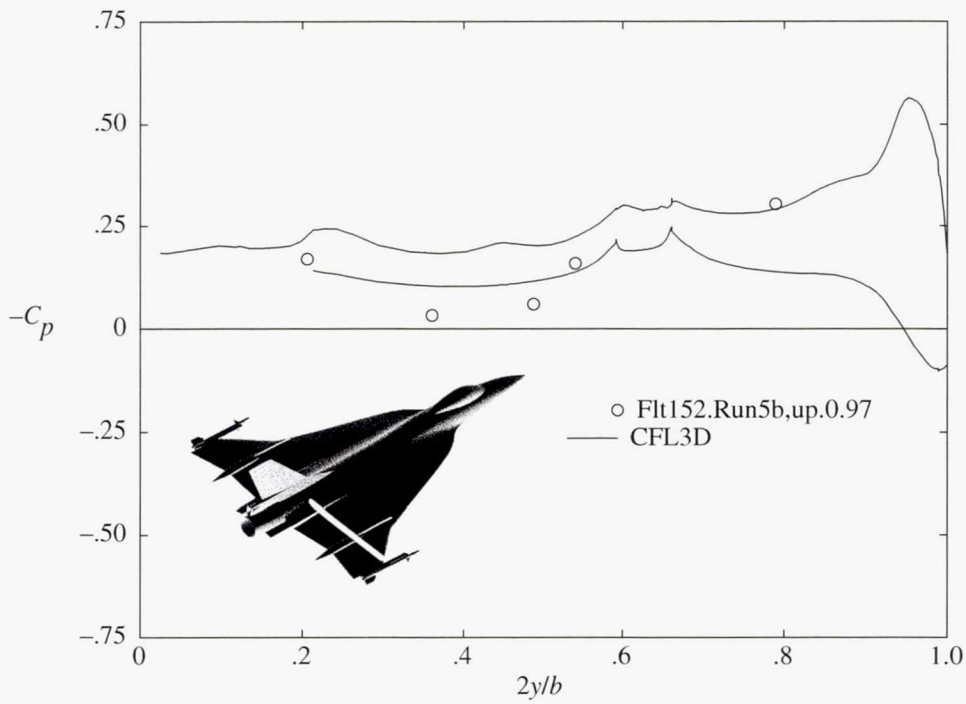


(n) FS 407.5.

Figure 22. Continued.

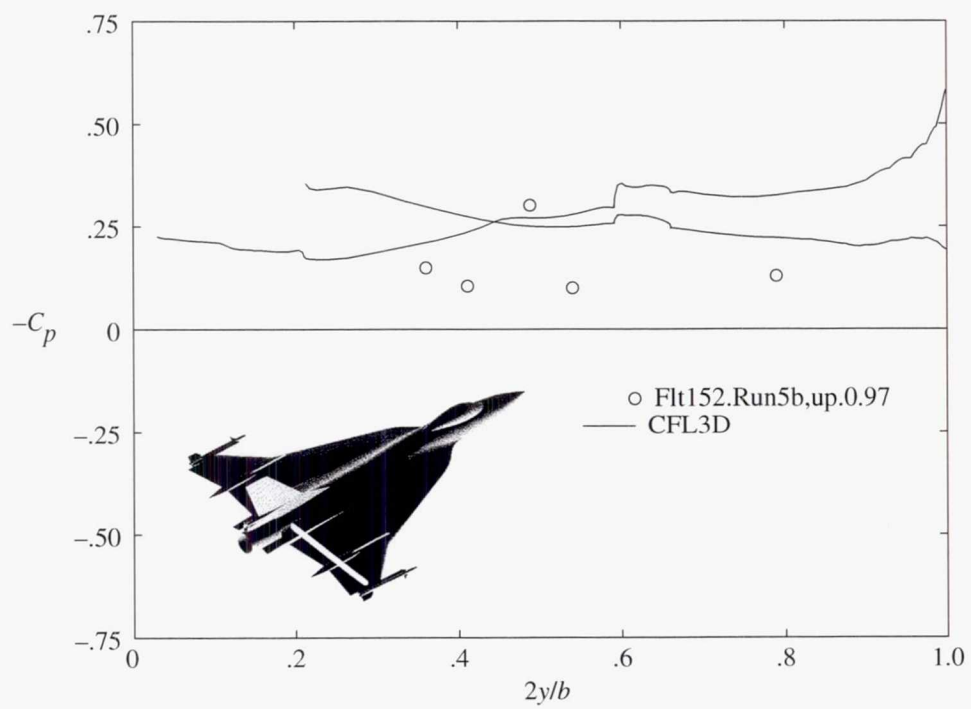


(o) FS 450.



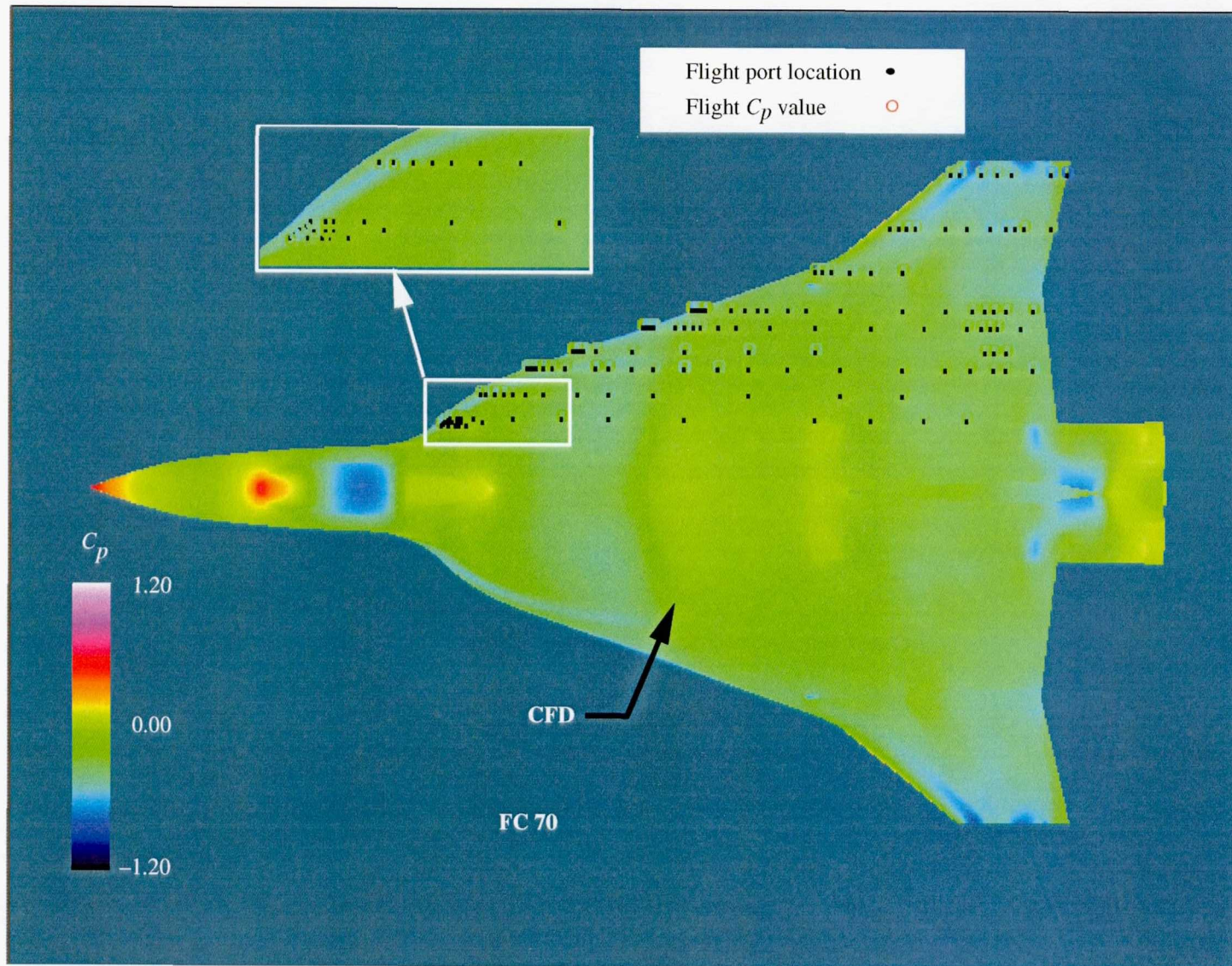
(p) FS 462.5.

Figure 22. Continued.



(q) FS 492.5.

Figure 22. Continued.



(r) Upper surface C_p distribution.

Figure 22. Concluded.

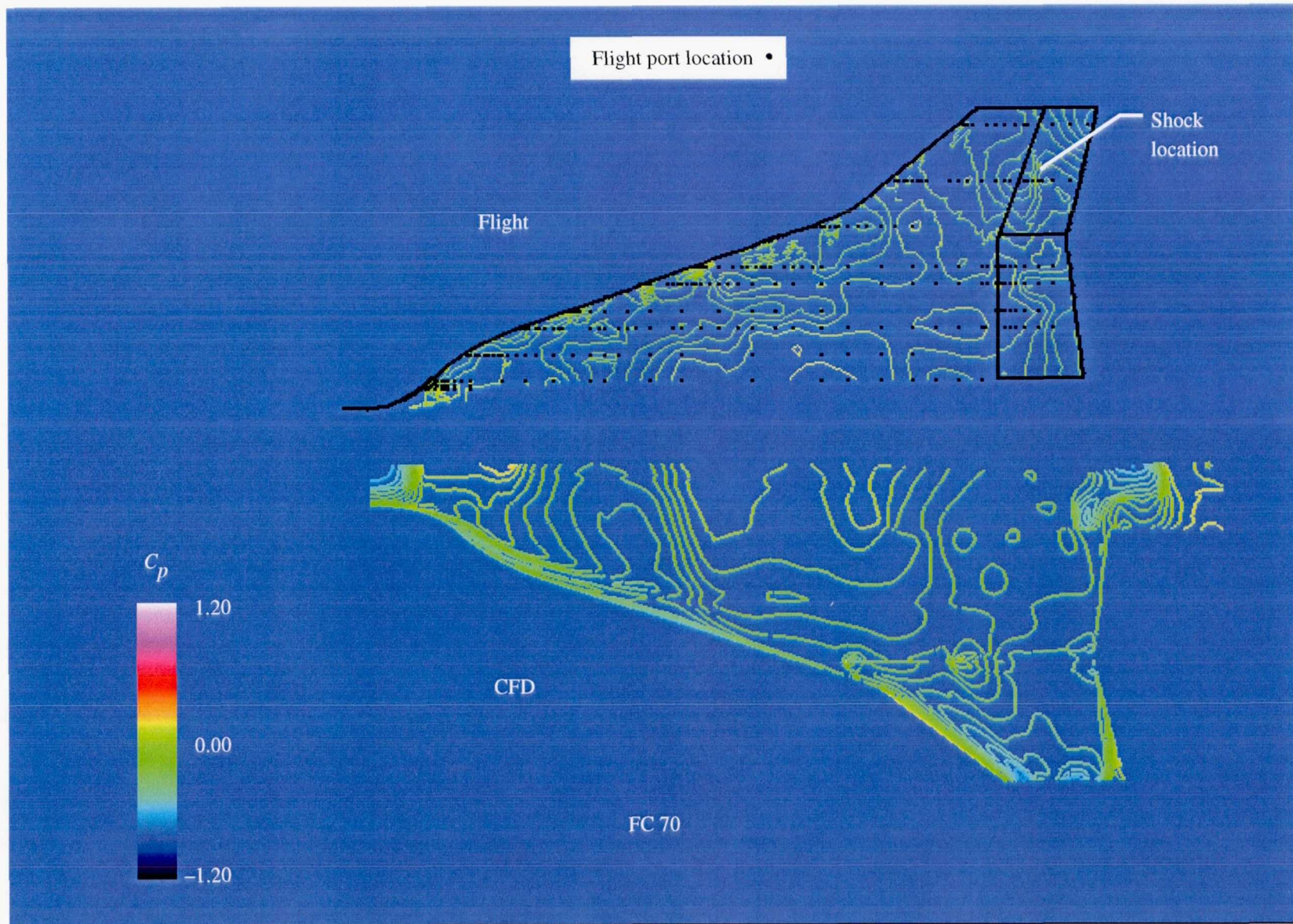
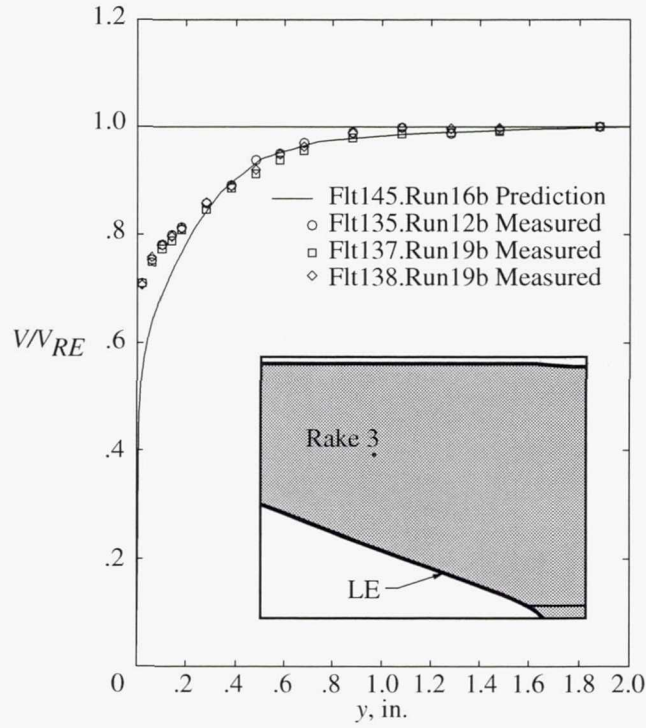
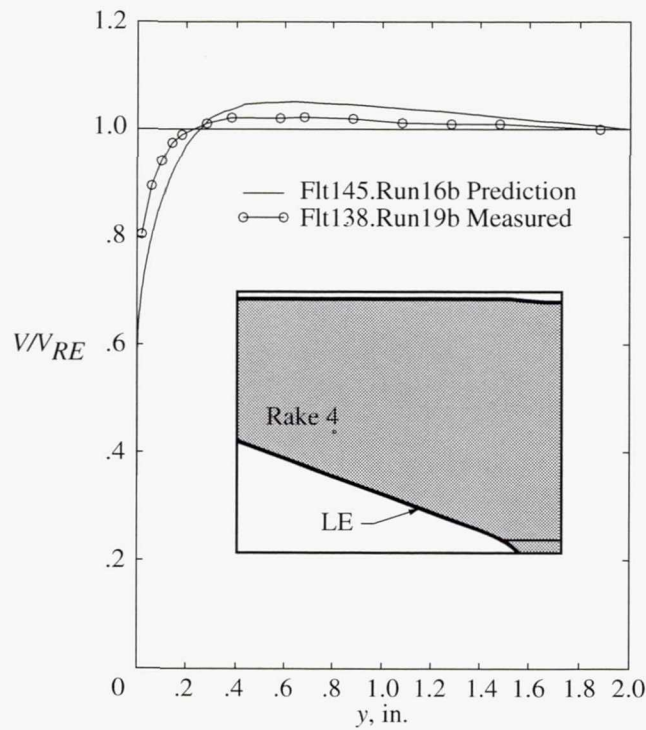


Figure 23. $C_{p,u}$ contours on F-16XL-1 airplane for FC 70 ($\alpha = 4.4^\circ$; $M_\infty = 0.97$; $R_n = 88.77 \times 10^6$).

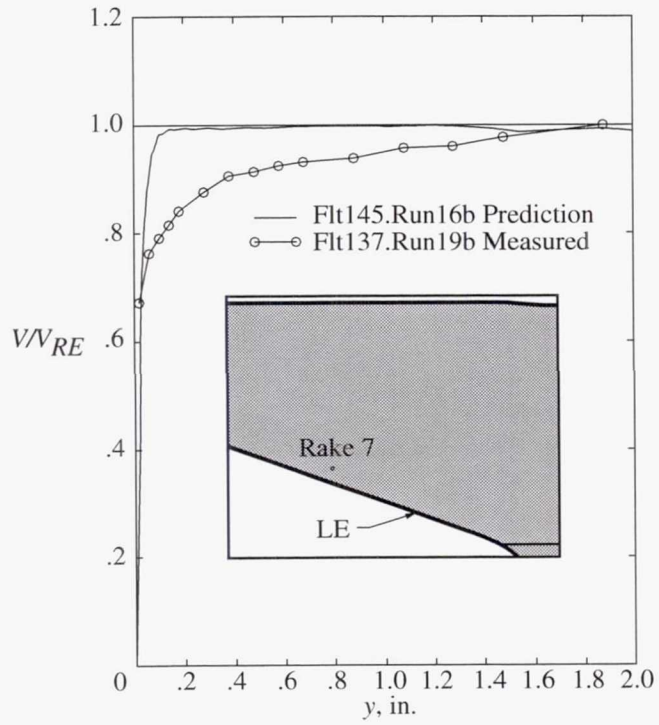


(a) Rake 3; FS 302.17, BL -52.93.

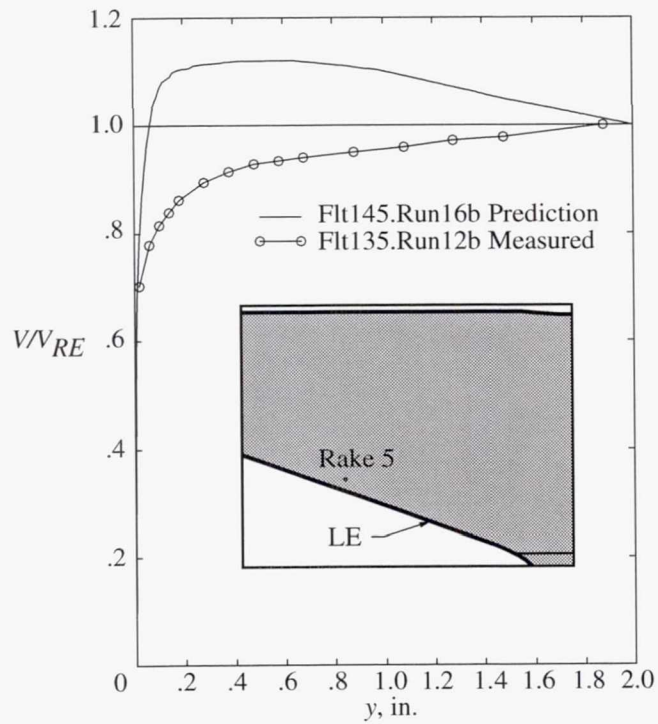


(b) Rake 4; FS 293.45, BL -76.22.

Figure 24. Predicted and measured velocity profiles for boundary-layer rakes on F-16XL-1 airplane for FC 7 ($\alpha_{nom} = 13^\circ$; $\beta_{nom} = 0^\circ$; $M_\infty = 0.29$; $h = 5000$ ft; $R_n = 44.4 \times 10^6$).

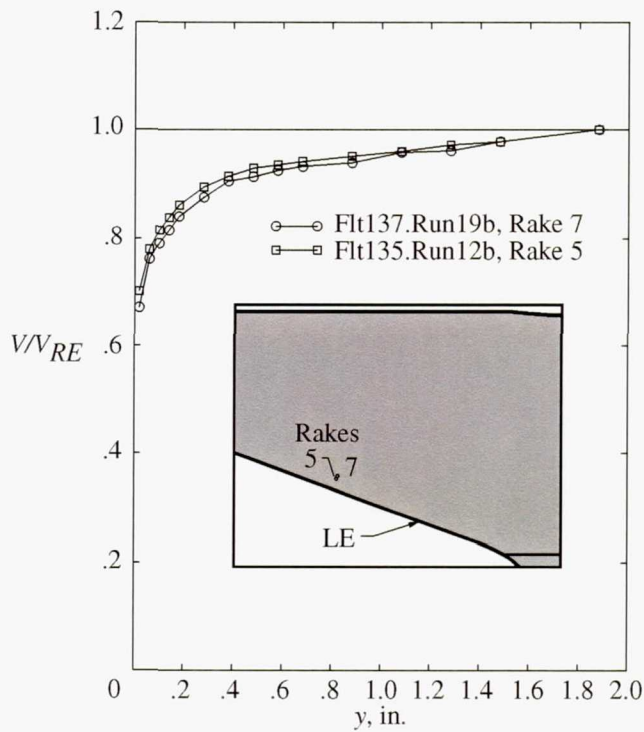


(c) Rake 7; FS 295.52, BL -94.33.

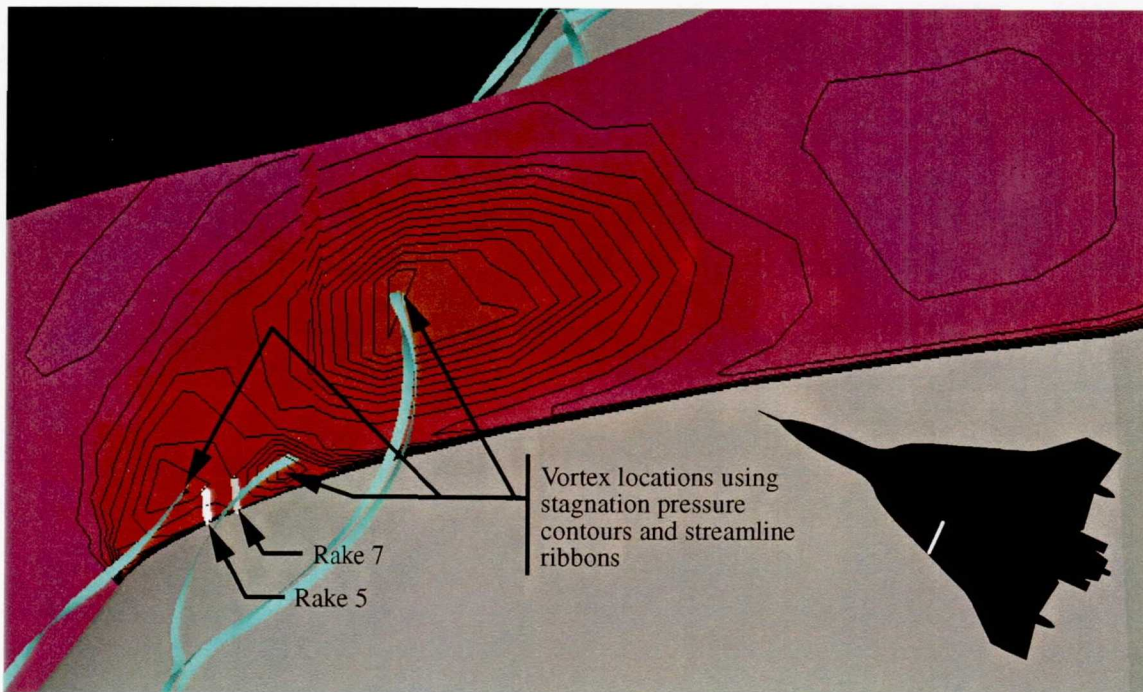


(d) Rake 5; FS 294.59, BL -96.06.

Figure 24. Concluded.

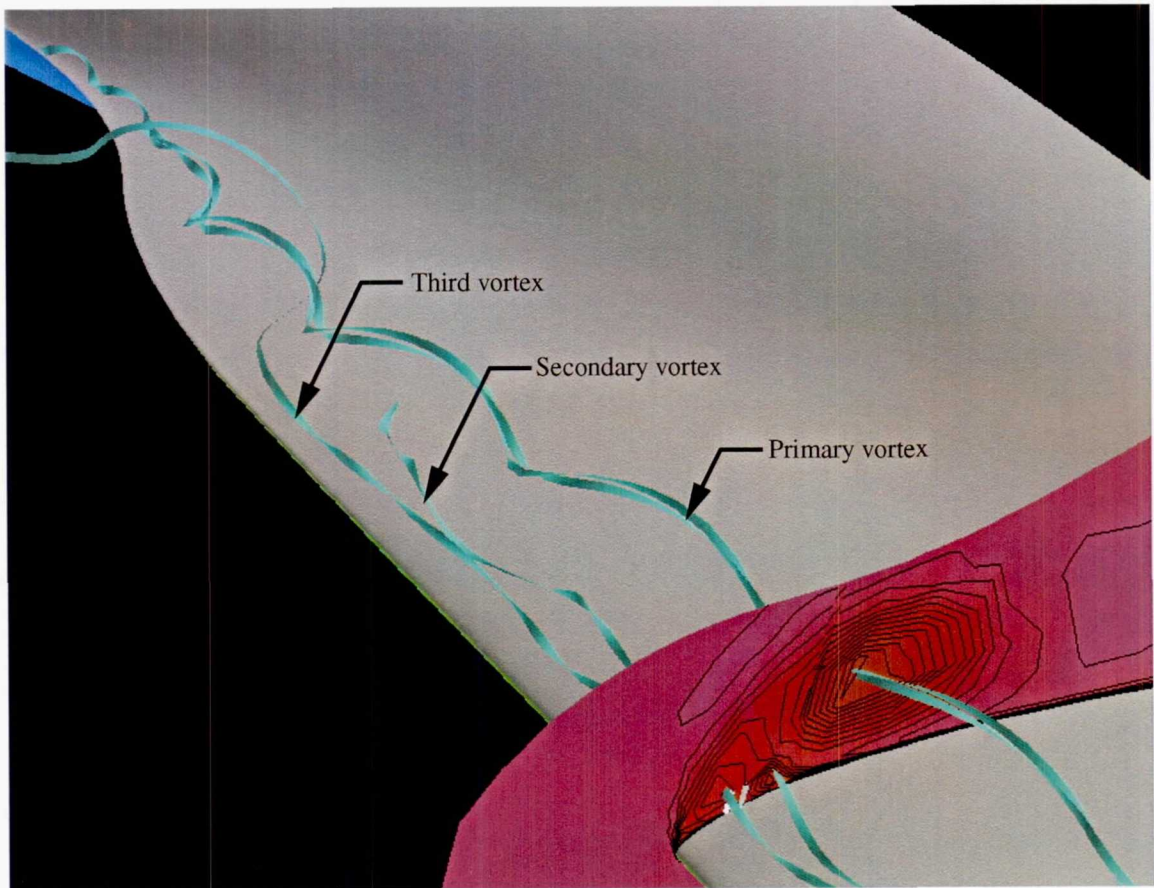


(a) Measured velocity profiles.



(b) Some predicted global features at FS 295.

Figure 25. Off-surface flow features for boundary-layer rake locations 7 and 5 on F-16XL-1 airplane for FC 7 ($\alpha_{\text{nom}} = 13^\circ$; $\beta_{\text{nom}} = 0^\circ$; $M_\infty = 0.29$; $h = 5000$ ft; $R_n = 44.4 \times 10^6$; FS \approx 295).



(c) Origination of predicted vortex systems inboard of wing crank.

Figure 25. Concluded.

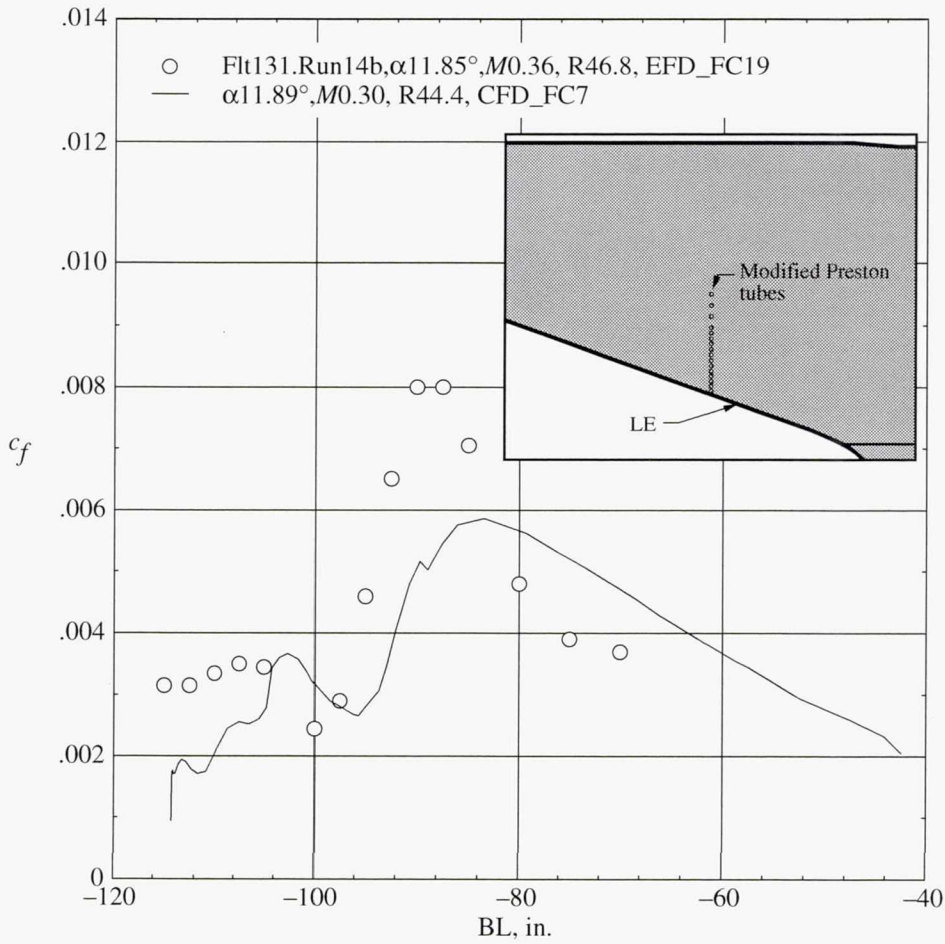
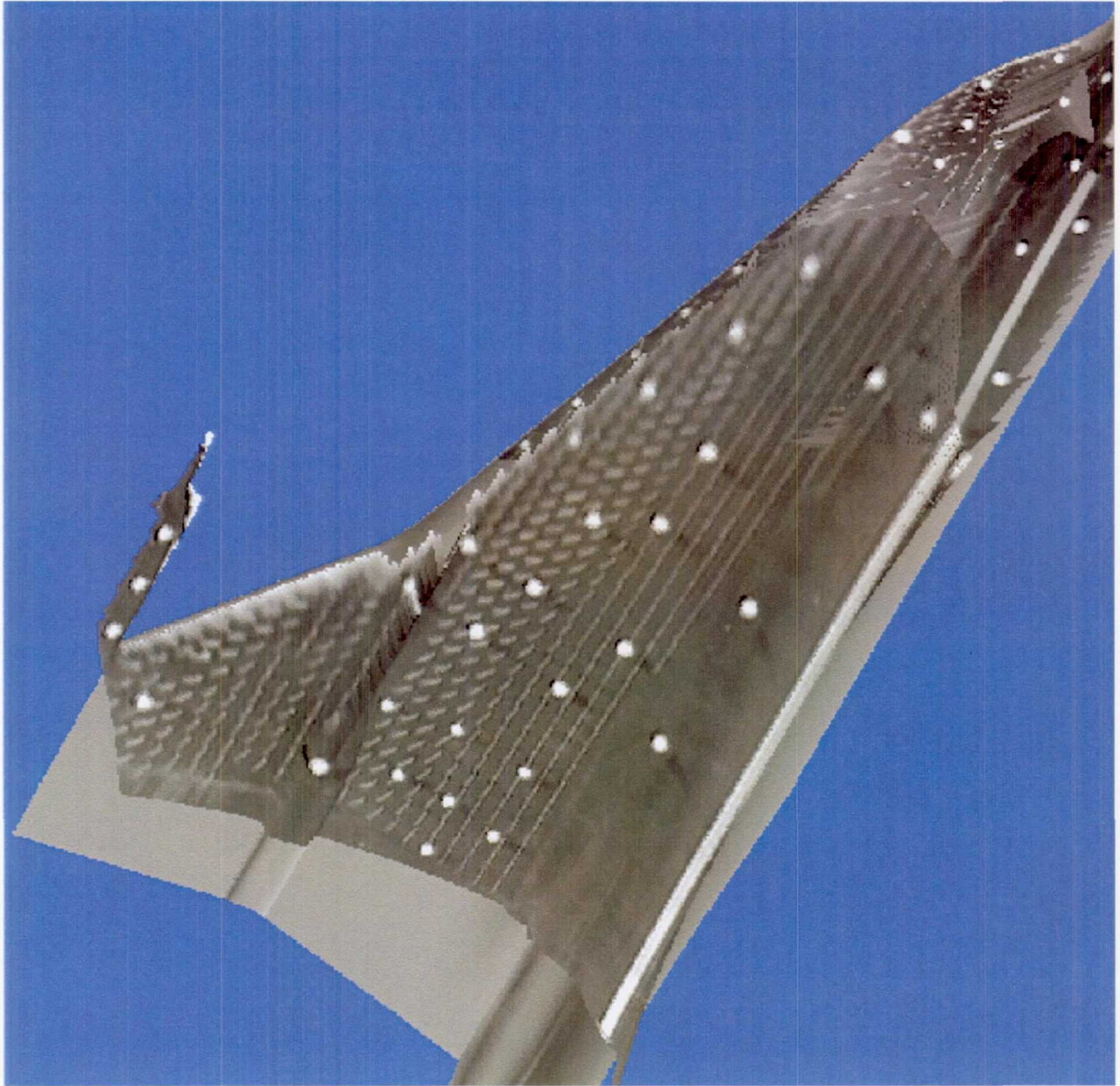
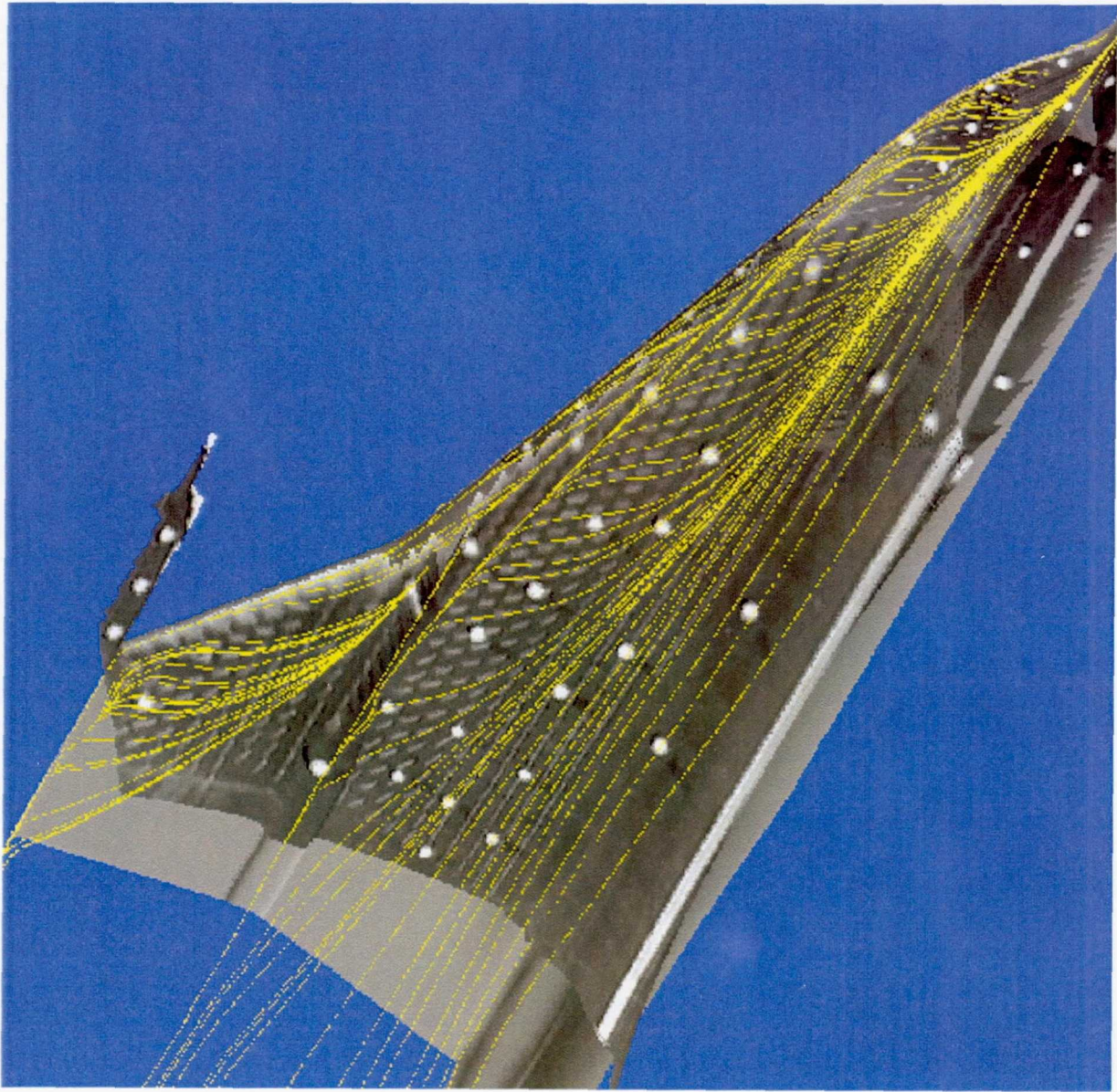


Figure 26. Predicted and measured c_f on F-16XL-1 airplane at FC 330 for $M_{\infty,avg} = 0.33$, $\alpha_{avg} = 11.9^\circ$, $\beta_{nom} = 0^\circ$, $R_{n,avg} = 45.6 \times 10^6$.



(a) Tuft images projected from three cameras onto aircraft grid.

Figure 27. Flight tuft data from three cameras on F-16XL-1 airplane and CFD solution at FC 46 ($\alpha = 10.4^\circ$; $M_\infty = 0.53$; $R_n = 46.90 \times 10^6$).



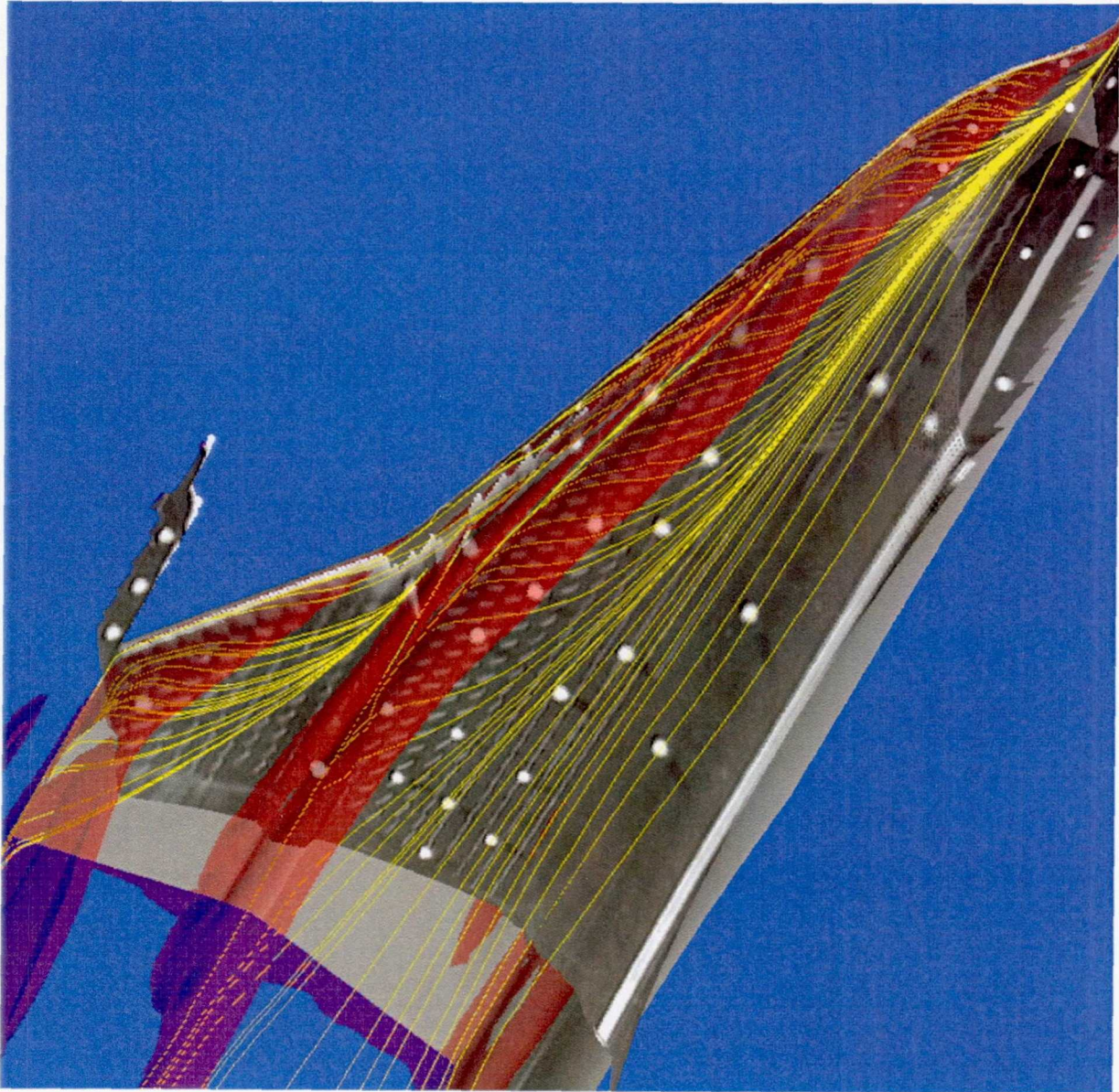
(b) Combination of tuft images and CFD surface streamlines.

Figure 27. Continued.



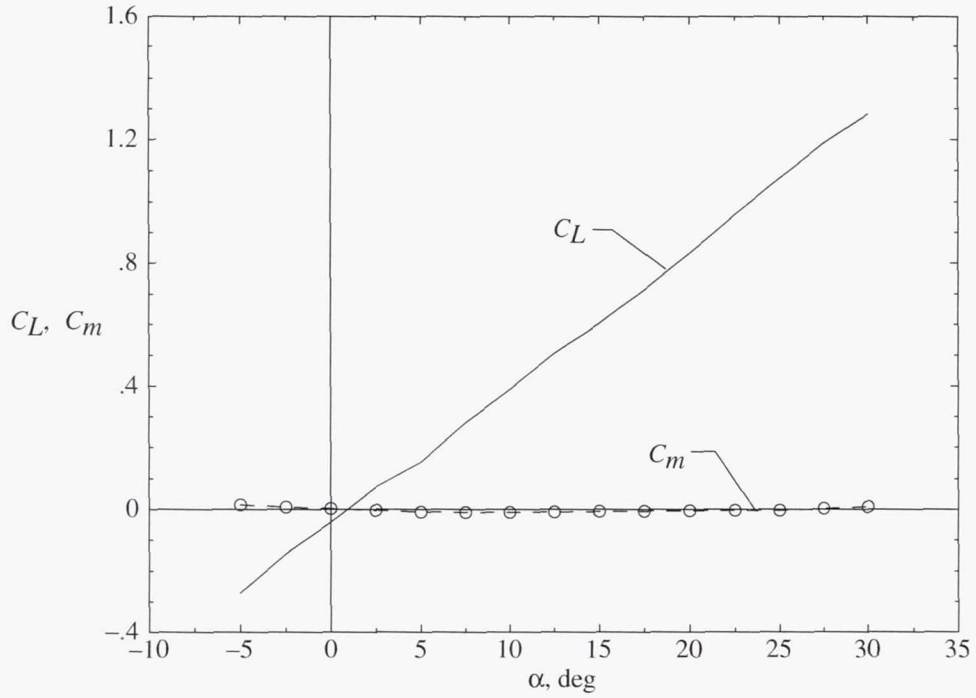
(c) Vortex systems determined from CFD stagnation pressures (PLOT3D) at 0.78.

Figure 27. Continued.

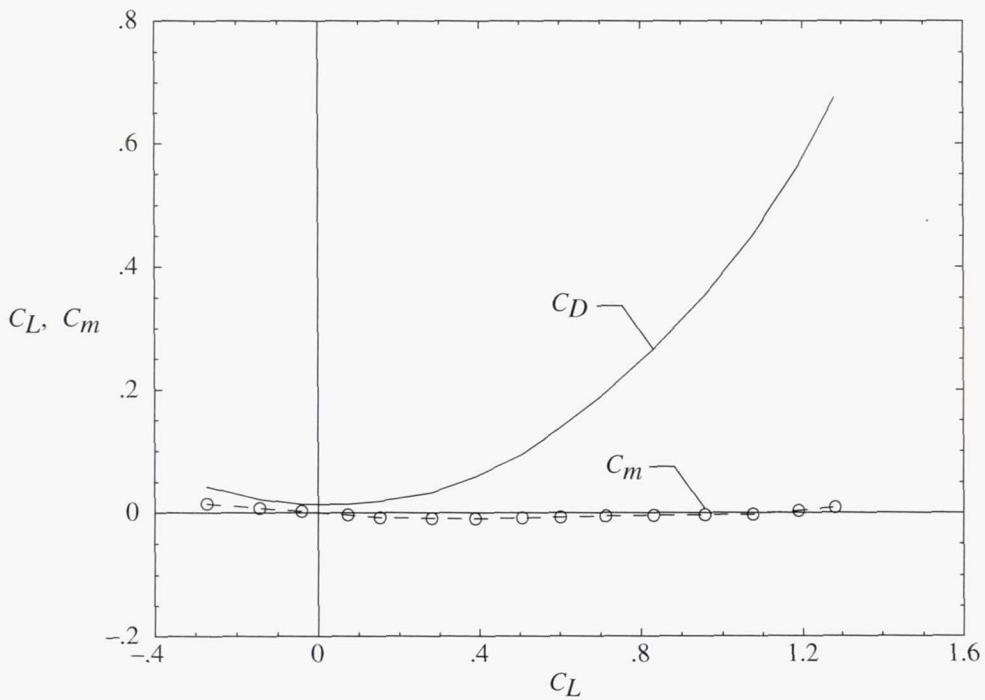


(d) Combination of tuft images, streamlines, and vortex systems.

Figure 27. Concluded.

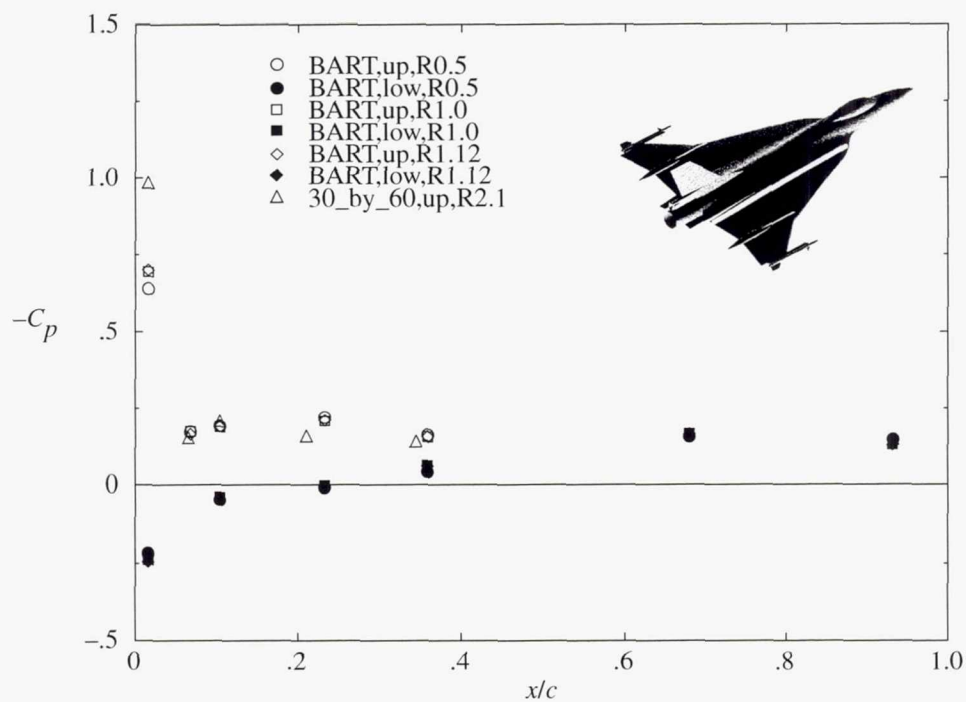


(a) C_D and C_m versus α .

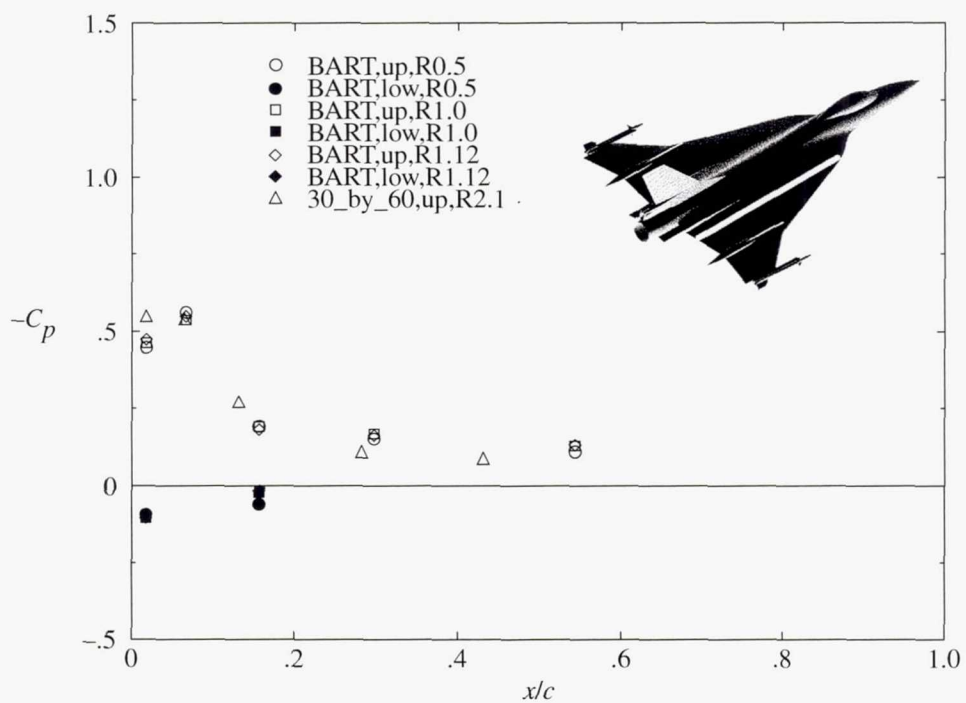


(b) C_D and C_m versus C_L .

Figure 28. Longitudinal aerodynamic characteristics of 0.18-scaled model of F-16XL-1 airplane with air dams and missiles on and controls undeflected at $M_\infty = 0.07$ and $R_n = 2.1 \times 10^6$.

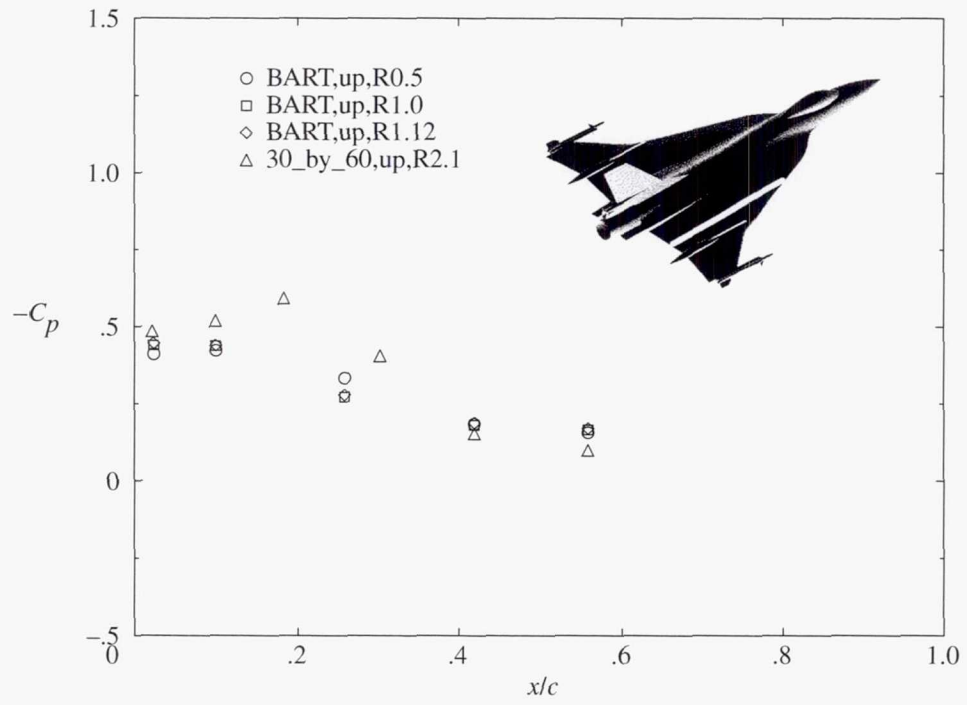


(a) BL 55.

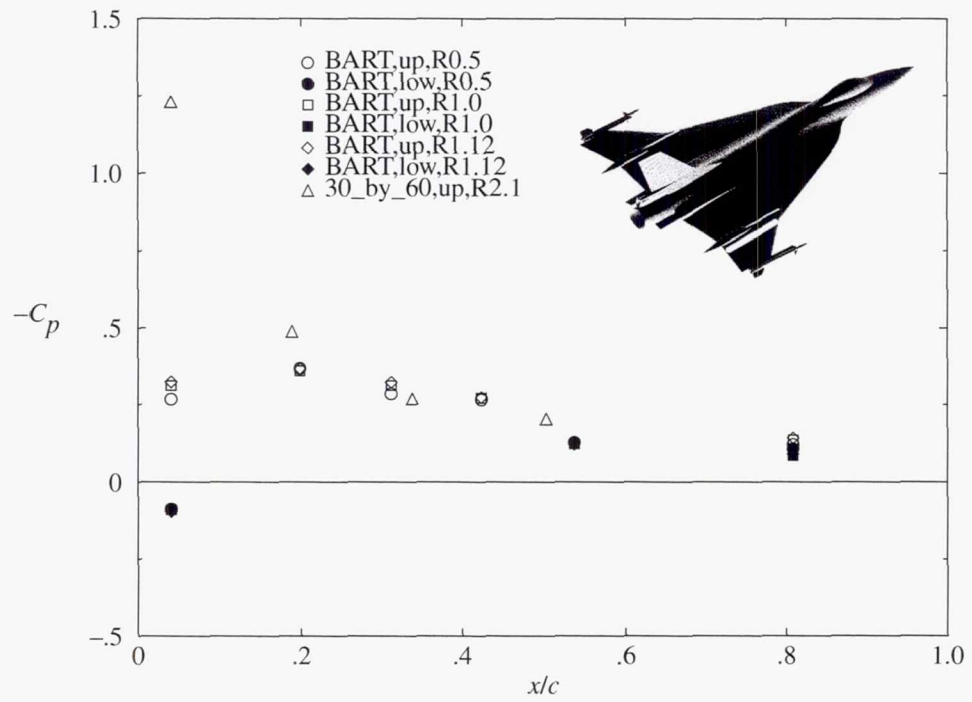


(b) BL 70.

Figure 29. Effect of R_n variation on local C_p for 0.04- (BART) and 0.18-scaled (30_by_60) models of F-16XL-1 airplane in BART and 30- by 60-Foot Tunnel, respectively, with air dams and missiles for $\alpha = 5^\circ$ at $M_\infty \leq 0.2$.

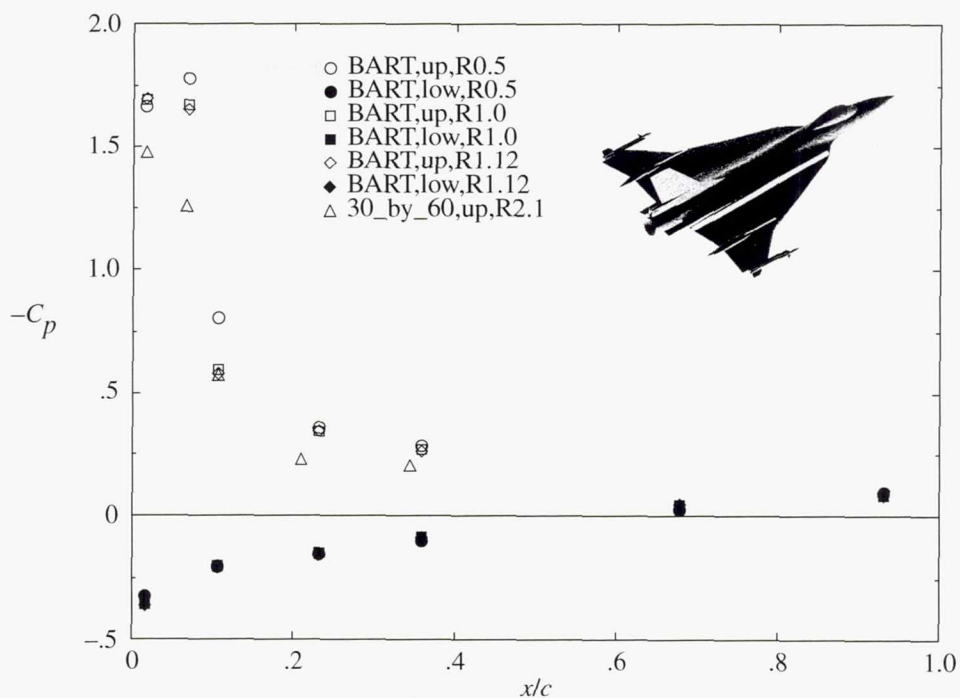


(c) BL = 95.

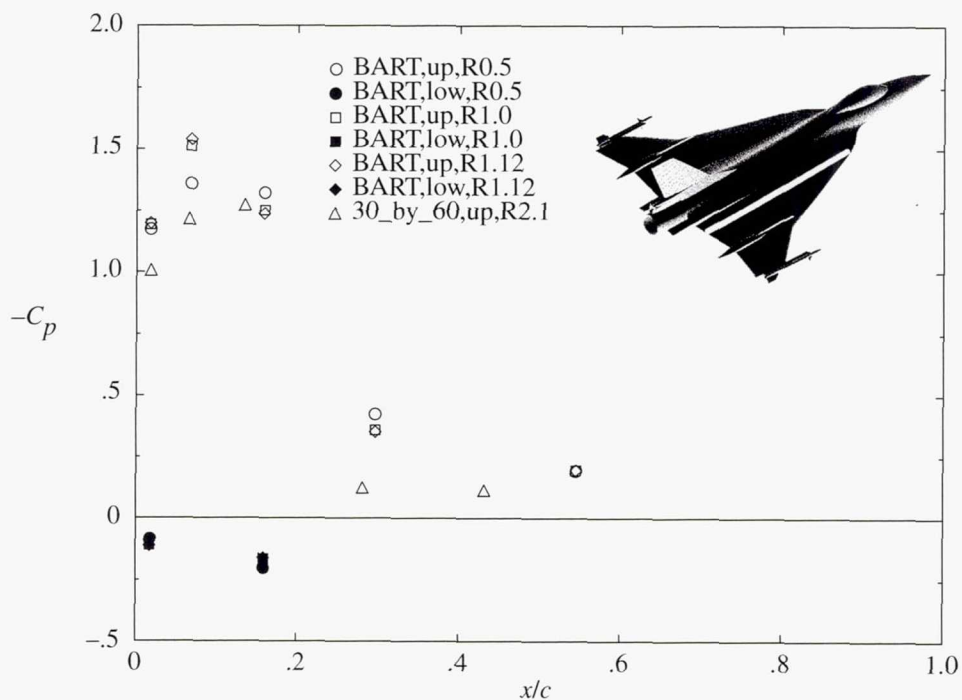


(d) BL = 147.5.

Figure 29. Concluded.

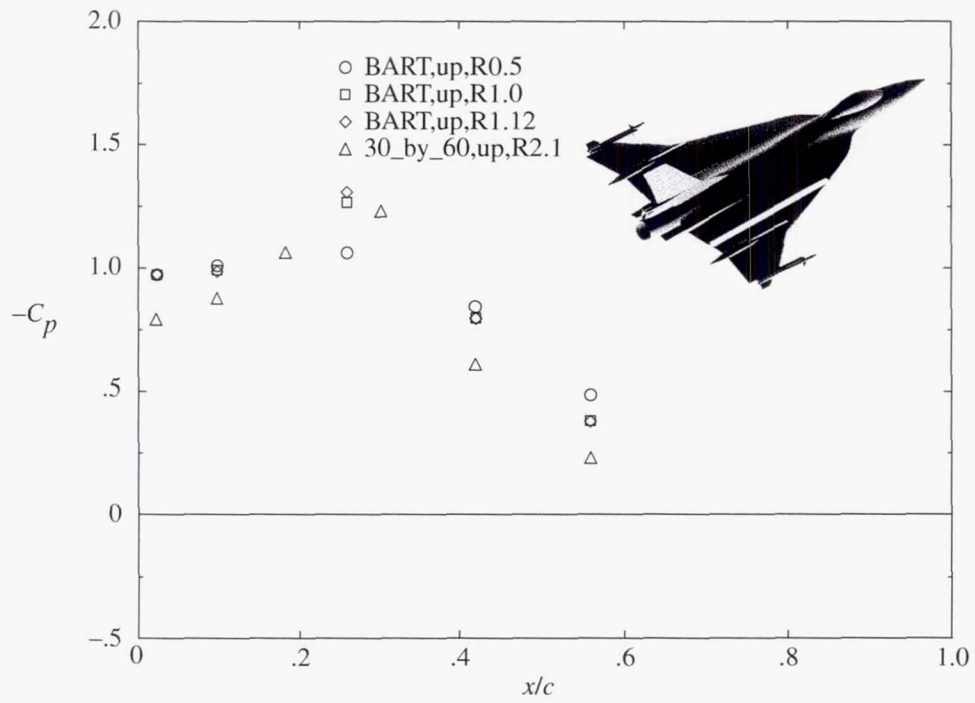


(a) BL 55.

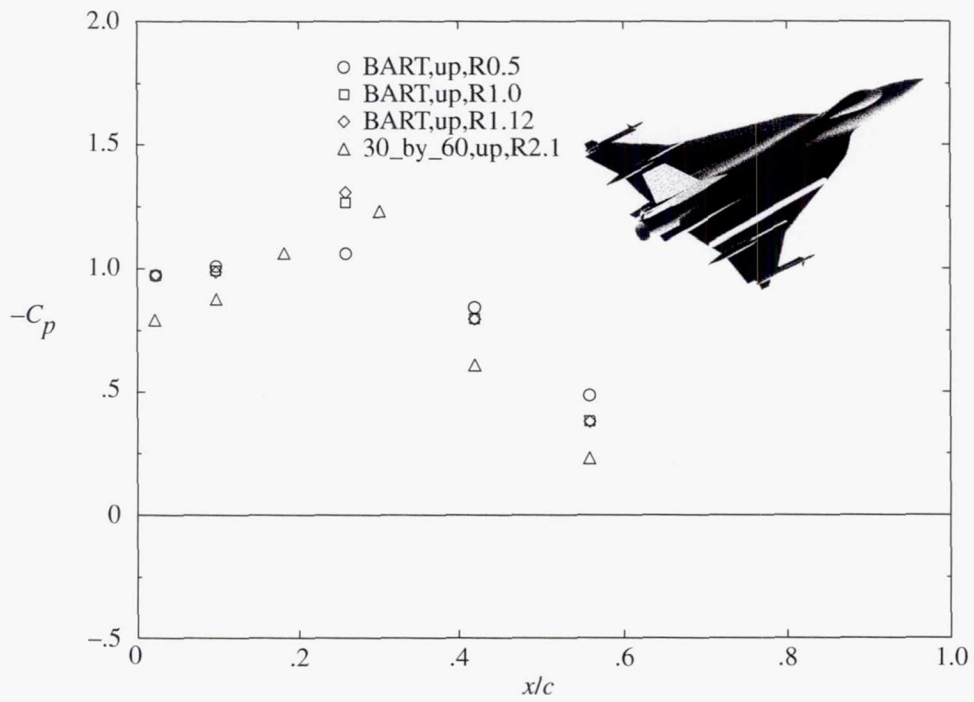


(b) BL 70.

Figure 30. Effect of R_n variation on local C_p for 0.04- (BART) and 0.18-scaled (30_by_60) models of F-16XL-1 airplane in BART and 30- by 60-Foot Tunnel, respectively, with air dams and missiles for $\alpha = 13^\circ$ at $M_\infty \leq 0.2$.

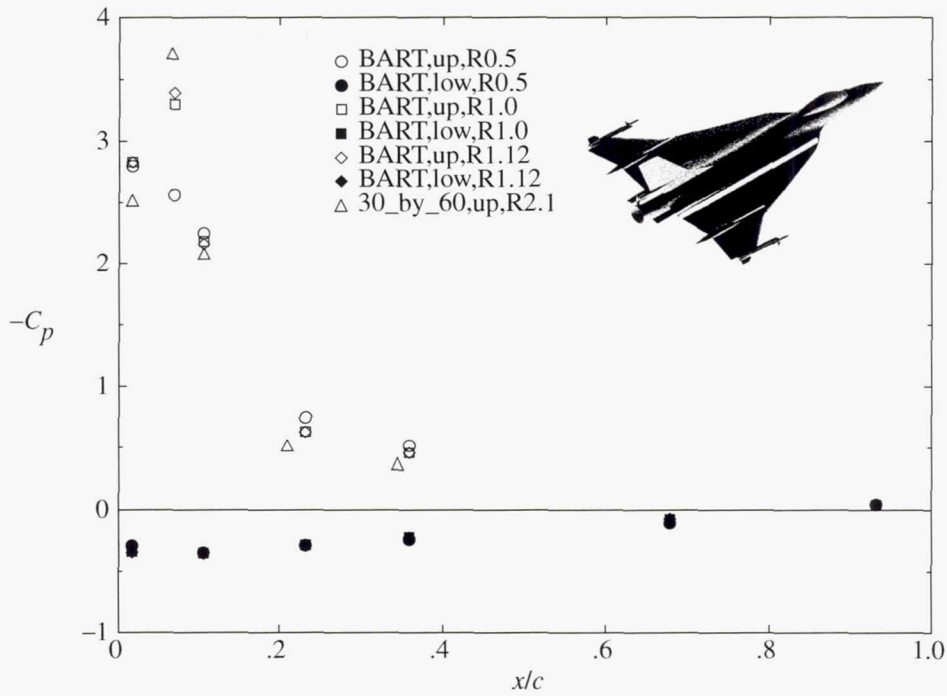


(c) BL 95.

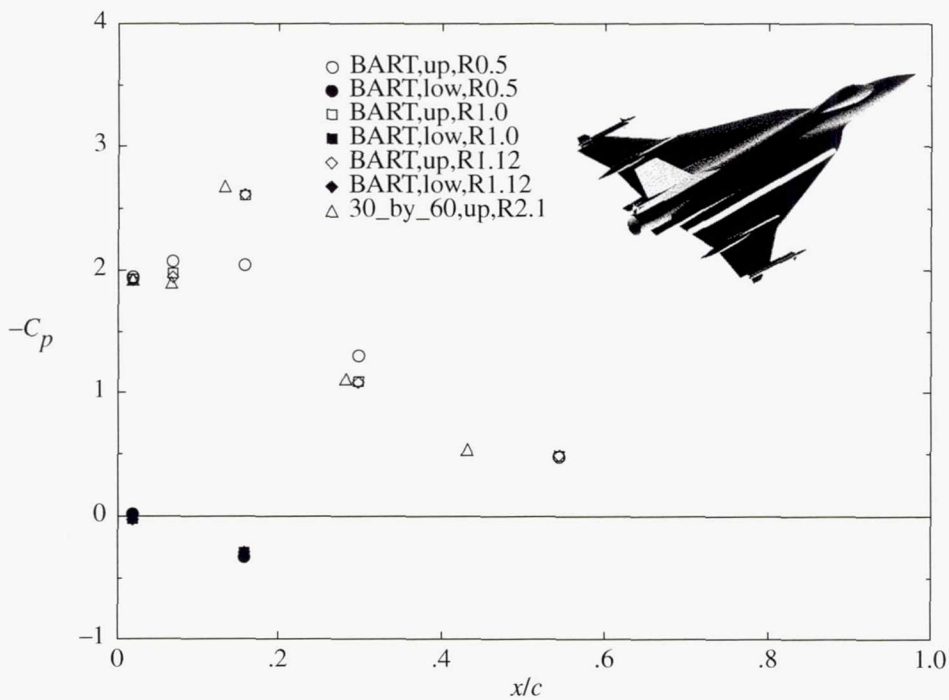


(d) BL 147.5.

Figure 30. Concluded.

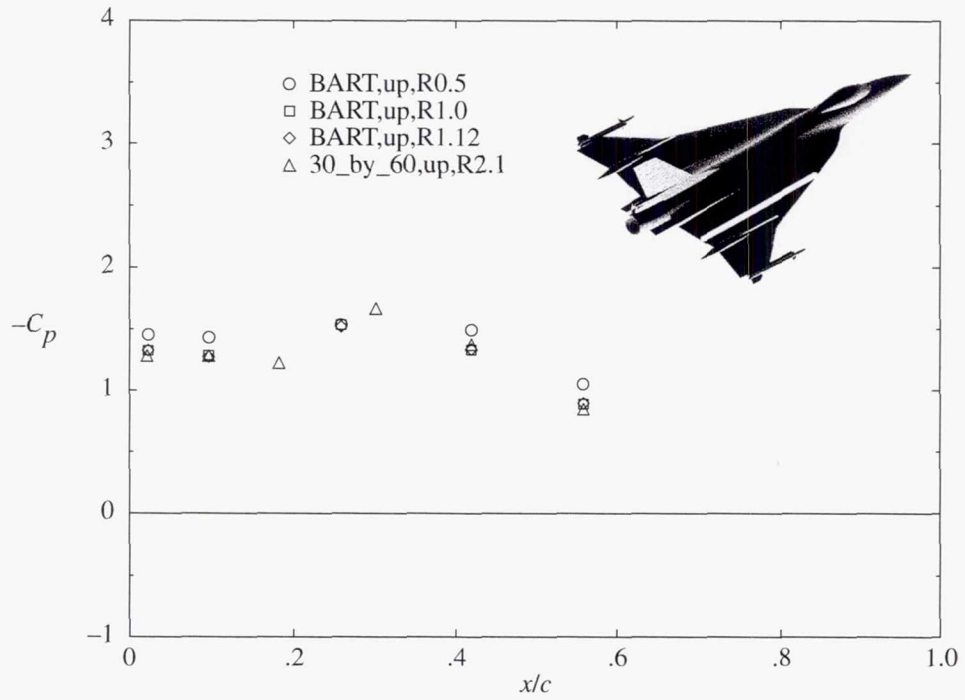


(a) BL 55.

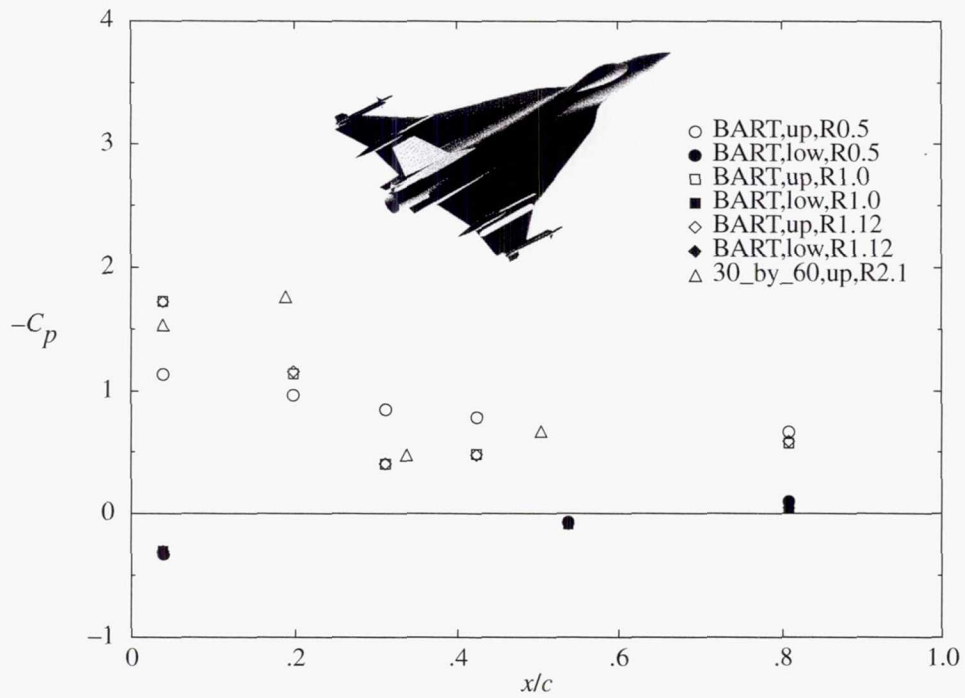


(b) BL 70.

Figure 31. Effect of R_n variation on local C_p for 0.04- (BART) and 0.18-scaled (30_by_60) models of F-16XL-1 airplane in BART and 30- by 60-Foot Tunnel, respectively, with air dams and missiles for $\alpha = 20^\circ$ at $M_\infty \leq 0.2$.

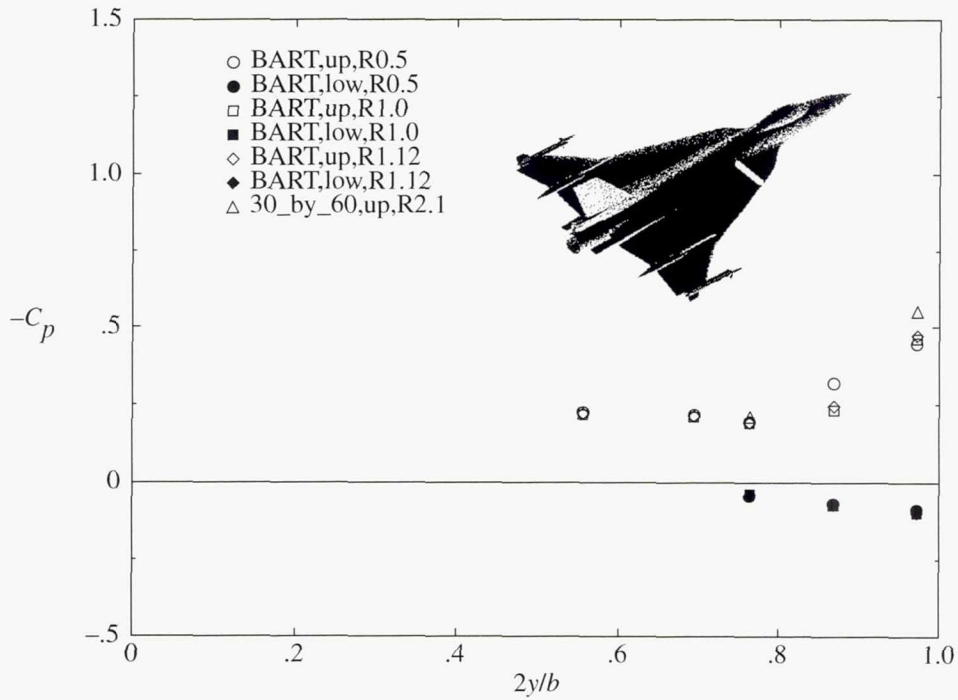


(a) BL 95.

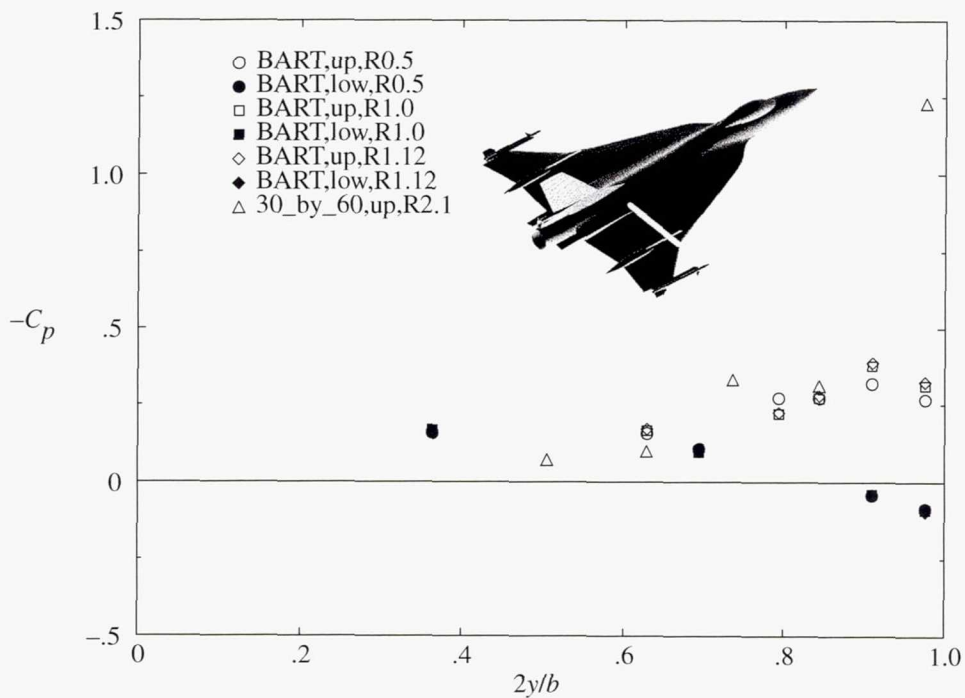


(b) BL 147.5.

Figure 31. Concluded.

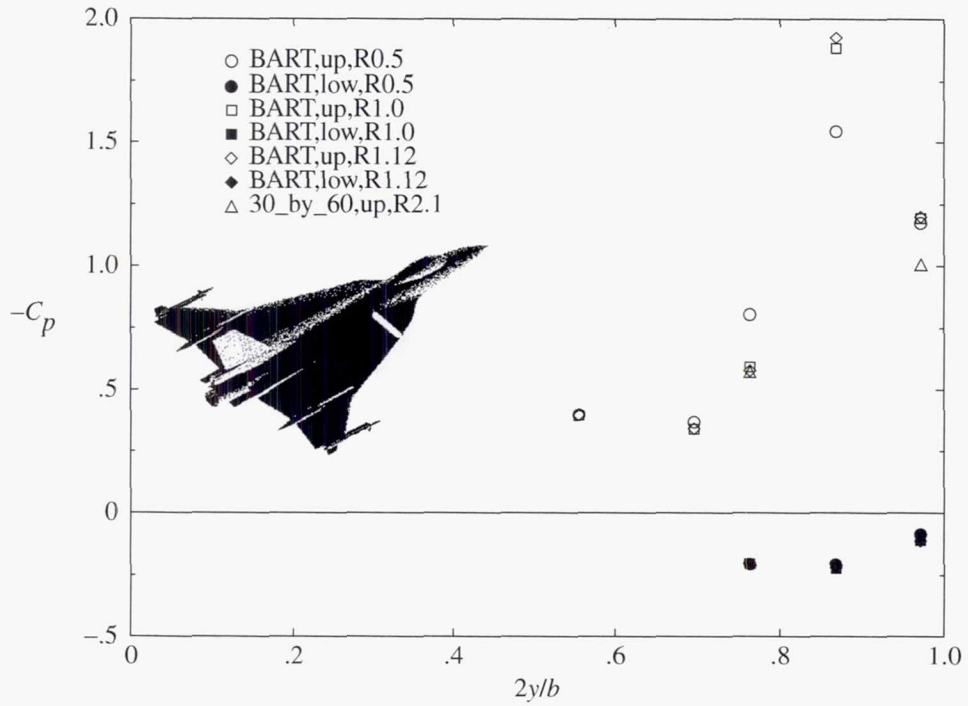


(a) FS 215.

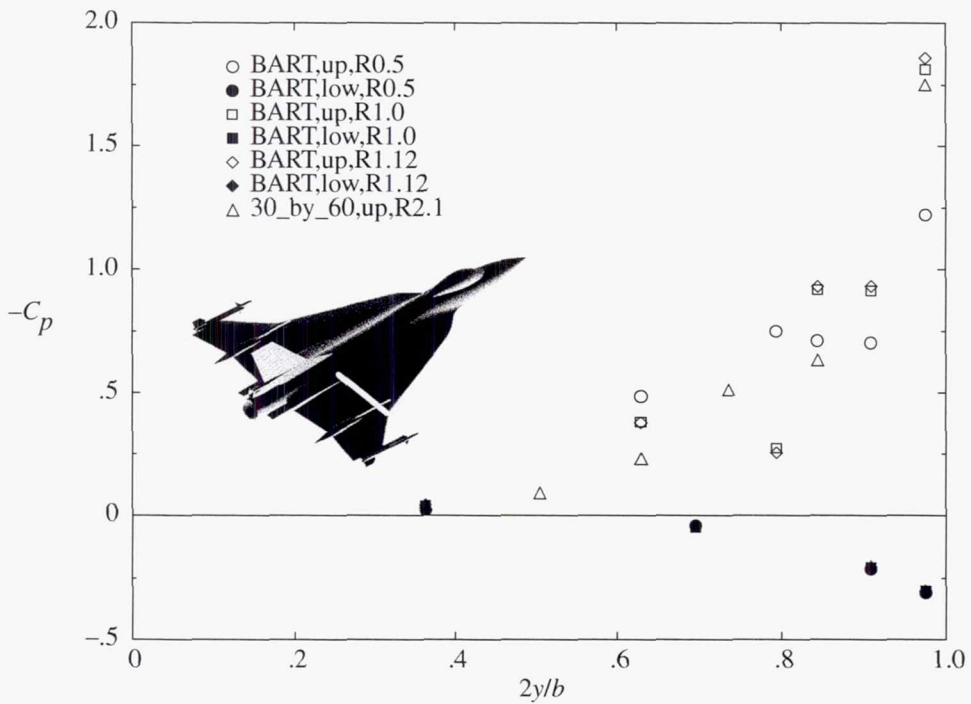


(b) FS 407.5.

Figure 32. Effect of R_n variation on local C_p for 0.04- (BART) and 0.18-scaled (30_by_60) models of F-16XL-1 airplane in BART and 30- by 60-Foot Tunnel, respectively, with air dams and missiles for $\alpha = 5^\circ$ at $M_\infty \leq 0.2$.

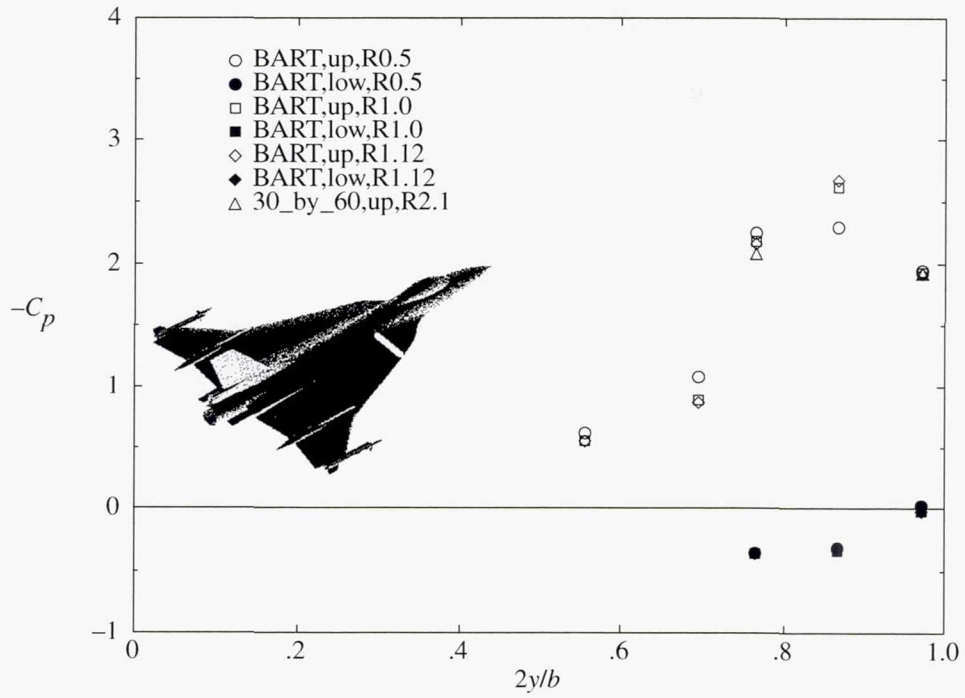


(a) FS 215.

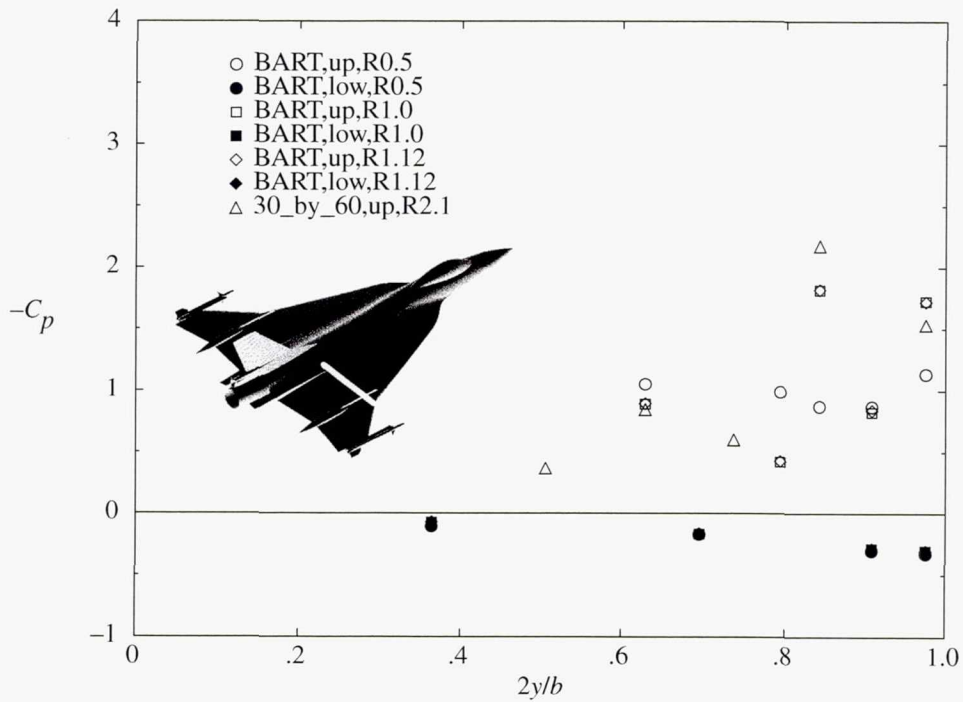


(b) FS 407.5.

Figure 33. Effect of R_n variation on local C_p for 0.04- (BART) and 0.18-scaled (30_by_60) models of F-16XL-1 airplane in BART and 30- by 60-Foot Tunnel, respectively, with air dams and missiles for $\alpha = 13^\circ$ at $M_\infty \leq 0.2$.

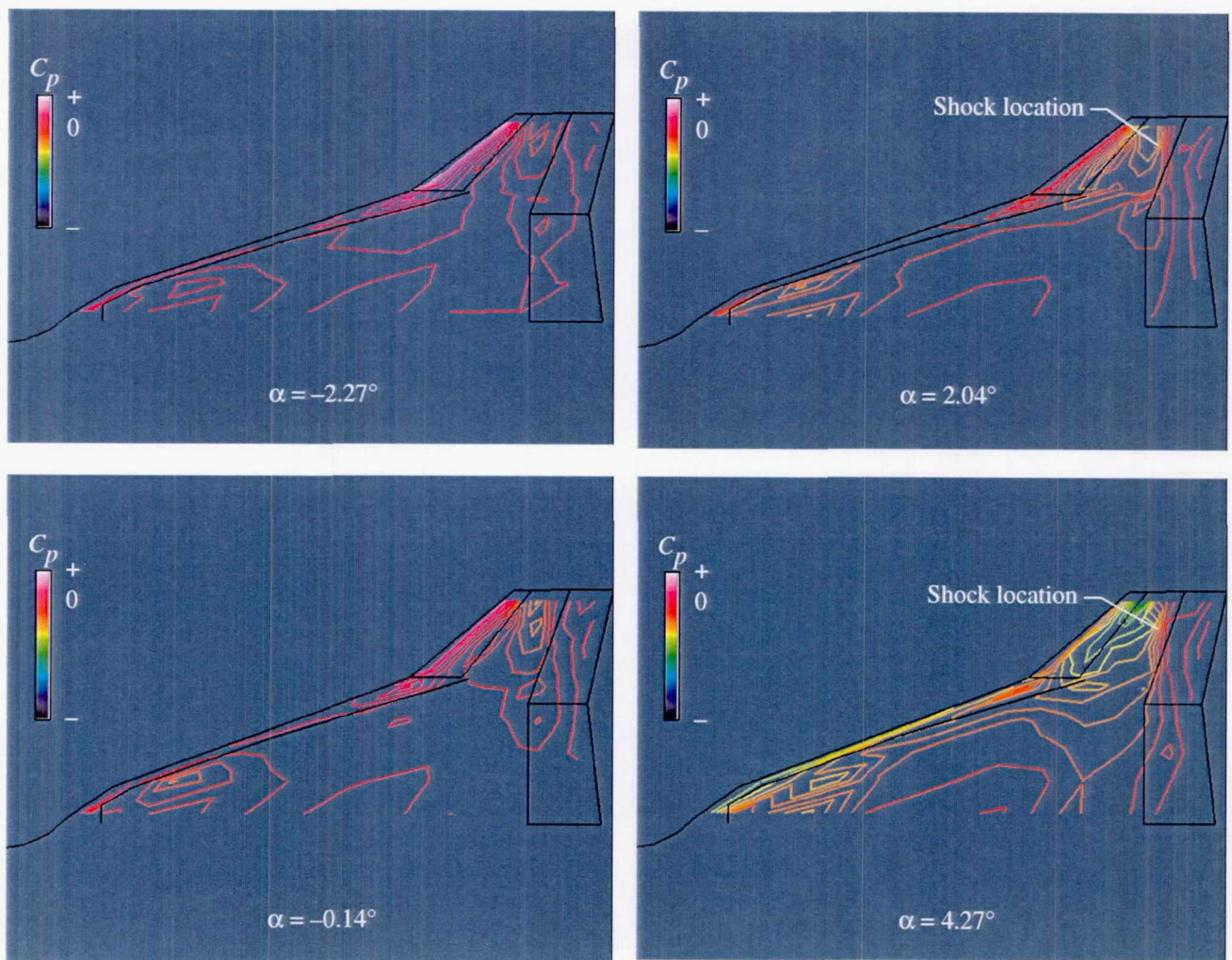


(a) FS 215.



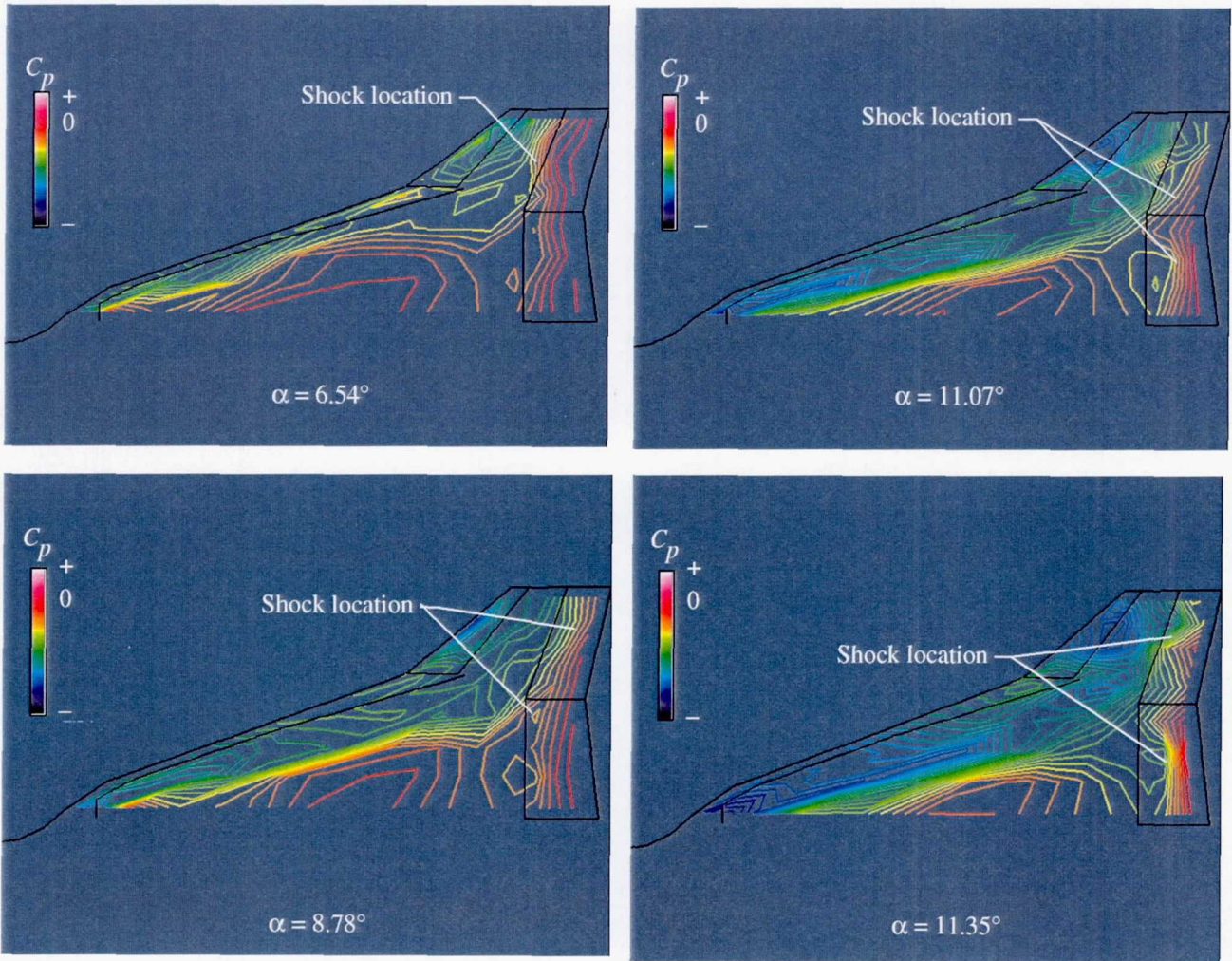
(b) FS 407.5.

Figure 34. Effect of R_n variation on local C_p for 0.04- (BART) and 0.18-scaled (30_by_60) models of F-16XL-1 airplane in BART and 30- by 60-Foot Tunnel, respectively, with air dams and missiles for $\alpha = 20^\circ$ at $M_\infty \leq 0.2$.



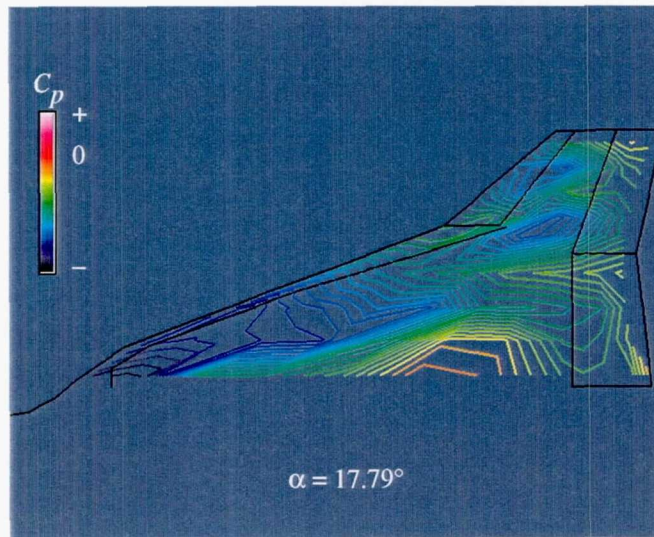
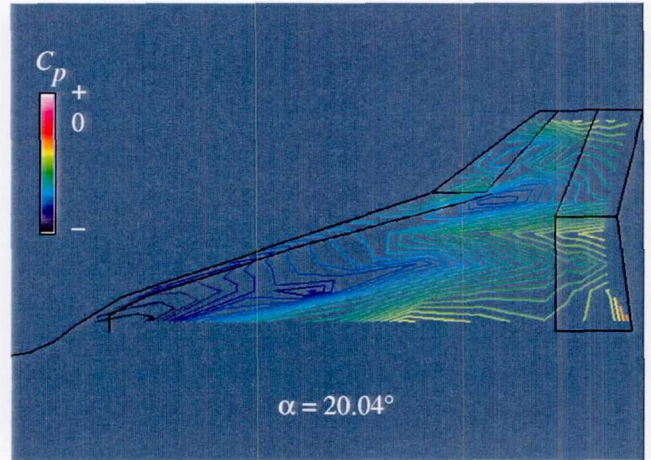
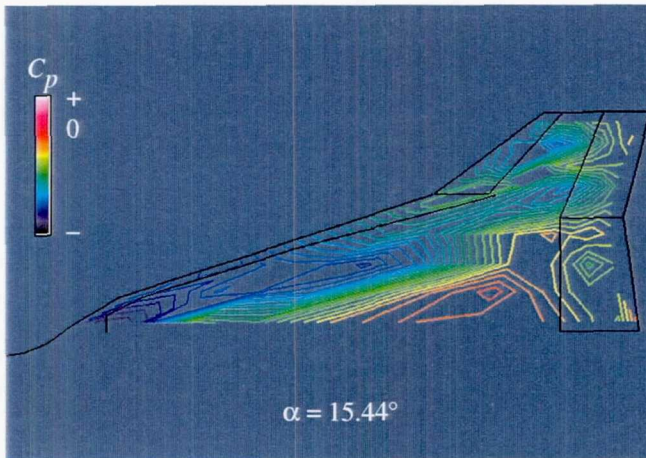
(a) $-2.27^\circ \leq \alpha \leq 4.27^\circ$.

Figure 35. Effect of α on $C_{p,u}$ contours for 0.11-scaled model in Ames 11-Foot Tunnel at $M_\infty = 0.95$ and $R_n = 2.3 \times 10^6$.



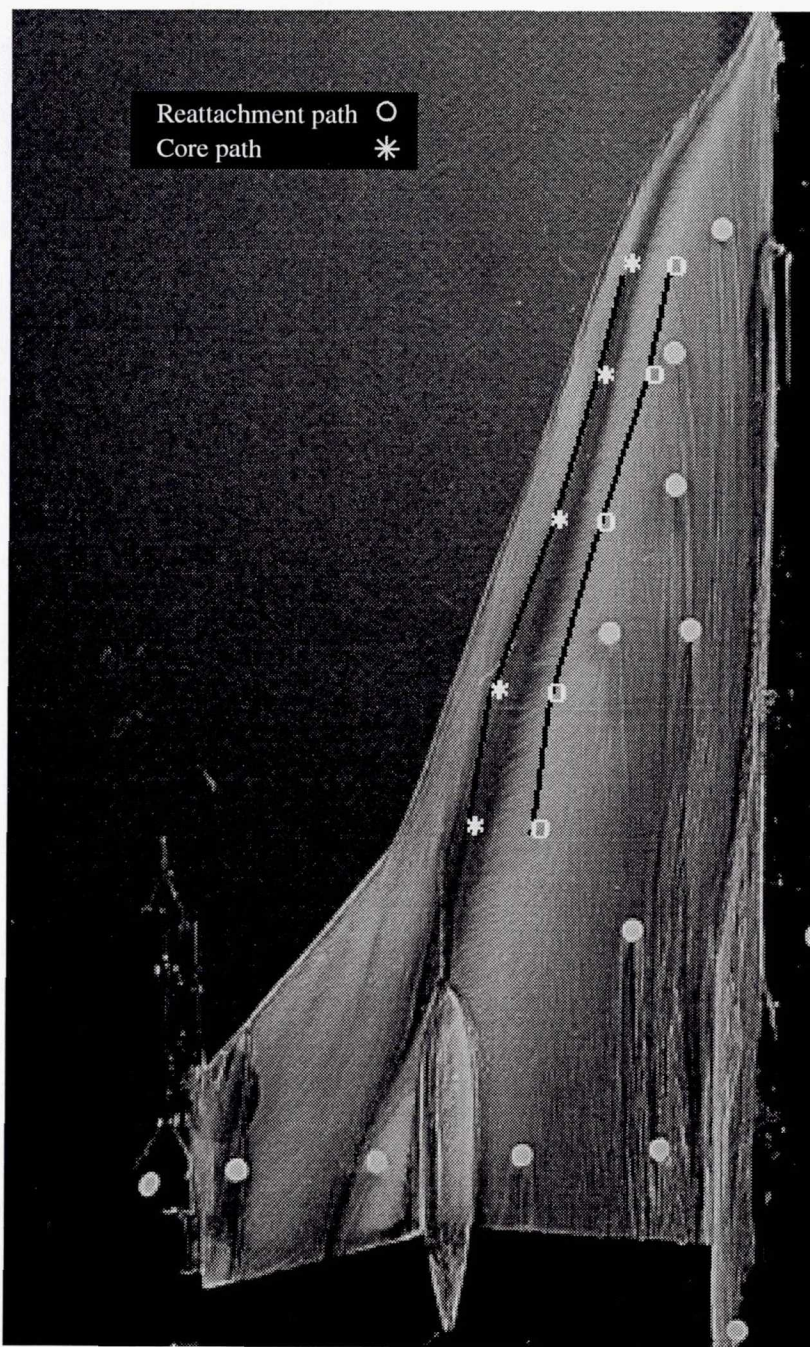
(b) $6.54^\circ \leq \alpha \leq 11.35^\circ$.

Figure 35. Continued.



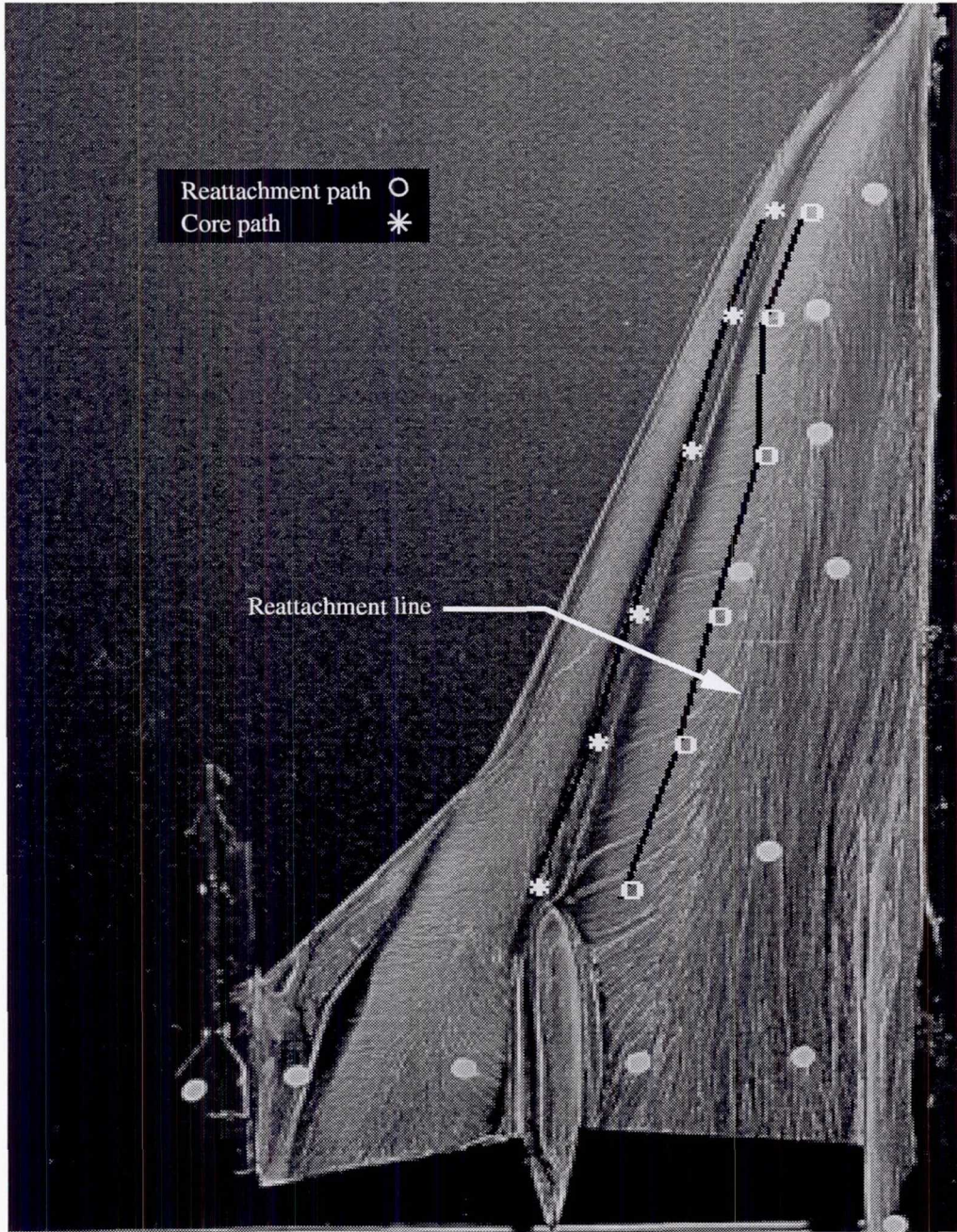
(c) $15.44^\circ \leq \alpha \leq 20.04^\circ$.

Figure 35. Concluded.



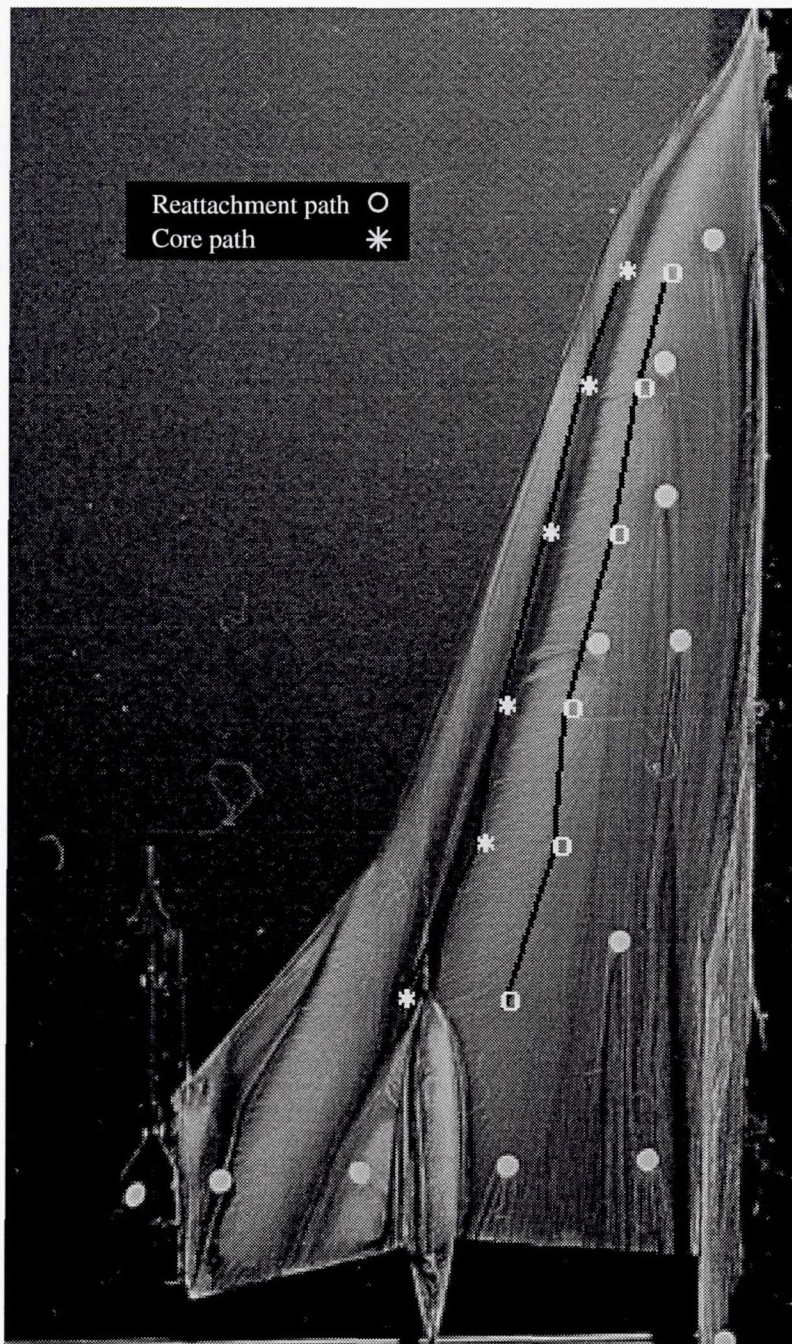
(a) $\alpha = 10^\circ$; $M_\infty = 0.15$; $R_n = 1 \times 10^6$.

Figure 36. Superposition of projected core path and reattachment path onto oil flow image for F-16XL-1 BART model without air dams.



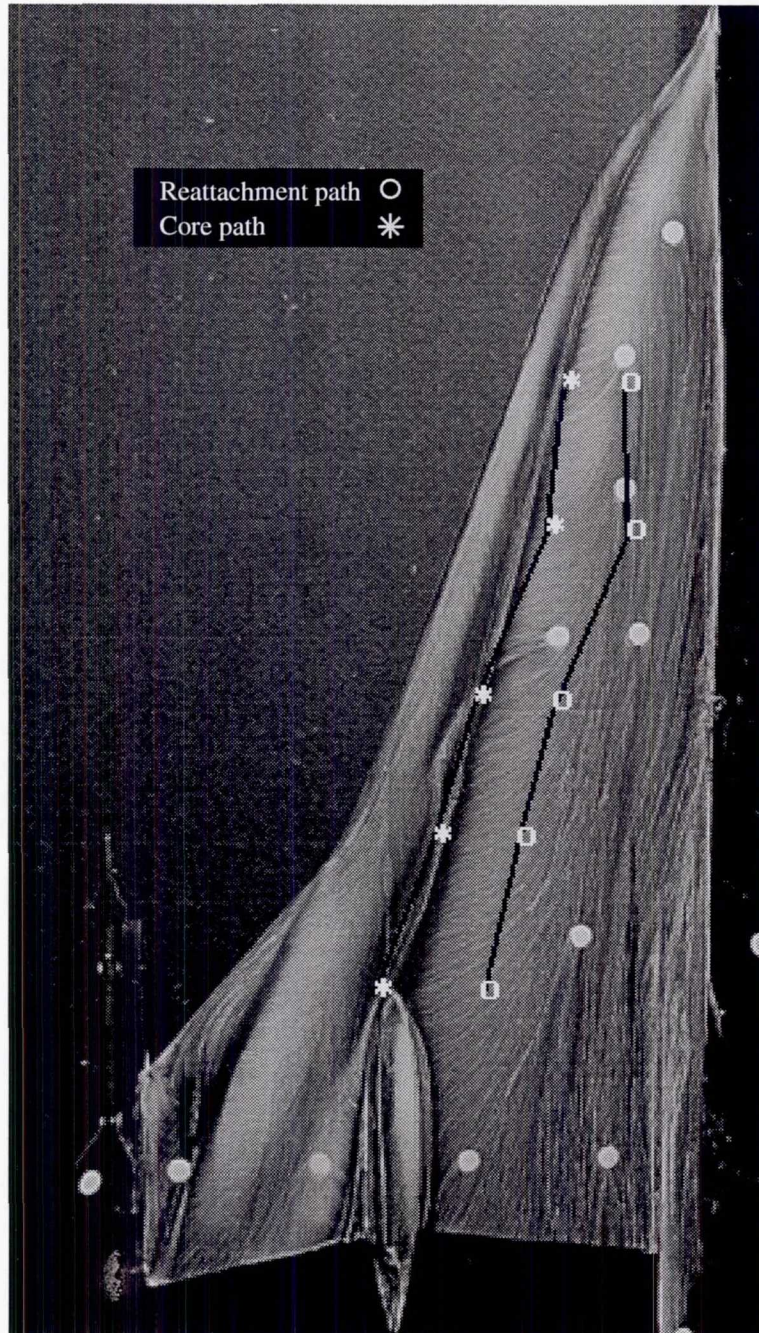
(b) $\alpha = 13^\circ$; $M_\infty = 0.07$; $R_n = 0.5 \times 10^6$.

Figure 36. Continued.



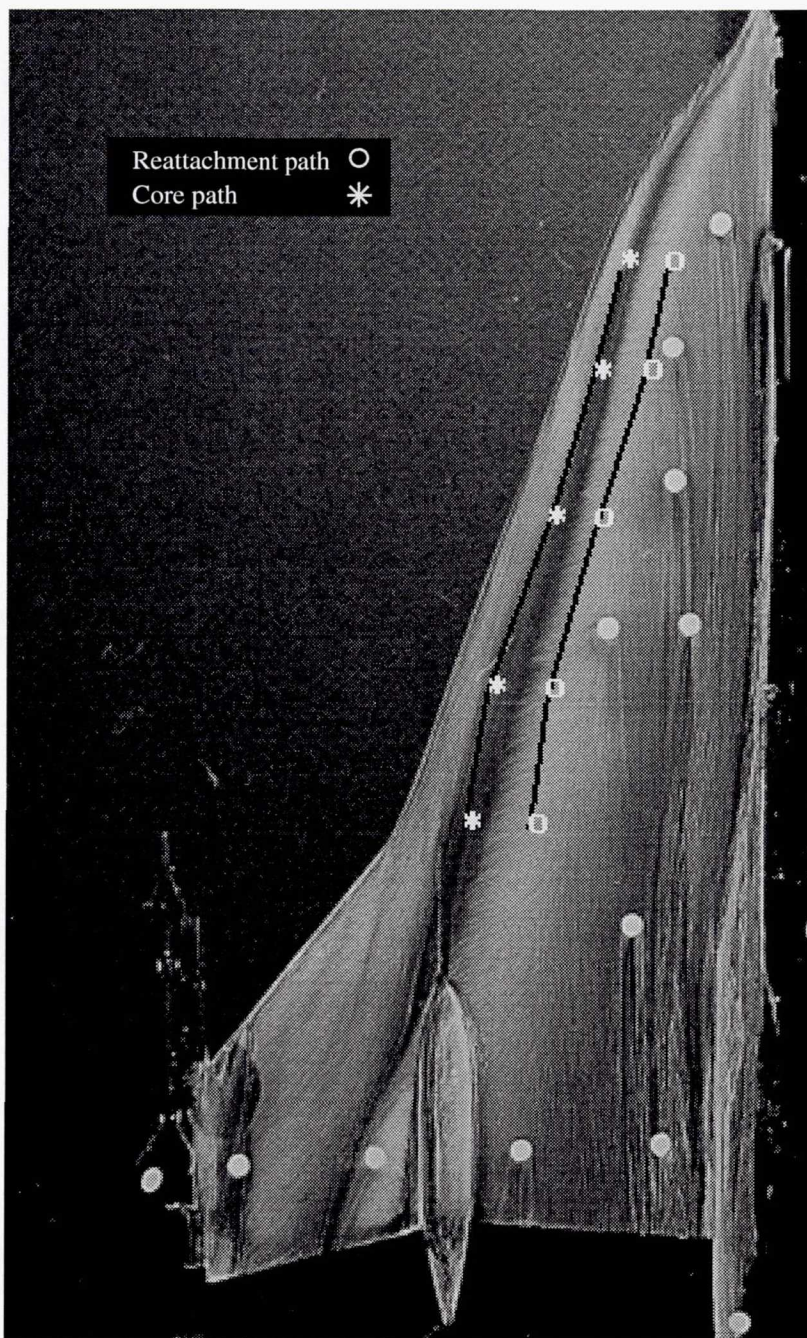
(c) $\alpha = 13^\circ$; $M_\infty = 0.15$; $R_n = 1 \times 10^6$.

Figure 36. Continued.



(d) $\alpha = 15^\circ$; $M_\infty = 0.07$; $R_n = 0.5 \times 10^6$.

Figure 36. Continued.



(e) $\alpha = 15^\circ$; $M_\infty = 0.15$; $R_n = 1 \times 10^6$.

Figure 36. Concluded.

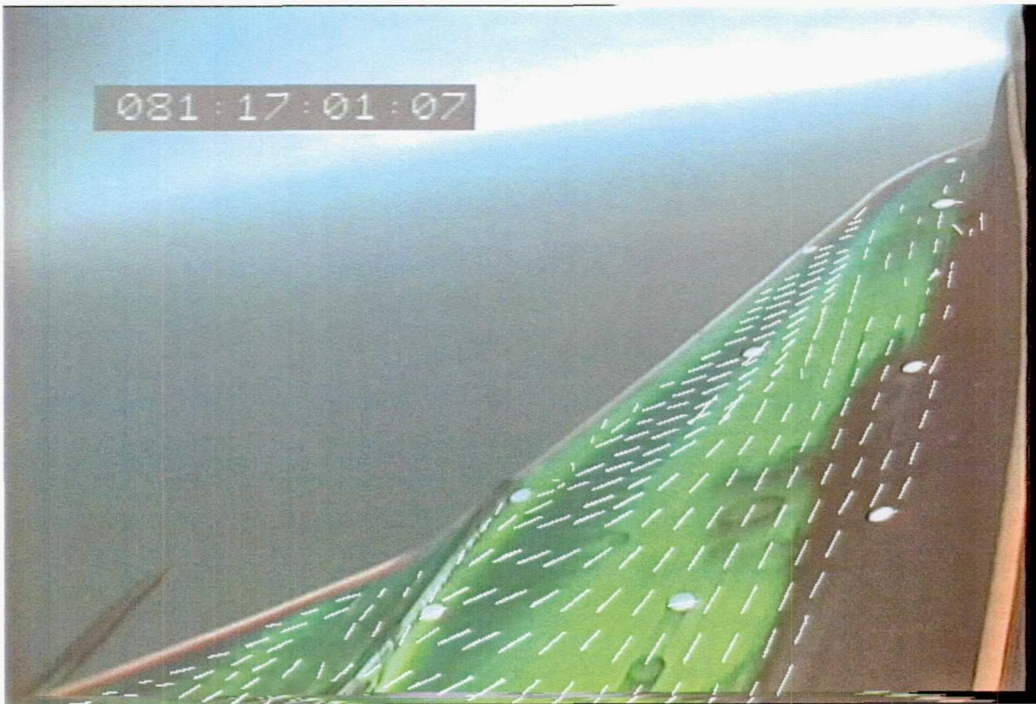


Figure 37. Superposition of liquid crystal and tuft image data for F-16XL-1 airplane at $\alpha \approx 13^\circ$, $M_\infty = 0.28$, and $R_n = 47 \times 10^6$.

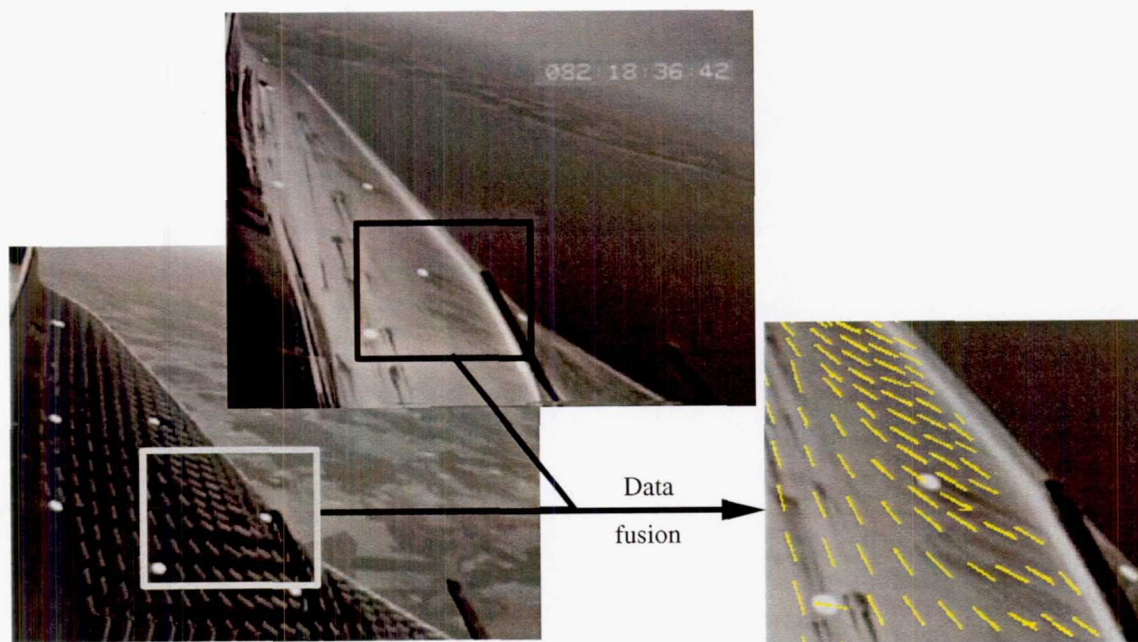


Figure 38. Superposition of liquid crystal and tuft image data for F-16XL-1 airplane at $\alpha \approx 13^\circ$, $M_\infty = 0.28$, and $R_\eta = 47 \times 10^6$.

REPORT DOCUMENTATION PAGE			Form Approved OMB No. 0704-0188	
Public reporting burden for this collection of information is estimated to average 1 hour per response, including the time for reviewing instructions, searching existing data sources, gathering and maintaining the data needed, and completing and reviewing the collection of information. Send comments regarding this burden estimate or any other aspect of this collection of information, including suggestions for reducing this burden, to Washington Headquarters Services, Directorate for Information Operations and Reports, 1215 Jefferson Davis Highway, Suite 1204, Arlington, VA 22202-4302, and to the Office of Management and Budget, Paperwork Reduction Project (0704-0188), Washington, DC 20503.				
1. AGENCY USE ONLY (Leave blank)	2. REPORT DATE February 2001	3. REPORT TYPE AND DATES COVERED Technical Publication		
4. TITLE AND SUBTITLE Flight, Wind-Tunnel, and Computational Fluid Dynamics Comparison for Cranked Arrow Wing (F-16XL-1) at Subsonic and Transonic Speeds		5. FUNDING NUMBERS WU 522-31-31-03		
6. AUTHOR(S) John E. Lamar, Clifford J. Obara, Bruce D. Fisher, and David F. Fisher				
7. PERFORMING ORGANIZATION NAME(S) AND ADDRESS(ES) NASA Langley Research Center Hampton, VA 23681-2199		8. PERFORMING ORGANIZATION REPORT NUMBER L-18018		
9. SPONSORING/MONITORING AGENCY NAME(S) AND ADDRESS(ES) National Aeronautics and Space Administration Washington, DC 20546-0001		10. SPONSORING/MONITORING AGENCY REPORT NUMBER NASA/TP-2001-210629		
11. SUPPLEMENTARY NOTES John E. Lamar, Clifford J. Obara, and Bruce D. Fisher: Langley Research Center, Hampton, VA; David F. Fisher: Dryden Flight Research Center, Edwards, CA.				
12a. DISTRIBUTION/AVAILABILITY STATEMENT Unclassified-Unlimited Subject Category 02 Availability: NASA CASI (301) 621-0390		12b. DISTRIBUTION CODE Distribution: Standard		
13. ABSTRACT (Maximum 200 words) Geometrical, flight, computational fluid dynamics (CFD), and wind-tunnel studies for the F-16XL-1 airplane are summarized over a wide range of test conditions. Details are as follows: (1) For geometry, the upper surface of the airplane and the numerical surface description compare reasonably well. (2) For flight, CFD, and wind-tunnel surface pressures, the comparisons are generally good at low angles of attack at both subsonic and transonic speeds; however, local differences are present. In addition, the shock location at transonic speeds from wind-tunnel pressure contours is near the aileron hinge line and generally is in correlative agreement with flight results. (3) For boundary layers, flight profiles were predicted reasonably well for attached flow and underneath the primary vortex but not for the secondary vortex. Flight data indicate the presence of an interaction of the secondary vortex system and the boundary layer and the boundary-layer measurements show the secondary vortex located more outboard than predicted. (4) Predicted and measured skin friction distributions showed qualitative agreement for a two vortex system. (5) Web-based data-extraction and computational-graphical tools have proven useful in expediting the preceding comparisons. (6) Data fusion has produced insightful results for a variety of visualization-based data sets.				
14. SUBJECT TERMS F-16XL-1; Flow physics; Subsonic; Transonic; Data fusion		15. NUMBER OF PAGES 168		16. PRICE CODE A08
17. SECURITY CLASSIFICATION OF REPORT Unclassified	18. SECURITY CLASSIFICATION OF THIS PAGE Unclassified	19. SECURITY CLASSIFICATION OF ABSTRACT Unclassified	20. LIMITATION OF ABSTRACT UL	